# Cobalt / Copper Multilayers: Interplay of Microstructure and GMR and Recrystallization as the Key Towards Temperature Stability

Dissertation zur Erlangung des Grades einer
Doktorin der Naturwissenschaften
der Fakultät für Physik der
Universität Bielefeld

vorgelegt von
**Sonja Heitmann**
aus Halle Westfalen

19. März 2004

**Erklärung**

Hiermit versichere ich an Eides statt, dass ich die vorliegende Arbeit selbständig verfasst und keine anderen als die angegebenen Hilfsmittel verwendet habe.

Bielefeld, 19. März 2004

(Sonja Heitmann)

Gutachter:

Prof. Dr. Günter Reiss
Prof. Dr. Friederike Schmid

Datum des Einreichens der Arbeit: 19. März 2004
Tag der Disputation: 10. Mai 2004

# Contents

**1 Preface** **1**

**2 Interlayer Exchange Coupling** **3**

**3 Giant Magneto-Resistance** **11**

**4 X-Ray Characterization** **21**

4.1 X-Ray Diffraction . . . . . . . . . . . . . . . . . . . . . . . . . . . 22

4.1.1 Peak Location of Diffracted X-Rays . . . . . . . . . . . . 22

4.1.2 Intensity of Diffracted X-Rays . . . . . . . . . . . . . . . 23

4.1.3 Shape of Diffraction Peaks . . . . . . . . . . . . . . . . . 27

4.2 Special Aspects . . . . . . . . . . . . . . . . . . . . . . . . . . . . 28

4.2.1 Preferred Orientation . . . . . . . . . . . . . . . . . . . . 28

4.2.2 Crystallite Size . . . . . . . . . . . . . . . . . . . . . . . . 29

4.2.3 Residual Stress and Strain . . . . . . . . . . . . . . . . . 32

4.2.4 Multilayer Satellites . . . . . . . . . . . . . . . . . . . . . 33

4.3 X-Ray Reflectometry . . . . . . . . . . . . . . . . . . . . . . . . . 42

4.3.1 Specular X-Ray Reflectometry . . . . . . . . . . . . . . . 43

4.3.2 XRR Pattern Analysis . . . . . . . . . . . . . . . . . . . . 54

**5 Sample Preparation and Characterization Techniques** **62**

5.1 Sample Preparation . . . . . . . . . . . . . . . . . . . . . . . . . . 62

5.2 Characterization Techniques . . . . . . . . . . . . . . . . . . . . . 66

5.2.1 Measurement of the Magnetoresistance . . . . . . . . . . 66
5.2.2 Measurement of the Magnetic Properties: MOKE . . . . 67
5.2.3 Microstructure Investigations: XRD and XRR . . . . . . 68
5.2.4 Investigations with AGM, TEM and AFM . . . . . . . . 72
5.2.5 Thermal Treatment . . . . . . . . . . . . . . . . . . . . . 72
5.2.6 Transport Measurements at Low Temperatures . . . . . 72

**6 Laboratory all-embracing Co/Cu Multilayer Study 73**

6.1 Intention of the Study . . . . . . . . . . . . . . . . . . . . . . 73
6.2 Series and Investigation Overview . . . . . . . . . . . . . . . . 74
6.3 Variation of Spacer Layer Thickness . . . . . . . . . . . . . . . 75
6.4 Variation of Magnetic Layer Thickness . . . . . . . . . . . . . 78
6.5 Variation of Buffer Layer Thickness . . . . . . . . . . . . . . . 79
6.6 Variation of Number of Double Layers . . . . . . . . . . . . . 81
6.6.1 Magnetic Characterization . . . . . . . . . . . . . . . . . 82
6.6.2 Microstructural Characterization . . . . . . . . . . . . . 86
6.6.3 Discussion of the Double Layer Variation Series . . . . . 95
6.7 Conclusions . . . . . . . . . . . . . . . . . . . . . . . . . . . . 96

**7 From Multilayers to Trilayers 101**

7.1 Double Layer Optimization . . . . . . . . . . . . . . . . . . . . 101
7.2 Buffer Layer Optimized Multilayers . . . . . . . . . . . . . . . 105

**8 Temperature Stability and Recrystallization 107**

8.1 Intention of the Study . . . . . . . . . . . . . . . . . . . . . . 109
8.2 Investigation Overview . . . . . . . . . . . . . . . . . . . . . . 110
8.3 GMR Characteristics . . . . . . . . . . . . . . . . . . . . . . . 112
8.4 Magnetic Characteristics . . . . . . . . . . . . . . . . . . . . . 116
8.5 Microstructure Characteristics . . . . . . . . . . . . . . . . . . 120

8.5.1 Peak Profile Fitting of XRD Scans . . . . . . . . . . . . 120

8.5.2 TEM Analysis on Selected Samples . . . . . . . . . . . . 126

8.5.3 Multilayer Satellite Analysis . . . . . . . . . . . . . . . . . 129

8.5.4 X-Ray Reflectometry . . . . . . . . . . . . . . . . . . . . . 134

8.6 Discussion of Magnetoresistive, Magnetic and Microstructural Changes during Annealing . . . . . . . . . . . . . . . . . . . . . . 136

8.6.1 Hypothesis of Layer Destruction Mechanism . . . . . . . 137

8.6.2 Calculation of GMR Characteristics . . . . . . . . . . . . 139

8.7 Elasticity Strain as the Driving Force of Recrystallization . . . . 147

8.8 Conclusion . . . . . . . . . . . . . . . . . . . . . . . . . . . . . . 154

**9 Summary** **157**

**Appendix** **159**

**A Useful Relations for X-Rays** **159**

**B Optical Constants** **160**

**C Crystal Structures and Powder Diffraction Files** **162**

**D Co-Cu Binary Phase Diagram** **167**

**Bibliography** **169**

**Publications and Conferences** **179**

**Acknowledgement** **181**

# Chapter 1

# Preface

One of the most fascinating discoveries in solid state physics in the past 20 years was that of the giant magneto-resistance (GMR) in 1988 [bai88], [bin89]. This finding triggered a tremendous research activity in order to understand the underlying physics as well as to explore its enormous technological potential. It took an incredible short period of only a decade between the discovery of the effect and its commercial availability as magnetic field sensors (1995) and hard-disk read-heads (1997). This development is the more astounding as metallic multilayers have been studied since 1935 [dum35], but it took the advances in vacuum technology in the 1970's accompanied by the progress in thin-film deposition techniques to enable the layer-by-layer growth. Since then the investigation of nanoscale multilayers and especially of metallic magnetic multilayers in which ferromagnetic and nonmagnetic layers alternate revealed new magnetic and transport properties.

The underlying physics of interlayer exchange coupling and GMR is largely understood nowadays but there are still discrepancies between experimental findings and theoretical models when it comes to detail. The crucial point has been identified to be the correct theoretical description of the scattering at lattice discontinuities and defects. The review papers of Schuller *et al.* and especially of Tsymbal and Pettifor try to reduce the findings of the vast number of publications on GMR to a common denomiator. The authors of both reviews come to the point that the correspondence between theory and experiments, but also the agreement between different theories and also between similar experiments, ends where dicontinuities in growth direction and at the interfaces come into account. They state “Disorder is a key ingredient in all these materials” [schul99] and “The principal challenge for first-principle modeling lies in the realistic description of the defect scattering” [tsy01].

In order to assess these findings from the experimental point of view, it is a disadvantage in all the studies presented so far that they are valid in their own laboratory but not necessarily in the laboratory of another research group. Many aspects of the interplay between microstructure and GMR have been unraveled in those single-laboratory studies but without finding a common sense in many aspects.

The aim of this thesis is to overcome the limit of only one preparation environment by investigating Co/Cu multilayers prepared in different laboratories with identical characterization methods and to find insight into the interdependence of microstructure and GMR on a laboratory-embracing scale. This aim is not a modest one and therefore this study is not restricted to a few selected samples but is funded on a vast resource of samples that comprises variations of all thickness parameters of the layer stack.

The second scope of this thesis concerns the thermal stability of Co/Cu multilayers which is a cruicial criterion in the application as magnetic field sensors in the automotive industry. The GMR multilayers presented up to date do not or only hardly fulfill the need of $200°C$ to $360°C$ short time temperature stability in the course of manufacturing as well as long-term stability in the range of $150°C$ to $200°C$ during up to 40000 hours of operation. In this thesis a recrystallization mechanism in Co/Cu multilayers is presented that fundamentally changes the microstructure of the multilayer in the course of a short-time annealing at high temperatures without losing its GMR and which enables the sample in the further course to withstand $400°C$ for many hours. These temperature stable multilayers are the ideal candidates for the automotive application as the short-time annealing can easily be performed in a back-end process. Furthermore, the mechanism of the layer preserving recrystallization is investigated in order to clear up the microstructural evolution as well as the driving force for this process.

# Chapter 2

# Interlayer Exchange Coupling

The phenomenon of antiferromagnetic coupling between ferromagnetic layers across a nonmagnetic spacer layer was first discovered by P. Grünberg *et al.* in 1986 [gru86]. They investigated the trilayer system Fe/Cr/Fe and used Brillouin Light Scattering for the detection of the antiferromagnetic coupling. The next step in the discovery of the phenomenon was made by Parkin, More and Roche in 1990 [par90] when they found the oscillatory nature of the coupling: dependent on the interlayer thickness the alignment of the ferromagnetic layers oscillates between antiferromagnetic and ferromagnetic. They had investigated the multilayer systems Co/Ru, Co/Cr and Fe/Cr and made clear that the oscillation period depends on the interlayer material.

Yafet made the first attempt to explain the oscillatory coupling behaviour in layered magnetic structures in 1987 [yaf87a], [yaf87b]. He suggested an indirect exchange coupling mediated by conduction electrons of RKKY-type, a coupling mechanism proposed by Rudermann, Kittel, Kasuya and Yosida in 1954/1956. Based on the RKKY interaction Yafet successfully explained the coupling behaviour. But the oscillation period of $\lambda = \pi/k_F$ with $k_F$ being the wavevector of the spherical Fermi surface of the interlayer material, which is about one monolayer, did not agree with experimental periods of about $1\,nm$.

This discrepancy was dissolved in 1991 by Bruno and Chappert [bru91] and Coehoorn [coe91] by taking into account the discrete thickness of the interlayer. At the same time an alternative model was proposed by Edwards *et al.* [edw91c], Bruno [bru95] and Stiles [sti93] which also correctly explains the experimental oscillation periods. This model is based on the formation of quantum well states within the nonmagnetic spacer, caused by spindependent electron reflection at the interfaces. The quantum confinement model has become the widely accepted one for the explanation of interlayer exchange coupling [bru99] and its most important aspects are given in the following.

The considerations start with a trilayer ferromagnet/diamagnet/ferromagnet with a parallel magnetization of the magnetic layers. A coupling between the magnetic layers is mediated by conduction electrons of the spacer material.

In ferromagnets, the density of states of the majority electrons of the 3d band is shifted below the Fermi energy $E_F$. As a consequence, there are no free states left in the majority spin direction but only in the minority spin direction. The probability for scattering is directly proportional to the density of states. Due to this, the resistance is much higher for the minority electrons than for the majority electrons. In the given case of parallel alignment of the magnetic layers the minority electrons are reflected at both interfaces whereas the majority electrons can propagate freely through the layer stack. In case of antiparallel magnetization on the other hand, this quantum confinement does not take place because the electrons are reflected at only one interface and not at both [gru99], [bue99].

The reflection of minority spin electrons at both interfaces leads to an interference of electron waves. If the electron wave vector normal to the interfaces $k_\perp$, is equal to $n\pi/D$ with the integer $n$ and the spacer thickness $D$, then standing electron waves will occur.

The thicker the spacer layer the more energy levels pass the Fermi energy and become filled. For those values of $D$ having the highest energy level filled up and lying far below $E_F$ a stabilization of the parallel alignment of ferromagnetic layers is expected because of a minimization of electron energy. On the other hand there are thickness values $D$ for which the highest energy level is right below $E_F$ and is started to be filled. Such a configuration of electron levels results in a destabilization of parallel alignment and thus to the antiparallel magnetization of the ferromagnets.

The oscillation between ferro- and antiferromagnetic magnetization depends on the thickness difference $\Delta D$ between two discrete energy levels passing $E_F$, thus

$$\lambda_D = \Delta D = \frac{\pi}{\mid k_\perp \mid} \tag{2.1}$$

where $\mid k_\perp \mid$ has to be taken at the Fermi level. Three important aspects have to be mentioned concerning this result:

1. The more the electrons are localized in the spacer the more pronounced are the changes in density of states and the higher the coupling amplitudes will become. Therefore, additionally to its oscillating nature, the coupling strength decreases with increasing interlayer thickness.

2. The oscillation period given above is in the order of nearest neighbour distances in the crystal and thus smaller than the experimentally observed ones. This problem is overcome when taking into account the discrete nature of the

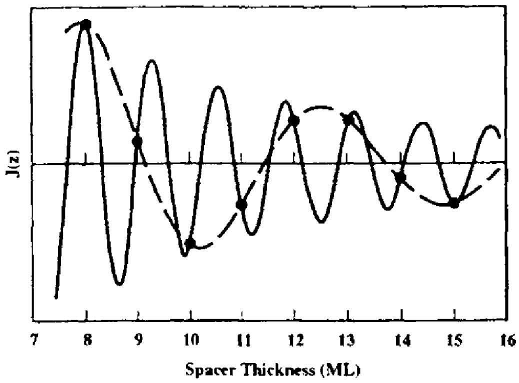

Figure 2.1: *Aliasing* effect of interlayer exchange coupling: due to the discrete thickness variation of the spacer the rapidly varying oscillation function is sampled at dicrete points and thus appears to be a slowly varying function (from [bue99]).

crystalline interlayer: the exchange coupling via spacer layer can be determined only for discrete values of the spacer thickness $D$ as this is a multiple of the interatomic distance $a$, $D = na$, with the integer $n$. As a consequence, the wave number $q$ has to be modified such that it comes to lie in the first Brillouin zone:

$$q =\mid 2k_{\perp} - \frac{2\pi m}{a} \mid \tag{2.2}$$

with $m$ being an integer. This modification of oscillation period is the so called *aliasing* or *Vernier* effect and is demonstrated in figure 2.1.

3. The relevant wave vectors for exchange coupling are the stationary spanning vectors of the Fermi surface which are attributed to large density of states. Depending on the Fermi surface and the crystalline orientation there can be several spanning vectors, resulting in a superposition of different oscillation periods. For the spacer material Copper different cross sections of the Fermi surface and the corresponding stationary spanning vectors are depicted in figure 2.2. It can be seen that for the [111] direction a single (long) period is predicted, for the [100] orientation there exists both a long and a short period and for the [110] direction there are even four different periods. Bruno and Chappert [bru91] and Stiles [sti93] have calculated the oscillation periods for Cu as spacer material and a survey of their results for the [100] and the [111] orientation is given in table 2.1.

4. The curvature and the reduced velocity of the Fermi surface determine the strength of the antiferromagnetic coupling: the stronger the spin-dependent reflection at the interface spacer - magnetic layer, the stronger the confinement and thus the oscillatory coupling (details in [sti93]). The probability for majority and minority electrons from the spacer layer to reflect from the interface with the magnetic material is compiled in figure 2.2.

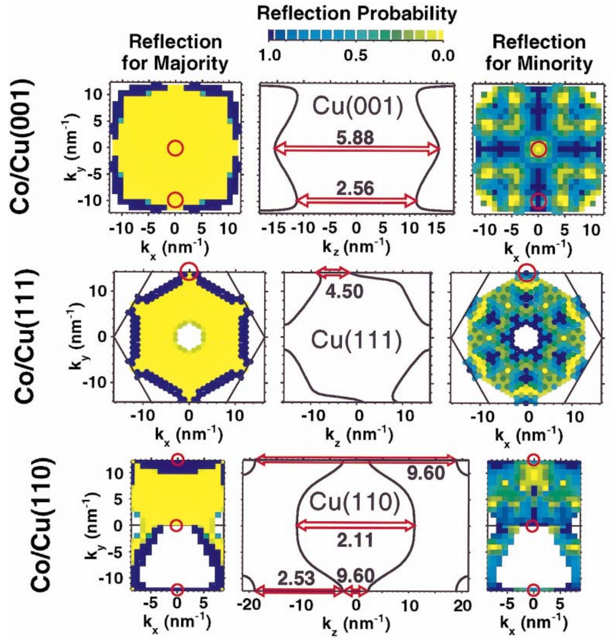

Figure 2.2: Cross sections of the Fermi surface of Cu and their stationary spanning vectors along the [100], [111] and [110] planes (middle row). Each critical spanning vector is labeled by its associated coupling period in monolayers. The left and right row show the interface reflection probability for majority and minority electrons [sti99].

Various models and methods for the calculation of the coupling strength have been used, which are reviewed in [sti99]. Especially for the system Co/Cu [100] there are several difficulties in the theoretical investigation of the coupling, concerning short and long period oscillation. For the first antiferromagnetic coupling maximum (AFCM) coupling energy values between 1.2 and 4.6 $mJ/m^2$ have been calculated. The experimentally measured coupling energies on the other hand are generally a factor of three smaller (0.16 to 0.39 $mJ/m^2$, see table 2.2). This discrepancy has not been cleared yet, but thickness fluctuations in the measured samples are proposed to be the reason. Experiments revealed, that the ratio of the two coupling strengths depends sensitively on the growth. Stamm *et al.* succeeded in amplifying the short period oscillations by growth at low temperature [sta98]. Furthermore, the Co layer thickness and even Cu capping layers influence the coupling strength as well as its period and phase, as theory and experiment reveal (details in [sti99]).

There is much more agreement between calculated and measured coupling energies in the Co/Cu [111] system which has only one spanning vector. Stiles quotes theoretical values of 0.59 and 0.67 $mJ/m^2$ for the first AFCM and experimental coupling energies between 0.15 and 1.1 $mJ/m^2$. But multilayers

| spacer | $d_{hkl}$ | oscillation period | | |
|---|---|---|---|---|
| Cu [111] | 2.0869 Å | $\Lambda$ | $= 4.5\,ML$ | $= 0.94\,nm$ |
| Cu [100] | 1.8073 Å | $\Lambda_1$ | $= 2.6\,ML$ | $= 0.470\,nm$ |
| | | $\Lambda_2$ | $= 5.9\,ML$ | $= 1.066\,nm$ |

Table 2.1: Theoretical oscillation periods [bru91], [sti93].

of type Co/Cu [111] have been found to be very sensitve to the growth mechanism: MBE fabricated samples did not show antiferromagnetic coupling in some research groups, whereas they did in others. Furthermore, as large GMR effect values as in sputtered samples have not been detected even in well antiferromagnetically coupled MBE samples. Sputtered samples did show highest GMR values of 65 % at first AFCM [par91b].

### Conclusions

In table 2.2 many experiments on Co/Cu [111] and [100] are drawn together. It is obvious that the theoretical oscillation periods are very close to the measured ones. The short oscillation period of Co/Cu [100] cannot be seen in all samples. The major reason seems to be interface roughness: only samples with atomically smooth interfaces reveal the short period [sta98].

The theoretical calculations suggest a stronger coupling of the first AFCM in [100] than in [111] Co/Cu. The experimental values on the other hand are in the same range for both orientations. Theoretical uncertainties as well as growth condition and magnetic layer thickness can be attributed to be the reason for that.

Samples fabricated by MBE have a tendency to be lacking the GMR effect, in contrast to sputtered samples. The experiments listed in the table do not give a close picture, because the MBE samples are sandwich structures in most of the cases whereas sputtered samples are all multilayers.

### Biquadratic Exchange Coupling

Besides the colinear alignment of two magnetic layers with an angle difference of 180° in case of antiferromagnetic coupling and of 0° in case of ferromagnetic coupling there has been found a noncolinear alignment of 90° characteristic. In contrast to the bilinear coupling treated so far, this 90° type of coupling is called biquadratic. The reason for the existence of biquadratic coupling has not been identified within a closed model but in contrast, three different explanations have been proposed. The first theoretical model to account for the biquadratic coupling phenomenon was the **fluctuation mechanism** and is based on the assumption on terraced interfaces. These terraces occur because of thickness variation of the spacer layer in the order of two monolayers, resulting in regimes characterized by ferromagnetic coupling and others of antiferromagnetic coupling behaviour. Assuming that these different areas are closely neighboured, a competition between these different coupling types occurs which is superimposed by the ferromagnetic exchange within the ferromagnetic layers. As a consequence, the magnetic moments orient orthogonally to each other [slo91], [dem98].

Another theoretical model for the explanation of biquadratic coupling is based on the magnetic dipole field of the magnetic layers. In case of ideally planar interfaces the magnetic dipole field decays exponentially with distance from the layer but in lateral direction the dipole field oscillates periodically with lattice constant. For ideal interfaces this dipole field is too small to cause any coupling, but in case of interfaces with roughness, the dipole field acts in a longer range. The phenomenon of 90° coupling occurs in case of one magnetic layer having rough and the other having a smooth interface: equivalently to the competing situation in the fluctuation model, the oscillating dipole field of the rough layer competes with the internal exchange coupling of the smooth layer, resulting in orthogonal orientation of the smooth layer to the dipole field and thus orthogonal to the rough magnetic layer [dem94]. This **magnetic dipole mechanism** is also the reason for the so called **orange peel effect**: in case of two magnetic layers, both of rough interfaces, the magnetic dipole field causes a ferromagnetic alignment of the layers [gru99].

The third theoretical attempt for the explanation of biquadratic exchange coupling is based on magnetic impurities at or near the interface and is called **loose interfacial spin model**. If magnetic impurities in form of single atoms or clusters are present in the nonmagnetic spacer then an indirect exchange between these paramagnetic clusters and the ferromagnetic layer takes place, resulting in an additional term of the total free energy and thus in biquadratic coupling [bue99]. Details on this mechanism can be found in [slo93].

In conclusion it has to be stated, that not only the spacer layer thickness but also the interface characteristic in terms of roughness and intermixing is an important parameter for interlayer exchange coupling.

### Phenomenological Description of Interlayer Exchange Coupling

Phenomenologically, the interlayer exchange coupling between two ferromagnetic films separated by a spacer layer can be described in terms of the interlayer exchange coupling energy $E_i$:

$$
\begin{aligned}
E_i &= -J_1 \frac{\vec{M}_1 \cdot \vec{M}_2}{\mid \vec{M}_1 \mid \cdot \mid \vec{M}_2 \mid} - J_2 \left( \frac{\vec{M}_1 \cdot \vec{M}_2}{\mid \vec{M}_1 \mid \cdot \mid \vec{M}_2 \mid} \right)^2 \\
&= -J_1 \cos(\Delta\phi) - J_2 \left(\cos(\Delta\phi)\right)^2
\end{aligned}
\tag{2.3}
$$

Here, $\Delta\phi$ is the angle between the magnetizations $\vec{M}_1$ and $\vec{M}_2$ of the magnetic layers. $J_1$ and $J_2$ are bilinear and biquadratic coupling constant, respectively. In case of a dominating parameter $J_1$ the energetic minimum of equation 2.3 determines a ferromagnetic coupling behaviour if $J_1$ is positive and an antiferromagnetic coupling in case of negative values of $J_1$. On the other hand, a dominating parameter $J_2$ characterizes a 90° coupling [gru99].

In case of multilayers, both terms have to be multiplied by a factor 2, because each magnetic layer is coupled to two neighboured ones.

| $d^{1st}$ [nm] | $d^{2nd}$ [nm] | $\Lambda_1$ [nm] | $\Lambda_2$ [nm] | $\mid J^{1st} \mid$ $[\frac{mJ}{m^2}]$ | $\mid J^{2nd} \mid$ $[\frac{mJ}{m^2}]$ | $G^{1st}$ [%] | $G^{2nd}$ [%] | Reference |
|---|---|---|---|---|---|---|---|---|
| Co/Cu [111] by MBE | | | | | | | | |
| 0.85 | $\approx 2.0$ | 1.1 - 1.2 | | 1.1 | - | - | - | S [joh92b] |
| 0.7 - 0.9 | 1.8 | $\approx 1.0$ | | - | - | 26 | 6 | ML [hal93] |
| 1.0 | 1.9 | 0.9 | | $> 0.27$ | 0.08 | - | - | ML [schrey93](1) |
| Co/Cu [111] by sputtering | | | | | | | | |
| 0.93 | 1.91 | $\approx 1.0$ | - | 0.15 | - | 65 | 25 | ML [par91b](2) |
| 0.9 | 2.0 | $\approx 1.2$ | - | 0.3 | 0.05 | 48 | 18 | ML [mos91](3) |
| Co/Cu [100] by MBE | | | | | | | | |
| 1.2 | 2.2 | 1.45 | 0.47 | 0.4 | - | - | - | S [joh92a](4) |
| 1.15 | 2.1 | 1.0 | - | 0.16 | 0.06 | - | - | S [qiu92] |
| 0.94 | 1.86 | - | - | 0.24 | 0.09 | - | - | S [blo94] (5) |
| 1.1 | 1.8 | 1.0 | 0.43 | - | - | - | - | S [sta98](6) |
| Co/Cu [100] by sputtering | | | | | | | | |
| 1.05 | 2.0 | $\approx 1.0$ | - | 0.15 | 0.068 | 48 | 40 | ML [len94] |
| - | 1.84 | - | - | - | $< 0.01$ | - | 5.8 | ML [gir92] |
| - | 2.1 | $\approx 1.0$ | - | - | 0.016 | - | 6.7 | ML [gir93] (7) |

Table 2.2: Comparison of experimental results concerning position of first and second antiferromagnetic coupling maximum in terms of Cu layer thickness ($d^{1st}, d^{2nd}$), long and short period of interlayer exchange coupling ($\Lambda_1$, $\Lambda_2$), coupling energy ($J^{1st}$, $J^{2nd}$) and GMR effect amplitude ($G^{1st}$,$G^{2nd}$). Values which have not been determined are indicated by a dash. Sandwich structures are denoted by "S", multilayers by "ML". Remarks:
(1) Third AFCM at $t_{Cu} = 2.8\,nm$ ($0.05\,mJ/m^2$).
(2) Weak [111] texture according to [ege92].
(3) Third AFCM at $t_{Cu} = 3.5\,nm$ (10 % GMR)
(4) Long and short oscillation period determined via fit. Third AFCM at $t_{Cu} = 2.6\,nm$, fourth AFCM at $t_{Cu} = 3.1\,nm$.
(5) Long and short period oscillation are clearly visible but have not been quantitatively determined.
(6) Position of first and second AFCM refer to the long period oscillation. After amplification of the short period oscillation the first AFCM is found at $t_{Cu} = 0.63\,nm$ and the second AFCM at $t_{Cu} = 1.45\,nm$.
(7) Further AFCM at $t_{Cu} = 3.0\,nm$ (2.5 % GMR), $4.0\,nm$ (3.5 % GMR), $5.0\,nm$ (4.5 % GMR).

# Chapter 3

# Giant Magneto-Resistance

The discovery of antiferromagnetic exchange coupling raised considerable interest. But from the applicational point of view an even more exciting discovery was the giant magneto-resistance (GMR) in 1988 by Baibich *et al.* and Binasch *et al.* [bai88], [bin89]. They investigated layered Fe/Cr systems with antiferromagnetically coupled magnetic layers and detected a resistance decrease when applying an external magnetic field, which causes the magnetic layers to align themselves parallel. As the change in electrical resistance was much larger than the anisotropic magneto-resistance (AMR), the new phenomenon was called “giant”. In general, GMR can be observed when an external magnetic field causes a switching of magnetic layers from antiparallel to parallel alignment. In multilayers consisting of a repetition of identical magnetic layers and their spacer, the antiparallel state can be achieved only if antiferromagnetic exchange coupling is present. But generally interlayer coupling is not a necessary condition. In spin valves different switching fields of hard and soft magnetic layers enable the state of antiparallel alignment, and also in granular materials GMR has been observed. The mechanism of GMR is sketched in the following.

### Electrical Resistivity

The main aspects in the understanding of the electric current in transition metals have been introduced by N. F. Mott in 1964 [mot64]. He stated that there are two largely independent conducting channels in metals, corresponding to the spin-up and spin-down electrons, because scattering processes without conservation of spin, called spin-flip, are small compared to processes where the direction of spin is conserved. Therefore, the resistivities for spin-up and spin-down electrons of a metal can be added in parallel:

$$\frac{1}{\rho} = \frac{1}{\rho_\uparrow} + \frac{1}{\rho_\downarrow} \tag{3.1}$$

The origin of the resistvity within each spin channel is the scattering of the electrons at any kind of disorder in the lattice such as lattice imperfections and impurities but also the scattering at phonons. Furthermore, in magnetic materials there is a contribution to the resistivity caused by spin-disorder. The Matthiesen's rule distinguishes between three kinds of resistivity concerning their temperature dependence and states that these contributions add up to the total resistivity $\rho_{tot}(T)$:

$$\rho_{tot}(T) = \rho_0 + \rho_p(T) + \rho_m(T) \tag{3.2}$$

where $\rho_0$ is the temperature independent residual resistivity, $\rho_p(T)$ is the phonon scattering and $\rho_m(T)$ is the contribution from spin-disorder [ros87]. The phonon scattering is temperature dependent as the number of phonons in a material increases with T. For $T \gg \Theta_D$ it is found that $\rho_p \propto T$ and for $T \ll \Theta_D$ the resistivity increases as $\rho_p \propto T^5$ [kop93]. On the other hand, the number of lattice imperfections does not depend on the temperature and also the residual resistance does not. Besides impurity and imperfections, there is a contribution to the residual resistivity caused by grain boundaries within a polycrystalline material. In a multilayered material, there is furthermore the film thickness as well as the interface roughness which have to be considered. In the following, these aspects are briefly treated.

Taking the model of a free electron gas, P. Drude found an expression for the electrical conductivity of a metal in terms of the mean free path of the electrons:

$$\frac{1}{\rho} = \frac{ne^2 l_\infty}{m^* v_F} = \frac{ne^2 \tau(E_F)}{m^*} \tag{3.3}$$

with $n$ being the density of the conduction electrons, $e$ the electron charge, $l_\infty$ the mean free path, $m^*$ the effective mass of the electrons and $v_F$ the Fermi velocity. $\tau(E_F)$ is the time of relaxation of the electrons, i. e. the time between two scattering events [kop93].

In thin films scattering at surfaces and interfaces comes into account and becomes the dominating scattering mechanism when the film thickness $d$ becomes much smaller than the mean free path $l_\infty$ of the electrons. The thickness dependent resistance $\rho(d)$ of a thin film is given in the theory of Fuchs and Sondheimer as

$$\frac{\rho_\infty}{\rho(d)} = 1 - \frac{3}{2}\int_1^\infty \left(\frac{1}{t^3} - \frac{1}{t^5}\right) \frac{1 - \exp\left(-\frac{d}{l_\infty}\right)}{1 - \exp\left(-p\frac{d}{l_\infty}\right)}\, dt \tag{3.4}$$

where $p$ is the specularity parameter which gives the probability that an electron is reflected specularly at the surface, $p = 1$ meaning that the electron has been reflected without losing its momentum in field direction [gro00]. For $d \gg l_\infty$ the thickness dependence is given by $1/d$ in accordance to experimental findings. In the case of $d \ll l_\infty$ and $l_\infty \rightarrow \infty$ the model predicts a vanishing resistance in spite of the surface scattering. This is a nonphysical result and shows up the limitations of the model which can only be overcome when considering quantum mechanical models.

Roughness of surfaces and interfaces enhances the resistance of a thin layer or a multilayer. Roughness on a microscopic scale is caused e. g. by terraces and dislocations and is treated as a distortion potential in quantum mechanical scattering models. Mesoscopic roughness on the other hand occurs in polycrystalline materials and is characterized by correlation lengths in the order of the crystallite size of about 20 to $100\,nm$. This kind of roughness can be treated as a fluctuation in film thickness and yields a mean film resistance as

$$\frac{\rho_{film}}{\rho_\infty} = \frac{d}{l} \int_0^l \frac{\rho_{local}(d(x))}{\rho_\infty \cdot d(x)}\, dx \tag{3.5}$$

here, $d$ is the average film thickness, $d(x)$ is the local film thickness, $\rho_{local}$ is the local resistivity and $\rho_\infty$ is the resistivity of the bulk material (for details see [brue92]).

A polycrystalline material is characterized by the presence of grain boundaries which enhance the resistivity of the material compared to the Drude formula 3.3. The scattering at grain boundaries depends on the average grain size $D$ and on the transmission $T$ of the boundaries but also on the mean free path $l_\infty$. Therefore, a function $grain(D, T, l_\infty)$ has to be considered in the Drude term [van89]:

$$\frac{1}{\rho} = \frac{ne^2}{m^* v_F} l_\infty \cdot grain(D, T, l_\infty) \tag{3.6}$$

### Spin-dependent scattering

In the section above it has been stated that the electrical current is carried within two largely independent spin channels. In ferromagnetic materials, the band structure causes different scattering probabilities within these channels:

Due to the low effective mass and high mobility of electrons in the valence $sp$ bands, they primarily determine the electric conductivity. But the $d$ bands play an important role in providing final states for scattering: the probability for a scattering process to occur depends on the number of unoccupied states in the vicinity of the Fermi energy. The higher the density of states $D(E_F)$ the more electrons will be scattered and the higher the resistance $\rho$ of the material will be:

$$\rho_\varsigma \propto D(E_F)_\varsigma \tag{3.7}$$

where the index $\varsigma$ denotes the orientation of the two separate spin channels $\uparrow$ and $\downarrow$. In case of ferromagnets the *d* bands are exchange split with a higher density of states at $E_F$ (see figure 3.1 on page 16). Furthermore, the minority bands represent hybridized *spd* bands having a high density of states. Therefore the mean free path of minority electrons associated with these bands is relatively short and the conductivity is low [tsy01]:

$$\rho_{\uparrow} < \rho_{\downarrow} \tag{3.8}$$

### Resistor Network Model

The spin-dependent electric current within a ferromagnet has been considered above. For the understanding of GMR the characteristics of electron scattering within a combination of different materials has to be understood.

A simple model to explain the basic mechanism of GMR is the resistor model by Edwards and Mathon [edw91b], [mat91]. The giant magneto-resistance is generally defined as the relative change of resistance from parallel to antiparallel alignment of the magnetic layers:

$$\frac{\Delta R}{R} = \frac{R_{\uparrow\downarrow} - R_{\uparrow\uparrow}}{R_{\uparrow\uparrow}}. \tag{3.9}$$

The electric current of these two orientations is determined by two independent spin channels $\uparrow$ and $\downarrow$ which are connected in parallel. The resistance of parallel $R_{\uparrow\uparrow}$ and antiparallel alignment $R_{\uparrow\downarrow}$ is accordingly calculated as

$$\frac{1}{R_{\uparrow\downarrow}} = \left(\frac{1}{R_{\uparrow}}\right)_{\uparrow\downarrow} + \left(\frac{1}{R_{\downarrow}}\right)_{\uparrow\downarrow} \qquad \text{and} \qquad \frac{1}{R_{\uparrow\uparrow}} = \left(\frac{1}{R_{\uparrow}}\right)_{\uparrow\uparrow} + \left(\frac{1}{R_{\downarrow}}\right)_{\uparrow\uparrow} \tag{3.10}$$

In the further deduction of GMR the most relevant question is how the resistances of the single layers have to be treated. Firstly, the geometry of electric current and layered structure has to be taken into account. The most common type of GMR measurement is the "current-in-plane" (CIP) configuration where the external magnetic field and the current are arranged parallel to the layer plane. On the other hand, in "current-perpendicular-to-plane" (CPP) configuration the magnetic field is still parallel to the layer plane but the current flows in direction of the plane normal. The latter type of measurement is of greater experimental effort. The electrical contacts have to be prepared lithographically or alternatively, a grooved substrate can be used to coerce the current in perpendicular direction [gij97]. In CIP geometry measurements can be performed with the four-point-contact method without additional demands concerning the sample. Therefore this is the most common GMR measurement geometry and also the method of choice throughout this thesis.

In CIP geometry, one important aspect is the mean free path of the electrons: in case of a very short mean free path the resistance of the single layers could be added in parallel. Consequently, there will be no difference in the resistance of parallel and antiparallel aligned magnetic layers and thus no GMR. But typical mean free path lengths are a few hundred Å, for example in Cu at room temperature 430 Å, so the electrons can be viewed as propagating freely through the spacer layer and sensing the magnetizations of the two consecutive ferromagnetic layers, seeing an average resistance of the layer stack. In my diploma thesis [hei00], $\Delta R/R$ is deduced step by step in the picture of an average resistance of one double layer and has been found to be

$$\frac{\Delta R}{R} = \frac{(\gamma - 1)^2}{4\left(\gamma + \frac{1}{\beta} \cdot \frac{N}{M}\right)\left(1 + \frac{1}{\beta} \cdot \frac{N}{M}\right)} \tag{3.11}$$

Here, $N$ and $M$ are the thickness of nonmagnetic and magnetic layer, respectively, and $\gamma$ and $\beta$ are defined as

$$\gamma = \frac{\rho^H}{\rho^L} \quad \text{and} \quad \beta = \frac{\rho^L}{\rho^N} \tag{3.12}$$

where $\rho^H$ and $\rho^L$ are the resistance values of the magnetic layer for minority and majority electrons, respectively, the indices $H$ and $L$ indicating high and low resistance. The spin-independent resistance of the spacer layer is given as $\rho^N$.

The most important parameter determining GMR is the spin asymmetry $\gamma$. A high value of $\gamma$ is necessary to obtain large GMR effect amplitudes.

As a function of the spacer thickness $N$, the GMR decreases monotonically which is in agreement with experimental results. But at large spacer thickness equation 3.11 predicts the GMR to falls off as $1/N^2$, whereas measurements reveal an exponential decrease. This discrepancy is not suprising because the model is based on a long mean free path compared to the layer thickness. In case of large spacer thickness, this condition is no longer satisfied.

There are even more restrictions concerning the resistor model:

Firstly, Gurney *et al.* measured a much smaller mean free path in thin films than in bulk materials. They determined values of $\lambda^{\uparrow} = 5.5\,nm$ and $\lambda^{\downarrow} \leq 0.6\,nm$ in a few $nm$ thick Co layers [gur93]. But a long mean free path is one of the prerequisites of the CIP resistor model.

Secondly, the model yields the same result for GMR in CIP as in case of CPP geometry. In the latter case the resistance of the single layers is connected in series. But experiments reveal a higher GMR in CPP than in CIP measurements.

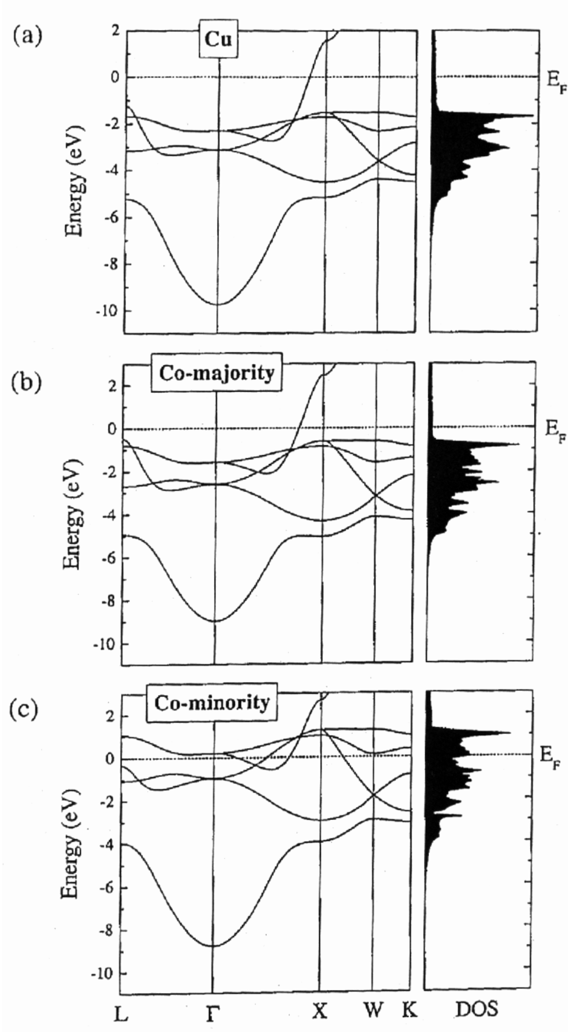

Figure 3.1: Electronic band structures (left panels) and the density of states (right panels) of Cu (a) and fcc Co for the majority-spin (b) and minority-spin (c)-electrons (from [tsy01]).

It is clear that the resistor model enables the basic understanding of GMR but it is far too simple to account for detailed experimental findings. In the following the most relevant aspects having influence on the GMR are discussed. Last but not least a short survey of more sophisticated GMR theories is given.

### Role of Bandstructure

The band structure of the magnetic and nonmagnetic layers is the most important property for GMR. On one hand, the band structure of the ferromagnet has to affect a large spin asymmetry. This has been deduced above. On the other hand, in a multilayer the interfaces between magnetic and nonmagnetic materials act as spin filters: When different band structures are present at the interface, then it acts as a potential step for the electrons with the transmission being smaller than 1. In case of a good band matching the transmission will be higher than in case of bad matching. In the material combination Co/Cu the band structure of Cu matches very well with the Co majority electron band structure, but it does not match with the Co minority electrons. Thus the interface itself acts as a spin filter, enhancing GMR due to the same mechanism as the magnetic materials themselves.

This mechanism of spin filtering has also to be taken into account when discussing roughness and intermixing at the interfaces. As both effects result in a laterally random potential they are expected to enhance the spin-dependent scattering and thus the GMR.

But the experimental results only partially reflect this property (for a review see [tsy01]). The controlled variation of interface roughness of different material combination yielded contradictory results. Whereas roughness has been found to increase the GMR in Fe/Cr systems, a reduction in GMR was recognized in the Co/Cu system. But the experiments have to be taken with care because a strict distinction between topological roughness and interdiffusion is hard to make. Discussions are made whether especially the results for Co/Cu are caused by interdiffusion rather than roughness.

All systems with highest GMR are immiscible (Fe/Cr, Co/Cu). This fact is an indication that intermixing can be a contraproductive parameter to GMR. There are two theories that claim the magnetic property of the intermixed interface responsible for this. Firstly, a reduction of magnetic moments in the intermixed region was suggested, reducing GMR. Secondly, misaligned spins at the interface have been proposed which are only weakly coupled to the magnetic layer, a configuration which is known as magnetically “dead” layers [tsy01].

In conclusion, roughness and interdiffusion principally have the chance to enhance the GMR, but only if the magnetic property of the interface is not affected in the way reduced magnetic moments and misaligned spins do.

### Role of Structural Defects

The presence of structural defects in the nonmagnetic layer will cause spin-independent scattering, whereas scattering at defects inside the magnetic material are supposed to be spin-dependent. But the spin asymmetry in the scattering potentials depend on structural details. If various types of defects are present then the scattering potential will be an average that weakly depends on the spin. Therefore, in general an enhancement of spin-independent scattering processes is expected which reduces the GMR.

The experimental fact that the systems Fe/Cr and Co/Cu with highest GMR values have the best lattice matching supports this point of view.

### Spacer Thickness Dependence

In GMR multilayers with identical magnetic layers the variation of the spacer thickness $t_{\mathrm{NM}}$ changes the interlayer exchange coupling. The oscillation between ferromagnetic and antiferromagnetic alignment is reflected in the GMR effect amplitude. But above that the spacer thickness influences the intrinsic GMR[1], as studies of Dieny *et al.* on uncoupled spin valves reveal: with increasing spacer thickness the GMR amplitude decreases monotonically. Two factors account for this fact. Firstly, the number of scattering events inside the spacer increases. As a consequence, the number of electrons traversing from the spacer to a neighboured magnetic layer is reduced and also the GMR. Secondly, the shunting inside the spacer layer is increased. Both contributions to GMR can be well represented by the phenomenological expression

$$\frac{\Delta R}{R} = \left(\frac{\Delta R}{R}\right)_0 \left[\frac{\exp(-t_{\mathrm{NM}}/l_{\mathrm{NM}})}{(1 + t_{\mathrm{NM}}/t_0)}\right] \tag{3.13}$$

where $t_0$ is an effective thickness representing the shunting of the current in the absence of the spacer layer, $(\Delta R/R)_0$ is a normalization coefficient and the parameter $l_{\mathrm{NM}}$ is related to the mean free path of the electrons in the spacer layer. Due to the fact that electrons which mostly contribute to GMR have out-of-plane velocities, $l_{\mathrm{NM}}$ is expected to be one half of the mean free path $\lambda_{\mathrm{NM}}$. The exponential factor in equation 3.13 represents the probability for an electron not to be scattered within the spacer layer. The shunting effect of the spacer is accounted for in the denominator.

Consequently, without consideration of the interlayer coupling, the largest GMR amplitudes are obtained for spacer layers as thin as possible and therefore having only a small amount of bulk scattering. However, the reduction of spacer thickness is limited by the existence of pinholes. Such holes in very thin spacer layers enable a direct ferromagnetic coupling of the magnetic layers and thus lead to a destruction of GMR.

In antiferromagnetically coupled multilayers $t_{\mathrm{NM}}$ has to be chosen in the range of antiferromagntic coupling and thus always is a compromise between interlayer coupling and intrinsic GMR [die94], [tsy01].

### Magnetic Layer Thickness Dependence

In contrast to the monotonic decrease in GMR with increasing spacer thickness, the variation of the thickness of the ferromagnetic layers $t_{\mathrm{F}}$ results in a broad maximum of GMR for thicknesses below $10\,nm$. The GMR decrease for large magnetic layer thicknesses is due to the increased shunting of the current inside

---

[1] The term intrinsic means that the GMR amplitude is always measured between perfectly parallel and antiparallel magnetization.

the layers. Concerning the decrease in GMR at low magnetic layer thicknesses, a distinction between spin valves and multilayers has to made. In the former case, the reduction of the magnetic layers leads to an enhancement of diffuse scattering at the outer boundaries. The maximum GMR in spin-valves is found for magnetic layer thicknesses between 6 and $10\,nm$. In multilayers with many repetitions of double layers the effect of the outer boundaries is reduced and cannot be the reason for decreasing GMR.

In contrast to spin-valves, the maximum GMR in multilayers is achieved for magnetic layer thicknesses between 1 and $3\,nm$. For layer thicknesses below these values, insufficient scattering of the electrons either within the magnetic material or at the interfaces between spacer and magnetic material can be accounted for the decrease in GMR: spin asymmetry in the conductivity in case of Co/Cu multilayers can be established if the minority electrons are scattered strongly whereas the majority electrons are only weakly scattered. But in case of magnetic layers which are smaller than the mean free path of the minority electrons, the electrons are insufficiently scattered and thus the conduction spin asymmetry is reduced. This mechanism accounts for bulk scattering. In case that interface scattering is of more importance, the magnetic layer has to be at least so thick that the interface properties are established that lead to different scattering rates of majority and minority electrons. It has been found that a few monolayers of the magnetic material are sufficient (for references see [die94]).

Equivalently to the dependence on spacer thickness, the GMR dependence on the magnetic layer thickness can be represented by the phenomenological expression

$$\frac{\Delta R}{R} = \left(\frac{\Delta R}{R}\right)_0 \left[\frac{1-\exp(-t_{\mathrm{F}}/l_{\mathrm{F}})}{(1+t_{\mathrm{F}}/t_0)}\right] \tag{3.14}$$

where the numerator accounts for the variation of scattering rates with magnetic layer thickness $t_{\mathrm{F}}$ and the denominator describes the shunting of the current. $(\Delta R/R)_0$ and $t_0$ have the same meaning as in equation 3.13. The parameter $l_F$ depends on the sample being a sandwich or a multilayer, as discussed above [tsy01], [die94].

### Conlusions

Spin-dependent scattering is the basic mechanism that leads to GMR. But spin asymmetry of the ferromagnetic material alone is not sufficient to yield a high effect amplitude. A good band matching of ferromagnet and spacer layer as well as good lattice matching have been shown to be two important ingredients for high GMR. There are only a few material combinations which fulfill both conditions, and these are Co/Cu and Fe/Cr. These two systems have in fact yielded the highest GMR effect amplitudes measured so far.

Furthermore, the thickness of magnetic layer and spacer influence the GMR amplitude. Whereas in exchange coupled multilayers there is only little latitude for the choice of spacer thickness at the maximum of antiferromagnetic coupling, there is an optimum magnetic layer thickness in the range between 1 and $3\,nm$.

### Survey of GMR Theories

The resistor model is oversimplified to account for GMR more than the basic understanding. A lot of effort was made to develop more reliable electronic transport theories in magnetic layered structures. A detailed review of GMR theories can be found in [tsy01] and a short extract is given here.

First theories such as free-electron models and single-band tight-binding models were based on simplified band structures. They capture the important aspects of GMR and have the advantage of being physically transparent. But they cannot account for a quantitative description of GMR. Therefore it is necessary to incorporate the correct band structure of the multilayer, which has been done in so called “multiband models”. But also the electrical transport has to be treated quantum-mechanically in order to predict conductivity and GMR in real metallic layered structures. The widely used semiclassical Boltzmann approach for electron transport breaks down in realistic magnetic multilayers because the subband energy splitting is comparable with the lifetime broadening due to scattering. The first-principle models seem to be the most reliable multiband model candidates because they can describe the defect scattering realistically. However, the proper treatment of all existing defects in a multilayer structure by first-principles is very complicated. Therefore, reliable simplifications within these models have to be made.

A number of important features of GMR that are observed experimentally can be explained within the *semiclassical free-electron model.* This is the variation of GMR versus spacer layer and magnetic layer thickness, the effect of specular and diffuse scattering at the outer boundaries and the enhancement of GMR with increasing number of double layers within a multilayer. On the other hand, the model is not suited for a quantitative prediction of GMR because it ignores the realistic band structure. Furthermore, it can not describe quantum mechanical effects which become important at small film thicknesses.

# Chapter 4

# X-Ray Characterization

X-ray diffraction (XRD) and x-ray reflectometry (XRR) are techniques that provide structural information of materials. The structural properties of a crystalline material can be classified as follows:

- Crystalline structure
- Defect structure
- Grain structure
- Phase structure

The crystalline structure is characterized by the arrangement of atoms in the unit cell of the ideal crystal, whereas in a nonideal crystal differences occur from the perfect atomic arrangement. The kind of those defects and their arrangement is called defect structure. The mulitlayers investigated in this thesis are polycrystalline, i. e. the material is made up of many small crystallites instead of being one single crystal of unique phase. Firstly, a polycrystalline sample is characterized by its grain structure which is the size, form, orientation and arrangement of the crystallites. Secondly, such a sample can contain more than one crystalline phase and thus has a phase structure, which comprises the kind, size, form, orientation and arrangement of the different phases [MC92, p. 198ff].

The chemical composition as well as the physical treatment determine the complete structure of a crystalline material. Besides x-rays, also electrons and neutrons are used to investigate the sample structure, but x-ray diffraction and reflectometry provide a number of advantages:

- XRD and XRR are nondestructive and noncontact.

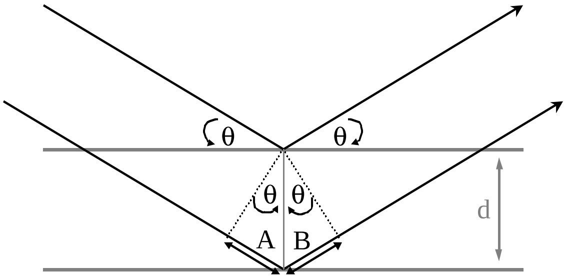

Figure 4.1: The Bragg law for parallel planes with spacing d. Dotted lines mark the wave normals of incident and diffracted waves. The distance $(A + B)$ must be equal to a whole number of wavelengths for total constructive interference and the graph visualizes this distance to be $(A + B) = 2d \sin\theta$, thus $n\lambda = 2d \sin\theta$.

- There is no or little prepartion effort.
- XRD and XRR are executable in most environments.

Besides the structural properties of a sample also the thickness and roughness of thin films and multilayers can be determined via XRD and XRR. Because of this, they have been the essential techniques for microstructural characterization used in this work and are explained thoroughly in the following sections. However, this is not a tutorial about crystallography and general diffraction physics, concerning these aspects the reader is referred to e. g. [cul78].

## 4.1 X-Ray Diffraction

When x-rays impinge on a sample, several types of interaction can occur: photoelectric effect, flourescence, production of Auger electrons, Compton scattering and coherent scattering. Only the last one, coherent scattering, leads to the phenomenon of diffraction. What happens is a perfectly elastic collision between a photon and an electron which leads to a change of direction of the photon but preserving its energy and phase [sny99].

### 4.1.1 Peak Location of Diffracted X-Rays

The easiest way to derive the directions in which the x-ray beam is scattered is to visualize the x-rays as being reflected from the planes of the crystal. Then, constructive interference can only occur if all waves scattered at a set of parallel planes come out in phase. This is the case when their difference in path length is an integer of the wavelength, $n\lambda$. Figure (4.1) visualizes that this path difference is equal to $(2\,d\,\sin\theta)$, with $d$ being the plane distance and $\theta$ the angle of incident and diffracted beam respectively. It follows, that the condition of diffration is given by

$$n\lambda = 2d\sin\theta \tag{4.1}$$

This is the so called Bragg law, derived by W. L. Bragg in 1913 [kri94].

In practice, not the order $n$ of diffraction for a given plane $(hkl)$ is considered but the first order diffraction for the virtual set of planes $(nh\,nk\,nl)$, so equation (4.1) becomes

$$\lambda = 2d_{hkl}\sin\theta \tag{4.2}$$

In a conventional XRD measurement, the angle of incidence relative to the sample surface is varied and the angle of detection is kept equal to it. Under this condition and according to Bragg's law only planes parallel to the sample surface can be detected. This fact is also called *mirror condition* [bun00, p. 925] and is of a very strict kind in case of single crystal investigation: if at all, there is only one family of planes $(nh\,nk\,nl)$ which can be detected in one measurement run. So this kind of measurement is useful for a polycrystalline material where for each family of planes $(hkl)$ there is always a considerable amount of crystallites satisfying the Bragg condition.

### 4.1.2 Intensity of Diffracted X-Rays

The peak location of the diffracted x-rays has been identified in the previous section, the next question is how their intensity can be determined. Here we have to leave the simplified picture of reflection and go back to x-rays as an electromagnetic wave which interacts with the electron inside the atom [sny99], [klu74], [kri94].

The oscillating electromagnetic field of the incoming x-radiation will cause the electron also to oscillate and reradiate the incident radiation through a solid angle of 360°. The intensity scattered from an electron has been shown by J. J. Thompson to be

$$I_e = \frac{I_0}{r^2}\left[\frac{e^2}{m_e c^2}\right]^2 \frac{1+\cos^2(2\theta)}{2} \tag{4.3}$$

$I_0$ is the intensity of the incoming beam and $r$ is the distance of the scattering electron to the detector. The second term is the classical radius of the electron with its charge $e$, its mass $m_e$ and the speed of light $c$. The third therm is called **polarization factor** which takes account of the fact that the scattering process partially polarizes the beam which was initially unpolarized [jen96].

If there are a number of electrons in one atom, then the more intensity is diffracted the more electrons are present. When viewed at an angle of 0° all scattered waves coming from different electrons are exactly in phase. But with increasing angle of view these different waves have increasingly different path lengths and this leads to partial destructive interference and therefore to a decreased net scattered intensity. For this reason for every type of atom the so called **normal atomic scattering factor** $f_0$ has to be taken into account. $f_0$ is equal to the number of electrons in the atom at $\theta = 0°$ and falls off rapidly as a function of $(\sin\theta)/\lambda$ [jen96]. The exact values of the function $f_0$ have to be calculated by integrating the scattered waves over the electron distribution around the atom.

So far the electron has been assumed as being free, but when the electron is part of an atom, the possibility of excitation into higher states of energy becomes possible in case the atom has an absorbtion edge close to the wavelength of the x-rays. When falling back into the ground state, a photon of corresponding energy is emitted which has a phase lag to the normally scattered photon. Therefore, the atomic scattering factor $f_0$ has to be corrected by introducing an additional real ($\Delta f'$) and imaginary ($\Delta f''$) term, called **anomalous dispersion corrections**, to yield an effective scattering $f$:

$$f = f_0 + \Delta f' + i\Delta f'' \tag{4.4}$$

Another fact is missing in this picture: the atom under investigation is vibrating about its lattice site and this vibration depends on the temperature as well as on the atomic mass and the bonding forces of its environment. For this reason, the so called **Debye-Waller temperature factor** $B$ is introduced, which is related to the mean square of the vibrational amplitude of the atom via $B = 8\pi^2 U^2$ and acts as a damping term on the slope of the atomic scattering factor:

$$f = f_0 \exp\left(-\frac{B\sin^2\theta}{\lambda^2}\right) \tag{4.5}$$

So far, the scattering at one atom has been considered but now we have to take a look at how the scattered waves from many atoms arranged in a crystal play together. This means that the scattered waves from the distinct atoms have to be added up according to their different positions in the unit cell, taking into account their atomic scattering factor $f_i$ and their phase factor $\Phi_i$. Doing this leads to the so called **structure factor** $F_{hkl}$ for any set of planes $hkl$:

$$F_{hkl} = \sum_{j=1}^{N}(f_j \cdot \Phi_j) = \sum_{j=1}^{N} f_j \exp\left[2\pi i(hx_j + ky_j + lz_j)\right] \tag{4.6}$$

where $N$ is the number of atoms in the unit cell.

In intensity calculations of a powder diffractogram the number of equivalent planes in a crystal, which are planes having the same plane distance, additionally has to be considered. In powder measurements, all such planes contribute to the same registered peak and this is expressed by the **multiplicity factor** $M_{hkl}$. For example, in a cubic lattice the planes (100), (010), (001), $(\bar{1}00)$, $(0\bar{1}0)$ and $(00\bar{1})$ have the same plane distance, so the multiplicity factor for the (100) plane is $M_{hkl} = 6$.

In a XRD measurement the incoming x-ray beam is in general not strictly monochromatic and additionally, it is not exactly parallel but more or less divergent. When we take a look at how long a given plane is in the position to reflect, these two aspects lead to differences in this time for different planes again depending on the angle of diffraction. For powder XRD measurements this so called **Lorentz factor** is given by:

$$L = \frac{1}{2\sin^2\theta\cos\theta} = \frac{1}{\sin(2\theta)\sin\theta} \tag{4.7}$$

The absolute intensity of a diffracted peak is proportional to the number of contributing unit cells. On one hand, this number depends on the size of the beam illuminating the sample and on the other hand it depends on the penetration depth wich is determined by the absorption of the material. In the Bragg-Brentano geometry with a briquette-shaped homogeneous sample, the irradiated volume of the sample remains constant for all diffraction angles in the case that a fixed divergence slit is used. Then the irradiated beam area is reduced with increasing $2\theta$ but the beam penetrates deeper at the same time. So the irradiated volume remains unchanged and in the intensity equation a constant factor $1/\mu_S$ needs to be considered, with $\mu_S$ being the **linear absorption coefficient** related to the sample material.[1]

Summarized all the aspects mentioned above, the **integrated intensity** $I_{(hkl)\alpha}$ per unit length of the diffraction circle for line $(hkl)$ of phase $\alpha$ of an ideally im-

---

[1] Besides the effect of absorption, three further effects influencing the relative intensities of a powder diffraction peaks can occur in case of large crystallites. Firstly, the *primary extinction* is the phenomenon of beams being multiply reflected at the lattice planes: each time a beam is reflected from a plane a phase shift of $\pi/2$ occurs. Therefore, a beam which is reflected back into the crystal at the underside of a plane has a phase shift of 180° to the incident beam and both interfere destructively. The result is a lowered intensity of strong reflections from very perfect crystals. Another effect which may occur in perfect crystallites is the diffraction of most of the intensity out of the crystal before the beam can penetrate significantly deep. This is called *secondary extinction* and also leads to a lower relative intensity of very strong peaks in comparison to weaker reflections. The third effect called *microabsorption* may occur in a polyphase mixture: if large crystallites of phase $\alpha$ lie above or below crystallites of phase $\beta$ the beam spends an unproportionate time in the large crystallites. This leads to falsified relative intensities regarding the phase mixture. All three effects can not be treated mathematically in a closed form but they become less important with decreasing crystallite size.

perfect crystal in a flat briquette-shaped sample, measured by a diffractometer with fixed receiving slit is calculated as

$$I_{(hkl)\alpha} = \frac{K_e K_{(hkl)\alpha} v_\alpha}{\mu_S} \tag{4.8}$$

$v_\alpha$ is the volume fraction of phase $\alpha$ in the specimen and $K_e$ comprises the constants for the given experimental system[2]:

$$K_e = \frac{I_0 \lambda^3}{64\pi r}\left(\frac{e^2}{m_e c^2}\right)^2 \tag{4.9}$$

The constant $K_{(hkl)\alpha}$ draws together the multiplicity factor $M_{hkl}$, the structure factor $F_{(hkl)\alpha}$, the Lorentz-polarization correction and the volume of the unit cell of phase $\alpha$, $V_\alpha$:

$$K_{(hkl)\alpha} = \frac{M_{hkl}}{V_\alpha^{\,2}} \mid F_{(hkl)\alpha} \mid^2 \left(\frac{1+\cos^2(2\theta)}{\sin^2\theta\cos\theta}\right)_{hkl} \tag{4.10}$$

The understanding of the diffracted intensity [jen96] enables to calculate the diffraction pattern when the crystallographic data and the factors mentioned above are known. Vice versa, it also enables to determine the crystal structure of unknown materials. Unfortunately, this way is more tricky because only the amplitude but not the phase of the diffracted x-ray beam is measured: $F_{hkl}$ is a complex number so only $\mid F_{hkl} \mid$ can be measured and the phase angle of the structure factor $\exp[-2\pi i(hk_j + ky_j + lz_j)]$ is lost during the measurement. This fact is called *phase problem.*

Some general intensity considerations shall close this section for clarity. In equation (4.8) the integrated intensity is proportional to the crystallite volume $v_\alpha$ of phase $\alpha$, a fact that is not clear at first when starting the intensity study with an ideal small single crystal. The crystal has to be small in the sense of no absorption to occur and "ideal" meaning that it has no imperfections. The direction of the primary beam is given by the unit vector $\vec{s}_0$ and the scattered intensity in direction of the unit vector $\vec{s}$ at a distance $R$ from the crystal is considered. The crystal is assumed to be a parallelopipedon with edges $N_1 a_1$, $N_2 a_2$ and $N_3 a_3$ parallel to the crystal axes $\vec{a}_1, \vec{a}_2, \vec{a}_3$.

Then the intensity $I_P$ diffracted from this small crystal is given by

$$I_P = I_e \mid F \mid^2 \frac{\sin^2(\frac{\pi}{\lambda})(\vec{s}-\vec{s}_0)\cdot N_1\vec{a}_1}{\sin^2(\frac{\pi}{\lambda})(\vec{s}-\vec{s}_0)\cdot \vec{a}_1} \cdot \tag{4.11}$$

$$\cdot \frac{\sin^2(\frac{\pi}{\lambda})(\vec{s}-\vec{s}_0)\cdot N_2\vec{a}_2}{\sin^2(\frac{\pi}{\lambda})(\vec{s}-\vec{s}_0)\cdot \vec{a}_2} \cdot \frac{\sin^2(\frac{\pi}{\lambda})(\vec{s}-\vec{s}_0)\cdot N_3\vec{a}_3}{\sin^2(\frac{\pi}{\lambda})(\vec{s}-\vec{s}_0)\cdot \vec{a}_3}$$

---

[2] Some of the constants apply to the case of an ideally imperfect crystal which has not been derived here. For details see e. g. [war69].

with $I_e$ being the Thompson scattering from a single electron as given in equation (4.3) and $F$ according to equation (4.6) [war69]. A diffracted beam only exists if the three Laue equations, which are an alternative expression to the Bragg law, are simultaneously satisfied:

$$\begin{aligned}(\vec{s}-\vec{s}_0)\cdot\vec{a}_1 &= h'\lambda \\ (\vec{s}-\vec{s}_0)\cdot\vec{a}_2 &= k'\lambda \\ (\vec{s}-\vec{s}_0)\cdot\vec{a}_3 &= l'\lambda\end{aligned}$$

In the case of an exact satisfaction of the three Laue equations, the intensity according to equation (4.11) would show a maximum intensity of

$$(I_P)_{max} = I_e \mid F \mid^2 {N_1}^2{N_2}^2{N_3}^2 \tag{4.12}$$

but this quantity will never be observed in practice. Firstly, because no ideal crystal does exist and secondly, because the primary beam is never perfectly parallel. Therefore, the observable quantity in a diffraction experiment is the integrated intensity per unit length of the diffraction circle as given in equations (4.8 - 4.10), depending on the volume $v \propto N_1N_2N_3$ and not on the square of the volume.

### 4.1.3 Shape of Diffraction Peaks

The profile of a given diffraction peak is the result of a number of independent contributing shapes, which origins can be divided into two categories: instrumental contributions and the intrinsic profile which includes sample effects. The observed diffraction profile $P(2\theta)$ is a convolution of all contributing profiles:

$$P(2\theta) = \int I(2\theta)S(2\theta - 2\theta')\, d(2\theta') \tag{4.13}$$

in the following expressed as

$$P(2\theta) = I(2\theta) \star S(2\theta) \tag{4.14}$$

where $I(2\theta)$ itself is the convolution of functions due to instrumental effects and $S(2\theta)$ again the convolution of functions due to sample effects [lan00].

In general, the peak shape is asymmetric and varies over the measured angle range. The individual contributions are briefly explained in the following.

**Instrumental Profile**

While the x-ray source image and focusing optics like incident and diffracted beam slit as well as receiving slit and monochromator cause symmetric broadening with Gaussian shape, there are in principle three sources of asymmetrical line broadening. Firstly, this is the flatness of the specimen. The sample should be curved to lie on the focusing circle, but a flat specimen is out of focus and produces a small asymmetry in the profile with a $\cot\theta$ dependence. Secondly, depending on the absorption coefficient of the sample, the x-ray beam is not reflected at the surface of the sample but penetrates into it. The smaller the absorption coefficient the deeper the beam penetrates into the material and the worse the focusing condition of the reflected beam becomes. For those materials, a substantial asymmetric profile is introduced. The third source of asymmetry is the axial divergence of the beam which also follows a $\cot\theta$ dependence.

Another contribution to the instrumental profile is the spectral distribution of the x-ray tube in use. The inherent spectral profile from the $K$ transition in a sealed x-ray tube with a copper anode has been shown to have a width of $1.18\cdot10^{-4}$ Å with Lorentzian profile which is not completely symmetric [sny99].

**Intrinsic Profile**

The intrinsic profile comprises the Darwin width of a diffracted x-ray beam as well as broadening effects due to the microstructure of the sample. These are caused by the crystallite size and strain of a sample.

The *Darwin width* of a x-ray beam diffracted at a perfect crystal is a consequence of the uncertainty principal ($\Delta p\Delta x = h$). The absorption coefficient of the specimen requires that the photon in the crystal is located in a rather small volume. So on the other hand $\Delta p$ and, via the deBroglie relation ($\Delta p = h/\Delta\lambda$), $\Delta\lambda$ have to be finite values. This distribution of wavelengths produces a finite width of the diffraction peak with Lorentzian profile shape [sny99].

## 4.2 Special Aspects

### 4.2.1 Preferred Orientation

In the two sections above the way how to calculate the diffraction pattern of a known crystal structure has been deduced. It is valid for single crystals and for polycrystalline powders, although both have to be treated a little differently. In an ideal polycrystalline powder sample the crystallites are randomly oriented, but in polycrystalline bulk materials this is commonly not the case. Here we find *preferred orientation* of crystallite directions. As a consequence, the intensity distribution of the observed peaks differs from the one of an ideal powder.

For a complete determination of preferred orientation pole figures of the sample have to be measured, that means that the intensity of a particular Bragg diffraction line is plotted as a function of the three-dimensional orientation of the specimen. Then a *pole density distribution function* can be defined:

$$P^i_{(hkl)}(\alpha\beta) = \frac{dV^i_y/V^i}{d\Omega} \tag{4.15}$$

where $P^i_{(hkl)}(\alpha\beta)$ is the volume fraction of the crystallites of phase $i$ having their crystal direction parallel to the sample direction, i. e. parallel to the diffraction vector. $V^i$ is the volume fraction of phase $i$ and $d\Omega$ describes the divergences of incident and diffracted beam [bun00].

The pole density relates the integral intensity measured in a textured sample to the corresponding intensity of a random sample [bun00]:

$$I^i_{(hkl)}(y) = I^i_{(hkl),random} \cdot P^i_{(hkl)}(y) \tag{4.16}$$

The intensity of an ideal polycrystalline sample with random orientation of all grains is documented for many thousand substances in the *Powder Diffraction File (PDF)* data base [PDF].

The diffractometer used for the investigations in this thesis does not provide the possibility to measure pole figures. Nevertheless, an estimation of preferred orientiation is possible on the basis of the PDF data. The comparison of the PDF integral intensities of the different diffraction peaks of one phase with the measured relation of integrated intensities enables to quantify the preferred orientation in form of deviations from the ideal relation.

### 4.2.2 Crystallite Size

When diffraction in an ideal infinite crystal occurs, i. e. when the Bragg condition (4.2) is satisfied with the angle of incidence being $\theta = \theta_0$, then the path difference between adjacent planes is exactly equal to $n\,\lambda$. When $\theta$ is increased or decreased, every plane has a counterpart deeper in the crystal which is exactly out of phase, so that the diffracted waves of these two planes cancel each other. The closer $\theta$ is to $\theta_0$ the deeper in the crystal lies the plane which is out of phase. Considered all planes of the unit cell, no net scattering will occur,

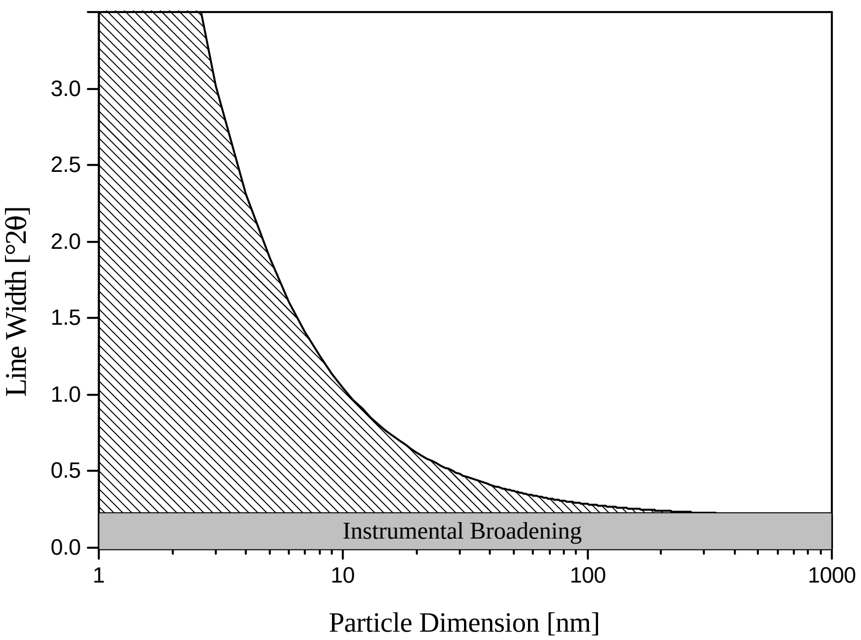

Figure 4.2: Line width as a function of particle size [jen96].

except for the case when the Bragg condition is exactly satisfied. But when the deeper planes needed to cancel the diffracted waves from the planes nearer to the surface are not present, there is net scattering also at angles $\theta \approx \theta_0$ and so the peak becomes broader. This is the fact for crystallites smaller than about $1\mu m$ and the smaller the crystallites the broader the peak will become. This effect of *particle size broadening* was first treated by P. Scherrer [scher18] who evaluated the interdependence of the mean crystallite dimension $\tau$ and the line broadening $\beta_\tau$ which is known as the *Scherrer equation*:

$$\tau = \frac{K\lambda}{\beta_\tau cos\theta} \tag{4.17}$$

$\beta_\tau$ is the full width in radians at half maximum of the observed peak, from which the instrumental broadening as well as broadening due to sample strain has to be subtracted. The factor $K$ is the so called shape factor and depends on the crystal structure. For cubic structure its value is about 0.9. For a given crystallite dimension $\tau$, the peak width increases as $(1/\cos\theta)$ and so particle size broadening is most pronounced at large values of $\theta$. In figure (4.2) the total line width according to this equation as a function of crystallite size is calculated for a fixed value of $\theta$.

To evaluate the maximum of the peak profile and the peak area in case of particle size broadening, further considerations have to be made. In equations (4.8-4.10) we have seen, that the integrated intensity produced by diffraction of a crystal with the total number of unit cells in the crystal being $N = N_1 N_2 N_3$ is given by

$$\int P(2\theta)d(2\theta) = K_e K_{hkl} N \tag{4.18}$$

The integrated intensity is equal to the peak area. The crystal considered here is assumed to be very small, meaning that absorption can be neglected. The Laue equations (4.12) can alternatively be expressed as $(\vec{s} - \vec{s_0})/\lambda = h_1\vec{b_1} \cdot h_2\vec{b_2} \cdot h_3\vec{b_3}$, where $h_1, h_2, h_3$ are continuous variables. The maximum of the peak profile is

$$P_{max}(2\theta) = \frac{K_e K_{hkl} \cos\theta}{\lambda \mid \vec{b_3} \mid} \sum_{n_1} \sum_{n_2} {N_3}^2(n_1 n_2) \tag{4.19}$$

according to equation (4.12). Here, $N_3(n_1 n_2)$ represents the number of cells in the row $(n_1 n_2)$ and hence the peak maximum depends on the square of the number of unit cells in z-direction, whereas the peak area depends on the volume of the crystallite. It is important to note, that equation (4.12) is not true for a large crystal due to the arguments given above, but here we are considering very small crystallites and thus the square dependence on the number of unit cells is justified.

The integral width of a reflection is defined as the ratio of the peak area to the peak maximum, so this value is the ratio of the two terms given above:

$$\beta(2\theta) = \frac{\int P(2\theta)d(2\theta)}{P_{max}(2\theta)} \tag{4.20}$$

and can be reduced to the simple form

$$\beta(2\theta) = \frac{\lambda}{L \cos\theta} \tag{4.21}$$

where $L$ is the effective particle dimension. This value is the volume average of the crystal dimension in $a_3$-direction, or put differently, normal to the reflecting planes [war69, p. 251ff]. This equation is similar to the Scherrer equation (4.17) but with the peak width defined differently and so without the necessity of using the constant $K$.

So far, one single crystallite has been considered. In a powder or non-epitaxial thin film sample, there are many crystallites and furthermore many crystallites oriented in the same direction. X-rays which are diffracted at different crystallites of identical orientation add up incoherently and thus the diffracted intensity is simply the sum of the single intensities.

In a sample of limited dimension perpendicular to the diffracting planes, the number of crystallites reduces with increasing crystallite size in the same direction. If the number of crystallites is given by $z$ and the crystallite size perpendicular to the diffracting planes is proportional to $N_3$ which is the number of unit cells, then $z \propto 1/N_3$. To yield the maximum peak height and the peak area for the whole sample, equations (4.18) and (4.19) have to be multiplied by $z$. In the case of constant crystallite size in the diffracting planes this is equivalent to a division by $N_3$. Thus the maximum peak height becomes proportional to $N_3$, the peak area becomes independent of $N_3$ and the integral width remains unchanged.

The Scherrer equation (4.17) or equivalenty equation (4.21) can be used to determine crystallite sizes as low as about 10 Å and the determination is the more exact the better instrumental and strain broadening can be separated from size broadening.

Finally, a few aspects concerning the distribution of particle sizes shall be considered. So far, we have spoken in terms of average partice size, but not of the way how different crystallite sizes may be distributed in a sample. This distribution in a powder and also in a polycrystalline solid depends on the material and on the preparation of the sample. The most common distribution which has been reported in the literature is the asymmetric lognormal distribution. But for thin films with a high degree of preferred orientation very often symmetric distributions have been found, which are approximated by the Gaussian distribution. Some care has to be taken concerning this kind of distribution as it would imply negative crystallite sizes in case of very small average sizes. When the distribution function is known, the diffraction peak can be calculated by summing up the intensities of the single crystallites, weighted by the distribution function. Vice versa, by adjusting the peak profile according to either of the distribution functions, the distribution can be determined. In calculating the peak profiles for gaussian and lognormal distributions having different dispersion $\sigma(D)/\langle D\rangle$ (where $\sigma(D)$ is the root of the variance and $\langle D\rangle$ is the arithmetic mean of the distribution function), Langford *et al* have shown, that the FWHM of the diffration peak decreases with increasing dispersion, which is true for both distribution functions [lan00b].

### 4.2.3 Residual Stress and Strain

Two principal types of stresses in a material have to be distinguished: macrostress and microstress. If the stress is uniformly compressive or tensile as depicted in figure (4.3 b) it is called *macrostress* and it will either compress or contract the crystal unit cell. Consequently, the observed diffraction peak is shifted, according to Bragg's law.

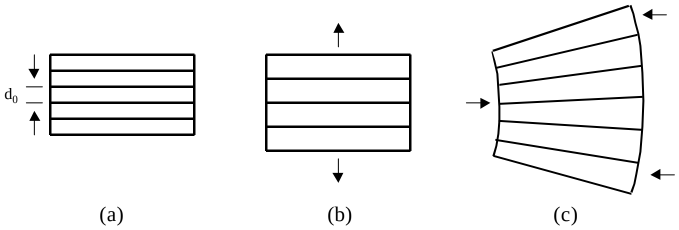

Figure 4.3: (a) Lattice planes without strain, (b) uniform strain with expanded interplane distance and (c) nonuniform strain with partly increased and partly decreased interplane distance [jen96].

On the other hand, if the stress is not uniform but contains tensile as well as compressive contributions (figure 4.3 c), then the $d$ values of the unit cell will be distributed about the normal, unstrained $d_{hkl}$ value. As a consequence, the observed diffraction peak will be broadened and this kind of stress is called *microstress* [sny99].

In a similar manner as for crystallite size broadening in equation (4.17) the additional broadening $\beta_\epsilon$ of an observed peak is related to the residual strain $\epsilon$ and the diffraction angle $\theta$ via

$$\beta_\epsilon = 4\epsilon \tan\theta \tag{4.22}$$

Fortunately, the two broadening effects differ in their $\theta$-dependence, a fact which allows to separate these effects [jen96].

### 4.2.4 Multilayer Satellites

Multilayers can show additional diffraction peaks around the structural Bragg peaks of the constituting materials due to their additional artificial periodicity on an atomic scale. Whether such superlattice peaks will occur, depends on the growth mode of the multilayer stack: satellite peaks are only observable if the layers scatter the radiation coherently.[3] The position and the intensity of those *multilayer satellites* is discussed in the following.

We consider a multilayer stack which is made up of alternating layers of the materials $A$ and $B$ in such a way that the double layer element looks like depicted in figure (4.4). The single layers $A$ and $B$ are textured and the interplanar distances in growth direction are given by $d_A$ and $d_B$ while $n_A$ and $n_B$ are the numbers of atomic layers per single layer. Then the products $n_A d_A$

---

[3] In section (8.7) coherent and noncoherent growth of a multilayer is described in detail. For a fast overview see figure (8.26) on page 149.

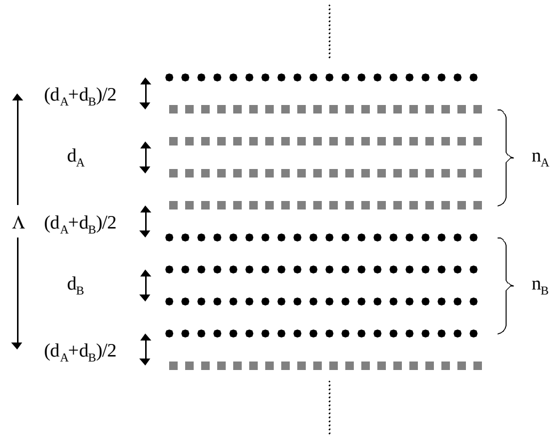

Figure 4.4: One dimensional step model of a multilayer stack consisting of alternating blocks of atomic planes of material $A$ and $B$, respectively [mic95].

and $n_B d_B$ are the single layer thicknesses and their sum $(n_A d_A + n_B d_B)$ is the double layer thickness, which is abbreviated by $\Lambda$ and sometimes also called *multilayer periodicity.* For the interplanar spacing of the interface between layer $A$ and $B$ an average distance of $(d_A + d_B)/2$ is assumed. This model is known as *one step* model and was introduced by Segmüller and Blakeslee [seg73]. The way the model is presented here follows [mic95].

For the whole multilayer stack an average lattice spacing $d_0$ can be defined as

$$d_0 = \frac{n_A d_A + n_B d_B}{n_A + n_B} = \frac{\Lambda}{n} \tag{4.23}$$

where the sum of the numbers of atomic layers $(n_A + n_B)$ has been denoted as $n$. Taking the average lattice spacing $d_0$, the scattering vector $\vec{q}$ can be written in growth direction as

$$q = \frac{2\pi L}{d_0} = \frac{4\pi \sin\theta}{\lambda} \tag{4.24}$$

In the last step, use was made of the Bragg equation with the diffraction angle $\theta$ and the x-ray wavelength $\lambda$. $L$ is a continuously running variable:

$$L = \frac{2 d_0 \sin\theta}{\lambda} \tag{4.25}$$

If the layers of the multilayer stack are grown in such a way that they scatter coherently, the amplitudes of the diffracted x-rays of layers $A$ and $B$ are connected by a well-defined phase factor $\exp(i\pi Ln)$. Therefore, the diffracted amplitude of one pair $(A, B)$ is given by

$$A(L) = f_A \cdot \frac{\sin\left(\frac{\pi n_A d_A L}{d_0}\right)}{\sin\left(\frac{\pi n_A d_A}{d_0}\right)} + \exp(i\pi Ln) f_B \cdot \frac{\sin\left(\frac{\pi n_B d_B L}{d_0}\right)}{\sin\left(\frac{\pi n_B d_B}{d_0}\right)} \tag{4.26}$$

where $f_A$ and $f_B$ are the scattering factors of the materials $A$ and $B$. For a multilayer with $N$ double layers of type $(A, B)$ the amplitude given above has to be multiplied by

$$A_N(L) = \frac{\sin(\pi nNL)}{\sin(\pi nL)} \tag{4.27}$$

In calculating the diffracted intensity, the square of the amplitudes has to be taken and the result can be written in terms of four intensity contributions:

$$I(L) = A_N^2(L) \cdot A(L) \cdot A^*(L) = I_N[I_A + I_B + I_{AB}] \tag{4.28}$$

$I_A$ and $I_B$ are the intensities produced by the isolated layers of material $A$ and $B$ with

$$I_A = f_A^2 \cdot \frac{\sin^2\left(\frac{\pi n_A d_A L}{d_0}\right)}{\sin^2\left(\frac{\pi n_A d_A}{d_0}\right)} \quad \text{and} \quad I_B = f_B^2 \cdot \frac{\sin^2\left(\frac{\pi n_B d_B L}{d_0}\right)}{\sin^2\left(\frac{\pi n_B d_B}{d_0}\right)} \tag{4.29}$$

The single layer terms $I_A$ and $I_B$ produce peaks at positions corresponding to the pure materials having a peak width according to the single layer thickness. In the top row of figure (4.5) these terms have been calculated for a Co/Cu multilayer with $N = 20$ double layers. The left column shows the calculation for a multilayer with $n_{Cu} = n_{Co} = 10$ and the right row for one with $n_{Cu} = 20$ and $n_{Co} = 10$ for comparison. In the calculation the scattering factors $f_{Cu}$ and $f_{Co}$ have been approximated by their atomic numbers $z_{Cu} = 29$ and $z_{Co} = 27$. The sum $(I_A + I_B)$ would be the XRD signal of a pair of single layers $(A, B)$ if they were not coherent.

The mixed term $I_{AB}$ with

$$I_{AB} = f_A \cdot f_B \cdot \cos(\pi Ln) \frac{\sin\left(\frac{\pi n_A d_A L}{d_0}\right)}{\sin\left(\frac{\pi n_A d_A}{d_0}\right)} \cdot \frac{\sin\left(\frac{\pi n_B d_B L}{d_0}\right)}{\sin\left(\frac{\pi n_B d_B}{d_0}\right)} \tag{4.30}$$

is also given in the top row of figure (4.5). It produces a peak at a position according to the average interplanar spacing $d_0$ and does only exist if the layers are coherently grown, because otherwise the phase factor $\exp(i\pi Ln)$ in the amplitude term (4.26) does not exist. Each of the three terms $I_A, I_B, I_{AB}$ is accompanied by finite-size oscillations, the so called *Laue satellites*. These oscillations can be observed in incoherent multilayers where the grain size equals the layer thickness [mic95]. The sum $(I_A + I_B + I_{AB})$ gives the diffraction signal of one coherent pair of layers $(A, B)$ and can be found in the middle row of figure (4.5).

The multiplicity factor $I_N$ for a layer stack built up of $N$ double layers $(A, B)$,

$$I_N = \frac{\sin^2(\pi LnN)}{\sin^2(\pi Ln)} \tag{4.31}$$

is characterized by strong equidistant peaks for $\pi Ln = \pi h$, where $h$ is an integer, thus if

$$Ln = \frac{2d_0 \sin\theta}{\lambda} n = h \quad \Leftrightarrow \quad \sin\theta = h\frac{\lambda}{2d_0 n} \tag{4.32}$$

In the case of $h = n$ this is the Bragg equation for the average interplanar spacing $d_0$ and the corresponding diffraction angle is denoted as $\theta_0$. The distance of the peaks is related to $1/n$ and therefore the larger $n$ the smaller the distance becomes. Between the peaks there are $N - 2$ modulation peaks according to the total thickness of the multilayer stack. The maximum height is $N^2$ and the full width at half maximum of the peaks is proportional to $(1/nN)$ [gla00]. The function $I_N$ is also given in the middle row of figure (4.5) but its intensity has been normalized for better comparison with the sum $(I_A + I_B + I_{AB})$ in the same graph.

In multiplying the term $I_N$ with the sum $(I_A + I_B + I_{AB})$, the middle peak at $\theta_0$ corresponding to the Bragg position of the average lattice spacing $d_0$ becomes surrounded by satellites, see bottom row of figure (4.5). Compared to the sum $(I_A + I_B + I_{AB})$, the middle peak decreases in width according to the larger crystallite size. To account for the instrumental line broadening, equation (4.28) has to be convoluted with a peak profile function having a peak width according to the limited resolution of the instrument. In the calculations presented in figure (4.5) a convolution has been performed with a Gaussian distribution function of width $\sigma = 0.1°$. Furthermore, the root square of the intensity has been taken to pronounciate the satellite peaks.

The general features of a high angle diffraction pattern of a coherent multilayer, described by the one step model are familiar now and subsequently, it is interesting to go the other way round and see how the multilayer properties can be deduced from the diffraction pattern [gla98].

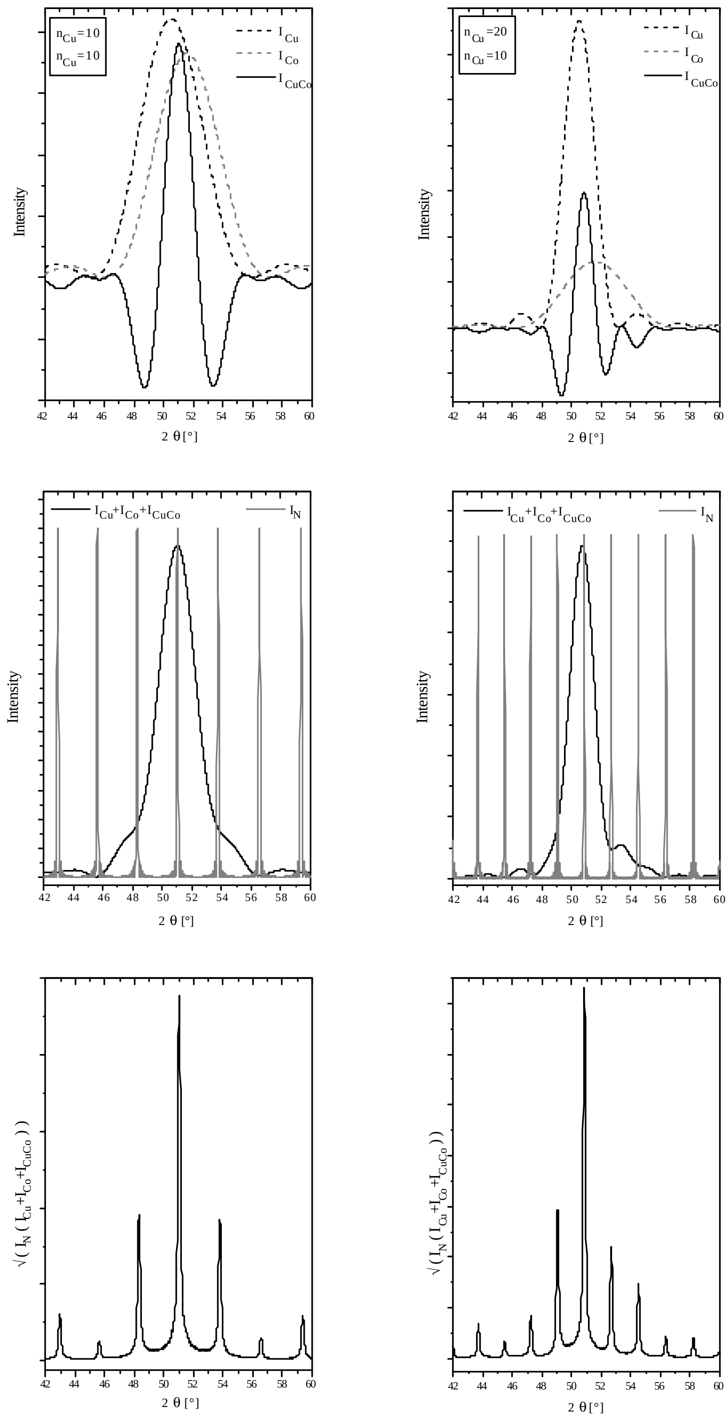

Figure 4.5: Calculation of the XRD pattern of Cobalt/Copper multilayers with $N = 20$ double layers according to the step model. On the left side the individual intensity contributions of equation (4.28) for a multilayer with $n_{Cu} = n_{Co} = 10$ are shown, on the right side those for $n_{Cu} = 20$, $n_{Co} = 10$. The total intensity in the bottom row has been convolved with a Gaussian distribution of width $\sigma = 0.1°$ to account for instrumental broadening and the square-root intensity scale has been chosen to pronounce the satellites.

The average lattice spacing $d_0$ can be determined from the position $\theta_0$ of the main peak via equation (4.23) and the Bragg equation (4.2) as

$$d_0 = \frac{n_A d_A + n_B d_B}{n_A + n_B} = \frac{\Lambda}{n} = \frac{\lambda}{2\sin\theta_0} \tag{4.33}$$

The mulitlayer period $\Lambda$ can be identified from the angular positions $\theta_m$ and $\theta_n$ of the satellite peaks of the order $m$ and $n$, respectively, via:

$$\Lambda = \frac{(m-n)\lambda}{2(\sin\theta_m - \sin\theta_n)} \tag{4.34}$$

If the interplanar spacings $d_A$ and $d_B$ are known, the quantities $n_A$ and $n_B$ can be calculated as

$$n_A = \frac{\Lambda(d_0 - d_B)}{d_0(d_A - d_B)} \quad \text{and} \quad n_B = \frac{\Lambda}{d_0} - n_A \tag{4.35}$$

The main difficulty in the determination of $n_A$ and $n_B$ is the fact that in general the interplanar spacings $d_A$ and $d_B$ are *not* known a priori, even if the constituting materials of the multilayer are well known. The reason are lattice distortions due to the mismatch of the materials. A multilayer can become coherent only if the in-plane lattice spacings of both materials approach to each other at the interface. But a distortion of the in-plane spacing leads to a distortion of the spacing perpendicular to it as well, and thus $d_A$ and $d_B$ will differ from the bulk values. Therefore, the values $d_0$ and $\Lambda$ which can be gained from the measurement do not determine the values of $n_A$ and $n_B$ automatically. In fact, to every pair $d_A, d_B$ they give the corresponding pair $n_A, n_B$. Therefore, it is interesting to see if there are further aspects of a satellite diffraction pattern which may allow to identify the paramaters $d_A, d_B$ and hence $n_A, n_B$ uniquely.

This important aspect is the height of the satellite peaks relative to the main peak. Within the one step model there are two main influences on the relative height of the satellite peaks. Firstly, the height of satellites of the same order need not have the same height and in fact asymmetric peak heights are the usual case. The reason for this is the asymmetric shape of the “sumpeak” ($I_A + I_B + I_{AB}$). By multiplication with $I_N$ the equidistant peaks of equal height are multiplied with different values of the sumpeak. This can be seen in the middle row of figure (4.5). Even when the number of monolayers is the same for both materials, the sumpeak will not be of symmetric shape in case of different scattering powers of the materials (left column in figure (4.5)). If the scattering powers are not taken into account, the satellites are more intense on that side of the main peak where the one material has its bulk peak which has

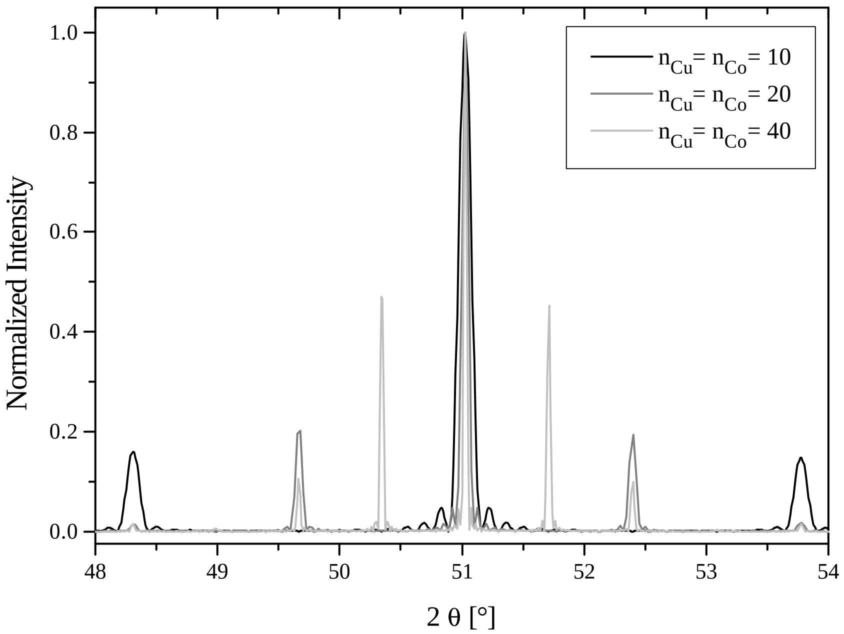

Figure 4.6: Normalized intensity of Cobalt/Copper multilayers with $N = 20$ double layers but different number of atomic layers $n_{Cu} = n_{Co}$ to visualize the increase of relative satellite intensity with increasing $n$.

more atomic layers than the other. This is shown in the right column of figure (4.5) where the satellite of the order $(-1)$ on the Copper side of the main peak is the strongest one.

Secondly, the relative height of the satellite peaks increases with $n$ because of the increasing intensity of the sumpeak, whereas the intensity of the multiplication function $I_N$ remains unchanged. Although the width of the sumpeak decreases, this is of no opposite effect because of the according decrease of the peak distances of $I_N$. In summary, not only the main peak increases in height but also its satellites, and their increase is larger than that of the main peak, as can be seen in figure (4.6).

Due to these arguments it is also clear, that an increasing number of double layers $N$ does not increase the relative intensity of the satellites.

Up to now the model of a perfect multilayer has been proposed, but a more realistic model has to consider for a number of imperfections such as interface roughness, interdiffusion and grain sizes smaller than the complete layer stack. A lot of models describing imperfect multilayer structures have been proposed and shall not be given here in detail but only in a few interesting aspects.

M. B. Stearns [ste88] has examined the case of a completely miscible random alloy having a linear variation in composition and she proposed a linear variation of the lattice constant across the interface, the so called trapezoidal interface model. Within this model she could explain nonsymmetrical satellite positions on one hand, and decreasing satellite heights with increasing interface thickness on the other hand.

Clemens and Gay [cle87] compared two different cases of interface roughness: Firstly, the case of a continuous fluctuation of the layer thickness given by a Gaussian distribution, and secondly, the discrete deviation from the average layer thickness by integers of the interplanar spacing. While the first model results in the loss of coherency for rather small values of roughness and therefore in a loss of satellites and broadening of the main peak, the relative height of the satellites is preserved in the second model for equal values of roughness. The first model accounts for multilayers having an amorphous phase which can be caused by interfacial disorder in systems where the constituents have a large size mismatch. For multilayers coherently grown, the case of discrete roughness is a realistic one.

### Multilayer Satellite Analysis: *SlerfWin*

The general features of multilayer satellites have been explained in section (4.2.4) and it has been outlined there that the main difficulty is the exact determination of the interatomic distances $d_A, d_B$ of the constituting materials as well as the number of atomic layers $n_A, n_B$. From equations (4.33) to (4.35) it is clear, that each pair of $d_A, d_B$ stricly determines the pair $n_A, n_B$ and that the relative height of the satellites gives a hint which pair of $n_A, n_B$ is the true one.

The identification of these four parameters has been performed with the help of the program *SlerfWin* by G. Gladyszewski which is based on a Monte Carlo method [gla91], [gla98], [gla00]. The nominal values of $d_A, d_B$ are given by the user, e. g. the bulk values, and the program calculates the diffraction profiles of the multilayer while changing the interplanar distances $d_A, d_B$. The variation range of $d_A, d_B$ is also given by the user as well as the number of steps. For each set of $d_A, d_B$ the program compares the calculation with the experimental data in form of a fitting factor $R$:

$$R = \frac{\sum(\sqrt{I_{exp}} - \sqrt{I_{cal}})^2}{\sum I_{exp}} \tag{4.36}$$

The result of the calculation is given in a contour plot of the fitting factor as a function of $d_A, d_B$ and the diffraction profile can be viewed for every calculated dataset.

Furthermore, the *SlerfWin* program accounts for interfacial and structural imperfections:

Firstly, it assumes interfacial roughness in terms of fluctuating numbers of monolayers in the superlattice unit cell according to a Gaussian distribution with the standard deviations $\sigma_A$ and $\sigma_B$.

Secondly, the model accounts for interdiffused interfaces and their profile is represented by an error function. The parameter which is adjusted in the calculations is the so called half interface thickness $\sigma_{int}$, given in monolayers.

Thirdly, the program assumes the multilayer to be built up of grains with an average grain thickness $\langle D_g \rangle$ and Gaussian distribution of deviation $\sigma_{Dg}$. For the calculation procedure the number of grains can be varied.

None of the microstructural parameters is determined via a fitting procedure of the program but are adjusted by the user. For a given set of parameters, the calculations are performed and the user has to decide which set of parameters approximates the measurement best. Although there are five parameters to be adjusted by hand this is possible because each of the parameters has its particular influence on the diffraction pattern. The parameters $\sigma_A$, $\sigma_B$, $\langle D_g \rangle$ and $\sigma_{Dg}$ are adjusted before the variation procedure. The half interface thickness $\sigma_{int}$ is determined by comparison of fitting results for different values of it with the help of the fitting factor $R$.

## 4.3 X-Ray Reflectometry

From the point of view of scan geometry, there is no difference between x-ray reflectometry (XRR) and x-ray diffraction (XRD) as both are $\theta - 2\theta$ scans which act in different angle ranges: XRD covers the large angle regime with $2\theta \geq 10°$ whereas for XRR $0° \geq 2\theta \geq 10°$. Nevertheless, both techniques give information about very different sample characteristics: XRD gives information about the crystal structure and texture, whereas XRR probes the layer thickness and interface roughness of the sample.

### Comparison of Methods

As we have seen in section (4.2), large angle XRD of multilayers can also give information about the layer thickness and roughness, but to yield this information it is necessary to have a good crystalline quality of the sample, whereas XRR does not depend on this. Furthermore, XRR analysis can provide more roughness parameters such as in-plane and vertical correlation lengths. Equivalently to reflectometry with x-rays, neutrons may be used. The advantage of using spin polarized neutrons as well as using synchrotron x-rays is to yield additional information about the magnetic properties of the sample [schrey94]. In contrast to x-ray diffractometers, neutron sources and synchrotrons are not acessible on laboratory scale and because of that, neutron diffration is not a convenient method for investigating extensive sample series.

Another common method for the determination of roughness of a film is the atomic force microscopy (AFM) which directly measures the film surface and gives a topographic image, i. e. is no integrative method. In spite of this, AFM is not suitable for the present investigation because it measures the surface of the sample but not the interfaces. In case of multilayers, the only way of investigating the whole stack of interfaces is to grow the multilayer sucessively and measure each surface separately. But even when accepting the enormous effort of measuring at least 40 samples in case of one multilayer with 20 double layers, the results do not necessarily give insight into the interface properties. Firstly, the surface is modified due to oxidation and contamination and secondly, the interaction of the surface with the layer that will be grown upon is missing. Furthermore, this measuring systematic still cannot give information on the vertical correlation of interface roughness. The same considerations are valid for scanning tunneling microscopy (STM) and scanning electron microscopy (SEM), which are not suitable here.

The only method which allows further insight into the interface properties of a multilayer is the High-Resolution Transmission Electron Microscopy (HRTEM). Because of the very high preparation expenditure this method is applicable only for selected samples. It has to be kept in mind that this method averages of the thickness of the sample which has been thinned down to a few atomic layers. This process of averageing especially hardens the judgement of the interface properties of a sample.

### Historical Review

X-ray reflectometry was measured first by A. H. Compton in 1923 on solid samples with smooth surfaces, where he discovered the critical angle of total reflection.[4] In 1931, H. Kiessig found oscillations of the reflected x-ray intensity of a thin layer on a substrate [kie31]. The position of these oscillations is related to the thickness of the thin film and nowadays these oscillations are called *Kiessig-fringes*. In 1940, DuMond and Youtz measured XRR of periodic multilayers and found peaks equivalent to Bragg peaks of crystals.[5] In 1954, Parratt presented a recursion formula for calculating reflectivity slopes, based on the optical Fresnel coefficients for reflection and transmission [par54]. To account for roughness, Névot and Croce introduced a kind of Debye-Waller factor in the Fresnel theory [nev80]. So far, specular reflectivity had been investigated, but already in 1963, Yoneda found peaks of diffusively scattered radiation, the so called *Yoneda wings* [yon63]. These peaks were explained as being caused by roughness of the layer, and although this was later found to be a mistake, it was of great interest to get information on in-plane roughness parameters. However, it was 1988 when the main research activities in diffuse XRR started: Sinha *et al.* showed how to gain quantitative lateral roughness information from non-specular reflectivity measurements. Since then a lot of effort has been done in analyzing surface and interface roughnesses quantitatively with XRR and nowadays the method is widely applied [boe95b].

## 4.3.1 Specular X-Ray Reflectometry

In contrast to non-specular x-ray reflectometry, which must be treated with dynamical or kinematical theory, XRR in specular geometry can also be described by an optical theory because the crystallinity of the sample can be ignored. The reason for this is the structure factor amplitude $F_{hkl}$ (equation 4.6) which is purely the sum of the electron density in the unit cell for the (000) reflection [few00]. In other words, the neglection of crystalline structure is justified as long as the interatomic distances are much smaller than $(\lambda / \sin\theta_i)$ where $\lambda$ is the wavelength of incident radiation and $\theta_i$ is the angle of incidence [boe95b].

---

[4] Phil. Mag. Vol. 45 (1923) p. 1121ff.

[5] J. Appl. Phys. Vol. 11 (1940) p. 357ff.

The refractive index of a material is in the most general case a complex number which pays attention to the fact that, speaking in terms of waves, the incident wave may be phase shifted and damped in its amplitude due to absorption effects:

$$n = 1 - \delta - i\beta = 1 - \frac{N_A r_e \lambda^2 \rho}{2\pi M}(f_0 + \Delta f' - i\Delta f'') \tag{4.37}$$

$N_A$ is Avogadro's number, $r_e$ is the classical electron radius, $\rho$ is the density of the material, $M$ is the atomic mass and the term in brackets is the atomic scattering factor. When considering compounds, $M$ and the atomic scattering factor are taken as averaged values using atomic fractions.

The dispersive correction $\delta$ is proportional to the real part of the average atomic scattering factor

$$\delta = \frac{N_A r_e \lambda^2 \rho}{2\pi M}(f_0 + \Delta f') \tag{4.38}$$

where $f_0 \cong Z$ for small scattering angles with $Z$ being the number of electrons of the atom. The absorptive correction $\beta$ can also be expressed in terms of the linear absorption coefficient $\mu$

$$\beta = \frac{N_A r_e \lambda^2 \rho}{2\pi M}\Delta f'' = \frac{\lambda\mu}{4\pi} \tag{4.39}$$

Both $\delta$ and $\beta$ are of the order $10^{-5}$ to $10^{-7}$ for the x-ray wavelength of $\mathrm{CuK}_\alpha$ and so the refractive index $n$ is smaller than one.[6] Thus for x-rays, any material is optically less dense (i. e. $n < 1$) than vacuum, having $n = 1$. Consequently, total reflection of x-rays entering the medium from vacuum side will occur for incident angles smaller than a critical angle $\theta_c$ [zab94], [pre96].

### Fresnel Reflectivity

The reflection and transmission of a plane electromagnetic wave at a single smooth interface between two materials 1 and 2 with different refractive indices $n_1 = 1$ and $n_2 = 1 - \delta_2 - i\beta_2$ is considered first.[7]

According to figure (4.7), the (x,y) plane is denoted as the layer plane and the z axis is in the direction of the normal vector of the layer. $\vec{k_i}$, $\vec{k_r}$ and $\vec{k_t}$ are the wave vectors of the incoming, reflected and transmitted beam, respectively, having the components

$$\vec{k_i} = k_i \begin{pmatrix} \cos\theta_i \\ 0 \\ -\sin\theta_i \end{pmatrix}, \quad \vec{k_r} = k_r \begin{pmatrix} \cos\theta_i \\ 0 \\ \sin\theta_i \end{pmatrix}, \quad \vec{k_t} = k_t \begin{pmatrix} \cos\theta_t \\ 0 \\ -\sin\theta_t \end{pmatrix} \tag{4.40}$$

---

[6] See table (B.1) for the optical constants of the materials used in this thesis.

[7] The description follows [zab94], [pre96], [boe95b], [schlom95] and [lan98].

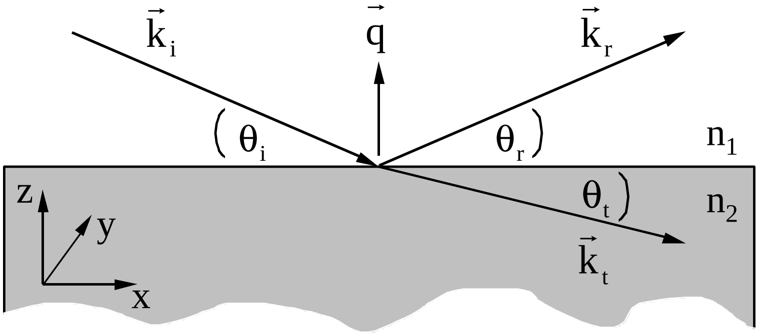

Figure 4.7: Reflection and transmission of x-rays at a single smooth interface.

with

$$k_i = k_r = \frac{2\pi}{\lambda} \quad \text{with} \quad k_t = \frac{2\pi}{\lambda'} \tag{4.41}$$

and $\theta_i$ being the angle of incidence, $\theta_r$ the angle of exidence and $\theta_t$ the angle between the transmitted - and thus refracted - beam and the interface. As specular scattering geometry is considered here, we have $\theta_i = \theta_r$. The vector $\vec{q}$ is the scattering vector, defined as $\vec{k_r} - \vec{k_i}$.

The corresponding electric fields are:

$$\begin{aligned} \vec{E_i} &= E_i \exp[i(\vec{k_i} \cdot \vec{r} - \omega t)] \\ \vec{E_r} &= E_r \exp[i(\vec{k_r} \cdot \vec{r} - \omega t)] \\ \vec{E_t} &= E_t \exp[i(\vec{k_t} \cdot \vec{r} - \omega t)] \end{aligned} \tag{4.42}$$

In the same manner the magnetic field for incident, reflected and transmitted beam have to be evaluated. The boundary conditions of Maxwell's theory of electromagnetic waves demand that across the interface the tangential components of the electric and magnetic field have to be continuous, thus $k_{i,x} = k_{t,x}$.

Taking all the aforementioned aspects into account, the Fresnel formulae for reflection and transmission are gained [pre96]:

$$r = \frac{E_r}{E_i} = \frac{k_{i,z} - k_{t,z}}{k_{i,z} + k_{t,z}} = \frac{-k_i \sin\theta_i + k_t \sin\theta_t}{-k_i \sin\theta_i - k_t \sin\theta_t} \tag{4.43}$$

$$t = \frac{E_t}{E_i} = \frac{2k_{i,z}}{k_{i,z} + k_{t,z}} = \frac{-2k_i \sin\theta_i}{-k_i \sin\theta_i - k_t \sin\theta_t} \tag{4.44}$$

The index of refraction is defined as $\lambda = n_2\lambda'$, so we have $k_t = n_2 k_i$. Taking also into account the law of refraction

$$\cos\theta_i = n_2 \cos\theta_t \tag{4.45}$$

we obtain:

$$r = -\frac{\sin\theta_i \cos\theta_t - \sin\theta_t \cos\theta_i}{\sin\theta_i \cos\theta_t + \sin\theta_t \cos\theta_i} \tag{4.46}$$

and

$$t = -\frac{2\sin\theta_i}{\sin\theta_i \cos\theta_t + \sin\theta_t \cos\theta_i} \tag{4.47}$$

Using the theorem of addition and the fact that the angles $\theta_i$ and $\theta_t$ are very small in the case of x-ray reflectometry, the Fresnel formulae (4.46) and (4.47) can be approximated to be

$$r = -\frac{\sin(\theta_i - \theta_t)}{\sin(\theta_i + \theta_t)} \approx -\frac{\theta_i - \theta_t}{\theta_i + \theta_t} \tag{4.48}$$

$$t = \frac{2\sin\theta_i \cos\theta_t}{\sin(\theta_i + \theta_t)} \approx \frac{2\theta_i}{\theta_i + \theta_t} \tag{4.49}$$

The reflectivity $R$ is defined as the ratio between the intensity of the reflected beam and the intensity of the incoming beam and can be calculated via the reflection coefficient $r$ as

$$R = \left|\frac{E_r}{E_i}\right|^2 = \mid r \mid^2 = rr^* \tag{4.50}$$

with $r^*$ being the complex conjugate of $r$. For the transmittivity $T$ with $R + T = 1$ we have

$$T = \left(\frac{k_{t,z}}{k_{i,z}}\right)\left|\frac{E_t}{E_i}\right|^2 = \left(\frac{k_{t,z}}{k_{i,z}}\right) tt^* \tag{4.51}$$

where $tt^*$ is called transmission coefficient and the factor $k_{t,z}/k_{i,z}$ accounts for the fact that the transmitted beam is refracted while the reflected beam is not.[8]

---

[8] The angle $\theta_t$ is a complex number, so it is convenient to write it as

$$\theta_t = \sqrt{{\theta_i}^2 - 2\delta_2 - i2\beta_2} = p_1 + ip_2 \qquad \text{with}$$

$$p_1^2 = \frac{1}{2}\left[\sqrt{(\theta_i^2 - 2\delta_2)^2 + 4\beta_2^2} + (\theta_i^2 - 2\delta_2)\right]; \quad p_2^2 = \frac{1}{2}\left[\sqrt{(\theta_i^2 - 2\delta_2)^2 + 4\beta_2^2} - (\theta_i^2 - 2\delta_2)\right].$$

So $rr^*$ and $tt^*$ are calculated as:

$$rr^* = \frac{(\theta_i - p_1)^2 + p_2^2}{(\theta_i + p_1)^2 + p_2^2} \qquad \text{and} \qquad tt^* = \frac{4\theta_i^2}{\theta_i^2 + 2p_1\theta_i + p_1^2 + p_2^2}$$

.

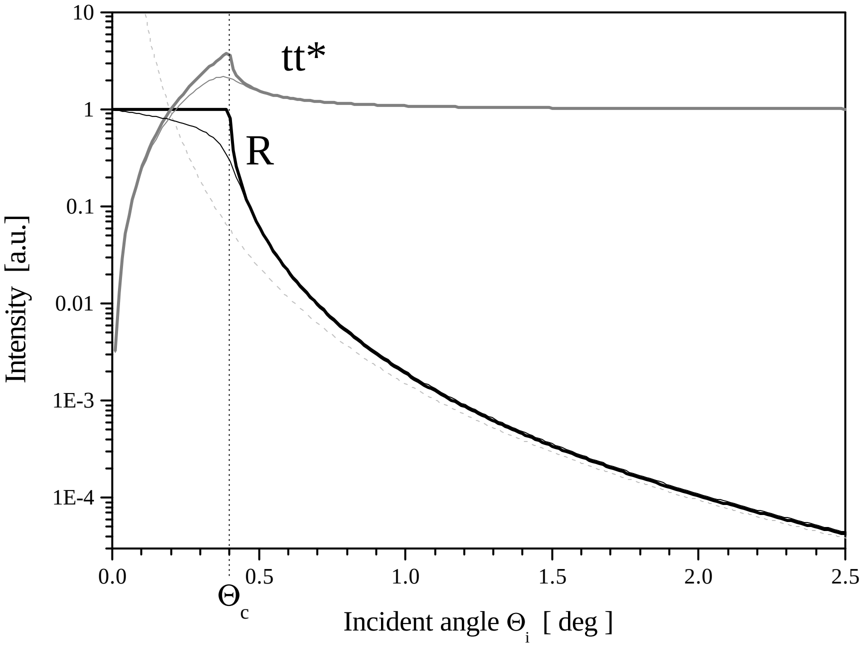

Figure 4.8: Calculated reflectivity R (black) and transmission coefficient tt* (grey) for $\delta_2 = \delta_{Cu} = 2.4437 \cdot 10^{-5}$. Bold lines: $\beta_2 = 0$; thin lines: $\beta_2 = 10 \cdot \beta_{Cu} = 5.4962 \cdot 10^{-6}$ The broken grey line corresponds to $\theta_i^{-4}$ (adapted from [zab94]).

$R$ and $tt^*$ are plotted in figure (4.8) to visualize the most important properties of specularly reflected x-rays at a smooth surface. The transmittivity $T$ is not shown as it is simply $T = R - 1$ and thus does not provide any additional information. The values of $\delta_2$ and $\beta_2$ used for the calculation correspond to those of Copper (see appendix B), but $\beta_2$ was multiplied by 10 to make the effect of absorption more obvious.

For $\theta_i$ smaller than the critical angle $\theta_c$ and in case of no absorption ($\beta_2 = 0$) the reflectivity is constantly $R = 1$ which denotes that we are in the region of total reflection. When absorption cannot be neglected, the reflectivity in the regime $\theta_i \leq \theta_c$ is smaller than one. For $\theta_i \gg \theta_c$ the reflectivity decays as $R \propto \theta_i^{-4}$ (broken grey line) and the transmittivity coefficient $tt^*$ goes to 1, i. e. the x-rays penetrate unimpeded into the medium. This case is the kinematical limit. The transmission coefficient shows a peak at $\theta_i = \theta_c$ with an amplitude of twice the incoming amplitude in case of no absorption. When absorption cannot be neglected, the peak is rounded and has a lower amplitude. This maximum of the transmission function is caused by a constructive interference of the incident wave and an evanescent wave localized near the surface.

For $\theta_i < \theta_c$ the penetration depth is typically 50 Å which is the reason for the surface sensitivity of x-rays at glancing angles. The penetration depth increases rapidly to many microns for $\theta_i > \theta_c$. In *Grazing Incidence Diffraction (GID)* the angle of incidence is always kept very close to $\theta_c$ to make use of this effect and to be sensitive to thin layers.

The critical angle of total reflection $\theta_c$ is determined via the law of refraction (equation 4.45) with $\theta_t = 0$. Then, $\cos\theta_c = n_2 \approx 1 - \delta_2$ for neglection of absorption. Evaluating the cosine function as $\cos x \simeq 1 - \frac{1}{2}x^2$ yields

$$\theta_c = \sqrt{2\delta} = \sqrt{\frac{N_A r_e \lambda^2 \rho}{\pi M}(f_0 + \Delta f')} \tag{4.52}$$

Due to this, the critical angle of total reflection depends sensitively on the density $\rho$ of the material. Put differently, in experimentally determining the critical angle of total reflection, the density of the material can be calculated. In the given example of $\delta_2 = 2.4437 \cdot 10^{-5}$ the critical angle is $\theta_c = 6.99\, mrad = 0.401^\circ$.

### Fresnel Reflectivity at Many Interfaces

So far, one single smooth surface has been considered, but in case of a thin film on a substrate there at least two interfaces[9] and in case of multilayers many more. In 1954, L. G. Parrat developed a recursion formula based on the Fresnel formulae for reflection and transmission of light at an ideally flat interface [par54]. The description of it given here follows [zab94] and [pre96].

As sketched in figure (4.9), we consider a multilayer stack of N single layers, including the substrate, which are enumerated beginning with the topmost layer as 1. The thickness of layer $j$ is denoted as $d_j$ and its refractive index as $n_j$. The amplitudes of the transmitted and reflected electric field in layer $j$ are $E_j^t$ and $E_j^r$. Then at each interface $(j-1, j)$ the tangential components of the electric and magnetic field vectors have to be continuous and the solution of the corresponding equations can be written as a recursion formula:

$$X_{j-1} = a_{j-1}^4 \left( \frac{R_{j-1,j} + X_j}{1 + R_{j-1,j} X_j} \right) \tag{4.53}$$

where

$$X_j = a_j^2 \frac{E_j^r}{E_j^t} \tag{4.54}$$

with

$$R_{(j-1),j} = \frac{k_{(j-1),z} - k_{j,z}}{k_{(j-1),z} + k_{j,z}} \tag{4.55}$$

---

[9] In most cases a thin metallic film on a substrate has a top oxide layer so this system has in fact three interfaces, including the surface.

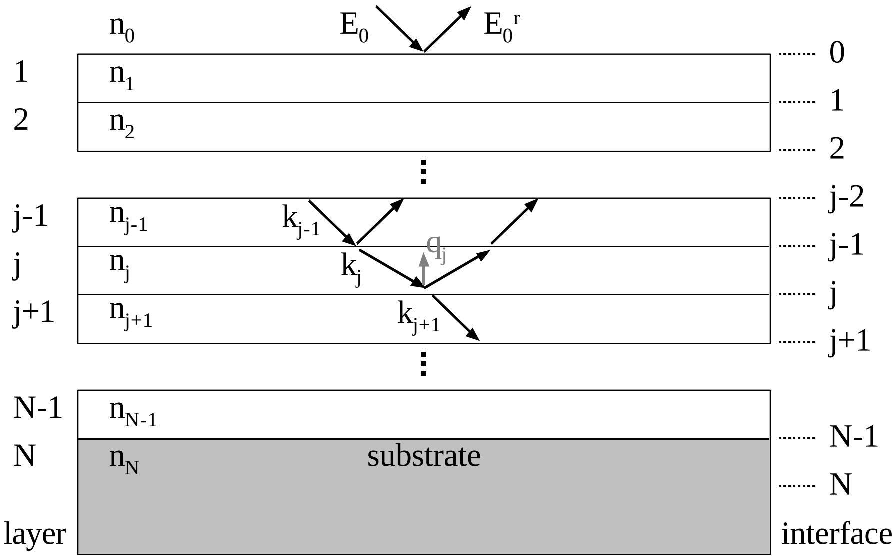

Figure 4.9: Scheme of reflection and transmission of x-rays at a multilayer, which can be calculated via a recursion formula.

and

$$a_j = \exp(iq_j d_j/2). \tag{4.56}$$

$X_j$ can be regarded as the generalized Fresnel reflectivity for the interface $(j, j+1)$ and $R_{j-1,j}$ is the Fresnel coefficient for reflection at the smooth interface between the layers $j-1$ and $j$ equivalent to equation (4.43). $a_j$ is a phase factor for the electric field always in the middle between two interfaces, where $q_j$ is the scattering vector in layer $j$. Therefore, the layer thickness $d_j$ comes into account which causes the occurrence of the *Kiessig fringes.*

The recursion starts at the undermost interface, i. e. the interface between substrate and the first layer deposited upon it. For the substrate $X_N = 0$ is assumed which means that due to its very large thickness ($d_0 \approx \infty$) no reflection takes place beneath this undermost interface, i. e. at the backside of the substrate. Then $X_{j-1}$ is calculated from bottom to top for each interface, ending with $X_0$ giving the ratio of reflected intensity $I_R$ to incoming intensity $I_0$:

$$\mid X_0 \mid^2 = \left| \frac{E_0^r}{E_0} \right|^2 = \frac{I_R}{I_0} \tag{4.57}$$

### Interfaces with Roughness

In the previous section it has been shown that the reflectivity drops off as $\theta_i^{-4}$. This is true for a perfectly flat surface, but in experiments the reflectivity has

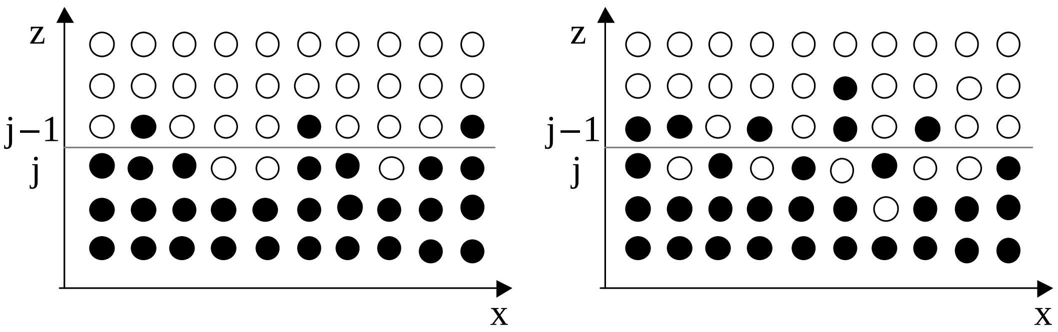

Figure 4.10: Interface of two materials $j-1$ and $j$ showing roughness (left) and interdiffusion (right). The straight lines mark the mean interface position (adapted from [zab94]).

been found to decrease much faster. The reason for this can be found in fact that every real surface and interface is characterized by some kind of roughness or interdiffusion on an atomic scale. The difference of these two cases becomes obvious in the local density gradient which is locally sharp in case of roughness but not in case of interdiffusion, see figure (4.10).

The idea of considering roughness in calculating XRR scans is to leave the picture of a steplike density profile and to assume a more continuous one. A convenient roughness model assumes an error function of the electron density across the interface $(j-1, j)$. The first derivative of the density profile yields the height distribution of the interface, and in case of an error function the height distribution is of Gaussian shape with width $\sigma_{(j-1),j}$ (figure 4.11). Therefore, the standard deviation $\sigma$ is a measure for the average vertical roughness and can be attributed to the RMS roughness.[10] According to Névot and Croce [nev80], the Fresnel coefficient $R_{j-1,j}(0)$ for reflection at the smooth interface $(j-1, j)$ is multiplied with a Debye Waller like factor to account for the roughness:

$$R_{(j-1),j}(\sigma) = R_{(j-1),j}(0)e^{-2k_{(j-1),z}\cdot k_{j,z}\cdot\sigma^2_{(j-1),j}} \tag{4.58}$$

This factor acts like a damping term of the specularly reflected x-rays and it reveals that in fact the reflectivity drops off faster than $\theta_i^{-4}$ in case of roughness or interdiffusion. As XRR is a technique which averages over a large lateral area of the sample and in specular diffraction geometry the projection of the electron density in direction parallel to the surface or interface normal is taken, it cannot be distinguished within this scattering geometry whether the interface is rough

---

[10] The root mean square deviation RMS is defined as $\sigma = \sqrt{\frac{1}{N}\sum_{i=1}^{N}(x_i-\bar{x})^2}$ with $x_1 ... x_N$ being the measured values and their average $\bar{x}$.

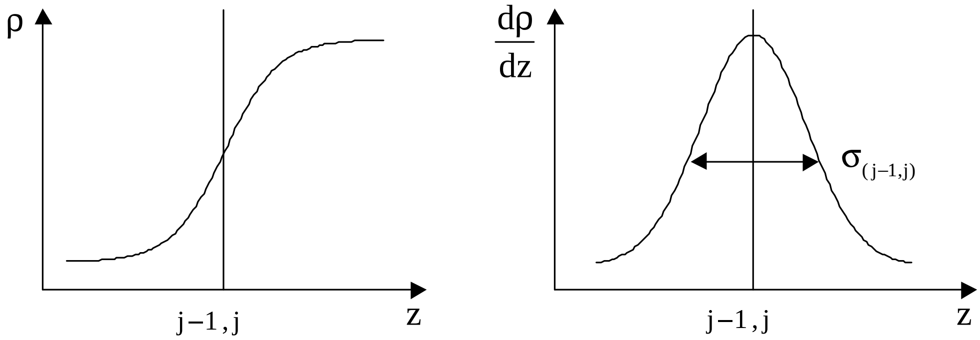

Figure 4.11: Roughness profile of an interface: Error function of electron density (left) and its derivative, the Gaussian function (right) with width $\sigma$ which corresponds to RMS roughness.

or interdiffused. But in case of a rough interface, i. e. local sharpness of the density gradient, the reduced specular intensity is redistributed in the non-specular scattering regime, whereas in case of interdiffusion this is not the case. Consequently, the only way of determining these interface properties is to measure the diffusively scattered intensity [zab94].

The assumption of Gaussian roughness in equation (4.58) is valid as long as the roughness is much smaller than the thickness of the corresponding layer. In case of larger or non-Gaussian roughness this method does not give the correct results and the electron density profile can be approximated by dividing the interface in a series of thin layers with varying electron density. The reflectivity is then calculated according to equation (4.55) for an ideally flat interface [pre96].

### Discussion of Specular XRR Scans

Figure (4.12) is a survey of calculated reflectometry scans of Copper single layers (a - c) and of Cobalt/Copper multilayers (d and e), all on a Silicon substrate. The grey line in (a) represents a scan of an infinitely thick Cu layer without roughness. It is equivalent to the calculated reflectivity in figure (4.8). The oscillating scan in (a) corresponds to a $30\,nm$ thick Cu layer on Si without roughness, denoted as $\mathrm{Si}_{\sigma=0}\,//\,\mathrm{Cu}_{\sigma=0}(30\,\mathrm{nm})$. It is characterized by so called *Kiessig fringes* which are due to interference of waves scattered from the surface and from the interface to the substrate. The position $\theta_{im}$ of the incident angle $\theta_i$ at which an interference maximum of the order $m$ occurs, is related to the layer thickness $d$ via

$$\sqrt{\sin^2\theta_{im} - \sin^2\theta_c} = \frac{m\lambda}{2d} \tag{4.59}$$

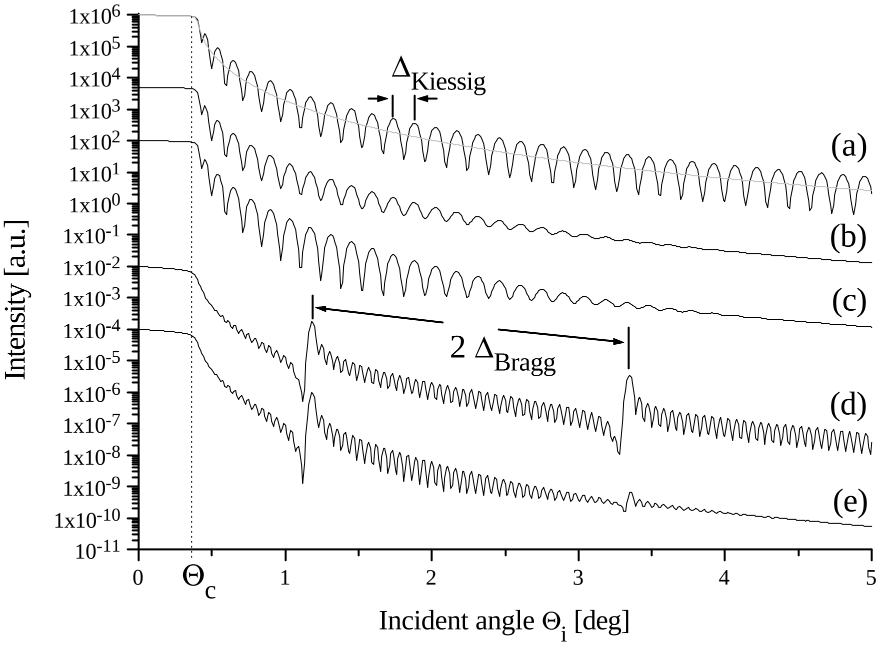

Figure 4.12: Calculated reflectivities. (a)-(c): $30\,nm$ thick Cu layer on a Si substrate. (a) No surface nor interface roughness, the grey line represents an infinitely thick and smooth Cu layer. (b) Rough interface but smooth surface. (c) Smooth interface but rough surface. (d) Co/Cu multilayer with smooth interfaces. (e) Multilayer with rough interfaces. (All calculations have been performed with *WinGixa* , based on the Parratt formalism [WinGixa].)

which is analogous to the Bragg equation modified by the influence of refraction. For small angles $\theta_i$ this equation can be written in the form[11]

$$\theta_{im}^2 - \theta_c^2 = m^2 \left(\frac{\lambda}{2d}\right)^2 \tag{4.60}$$

This is $\theta_{im} = 0.147°$ in the given example of $d = 30\,nm$ and CuK$_{\alpha_1}$ radiation. For an approximation, the layer thickness can be determined via

$$d \approx \frac{\lambda}{2\Delta_{Kiessig}} \tag{4.61}$$

by measuring the distance between adjacent interference maxima $\Delta_{Kiessig}$ [Holy99].

---

[11] This equation gives the recipe for determinig the layer thickness from a reflectivity scan "by hand": plotting $\theta_{im}^2$ versus $m^2$ gives a linear dependence. The slope of the line yields $d$ and additionally its intersection point with the $\theta_{im}^2$ axis gives the critical angle. In this work any layer thickness has been determined via fitting the XRR curve.

The amplitude of the Kiessig fringes depends on the density contrast between the layers and on the roughness of surface and the interfaces. For a rough surface, the transmittivity is larger than for a smooth surface and thus the intensity of the interference fringes is enhanced. This is the case for the scan (c) in figure (4.12) with $\mathrm{Si}_{\sigma=0}\,//\,\mathrm{Cu}_{\sigma=0.5\,\mathrm{nm}}(30\,\mathrm{nm})$. The contrary case of a smooth surface but rough interface as in scan (b) with $\mathrm{Si}_{\sigma=0.5\,\mathrm{nm}}\,//\,\mathrm{Cu}_{\sigma=0}(30\,\mathrm{nm})$ shows reduced Kiessig fringes because of the high reflectivity of the surface. If both, surface and interface are rough, the reflected intensity drops off drastically with the incident angle and the fringes are highly damped.

The scans (d) and (e) in figure (4.12) correspond to the multilayer system $[\,\mathrm{Cu}(2\,\mathrm{nm})\,/\,\mathrm{Co}(2\,\mathrm{nm})\,]_{20}$ without roughness (d) and with roughness of $\sigma = 0.5\,nm$ for each interface (e). The characteristic of these scans is the occurrence of peaks related to the double layer thickness $D = d_{Cu} + d_{Co}$, generally denoted as $D = d_A + d_B$. The position of the peaks can be calculated equivalent to equation (4.59), i. e. via the modified Bragg law

$$\sqrt{\sin^2\theta_{im,Bragg} - \sin^2\langle\theta_c\rangle} = \frac{m\lambda}{2D} \tag{4.62}$$

where the critical angle $\theta_c$ is averaged over the multilayer period ($\theta_c = 0.398°$ in the present case).

Again, for sufficiently large angles $\theta_i$ the spacing of the so called *Bragg maxima* $\Delta_{Bragg}$ can be approximated by

$$D \approx \frac{\lambda}{2\Delta_{Bragg}} \tag{4.63}$$

For the given example we have $\Delta_{Bragg} = 1.103°$, but in the scan exactly the doubled value is found. The reason for this is an additional relationship between the amplitude of the Bragg maxima and the thickness of the single layers $d_A$ and $d_B$. When these thickness values obey

$$m = p\left(\frac{d_A}{d_B} + 1\right) \tag{4.64}$$

with the integer $p$, then the $m$th Bragg peak vanishes [Holy99], thus every second Bragg maximum of the multilayer $[\,\mathrm{Cu}(2\,\mathrm{nm})\,/\,\mathrm{Co}(2\,\mathrm{nm})\,]_{20}$ is cancelled, see figure (4.12 (d) and (e)). The number of Kiessig fringes between two Bragg maxima is in most cases $N-2$ with $N$ being the number of double layers. This relation becomes obvious when comparing equations (4.63) and (4.61) and writing the total thickness for the multilayer case as $d = ND$

$$\Delta_{Bragg} \approx \frac{\lambda}{2D} = N\frac{\lambda}{2d} \approx N\Delta_{Kiessig} \tag{4.65}$$

One last aspect concerning Co/Cu multilayers shall be considered. Due to their almost identical electron densities, the x-ray contrast of Co and Cu is principally weak. But what can be taken advantage of is to use a wavelength which lies between the absorption edges of both materials and this was done in this study by using CuK$_\alpha$ radiation. The effect of anomalous dispersion enhances the scattering contrast [zab94]. In figure (B.1) in the appendix the absorption edges of Co and Cu are sketched.

### 4.3.2 XRR Pattern Analysis

X-ray reflectometry scans in specular geometry have been analyzed by fitting a model layer system to the measured data. The fit was performed with the Philips program *WinGixa*. This program calculates the reflectivity of the given layer model within the Fresnel theory and uses the Parrat recursion formalism. The interface roughness is taken into account in the way proposed by Névot and Croce. *WinGixa* uses the simplex method as minimalization procedure. The program can handle single layers as well as multilayers and the parameters thickness, roughness, density and the absorption coefficient of every given layer in the model can be determined. The user can freely choose the number of parameters to be varied within a fitting run and there are no limitations how to combine the varied parameters.

The performance of a succeeding fit is a challenge: Firstly, the fit model has to chosen with care. It is a great help to know the sputter sequence of the layer stack. In the case of a multilayer with $n$ repetitions of a double layer of type $A/B$ the user has to decide whether to fit the stack $[A/B]_n$ containing only the layer parameters for the two layers $A$ and $B$, or to fit the stack $A_1/B_1/A_2/B_2/A_3/B_3/....A_n/B_n$, comprising the parameters for $2n$ layers. Furthermore, the oxidation of the surface layer introduces a further layer with unknown parameters. Secondly, the user has to choose carefully which parameters are varied. In general, the layer thickness and roughness are the most interesting values. But the density and absorption of the layer have to be varied also in case the material is not known well. The third cruicial aspect is the fitting strategy. It is of no use to vary all parameters for all layers at the same time because the program will randomly find a paramater which minimizes the deviations from the measurement. For example, if the layer thickness is completely wrong, the calculated Kiessig fringes do not coincide with the measured ones. In such a case, the program tends to increase the roughness to unreasonable values, which results in a flattening of the fringes.

The aforementioned aspects can be summarized to three “golden rules” for the performance of successful XRR fits:

- The number of fit parameters should be as few as possible but nonetheless as much as necessary.
- The starting values of the parameters have to be very close to the true values.
- Concerning the choice and combination of varied parameters: Never trust the fitting program but only yourself! In most cases it is clever to adjust the thickness first and the roughness afterwards.

To achieve the first two aims it is a good idea to perform studies on single layers or on combinations of a few materials of the whole multilayer stack, such as

- thickness calibrations in order to gain precise starting values,
- fit of the pure substrate in order to determine its roughness,
- fit of thick single layers for determination of density and absorption, being able to keep these parameters held fixed in further fit procedures.
- XRR oxidation studies in order to determine the parameters of the oxidation layer.

Being now able to keep density and absorption fixed during the fit, there are still two parameters per layer left which have to be determined, that is the thickness and the roughness. In a multilayer with 20 double layers, a buffer and an oxidized surface this makes 85 parameters, including one parameter for the substrate roughness. In the following, a study is presented which explains two different fitting strategies of a multilayer and compares the results. The multilayer investigated is: $Si\ /\ SiO_2\ //\ Py_{3.0\,nm}/[Co_{1.6\,nm}\ /\ Cu_{2.14\,nm}]_{20}\ /Cu_{2.2\,nm}$

- <u>Strategy 1: "A Priori" Fit</u>

  The principal idea of the "a priori" fit is to start with a model which comprises the double layers in one stack in order not to regard every layer separately. The advantage is to start with small number of parameters. The number of parameters is enhanced step by step by subsequent division of the multilayer stack into new stacks with less double layers. After each division step the stacks are fitted. This procedure is performed as long as the stack is completely dissolved into single layers, i. e. until the maximum number of parameters is considered. For clarity, the steps of the fitting procedure are denoted more detailed in the following:

  - Fit model (3 stacks): $[Py/Co/Cu/Co]_1//[Cu/Co]_{18}//[Cu/CuO]_1$ with carefully chosen starting parameters
  - 1st fitting run: Cu and Co thickness of stack 2
  - 2nd fitting run: Cu and Co roughness of stack 2
  - Dividing the resulting 2nd stack into two stacks, thus: $[Py/Co/Cu/Co]_1//[Cu/Co]_6//[Cu/Co]_{12}//[Cu/CuO]_1$
  - 1st fitting run: Cu and Co thickness of stack 2
  - 1st fitting run: Cu and Co thickness of stack 3
  - 1st fitting run: Cu and Co thickness of stack 2+3
  - Fit of Cu and Co roughness in the same way
  - Dividing the resulting 2nd and 3rd stack into two stacks each, thus: $...//[Cu/Co]_3//[Cu/Co]_3//[Cu/Co]_6//[Cu/Co]_6//...$ while the first and last stack are not changed. Equivalent fitting sequence.
  - Division of the resulting 4th and 5th stack with 6 DL into two stacks each having 3DL: $[Py/Co/Cu/Co]_1//\{[Cu/Co]_3\}_6//[Cu/CuO]_1$, equivalent fitting sequence
  - Last division step: dissolution of all stacks into single layers, thus 42 layers: $[Py/Co_1/Cu_1/Co_2/Cu_2/.../Co_{20}/Cu_{20}/CuO]_1$
  - thickness and roughness variation of each of the 85 parameters, including the substrate roughness

The second fitting strategy is not solely based on the multilayer with 20 double layers alone, but it takes into account the XRR measurements of a multilayer series with varying number of double layers:
$Py_{3.0\,nm}/[Co_{1.6\,nm}\ /\ Cu_{2.14\,nm}]_n\ /Cu_{2.2\,nm}$ with $n = 0, 1, 2, 3, 4, 6, 10, 14, 20$.

- Strategy 2: “Successive” Fit

  This fitting strategy accounts for the fact that due to the growth process and the evolution of the microstructure the layer characteristics can change from bottom to top. Therefore, the layers cannot be comprised in multilayer stacks but have to be fitted separately. In order to reduce the number of unknown parameters, the fitting starts with a sample that only consists of buffer and capping layer. The values which are determined for the layers in this fitting run are taken as starting values for the next sample, which is built up of one additional bilayer besides buffer and capping layer. In this manner the samples with an increasing number of double layers are fitted and each fit is based on the previous one. For clarity, the steps are explained in detail below:

1. Sample $n = 0$:
   - Fit model (1stack): $[Py/Cu/CuO]_1$
   - Nominal starting parameters
   - Fitting layer thickness (3 parameters)
   - Fitting interface and surface roughness (4 parameters)
2. Sample $n = 1$:
   - Fit model (1stack): $[Py/Co/Cu/CuO]_1$
   - Starting parameters based on fit result of sample $n = 0$
   - 1st fitting run: new layers
   - 2nd fitting run: all layers
3. Sample $n = 2$:
   - Fit model (1stack): $[Py/Co/Cu/Co/Cu/CuO]_1$
   - Starting parameters based on fit result of sample $n = 1$
   - Equivalent fitting strategy
4. Sample $n = 3$:
   - Fit model (1stack): $[Py/Co/Cu/Co/Cu/Co/Cu/CuO]_1$
   - Starting parameters based on fit result of sample $n = 2$
   - Equivalent fitting strategy
5. So on until sample with $n = 20$

Figure 4.13 compiles the measured XRR scan with the two different fitting strategies. The upper row shows the whole scan range and it can be stated that both procedures have yielded very well approximations to the measurement. The middle angle range is given enlarged in the lower row and reveals the differences in both strategies: the calculated reflectivity gained in the “a priori” way is in perfect agreement to the measured scan. The position and slope of the fringes fit exactly and there are marginal differences concerning the amplitude of the fringes between second and third Bragg peak. On the other hand, the fit which has been “successively” performed does not perfectly coincide with the measurement. The position of the fringes and Bragg peaks widely agree, but the slope and the amplitude of the fringes show deviations from the XRR scan.

The thickness values for every layer determined by fitting are compared in figure 4.14 for both strategies. Calculating the average thickness of Co and Cu for the whole stack, both procedures yield the same mean value but different standard deviations:

| | “A Priori” | “Successive” |
|---|---|---|
| $d_{Co}$ | $(1.54 \pm 0.02)\,nm$ | $(1.54 \pm 0.09)\,nm$ |
| $d_{Cu}$ | $(1.93 \pm 0.06)\,nm$ | $(1.93 \pm 0.11)\,nm$ |

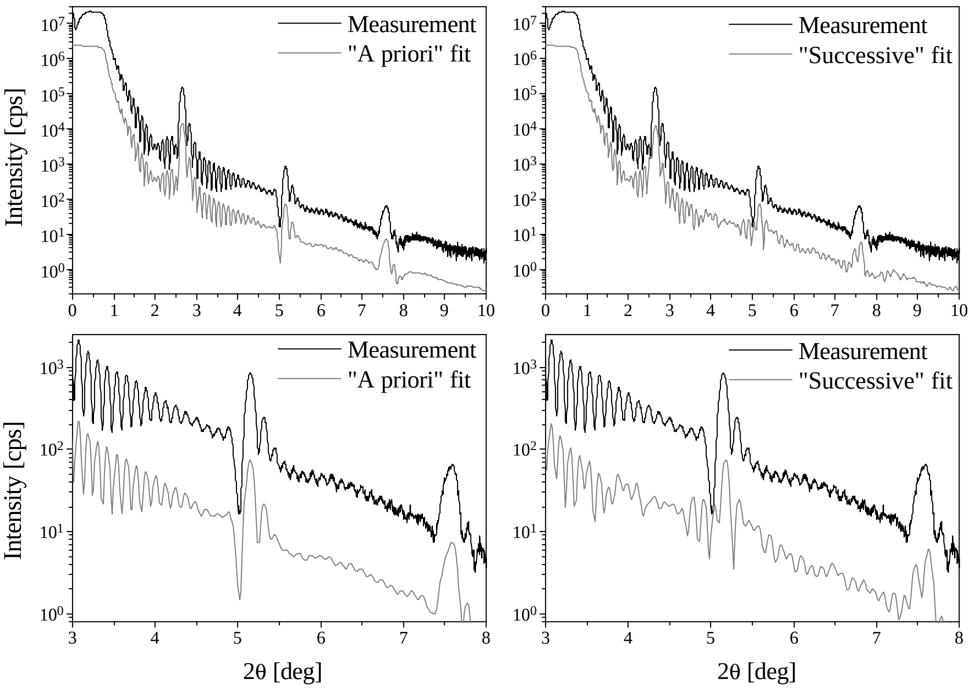

Figure 4.13: Comparison of two different fitting strategies called "a priori" and "successive" of the XRR measurement of the sample Si // $Py_{3.0\,nm}/[Co_{1.6\,nm}\ /\ Cu_{2.14\,nm}]_{20}\ /Cu_{2.2\,nm}$. The lower row shows enlarged details. The measured reflectivity is given as a black line whereas the fitting curves are coloured in grey. The fits are set off for clarity.

The standard deviation is considerably smaller for the "a priori" approach than for the "successive" approch and this becomes clear in figure 4.14. Especially the "successive" thickness values for layer numbers higher than 22 do hardly show a common level. This is in contrast to the "a priori" results which are characterized by smooth slope for Co as well as for Cu. The average thickness values given in the table above differ from the nominal values and especially the thickness of the first Copper layer is much too small. These facts are no specialities of the fitting strategy and are not discussed here but lateron in chapter 6.6.

The comparison of interface roughness is given in figure 4.15. For both procedures, the average Co and Cu roughness for the whole stack has been calculated:

| | "A Priori" | "Successive" |
|---|---|---|
| $\sigma_{Co}$ | $(0.37 \pm 0.05)\, nm$ | $(0.44 \pm 0.12)\, nm$ |
| $\sigma_{Cu}$ | $(0.34 \pm 0.04)\, nm$ | $(0.33 \pm 0.04)\, nm$ |

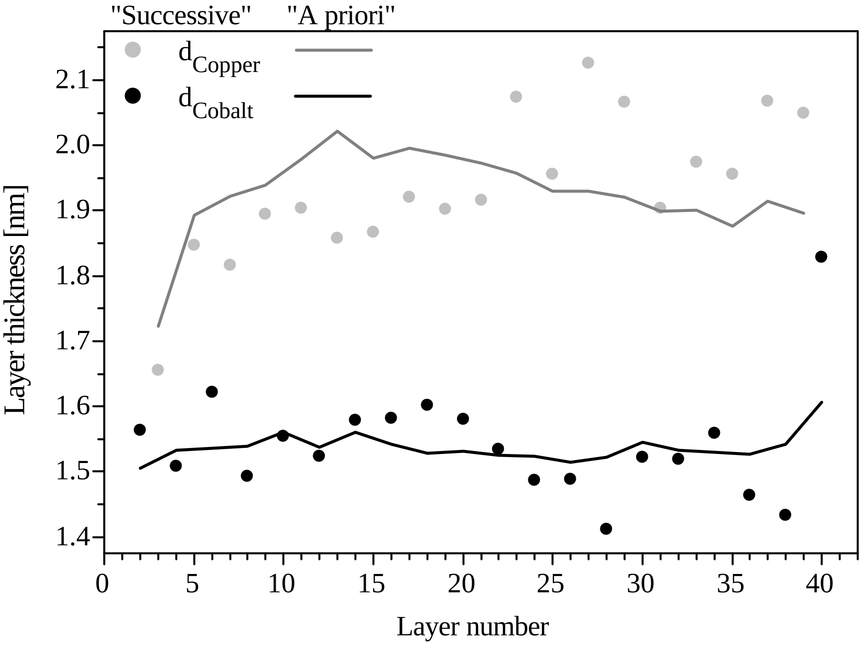

Figure 4.14: Comparison of Co (black) and Cu (grey) single layer thickness determined via different fitting strategies: “A priori” (lines) and “successive” (dots). The layer number refers to the fit model.

It is interesting to see that $\sigma_{Cu}$ is identical for both strategies whereas the mean value of $\sigma_{Co}$ as well as its standard deviation clearly differ. Again, it is instructive to take a look at the single values and their slope. The “a priori” values of Co and Cu are characterized by a very smooth slope and slightly increasing behaviour with increasing layer number. Furthermore, the slope of both materials is approximately parallel. The picture is very different for the “successive” fitting strategy. On one hand, the Cu roughness varies smoothly from layer to layer but shows an enhanced plateau for the layer numbers 9 to 25. On the other hand, there are values of the Co roughness which vary strongly for the first 5 Co layers but reach a common level for the layer numbers 12 to 24. The roughness for higher layer numbers increases strongly and linearly up to $0.7\,nm$.

Finally, it has to be concluded that the “a priori” fitting strategy yields definitely more reliable results than the “successive” procedure because

1. the calculated reflectivity based on the “a priori” strategy approximates the measurement almost perfectly;
2. strongly varying thickness values that are not correlated with the roughness are unreasonable (the only explanation could be a nonconstant power of the sputtering source);

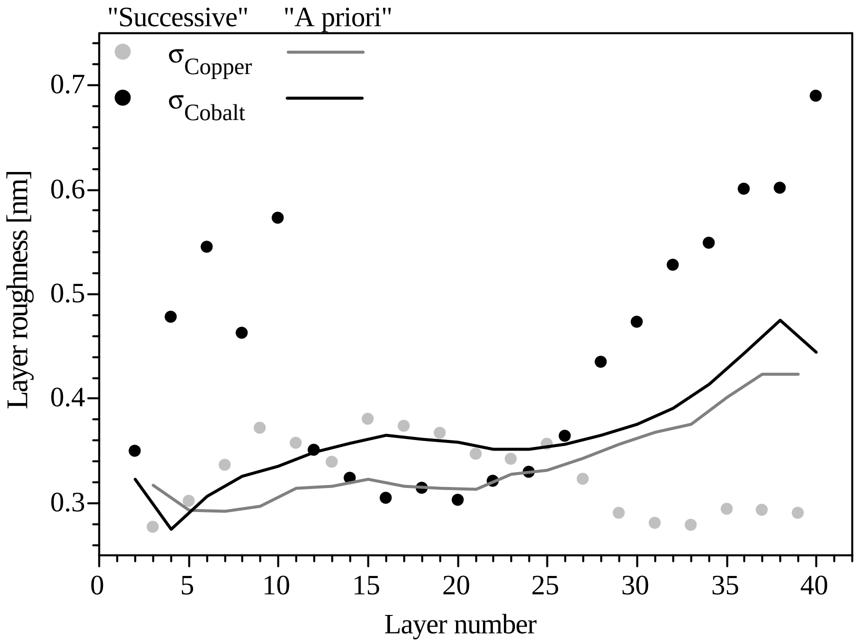

Figure 4.15: Comparison of Co (black) and Cu (grey) roughness determined via different fitting strategies: “A priori” (lines) and “successive” (dots). The layer number refers to the fit model.

3. concerning the “successively” determined roughness for the layer numbers 2 to 11 and 28 to 41 and taking into account the mechanism of layer growth, it is not realistic to have subsequent layers of alternating high and low roughness.

The conclusion that the “a priori” fitting strategy is the more successful one is quite astounding because it requires the determination of 85 parameters based on one single measurement. Therefore, one would expect that it is the great advantage of the “successive” procedure that the number of parameters to be determined is increased step by step, based on a number of measurements. How can the disadvantage be explained? The crucial point seems to be that identically sputtered layer sequences do not necessarily give identical layers and therefore, it does not help to fix the supposedly known parameters. The reason for the layer fluctuations may be found in the stability of the sputter conditions. But in the first line it is the sensitivity of the XRR method which detects difference of tenth of Angstrøms. Due to these nonfixable parameters, the layer model of the “successive” approach contains more unknown constants than the “a priori” strategy and therefore violates the rule “as few parameters as possible”. As a consequence, the fit may end in an impasse. Nonetheless, it is important to state that the “successively” calculated reflectivity is very good and the agreement between the mean values of both procedures are small.

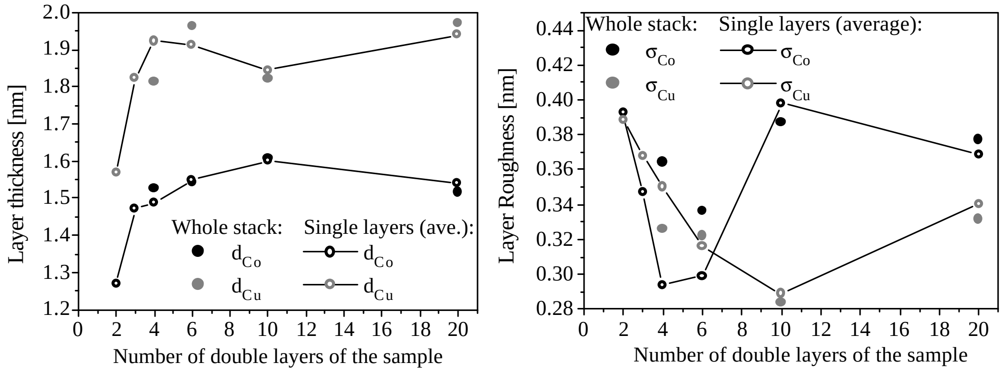

Figure 4.16: Comparison of “a priori” fit as a whole DL stack and the average values after fitting every single layer; sample Si // $Py_{3.0\,nm}/[Co_{1.6\,nm}$ / $Cu_{2.14\,nm}]_{20}$ $/Cu_{2.2\,nm}$.

Even if the “successive” strategy would lead to more realiable results than the “a priori” approach, it would not be the practicable procedure because it is extremly time consuming: instead of one sample many samples have to be prepared, measured and fitted.

Now that the best fitting strategy has been found, it is not clear yet whether it is necessary to determine the parameters of every single layer in a 20 DL stack. Putting the question differently, is there a difference between the average thickness and roughness parameters determined by fitting the whole DL stack (i. e. the first fit of the “a priori” strategy) and those determined separately for every layer (i. e. the last step of the “a priori” approach):

whole stack $[Py/Co/Cu/Co]_1 \; // \; [Cu/Co]_{n-2} \; // \; [Cu/CuO]_1$
single layers $[Py/Co_1/Cu_1/Co_2/Cu_2/.../Co_n/Cu_n/CuO]_1$

This comparison is made in figure 4.16 for different samples having an increasing number of double layers. The values determined for every single layer have been averaged and in both cases the layers $Co_1$, $Cu_1$ of the buffer as well as the Cu layer of the cap have not been taken into account. The model stacks are equal up to $n = 3$. The graphs reveal that for the samples with $n > 6$ the differences in thickness as well as in roughness can be neglected. The samples with $n = 4$ and 6 are the exceptions from this finding, differing in the resulting Cu thickness and also a little in the roughness. This result is quite interesting, because it justifies the simple fitting model. Nonetheless, this finding need not necessarily be true for any multilayer sample and in general, care has to be taken with every sample and the choice of the model layer stack.

# Chapter 5

# Sample Preparation and Characterization Techniques

## 5.1 Sample Preparation

All samples investigated in this thesis have been fabricated by magnetron sputtering. The idea of sputtering is to bombard the target material with high energetic ions, accelerated due to the high negative potential of the target of 100 to 1000 Volts and to deposit the atoms which have been knocked out of the target on a substrate placed on the opposite. For a review on the magnetron sputtering technology see e. g. [pen95].

In this thesis six different sample series have been investigated. They have been prepared in three different laboratories on four different sputtering systems:

**Series Bielefeld** has been prepared in March 2002 in a *Leybold Dresden CLAB600* sputtering system in the Bielefeld University laboratory. It has six magnetron sources measuring four inch in diameter. Two of the sources are capable of sputtering magnetic materials, one source is operable in rf mode for sputtering isolating materials and the other three sources are used for sputtering nonisolating and nonferromagnetic materials. All of the sources are placed in one vacuum chamber having a base pressure of $1 \cdot 10^{-7}\,mbar$. Between sputtering chamber and load lock there is a separate vacuum chamber with an automatic handling arm which enables to load the substrate into the sputtering chamber without breaking the vacuum. The distance between target and substrate is $(11.5 \pm 0.3)\,mm$, depending on the target thickness. Sputtering pressure, power of the sources and sputtering rates are given in the table below. The sputtering rates have been determined via thickness determination with x-ray reflectometry on extra samples: Single layers of the regarding material were sputtered in the way like a multilayer with a single layer thickness of about two nanometers, so often as to get a final layer of about 30 *nm*, e. g. $[\mathrm{Cu}_{2\,\mathrm{nm}}]_{15}$. For each material, two samples with different single layer thicknesses were prepared in order to determine the sputtering offset correctly. The sputtering offset occurs because of the shutter technique: The sputtering time per layer is determined by the opening time of the shutter while the substrate itself does not move. Therefore, the mimimum sputtering time is determined by the time needed for opening the shutter and closing again, which takes up to one second alltogether. The sputtering time given by the user is not included here, this time starts to count in the instant of the shutter being open and this the reason for the offset. The substrates used in this series were pieces of size $(18 \cdot 18)\,mm^2$ cut out of a silicon wafer having [100] orientation and a layer of thermal oxide 850 *nm* thick, which we kindly received from the *Robert Bosch GmbH, Stuttgart.* Directly before loading they have been cleaned in acetone and ethanol, respectively, and dried in a nitrogen gas stream.

Series **Bielefeld**

Type : $\mathrm{Si}_{[100]}(\mathrm{SiO}_2)_{850\,\mathrm{nm}}$ // $\mathrm{Py}_\mathrm{z}/[\mathrm{Co}_\mathrm{y}/\mathrm{Cu}_\mathrm{x}]_\mathrm{n}$ / Cu

(The variation range of the parameters $x, y, z, n$ is given in chapter 6.)

| Pressures [mbar]: | $\mathrm{p}_{\mathrm{base}} = 1 \cdot 10^{-7}$ | $\mathrm{p}_{\mathrm{Ar}} = 1 \cdot 10^{-3}$ |
|---|---|---|

| Targetmaterial | Sputtering Power | Sputtering Offset and Rate |
|---|---|---|
| Cu | 105 W (1.3 W/cm$^2$) | 0.4 nm + 0.9 nm/s · t[s] |
| Co | 120 W (1.5 W/cm$^2$) | 0.2 nm + 0.3 nm/s · t[s] |
| Py = $\mathrm{Ni}_{81}\mathrm{Fe}_{19}$ | 120 W (1.5 W/cm$^2$) | 0.2 nm + 0.4 nm/s · t[s] |

**Series Multi 1**, **Multi 2** and series **Thermo 1 and 2** have also been sputtered in the Bielefeld University laboratory, but in a sputtering system type *L560 Leybold Dresden.* This system has four dc magnetron sources measuring four inch in diameter, of which three are capable of sputtering magnetic materials. The four sources are placed together in a vacuumchamber having a base pressure of about $8 \cdot 10^{-7}\,mbar$, which is placed directly beneath the load lock. The substrate is loaded manually into the sputtering chamber without breaking the vacuum. The distance of target to substrate is 11 *cm* minus the target thickness. Further details of this sputtering machine are given in [hei00]. The sputtering rates have been determined via thickness determination with x-ray reflectometry on extra samples in the way explaned above. The reason for the sputtering offset is the same as in machine *CLAB 600.*

Series **Multi 1** (May 2002)

Type : $\mathrm{Si_{[100]}(SiO_2)_{100\,nm}}$ // $\mathrm{Py_z/[Co_y/Cu_x]_n}$

(The variation range of the parameters $x, y, z, n$ is given in chapter 7.)

Pressures [mbar]: $\mathrm{p_{base}} = 8 \cdot 10^{-7}$ $\mathrm{p_{Ar}} = 1 \cdot 10^{-3}$

| Targetmaterial | Sputtering Power | Sputtering Offset and Rate |
|---|---|---|
| Cu | 90 W (1.1 W/cm$^2$) | 0.4 nm + 0.5 nm/s $\cdot$ t[s] |
| Co | 93 W (1.2 W/cm$^2$) | 0.2 nm + 0.2 nm/s $\cdot$ t[s] |
| Py = $\mathrm{Ni_{81}Fe_{19}}$ | 102 W (1.3 W/cm$^2$) | 0.3 nm + 0.3 nm/s $\cdot$ t[s] |

Series **Multi 2** (April 2002)

Type : Glass // $\mathrm{Py_z/Co_{y1}/[Cu_x/Co_{y2}]_n}$

(The variation range of the parameters $x, y1, y2, z, n$ is given in chapter 7.)

Pressures [mbar]: $\mathrm{p_{base}} = 8 \cdot 10^{-7}$ $\mathrm{p_{Ar}} = 1 \cdot 10^{-3}$

| Targetmaterial | Sputtering Power | Sputtering Offset and Rate |
|---|---|---|
| Cu | 90 W (1.1 W/cm$^2$) | 0.4 nm + 0.5 nm/s $\cdot$ t[s] |
| Co | 93 W (1.2 W/cm$^2$) | 0.2 nm + 0.2 nm/s $\cdot$ t[s] |
| Py = $\mathrm{Ni_{81}Fe_{19}}$ | 102 W (1.3 W/cm$^2$) | 0.2 nm + 0.3 nm/s $\cdot$ t[s] |

Series **Thermo 1** (January 2003)

Type : $\mathrm{Si_{[100]}(SiO_2)_{100\,nm}}$ // $\mathrm{Co_z/Cu_x/[Co_y/Cu_x]_{40}}$

(The variation range of the parameters $x, y, z$ is given in chapter 8.)

Pressures [mbar]: $\mathrm{p_{base}} = 8 \cdot 10^{-7}$ $\mathrm{p_{Ar}} = 3 \cdot 10^{-3}$

| Targetmaterial | Sputtering Power | Sputtering Offset and Rate |
|---|---|---|
| Cu | 91 W (1.1 W/cm$^2$) | 0.2 nm + 0.6 nm/s $\cdot$ t[s] |
| Co | 97 W (1.2 W/cm$^2$) | 0.1 nm + 0.3 nm/s $\cdot$ t[s] |

Series **Thermo 2** (March 2003)

Type : $\mathrm{Si}_{[100]}(\mathrm{SiO}_2)_{100\,\mathrm{nm}}$ // $\mathrm{Co}_\mathrm{z}/\mathrm{Cu}_\mathrm{x}/[\mathrm{Co}_\mathrm{y}/\mathrm{Cu}_\mathrm{x}]_{40}$

(The variation range of the parameters $x, y, z$ is given in chapter 8.)

Pressures [mbar]: $\mathrm{p}_{\mathrm{base}} = 8 \cdot 10^{-7}$ $\mathrm{p}_{\mathrm{Ar}} = 1 \cdot 10^{-3}$

| Targetmaterial | Sputtering Power | Sputtering Offset and Rate |
|---|---|---|
| Cu | 90 W (1.1 W/cm$^2$) | 0.4 nm + 0.5 nm/s $\cdot$ t[s] |
| Co | 95 W (1.2 W/cm$^2$) | 0.1 nm + 0.2 nm/s $\cdot$ t[s] |

The samples of series **Bosch I and II** have been fabricated in July of 2001 in the laboratory of the *Robert Bosch GmbH* in Stuttgart. This *Von Ardenne* sputtering system of type *CS 730 S* has six dc magnetron sources of $90\,mm$ in diameter and a base pressure of $2 \cdot 10^{-7}\,mbar$. The distance of target to substrate is 40 to $45\,mm$, depending on source and thickness of the target. The sources are equipped with shapers for homogenization of the layers. Sputtering is performed in the wobble mode without the use of a shutter. The thickness of the layers is determined by the rotation speed of the substrate holder. The sputtering rates given in the table below are valid for a rotation speed of one round per minute of the substrate holder. For deposition of the materials Cu, CuAgAu and CoFe the substrate was only driven once beneath the source. The sputtering rates have been determined via spectroscopic ellipsometry on four samples with different numbers of wobble rotations. The substrates used in this series were pieces of size $(20 \cdot 20)\,mm^2$ cut out of a silicon wafer having [100] orientation and a layer of thermal oxide $850\,nm$ thick. Before cutting into pieces the wafer is covered with an acetone soluble protection layer and before sputtering, the pieces are cleaned in acetone and isopropanol in ultrasonic bath [ps].

Series **Jena** has been sputtered at the *Institut für Physikalische Hochtechnologie (IPHT)* in Jena in September 2001. The *Unaxis* sputtering system called "Cyberite" has nine dc magnetron sources of $300\,mm$ in diameter and a base pressure of $1 \cdot 10^{-8}\,mbar$. The sources are equipped with shapers for homogenization of the layers and so the substrate is rotated while sputtering without the use of a shutter. The distance of target to substrate is $10\,cm$ for Cu and Ta, $12.5\,cm$ for CoFe and $15\,cm$ for Fe. The substrates used in this series were pieces of size $(20 \cdot 20)\,mm^2$ cut out of a silicon wafer having [100] orientation and a layer of thermal oxide $1000\,nm$ thick. There was no cleaning of the substrates before sputtering. Sputtering rates have been determined via surface profiling on $70\,nm$ thick single layers and are given in the table below with approximated values [rm].

**Series Bosch I and II**

I : $Si_{[100]}(SiO_2)_{850\,nm}$ // $Fe_z/[(Co_{90}Fe_{10})_y/Cu_x]_n$ / Ta

II : $Si[100](SiO_2)_{850\,nm}//Fe_z/[(Co_{90}Fe_{10})_y/(Cu_{85}Ag_{10}Au_{75})_x]_n/Ta$

(The variation range of the parameters $x, y, z, n$ is given in chapter 6.)

Pressures [mbar]: $p_{base} = 2 \cdot 10^{-7}$ $p_{Ar} = 5 \cdot 10^{-3}$

| Targetmaterial | Sputtering Power | Sputtering Rate $[\frac{nm}{round\,@\,1\,rpm}]$ |
|---|---|---|
| Cu | 96 W (1.5 W/cm$^2$) | 9.02 |
| CuAgAu | 96 W (1.5 W/cm$^2$) | 9.60 |
| CoFe | 50 W (0.8 W/cm$^2$) | 2.55 |
| Fe | 150 W (2.4 W/cm$^2$) | 4.35 |

Series **Jena**

Type : $Si_{[100]}(SiO_2)_{1000\,nm}$ // $Fe_z/[(Co_{90}Fe_{10})_y/Cu_x]_n$ / Ta

(The variation range of the parameters $x, y, z, n$ is given in chapter 6.)

Pressures [mbar]: $p_{base} = 1 \cdot 10^{-8}$ $p_{Ar} = 5 \cdot 10^{-3}$

| Targetmaterial | Sputtering Power | Sputtering Rate [nm/s] |
|---|---|---|
| Cu | 1500 W (2.1 W/cm$^2$) | $\approx 2$ |
| CoFe | 800 W (1.1 W/cm$^2$) | $< 2$ |
| Fe | 1500 W (2.1 W/cm$^2$) | $\approx 2$ |
| Ta | 1500 W (2.1 W/cm$^2$) | $\approx 2$ |

## 5.2 Characterization Techniques

### 5.2.1 Measurement of the Magnetoresistance

The magnetoresistance of the samples has been measured using the four-point method: Four electrical contact needles equidistantly arranged in a row are directly pressed onto the sample. The outer contacts transport the current, provided by an adjustable constant current source. The two inner contacts measure the voltage drop on the sample. While determining the resistance of the sample in this way, an outer magnetic field with direction in plane of the layer stack is driven from negative to positive values and the way back. The maximum field values up to which 0.45 Teslas are achieveable and the steps of field variation can be chosen by the user.

While driving one magnetic field loop, seven different samples can be measured at the same time, having separate contacts to the constant current source and to the voltmeter. Details on this home-built apparatus are given in [mro98].

The technical accuracy of the measurement of the magnetoresistance is of 0.01 %, but in fact the exactness of the magnetoresistance determination is of the order 0.1 to 1 %, depending on the sample. There are two reasons for this fact, both having their origin in the sputtering process. Firstly, both sputtering systems of the Bielefeld laboratory do not sputter homogeniously in thickness. Depending on the position of the substrate above the source, this inhomogeniousness is more or less drastic. Because the effect amplitude of a multilayer system showing GMR depends on the spacer layer thickness, it is clear that thickness inhomogenity leads to GMR effect inhomogenity.[1] Secondly, the sputtering sources are of magnetron type, which means that they produce a magnetic field that acts up to the substrate position. Sputtering magnetic materials thus results in an anisotropy of the sample. Again, this anisotropy is a function of the position of the sample, resulting in an inhomogenity of the GMR effect.

Besides the measurement at the Bielefeld University Laboratory, the GMR of the samples of series **Bosch** and **Jena** has been determined in the laboratory of the *Robert Bosch GmbH.* The measurement technique is also based on the four-point method. The difference of the *Agilent Data Aquisition* measurement arrangement to that described above, is the automatic choice of current depending on the resistance of the sample. Furthermore, it has an array of measuring contacts which can be chosen individually for characterizing every selected area on a 4” wafer.

### 5.2.2 Measurement of the Magnetic Properties: MOKE

The magnetic properties of a sample as well as its electrical characteristics determine the magnetoresistance loop. Thus, measuring the magnetization versus field gives additional information. Series **Bielefeld**, **Multi 1**, **Multi 2** and **Thermo 1 and 2** have been magnetically characterized by MOKE measurements:

Polarized light changes its polarization when being reflected from a magnetic surface, this is the essence of the **magneto-optic Kerr effect (MOKE)**. MOKE measurements were performed in a home-built magnetometer using

---

[1] The characterization of a 4” wafer sputtered in the *Leybold L560* is given in [hei00].

linearly polarized light of wavelength $\lambda = 675\,nm$. A laser diode ($0.5\,mW$) is focused, giving a spot of $\sim 100\,\mu m$ on the sample surface. Furthermore, the laser diode is characterized by a stability of $0.08\,\%$. For an air gap of $2.5\,mm$ between the ferrite coils, magnetic field loops with $H_{max} \approx \pm 0.35\,T$ are driven with direction parallel to the sample surface but perpendicular to the polarization of the light. Proportional to the net magnetization of the material reflecting the light, the polarization of the light changes from linear to elliptical, although principally it is not possible to gain quantitative information on the magnetization. The light reflected from the surface is polarized a second time by the analyzer and finally, the intensity is detected by a photodiode. For metals, which are good conductors, the laserlight can penetrate typically only 10 to $20\,nm$ into the sample surface. Therefore, a magnetic material being close to the surface gives a higher Kerr signal than a material lying deeper inside the sample, which means that a MOKE measurement automatically gives dephth information of the sample. Transparent layers, e. g. overlayers, do not affect the Kerr signal in a significant way, and so even samples sputtered on glass substrates can be measured from their backside. A more detailed overview on MOKE can be found in [fow92] and details on the apparatus are given in [sud00].

### 5.2.3 Microstructure Investigations: XRD and XRR

X-ray diffraction and reflectometry have been measured on a *Philips X'Pert PRO MPD* diffractometer of Type PW3050/60, having a vertical $\theta/\theta$ configuration in Bragg-Brentano parafocusing geometry. Therefore, the x-ray tube together with the incoming beam optics is mounted on a moveable goniometer arm, the sample stage is fixed and the detector together with the diffracted beam optics is mounted on the second goniometer arm. The goniometer radius is $220\,mm$ and the smallest stepsize possible is $0.001°$ in $\omega$ and $2\theta$. The schematic drawing of the diffratometer is shown in figure 5.1 and will be explained in detail in the following. X-rays of type Cu-$K_\alpha$ with ($\lambda = 1.54\,\text{Å}$) have been applied, where the ratio of $K_{\alpha 1}$ to $K_{\alpha 2}$ is 2:1.

#### Incoming Beam Path

The radiation is produced by an ceramic **x-ray tube**, having a Cu anode and a long fine focus with focus dimension of $12 \cdot 4\,mm^2$. The maximum power of the tube is $2.2\,kW$ and measurements were usually performed with $50\,kV$ high tension and $40\,mA$ anode current. The tube is cooled by a closed cooling water system.

The emerging radiation passes a $0.04\,rad$ **soller slit** in order to control the axial divergence of the beam. The soller slit consists of parallel plates of an x-ray absorbing material and so solely rays not crossing a plate can pass. Soller

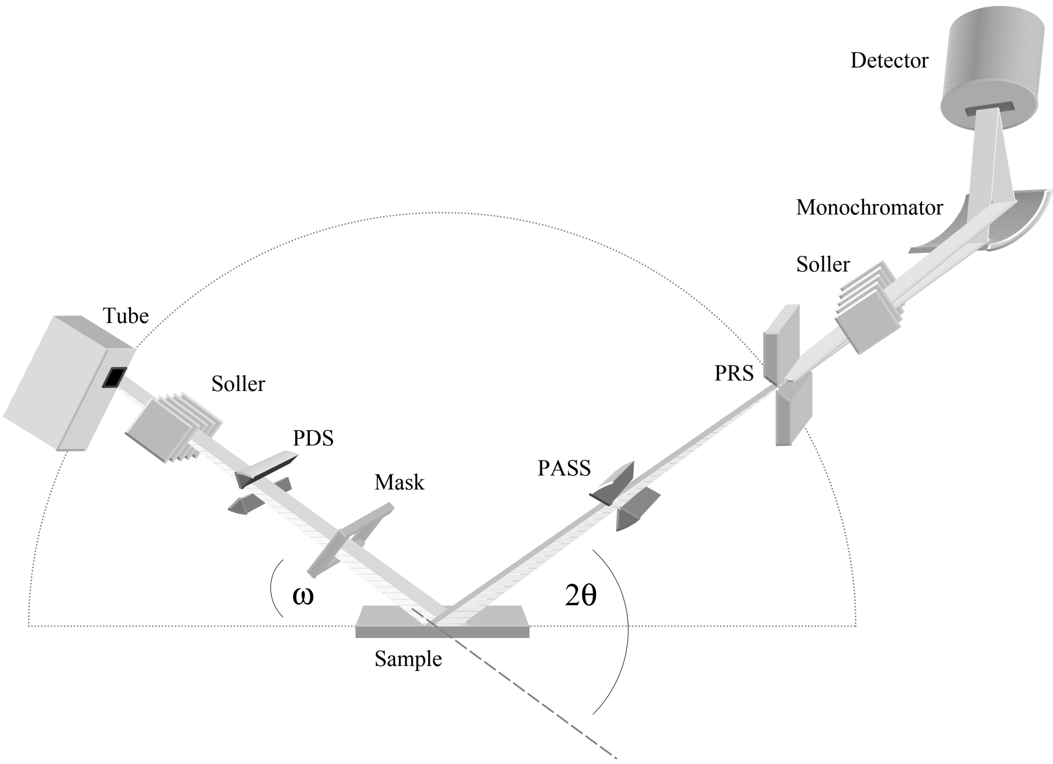

Figure 5.1: Schematic beam path of the *Philips X'Pert* Diffractometer.

slits improve the peak shape and the resolution in $2\theta$-type scans, especially at low scattering angles.

Control of the divergence in equatorial direction is done by a programmable **divergence slit** (PDS). The width of the PDS is chosen as large as the x-ray beam is completely accepted by the sample.

A **mask** at the end of the primary beam path limitizes the beam in axial direction which again has to be chosen such that the irradiated area is not larger than the sample.

Between divergence slit and mask a Ni attenuation foil, $0.125\,mm$ tick, can be switched into the beam path, either depending on the detected intensity, the diffraction angle or in fixed mode in order to prevent damaging the detector by too high counting rates. The attenuation factor is 137.

### Sample Stage

The sample stage is motorized in z-direction for adjustment of the sample surface height with respect to the beam path. Variations can be made in steps of $0.3\,\mu m$. The samples are laid on the sample stage without the necessity of fixing.

### Diffracted Beam Path

Radiation being diffracted or reflected from the sample is limited by a programmable **anti-scatter-slit** (PASS) in equatorial direction, in the first step. Afterwards, it passes the programmable **receiving slit** (PRS), which is the natural focusing point on the goniometer circle. Accordingly, the aperture of the receiving slit determines the resolution but also cruically the intensity.

Before entering the detector, the x-rays pass a $0.04\,rad$ **soller slit** and a curved pyrolytic graphite **monochromator** in order to cancel the Cu-$K_\beta$ and possible flourescence radiation. Finally, the x-rays are detected by a sealed proportional detector with a maximum count rate of $750\,kcps$.

### Programmable Divergence and Anti-Scattering Slits

The divergence slit and the anti-scatter slit can be held fixed during the measurement at a given aperture angle. Then the irradiated sample area becomes smaller with increasing angle of incidence. This has to be accounted for in analyzing diffracted intensities. Another possibility provided by the diffractometer is to adjust the slits such that the irradiated sample area is kept constant at a given value.

Thin film analysis can be performed in the “beam tunnel” configuration, where the anti-scatter slit and receiving slit are set with equal apertures, which is achieved by setting the PASS to “0°”.

### Thin Film Optics

Besides the diffracted beam path described above, the diffractometer is provided with a second diffracted beam path: The so called thin film optics. In case of very asymmetrical measuring arrangements, e. g. grazing incidence diffraction where the incident angle is held fixed at a small value and high diffraction angles shall be detected, the standard arrangement is not adequate. The essential difference of the thin film optics is to use a parallel plate collimator instead of the anti-scatter slit. This collimator consists of parallel plates which define the equatorial acceptance angle as seen by the detector. The equatorial acceptance of the parallel plate collimator is 0.27°. In the thin film configuration a flat graphite monochromator is used and the radiation is detected by a sealed proportional detector.

Both secondary optics are mounted fixed on one goniometer arm.

For general information on x-ray diffractometers and their components refer to [bis89]. For further details on the *Philips* goniometer see [XP00].

### Sample Adjustment

For a correct measurement with the diffractometer the sample has to be adjusted very carefully in its surface height in order to prevent errors in the diffraction angle.

When the sample is displaced in height by the amount of $s$, then the magnitude of the so called specimen displacement error is given by

$$\Delta 2\theta = -2s(cos\theta/R) \tag{5.1}$$

where $R$ is the radius of the goniometer [bis89]. Therefore, at moderate to low angles with $\cos\theta$ close to unity and the given goniometer radius of $220\,mm$, the error in $2\theta$ is about $(0.5 \cdot 10^{-3})^\circ$ for every $1\,\mu m$ sample displacement.

The sample height adjustment is performed in three steps, including the correction of sample tilt in the direction of the beam. Firstly, the incoming beam is set to $\omega = 0^\circ$ and a detector scan is performed around the zero position without the sample or the sample holder inside the beam. The countrate at the maximum of the detected direct beam is registered. Then, while detecting the direct beam counting rate, the sample is brought into the beam path until the countrate is one half of the original value. At last, an omega-scan is performed around the zero position with the sample inside the beam: this scan corresponds to a rotation of the sample in beam direction. If the sample is at correct height without any tilt angle, the detected peak is centered at $\omega = 0^\circ$ with a peakheight being one half of the direct beam.

**XRD and XRR Measurements**

X-ray diffraction and reflectometry measurements were usually performed under the following conditions:

**Measurement Settings**

| | **XRD 1** | **XRD 2** | **XRR** |
|---|---|---|---|
| Tube settings | 50 kV; 40 mA | 50 kV; 40 mA | 50 kV; 40 mA |
| PDS | 15 mm | 15 mm | $(1/32)^\circ$ |
| Mask | 15 mm | 15 mm | 15 mm |
| PASS | 15 mm | 15 mm | 0° |
| PRS | 0.1 mm | 0.1 mm | 0.1 mm |
| Scan type | Gonio step scan | Gonio step scan | $(2\theta - \omega)$ step scan |
| Angle range | $10^\circ \leq 2\theta \leq 140^\circ$ | $30^\circ \leq 2\theta \leq 55^\circ$ | $0^\circ \leq 2\theta \leq 10^\circ$ |
| Step size | 0.04° | 0.04° | 0.004° |
| Time per step | 5 s | 30 s | 10 s |

The dynamical intensity range of x-ray reflectometry measurements of the Goniometer under the conditions given above is about seven orders of magnitude.

### 5.2.4 Investigations with AGM, TEM and AFM

Series **Bosch** and **Jena** have been characterized magnetically with an **Alternating Gradient Magnetometer (AGM)** at the *Institut für Werkstoffkunde, Dresden* by D. Elefant, and two selected samples of series **Thermo 1** have been measured by I. Ennen with a *MicroMag 2900* AGM at the University of Bielefeld.

Two samples of series **Bielefeld** as well as two samples of series **Thermo 1** have been sent to G. Schmitz to the University of Münster for **Transmission Electron Microscopy (TEM)** investigations.

The surface of the $850\,nm$ $SiO_2$ wafer has been investigated by D. Meyners with **Atomic Force Microscopy (AFM)** at the University of Bielefeld.

### 5.2.5 Thermal Treatment

The microstructure of the samples of series **Thermo 1 and 2** was determined in their as prepared state and after annealing. The annealing was performed in a vacuum system of $1 \cdot 10^{-7}\,mbar$ base pressure. The sample is moderately pressed on a copperplate connected to heating wires and pipes for cooling with compressed air. The heating characteristic is about $50^\circ\,C$ per minute and cooling down from $500^\circ\,C$ to $25^\circ\,C$ takes 50 minutes, showing a nonlinear cooling behaviour.

### 5.2.6 Transport Measurements at Low Temperatures

One sample of series **Thermo 1** has been lithographically patterned to a line of width $20\,\mu m$ and length $1.74\,mm$ in its as prepared state as well as after annealing, separately. The temperature dependence of the resistance and the magnetoresistance of the lines was measured in a closed cycle Helium cryostat having a temperature range of 10 to $330\,K$.

# Chapter 6

# Laboratory all-embracing Co/Cu Multilayer Study

## 6.1 Intention of the Study

The investigation of the GMR effect in Co/Cu multilayers is always a superposition of interlayer exchange coupling and spin-dependent transport. The literature review given in chapter 2, table 2.2 has made clear, that there is principal agreement about the characteristics of antiferromagnetic exchange coupling in Co/Cu multilayers, i. e. about its coupling period and the position of the coupling maxima. On the other hand, there are very large differences concerning the GMR effect amplitudes found by different research groups which are not correlated to the antiferromagnetic coupling strength. In the first years of GMR research of Co/Cu multilayers it was striking that all samples prepared by MBE did not yield any GMR effect although some of them were coupled much stronger than samples prepared by sputtering, showing large GMR amplitudes. In the meantime it has been proven that GMR effect can also be realized in MBE samples although the amplitudes reached are not as high as in sputtered multilayers [hal93].

Besides the differences in GMR effect concerning the preparation method, the effect has also been found to vary from laboratory to laboratory in spite of almost identical preparation conditions. In order to explain the differing results, a number of research groups has characterized the interface roughness and further microstructural parameters. In most cases, these studies explained the interdependence of the microstructural parameter of interest and the GMR amplitude of the investigated samples, but the findings were not necessarily valid for multilayers of other research groups. Therefore it has to be balanced at the present date, that even though Co/Cu multilayers are the most investigated

GMR system, there is no common sense which microstructural features are responsible for the gain of high GMR effect amplitudes.

The idea of the multilayer study performed in this thesis is to overcome the laboratory-limited point of view and to investigate samples prepared in different laboratories with identical characterization methods. In order to clear up the interplay between microstructure and GMR, the study is not performed on a few selected samples but on extensive series of many varied parameters.

## 6.2 Series and Investigation Overview

| | | | |
|---|---|---|---|
| **Bielefeld** | | | |
| $\mathrm{Si_{[100]}(SiO_2)_{850\,nm}}$ // $\mathrm{Py_z/[Co_y/Cu_x]_n}$ / $\mathrm{Cu_{(2.2\,nm)}}$ | | | |
| $0 \leq z \leq 5.8\,nm$, | $0.4 \leq y \leq 5.9\,nm$, | $1.8 \leq x \leq 2.5\,nm$, | $0 \leq n \leq 30$ |
| Ref.: $z = 3.0\,nm$, | $y = 1.6\,nm$, | $x = 2.14\,nm$, | $n = 20$ |
| **Jena** | | | |
| $\mathrm{Si_{[100]}(SiO_2)_{1000\,nm}}$ // $\mathrm{Fe_z/[(Co_{90}Fe_{10})_y/Cu_x]_n}$ / $\mathrm{Ta_{(5\,nm)}}$ | | | |
| $0 \leq z \leq 5.0\,nm$, | $0.5 \leq y \leq 1.7\,nm$, | $0.6 \leq x \leq 3.3\,nm$, | $2 \leq n \leq 50$ |
| Ref.: $z = 1.7\,nm$, | $y = 1.2\,nm$, | $x = 2.15\,nm$, | $n = 20$ |
| **Bosch I** | | | |
| $\mathrm{Si_{[100]}(SiO_2)_{850\,nm}}$ // $\mathrm{Fe_z/[(Co_{90}Fe_{10})_y/Cu_x]_n}$ / $\mathrm{Ta_{(15\,nm)}}$ | | | |
| $0 \leq z \leq 3.6\,nm$, | $0.5 \leq y \leq 1.7\,nm$, | $2.0 \leq x \leq 2.6\,nm$, | $2 \leq n \leq 35$ |
| Ref.: $z = 1.5\,nm$, | $y = 1.2\,nm$, | $x = 2.21\,nm$, | $n = 20$ |
| **Bosch II** | | | |
| $\mathrm{Si[100](SiO_2)_{850\,nm}//Fe_z/[(Co_{90}Fe_{10})_y/(Cu_{85}Ag_{10}Au_{75})_x]_n/Ta_{(15\,nm)}}$ | | | |
| $0 \leq z \leq 3.6\,nm$, | $0.6 \leq y \leq 1.8\,nm$, | $2.1 \leq x \leq 2.7\,nm$, | $2 \leq n \leq 35$ |
| Ref.: $z = 1.3\,nm$, | $y = 1.2\,nm$, | $x = 2.27\,nm$, | $n = 20$ |

Four multilayer series have been prepared in three different laboratories. All sample series have been successively varied in their spacer layer thickness (parameter $x$), magnetic layer thickness (parameter $y$), buffer layer thickness (parameter $z$) and their number of double layers (parameter $n$). The variation in spacer layer thickness is restricted to a range around the second antiferromagnetic coupling maximum (AFCM) because this is the maximum of choice concerning industrial application. During the variation of one parameter all other parameters are held fixed. These fixed values characterize the so called reference system. The stacking sequence, the variation range and the reference values of the parameters of all series are listed above. For clarity, the multilayer stack is additionally indicated in each section.

The samples have been prepared under the conditions given in chapter 5. The magnetoresistance was determined for all samples, whereas magnetic and microstructural investigations were performed on selected samples. In the following sections the results of transport, magnetic and microstructural characterization of the samples are presented.

## 6.3 Variation of Spacer Layer Thickness

The GMR effect amplitude as a function of the spacer layer thickness around the second AFCM is based on the samples:

| | | | | |
|---|---|---|---|---|
| Bielefeld | Si // | $\{\mathrm{Py}_{3.0\,\mathrm{nm}}/$ | $[\mathrm{Co}_{1.6\,\mathrm{nm}}\ /\ \mathrm{Cu}_{\mathrm{x}}]_{20}\ /$ | $\mathrm{Cu}_{2.2\,\mathrm{nm}}\}$ |
| Jena | Si // | $\{\mathrm{Fe}_{1.7\,\mathrm{nm}}/$ | $[\mathrm{CoFe}_{1.2\,\mathrm{nm}}\ /\ \mathrm{Cu}_{\mathrm{x}}]_{20}\ /$ | $\mathrm{Ta}_{5.0\,\mathrm{nm}}\}$ |
| Bosch I | Si // | $\{\mathrm{Fe}_{1.5\,\mathrm{nm}}/$ | $[\mathrm{CoFe}_{1.2\,\mathrm{nm}}\ /\ \mathrm{Cu}_{\mathrm{x}}]_{20}\ /$ | $\mathrm{Ta}_{15\,\mathrm{nm}}\}$ |
| Bosch II | Si // | $\{\mathrm{Fe}_{1.3\,\mathrm{nm}}/$ | $[\mathrm{CoFe}_{1.2\,\mathrm{nm}}\ /\ \mathrm{CuAgAu}_{\mathrm{x}}]_{20}\ /$ | $\mathrm{Ta}_{15\,\mathrm{nm}}\}$ |

The result of the spacer variation is presented in figure 6.1. The largest GMR amplitude of 31 % is yielded by series Jena, followed by the samples prepared in Bielefeld with a maximum GMR value of 27 %, Bosch I with 24.5 % and finally Bosch II having 21 %. The spacer layer thickness that corresponds to the maximum GMR amplitude is not the same for the four series. Speaking in terms of increasing spacer thickness, the Bielefeld sample with $t_{Cu} = 2.05\,nm$ is the first one that reaches its GMR maximum, followed by Jena with $t_{Cu} = 2.1\,nm$ and Bosch I and II both having $t_{Cu} = 2.2\,nm$.

Furthermore, the four series differ in the thickness range of their second AFCM. The full width at half maximum (FWHM) of the second AFCM peak is estimated on the base of interpolation and extrapolation of data points. The series Bielefeld, Jena and Bosch I have a comparable FWHM of $\Delta t_{Cu} = 0.58\,nm$, $\Delta t_{Cu} = 0.51\,nm$ and $\Delta t_{Cu} = 0.48\,nm$, respectively. The FWHM of the Bosch II series is distinctively smaller with $\Delta t_{Cu}$ only being $0.37\,nm$.

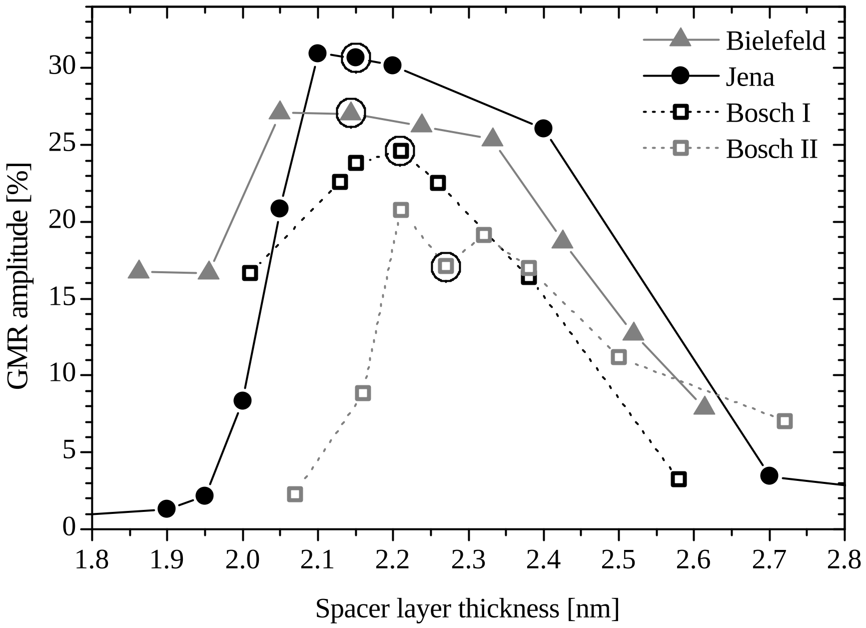

Figure 6.1: GMR amplitude as a function of the spacer layer thickness of the series Bielefeld (Cu/Co), Jena (Cu/CoFe), Bosch I (Cu/CoFe) and Bosch II (CuAgAu/CoFe). The data points marked by circles refer to the spacer thickness of the reference system.

The fourth characteristic of the spacer variation is the position of maximum GMR amplitude relative to the slope of the AFCM peak. It is clearly visible for the series Bielefeld, Jena and Bosch II that the GMR amplitude reaches its maximum shortly after the beginning of the AFCM. This is in contrast to series Bosch I having its GMR maximum in the centre of the AFCM peak.

### Discussion

The results of the spacer variation reveal two important interdependencies. Firstly, the oscillating nature of the interlayer exchange coupling becomes obvious. The variation range investigated in this study covers the second AFCM as well as the beginning of the neighboured ferromagnetic exchange coupling. Secondly, the slope of the GMR amplitude reflects the properties of spin-dependent transport. The AFCM peak is characterized by a steeper slope on the increasing side than on the decreasing side and furthermore, the maximum GMR amplitude is shifted towards smaller values instead of being located in the centre of the peak. The explanation for this behaviour is the effect of shunting with increasing spacer thickness. On one hand, the spacer has to be as thick as necessary to adjust the AF coupling and on the other hand, the spacer should be as thin as possible to reduce the shunting (see chapter 3).

It is interesting to compare the spacer variation results presented here with those of other research groups. The most often referenced paper concerning Co/Cu multilayers is definitely the one of Parker *et al.* in which they present the first evidence for antiferromagnetic exchange coupling in Co/Cu multilayers with large GMR effect amplitudes [par91b]. Their spacer variation $Si/Fe_{4.0\,nm}/[Co_{1.0\,nm}/Cu_{t_{Cu}}]_{16}/Cu_{1.9\,nm}$ yields a maximum GMR amplitude of 25 % at second AFCM with $t_{Cu} = 1.91\,nm$ and a FWHM of approximately $0.7\,nm$. The Cu thickness corresponding to the position of maximum GMR is considerably smaller than the values of the series investigated here, the difference being between 0.2 and $0.3\,nm$. The FWHM of $0.7\,nm$ is distinctively larger compared to the four variation series. The position of the maximum amplitude relative to the slope of the AFCM peak is shifted to smaller values in agreement to the findings in this thesis. The GMR amplitude observed by Parkin and coworkers does not reach the level of Jena and is slightly smaller than the maximum obtained in Bielefeld, but it has to be kept in mind that this is a comparison of 16 with 20 bilayers.

In 1994, Lenczowski and coworkers found the second AFCM of the multilayer stack $Si/Cu_{30.0\,nm}/[Co_{1.6\,nm}/Cu_{t_{Cu}}]_{100}/Au_{5.0\,nm}$ to be of 40 % GMR amplitude at $t_{Cu} = 2.0\,nm$. The FWHM of their spacer variation is only $\approx 0.2\,nm$ [len94]. The comparison of these findings to the series studied here has to be taken with care because of the extraordinary thick Cu buffer and the large number of 100 double layers.

Paul *et al.* have performed interface roughness studies of Co/Cu multilayer stacks at the first and second AFCM [pau03]. They did not perform a spacer but a bilayer variation for two different Cu thickness values in the range of the second AFCM with $SiO_2/Co_{1.45\,nm}/[Cu_{2.20\&2.50\,nm}/Co_{1.45\,nm}]_N$ being the stacking sequence. In order to compare the interfaces at the end of this chapter, the GMR amplitudes are given here. In the case of 20 bilayers they found a GMR amplitude of 20 % at $t_{Cu} = 2.20\,nm$ and of 5 % at $t_{Cu} = 2.5\,nm$. Both values are small compared to series Bielefeld, Jena and Bosch I.

The explanation of the differing GMR amplitudes as well as of the positions and slopes of the AFCM peak of the four series is expected to be given with the knowledge of the microstructure and especially of the interface roughness of the samples. Therefore, the discussion of the results of the groups mentioned above will be given at the end of this chapter.

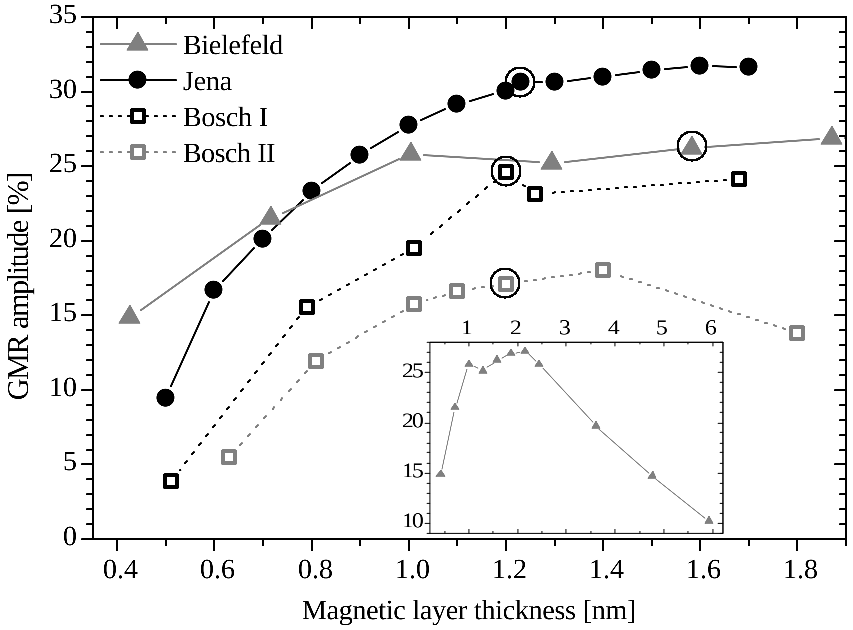

Figure 6.2: GMR amplitude as a function of the magnetic layer thickness of the series Bielefeld (Cu/Co), Jena (Cu/CoFe), Bosch I (Cu/CoFe) and Bosch II (CuAgAu/CoFe). The data points marked by circles refer to the magnetic layer thickness of the reference system. For series Bielefeld the Co thickness has been varied up to 6 $nm$ and the corresponding GMR amplitudes are given in the inset.

## 6.4 Variation of Magnetic Layer Thickness

The GMR effect amplitude at the second AFCM as a function of the magnetic layer thickness is presented in figure 6.2 and is based on the samples:

| | | | | |
|---|---|---|---|---|
| Bielefeld | Si // | $\{\mathrm{Py}_{3.0\,\mathrm{nm}}/$ | $[\mathrm{Co}_{\mathrm{y}}\ /\ \mathrm{Cu}_{2.14\,\mathrm{nm}}]_{20}\ /$ | $\mathrm{Cu}_{2.2\,\mathrm{nm}}\}$ |
| Jena | Si // | $\{\mathrm{Fe}_{1.7\,\mathrm{nm}}/$ | $[\mathrm{CoFe}_{\mathrm{y}}\ /\ \mathrm{Cu}_{2.15\,\mathrm{nm}}]_{20}\ /$ | $\mathrm{Ta}_{5.0\,\mathrm{nm}}\}$ |
| Bosch I | Si // | $\{\mathrm{Fe}_{1.5\,\mathrm{nm}}/$ | $[\mathrm{CoFe}_{\mathrm{y}}\ /\ \mathrm{Cu}_{2.21\,\mathrm{nm}}]_{20}\ /$ | $\mathrm{Ta}_{15\,\mathrm{nm}}\}$ |
| Bosch II | Si // | $\{\mathrm{Fe}_{1.3\,\mathrm{nm}}/$ | $[\mathrm{CoFe}_{\mathrm{y}}\ /\ \mathrm{CuAgAu}_{2.27\,\mathrm{nm}}]_{20}\ /$ | $\mathrm{Ta}_{15\,\mathrm{nm}}\}$ |

Starting with a magnetic layer thickness of about 0.5 $nm$, the GMR amplitude of all series increases with magnetic layer thickness. Series Jena is characterized by the steepest rise in GMR and reaches an amplitude of about 28 % at a CoFe thickness of 1.0 $nm$. This is comparable to the Bielefeld series which reaches 26 % at the same thickness of Co. In the further course of enhancing the magnetic layer thickness the samples prepared in Jena increase to 32 % at

1.6 $nm$, the GMR of the Bielefeld series does marginally grow up to a maximum amplitude of 27 % at 2.1 $nm$. Changing the magnetic layer thickness to even larger values up to 6 $nm$ results in a slow decrease of the GMR amplitude as has been proven for the Bielefeld samples. The variation range of series Jena ends at 1.7 $nm$ and no decrease in GMR is seen up to there. This is also the case for the Bosch I series. Compared to Bielefeld and Jena, the area of increasing GMR of Bosch I samples is shifted towards higher magnetic layer thickness and the maximum amplitude of 24 % is yielded at $t_{Co} = 1.2\,nm$. Although the full width at half maximum of the magnetic layer variation can not be determined for Jena and Bosch I samples, it is clearly visible that the width of the Bosch II series is distinctively smaller. The maximum GMR amplitude of 19 % is measured at 1.2 $nm$.

### Discussion

The results of the magnetic layer variation agree very well with the principles treated in chapter 3 and the general finding, that for multilayers a broad maximum of GMR is found for thickness values between 1 and 3 $nm$. Below these values, there is insufficient scattering within the magnetic layers or at the interfaces and above 3 $nm$ the effect of shunting comes into account.

It is interesting to note that below 0.8 $nm$ Co thickness the GMR amplitudes of series Bielefeld are larger than those of Jena, whereas for $t_{Co} > 0.8\,nm$ Jena overtakes Bielefeld. The explanation for this observation as well as for the larger amplitude of Jena samples has to be given with the knowledge of microstructure.

The findings for series Bosch I and II which reach the GMR plateau at considerable higher values for $t_{Co}$ have to be corrected because the XRR analysis presented further below uncovers a calibration error. The magnetic layers with nominal thickness of 1.2 $nm$ do in fact have only 0.9 $nm$. Assuming that this error is of offset type, the GMR amplitudes of series Bosch I and II in figure 6.2 are shifted by 3 Å to the left. As a consequence, samples of series Bosch I would coincide with the samples prepared in Jena for $t_{Co}$ up to 0.9 $nm$.

## 6.5 Variation of Buffer Layer Thickness

The GMR effect amplitude as a function of the buffer layer thickness at the second AFCM is presented in figure 6.3 and is based on the samples:

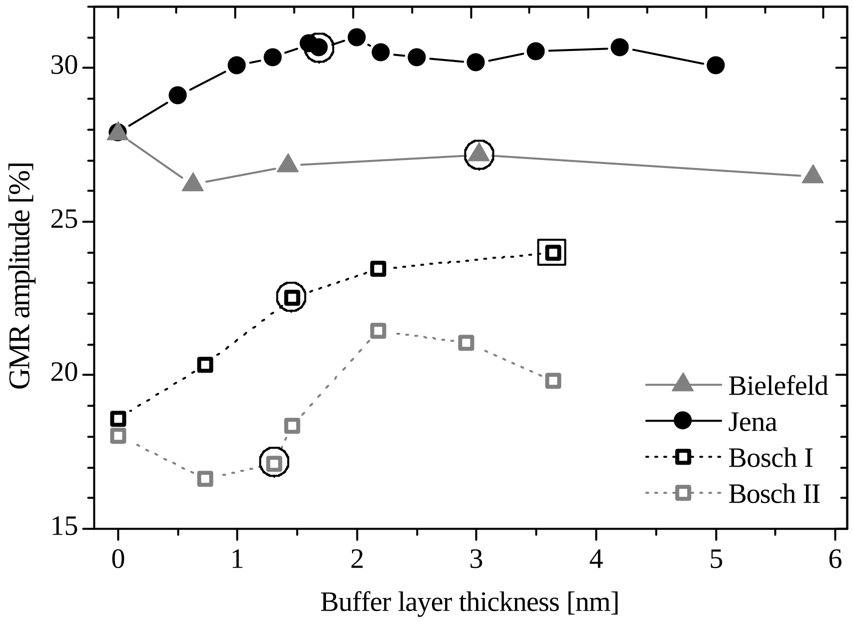

Figure 6.3: GMR amplitude as a function of the buffer layer thickness of the series Bielefeld (Cu/Co), Jena (Cu/CoFe), Bosch I (Cu/CoFe) and Bosch II (CuAgAu/CoFe). The data points marked by circles refer to the buffer layer thickness of the reference system. The data point marked with a box has a slightly different magnetic layer thickness of $1.17\,nm$.

| | | | | |
|---|---|---|---|---|
| Bielefeld | Si // | $\{\mathrm{Py_z}/$ | $[\mathrm{Co_{1.6\,nm}}\ /\ \mathrm{Cu_{2.14\,nm}}]_{20}\ /$ | $\mathrm{Cu_{2.2\,nm}}\}$ |
| Jena | Si // | $\{\mathrm{Fe_z}/$ | $[\mathrm{CoFe_{1.2\,nm}}\ /\ \mathrm{Cu_{2.15\,nm}}]_{20}\ /$ | $\mathrm{Ta_{5.0\,nm}}\}$ |
| Bosch I | Si // | $\{\mathrm{Fe_z}/$ | $[\mathrm{CoFe_{1.2\,nm}}\ /\ \mathrm{Cu_{2.21\,nm}}]_{20}\ /$ | $\mathrm{Ta_{15\,nm}}\}$ |
| Bosch II | Si // | $\{\mathrm{Fe_z}/$ | $[\mathrm{CoFe_{1.2\,nm}}\ /\ \mathrm{CuAgAu_{2.27\,nm}}]_{20}\ /$ | $\mathrm{Ta_{15\,nm}}\}$ |

A buffer layer, also called seed layer, is used in order to improve the growth conditions for subsequent layers and thus to enhance the GMR amplitude. The graph reveals that this concept does not work equally well for the different sample series.

Bosch II samples do profit the most by the use of a Fe buffer. The GMR amplitude is increased from 18.5 % without buffer to 23.5 % with $t_{Fe} = 2.2\,nm$ which is a relative increase by 27 %. Unfortunately, the buffer thickness which yields the highest GMR amplitude is not the same as the one chosen in the reference system. This seems to be one important reason for the generally low GMR level of this series.

The GMR amplitudes of series Bosch I are also considerably enhanced with the buffer thickness, whereas the influence of the buffer on series Bielefeld is quite small. Interestingly, for these samples the renunciation of a buffer layer at all seems to be the best choice. But it has to be stated that this observation does not agree with the general findings of buffer layer dependence of the GMR in Co/Cu multilayers prepared in Bielefeld. For every buffer thickness the multilayers sputtered in Jena reach the highest GMR level of all series and a slight enhancement of GMR with buffer thickness can be seen up to $1\,nm$ of $t_{CoFe}$.

In principle, samples of the buffer variation series are the ideal candidates in order to correlate microstructural characteristics with the observed GMR: the thickness of magnetic and spacer layer remain unchanged in the stack and therefore any changes in AF coupling, magnetic and transport properties should be caused by microstructural changes. This is why a number of microstructural features of the series have been determined within this study. Depending on the buffer layer thickness, the crystallite size as well as the Co/Cu lattice spacing in growth direction have been found to vary considerably. But despite of these findings, no correlation has been found between these characteristics and the GMR amplitude for none of the investigated series. Because of the lack of interdepence between microstructure and GMR the results are not shown here but will be a point of discussion at the end of the chapter.

## 6.6 Variation of Number of Double Layers

The GMR effect amplitude at the second AFCM as a function of the number of double layers is presented in figure 6.4 and is based on the samples below:

| | | | | |
|---|---|---|---|---|
| Bielefeld | Si // | {Py$_{3.0\,\mathrm{nm}}$/ | [Co$_{1.6\,\mathrm{nm}}$ / Cu$_{2.14\,\mathrm{nm}}$]$_\mathrm{n}$ / | Cu$_{2.2\,\mathrm{nm}}$} |
| Jena | Si // | {Fe$_{1.7\,\mathrm{nm}}$/ | [CoFe$_{1.2\,\mathrm{nm}}$ / Cu$_{2.15\,\mathrm{nm}}$]$_\mathrm{n}$ / | Ta$_{5.0\,\mathrm{nm}}$} |
| Bosch I | Si // | {Fe$_{1.5\,\mathrm{nm}}$/ | [CoFe$_{1.2\,\mathrm{nm}}$ / Cu$_{2.21\,\mathrm{nm}}$]$_\mathrm{n}$ / | Ta$_{15\,\mathrm{nm}}$} |
| Bosch II | Si // | {Fe$_{1.3\,\mathrm{nm}}$/ | [CoFe$_{1.2\,\mathrm{nm}}$ / CuAgAu$_{2.27\,\mathrm{nm}}$]$_\mathrm{n}$ / | Ta$_{15\,\mathrm{nm}}$} |

It can be seen for all sample series, that a multilayer made up of only 2 double layers (in the further course shortly denoted as DL) does not show a noticeable GMR effect. When another DL is added to the stack, the Jena sample is the first to have an effect amplitude of 9 % whereas the other series start to have GMR with at least 4 DL. For all series a rapid increase in GMR amplitude is

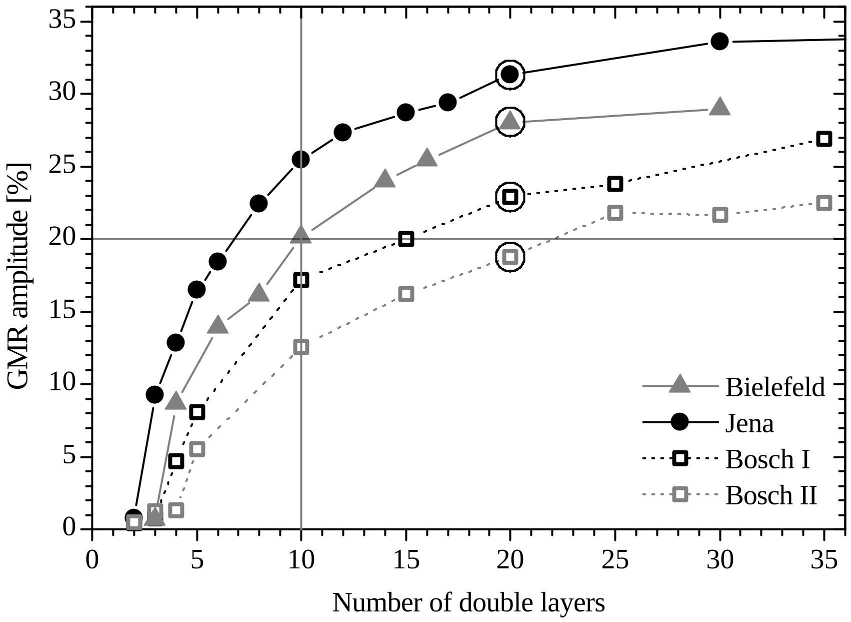

Figure 6.4: GMR amplitude as a function of the number of double layers of the series Bielefeld (Cu/Co), Jena (Cu/CoFe), Bosch I (Cu/CoFe) and Bosch II (CuAgAu/CoFe). The data points marked by circles refer to the number of double layers of the reference system. The lines are guides for the eye at the characteristic values of 10 double layers and 20 % GMR amplitude.

detected with every added bilayer up to 10 DL. Since then, the increase goes on much smoother and starts to saturate at 20 DL for the Bielefeld and Jena samples and at 25 DL for series Bosch II. Series Bosch I is an exception here as it does not show saturation even with 35 DL.

### 6.6.1 Magnetic Characterization

A priori, it is not clear to see why samples having only 2 or 3 bilayers have no or only little GMR and why the number of double layers necessary to yield a given GMR amplitude differs for the four sample series. In order to answer these questions, magnetic measurements of the double layer variation series have been performed. Series Jena and Bosch I and II were measured with AGM at the *IFW Dresden* and series Bielefeld was characterized with MOKE in Bielefeld.

Figure 6.5 is a survey of MOKE hysteresis loops of selected samples of series Bielefeld. The direct comparison of the samples with 3 and 4 DL makes clear that the AF coupling starts with the fourth DL. Every bilayer grown upon the fourth DL is AF coupled and the hysteresis loop of the 20 DL sample does

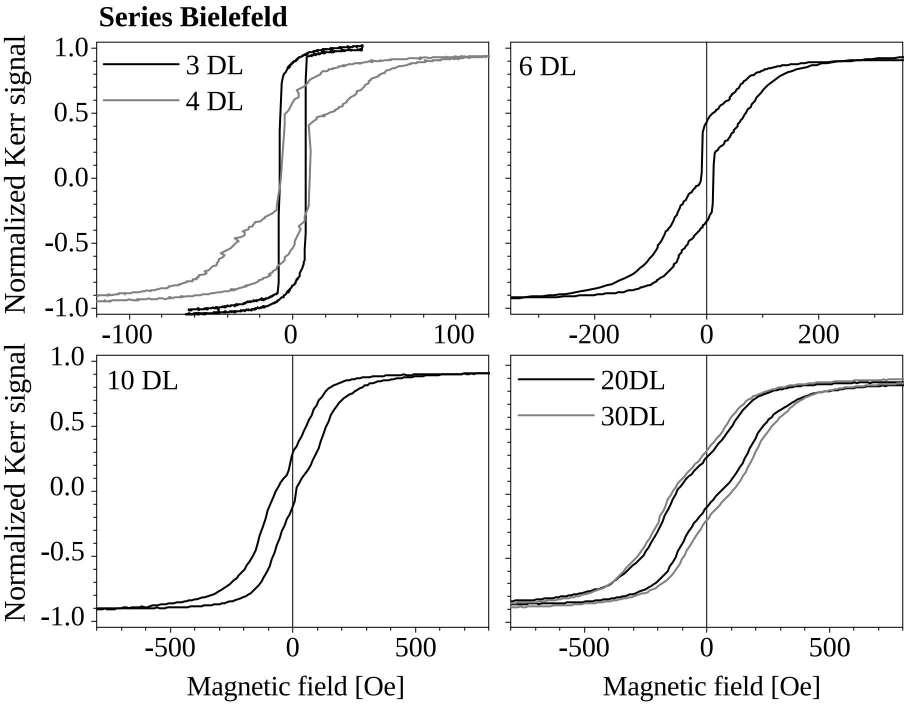

Figure 6.5: MOKE hysteresis loops as a function of the number of double layers (DL) of selected samples of series Bielefeld. The scale of the normalized Kerr signal is the same for all graphs.

not show a ferromagnetic middle part any more. Sputtering more than 20 bilayers does not give rise to a further enhancement of AF coupling. Because the Co layer thickness is identical for all samples, the saturation magnetic field enables to compare the antiferromagnetic coupling. The saturation field as a function of the number of double layers is given in figure 6.6. The sample with zero DL is the pure Permalloy buffer. Samples having up to 3 bilayers show a pure ferromagnetic characteristic with a saturation field below 10 $Oe$. Starting with DL $= 4$ the AF coupling increases almost linearly up to 10 DL and is saturated at 16 DL. The sample with 30 bilayers shows a slight decrease in saturation, maybe due to the accumulated roughness of the topmost layers. In summary, the samples prepared in the Bielefeld laboratory “need” a buffer of 3 double layers before the antiferromagnetic coupling of the Co layers can be established.

Figure 6.7 draws together the most significant hysteresis loops of series Jena. In contrast to MOKE measurements, AGM has the advantage of giving a quantitative signal and furthermore, the detected signal refers to the whole sample with an equal weight of every layer. Therefore, the AGM hysteresis loops allow to quantify the amount of non-AF coupled layers. The sample made

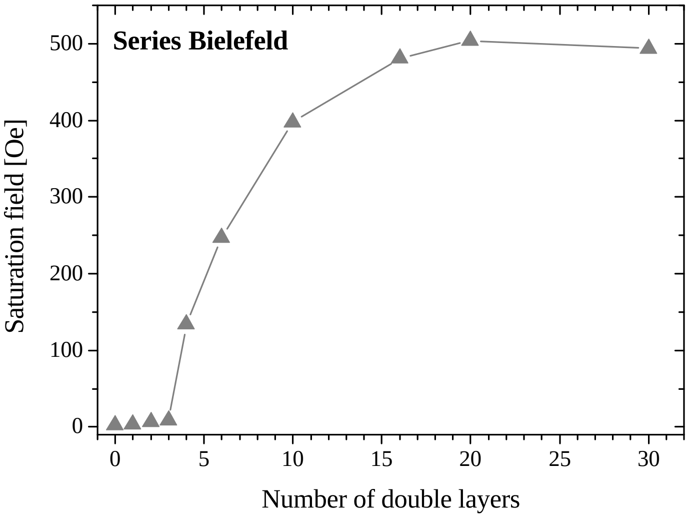

Figure 6.6: Saturation field of the MOKE hysteresis loops as a function of the number of double layers of series Bielefeld. The sample with DL = 0 consists of the pure Permalloy buffer.

up of only 2 bilayers is characterized by a pure ferromagnetic hysteresis loop having a saturation magnetization of $6 \cdot 10^{-5}\,emu$. When the third DL is added to the stack, the hysteresis loop shows the first indication of antiferromagnetic coupling and the sample with 4 DL is unambiguously antiferromagnetically coupled. But for every sample the two first grown double layers are not AF coupled, which is proven by the ferromagnetic middle part of every hysteresis loop. To make clear that the amount of ferromagnetic coupling does not change no matter how many double layers are grown, the saturation magnetization of the 2 DL sample has been indicated in each graph as grey lines. In conclusion, each bilayer added to the first 2 DL of the multilayer stack is AF-coupled and the coupling behaviour of the first 2 DL is not affected by the layers grown upon.[1] In summary, the Jena samples are characterized by only two non-antiferromagnetically coupled double layers.

The AGM measurements of the series Bosch I and II have also been performed at the *IFW Dresden* and have been evaluated by D. Elefant [ele01]. The hysteresis loops of the samples principally have the same characteristic and thus are not shown here. The investigation revealed, that Bosch I samples

---

[1] Due to the production of heat during the sputtering process one might think of an annealing effect for samples with many double layers: the longer the sputtering process takes the more heat is transported into the sample. Gentle heat treatment is known to be able to smooth the interfaces in a multilayer. On the other hand, a reason for ferromagnetic coupling to occur is the presence of interface roughness. In conclusion, it might principally be possible to enhance the AF coupling of the first 2 DL by increasing the number of double layers grown upon.

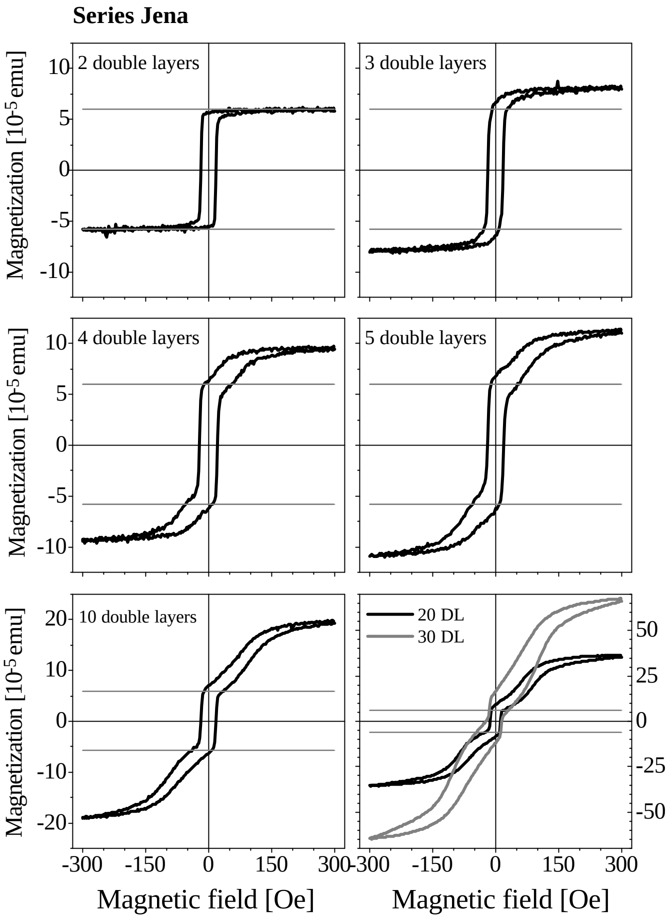

Figure 6.7: AGM hysteresis loops of selected samples of series Jena. The scale of the magnetic field is the same for all graphs. The upper four graphs draw together the samples with 2 to 5 DL on the same scale of magnetization. Additionally, the saturation magnetization of the sample with 2 DL is marked as grey lines for these measurements. The lower two graphs compare the samples with 10, 20 and 30 DL.

are characterized by 4 ferromagnetically coupled double layers whereas series Bosch II does even have 5 non-AF coupled bilayers.

In conclusion, the magnetic properties of the samples coincide very well with the evolution of GMR with increasing number of double layers. The GMR effect amplitude of the multilayers having at least one AF coupled double layer is in the range of 8 to 9 % for the series Bielefeld (4DL), Jena (3DL) and Bosch I (5DL).

The identification of the ferromagnetically coupled layers does help to understand the GMR properties of the samples but it is not clear yet why these layers are not AF-coupled. Furthermore, the four sample series are not only characterized by a different "offset" of non-AF coupled double layers but also by a different increase of GMR amplitude with the number of bilayers. Therefore, selected microstructural properties of the samples are investigated and dicussed in the following.

### 6.6.2 Microstructural Characterization

X-ray reflectometry (XRR) measurements have been performed on selected samples with varying number of double layers of the series Bielefeld, Jena and Bosch I. In chapter 4.3 it has been thoroughly described how the single layer thickness $d$ and interface roughness $\sigma$ of a multilayer are determined via a fit to the XRR measurement. Furthermore, in chapter 4.3.2 it has become clear that the determination of reliable values for $d$ and $\sigma$ for every single layer of a multilayer having 20 double layers is a very delicate and time consuming task. On the other hand, reliable mean values for thickness and roughness can be determined by fitting the whole double layer stack.[2] This so called "a priori" fitting procedure has been chosen here to fit every sample of the double layer variation series. The appropriate fit models were

| | |
|---|---|
| Bielefeld | $SiO_2$ // $[Py\ /Co\ /Cu\ /Co/]_1$ // $[Cu\ /\ Co]_{n-2}$ // $[Cu\ /CuO]_1$ |
| Jena | SiO2 // $[Fe]_1$ // $[CoFe\ /\ Cu]_n$ // $[Ta\ /Ta_2O_5]_1$ |
| Bosch I | $SiO_2$ // $[Fe]_1$ // $[CoFe\ /\ Cu]_n$ // $[Ta\ /Ta_2O_5]_1$ |

For series Bielefeld an extended buffer in form of the first Co and Cu layers has been introduced in the model stack because the first Cu layer is characterized by an extraordinary small thickness which is discussed below. Such a deviation has not been found for the series Jena and Bosch I and this is why all Co and Cu layers are fit together in one layer stack.

For series Bielefeld, the values of the Co and Cu single layer thickness as determined by the XRR fit procedure are comprised in figure 6.8. The fit has been performed for the samples of series Bielefeld with $\mathrm{DL} = 2, 3, 4, 6, 10, 20$. The thickness of the first Co and Cu layer is extraordinary small as can be seen in the graph for $\mathrm{DL} = 2$. This large deviation from the nominal thickness can only be explained with a distinctive feature of the sputtering process: the predeposition phase in the sputter machine *CLAB 600* is performed at low power

---

[2] The XRR fitting study in chapter 4.3.2 has in fact been performed on the double layer variation of series Bielefeld. It it therefore interesting to have a look at the results presented there (pages 54 ff.) in supplemention to those given here.

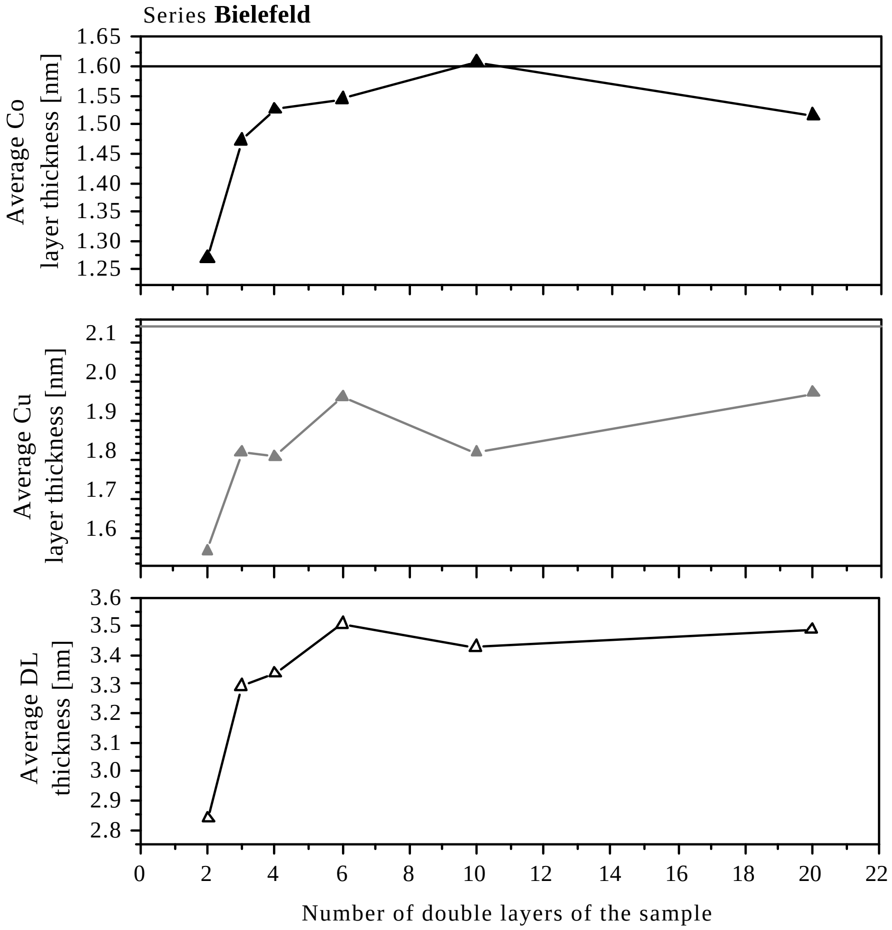

Figure 6.8: Average Co (upper row) and Cu (middle row) layer thickness as a function of the number of double layers of the Bielefeld samples. The values have been determined by a XRR fit of the whole stack. The black line at $d_{Co} = 1.6\,nm$ and the grey line at $d_{Cu} = 2.14\,nm$ mark the nominal thickness values. The sum of the Co and Cu layers is equal to the bilayer thickness which is given in the lower row.

and the machine changes to full power immediately before the deposition of the layer is started. As a consequence, the oxidized surface of the sputter targets is not completely removed and the effective sputter time is reduced for the first layer of each material. Going on in the dicussion of figure 6.8, it can be seen that up to about 4 DL the Co and Cu layer thickness increases and starts to saturate at 6 DL. Since then, the double layer thickness (lower graph) keeps a constant value of $3.5\,nm$. The thickness evolution of the first 5 DL may be explained with a special characteristic of growth which is also reflected in an enhanced interface roughness up to 6 DL and is disussed lateron.

A further characteristic of the Bielefeld samples is the deviating Cu thickness of $1.96\,nm$ compared to the nominal value of $2.14\,nm$. The sputter rate has been calibrated with the XRR method itself and it is therefore hard to see the reason for the reduced thickness of about $0.2\,nm$. In contrast to the Co/Cu multilayers, the calibration samples are made of pure Cu, although sputtered in the multilayer fashion (see chapter 5.1). In principle, there are two aspects which could be responsible for this finding. Firstly, the layers in a Co/Cu multilayer are strained due to coherency stress and this in-plane strain also affects the out-of-plane strain and one might think of this mechanism affecting the thickness of the layer. In the calibration samples of the pure material, there is no coherency stress present. But this mechanism could only explain the inverse effect: the chereny stress of Cu sandwiched in two Co layers leads to thicker instead of thinner Cu. The second explanation pays account for the growth characteristic of a pure and thick Cu layer which can be very different from that inside a multilayer. A single sputtered Cu layer has found to be of polycrystalline fcc type. The multilayers investigated in this comparison study show a strong fcc [111] texture, but the lattice spacing of [111] is smaller than the [100] spacing. Assuming that the number of monolayers grown per time is constant, then the stack of [111] orientation will be thinner than the stack with a considerable fraction of [100] grains. An estimation of size of this texture effect does in fact give a good agreement with the experimental finding. The nominal Cu layer thickness is $2.14\,nm$ which is an average number of monolayer of 8.2 in case of polycrystallinity.[3] Calculating the average layer thickness for a layer with $80\,\%$ [111] grains and $20\,\%$ [100] grains gives $1.96\,nm$, which is exactly the experimentally determined layer thickness. The volume fractions have not been determined for the Bielefeld samples because of the very small [200] peak and therefore the considerations above have to be taken as an estimation. Nonetheless, it becomes clear that the microstructural differences in the Cu layers can in fact account for the thickness. The considerations are also true for the Co layers. Co single layers are of hcp type and polycrystalline but in a multilayer they grow as fcc type. As long as the fcc growth is also polycrystalline, there are only marginal differences in the layer thickness, but when texture comes into account the values also deviate. Consequently, the sputter rate calibration with single layers is not the method of choice for multilayers.

The layer thickness as a function of the double layers of series Jena is given in figure 6.9. Taking a look at the lower row of the graph, it is striking that the average double layer thickness deviates mariginally from the nominal value of $d_{DL} = 3.35\,nm$ and that the maximum difference is only $\Delta t_{DL} = 0.03\,nm$ in the case of 10 double layers. Nonetheless, there is a common feature between series

---

[3] The polycrystallinity is approximated by volume fraction of $33\,\%$ [100], [110] and [111], respectively.

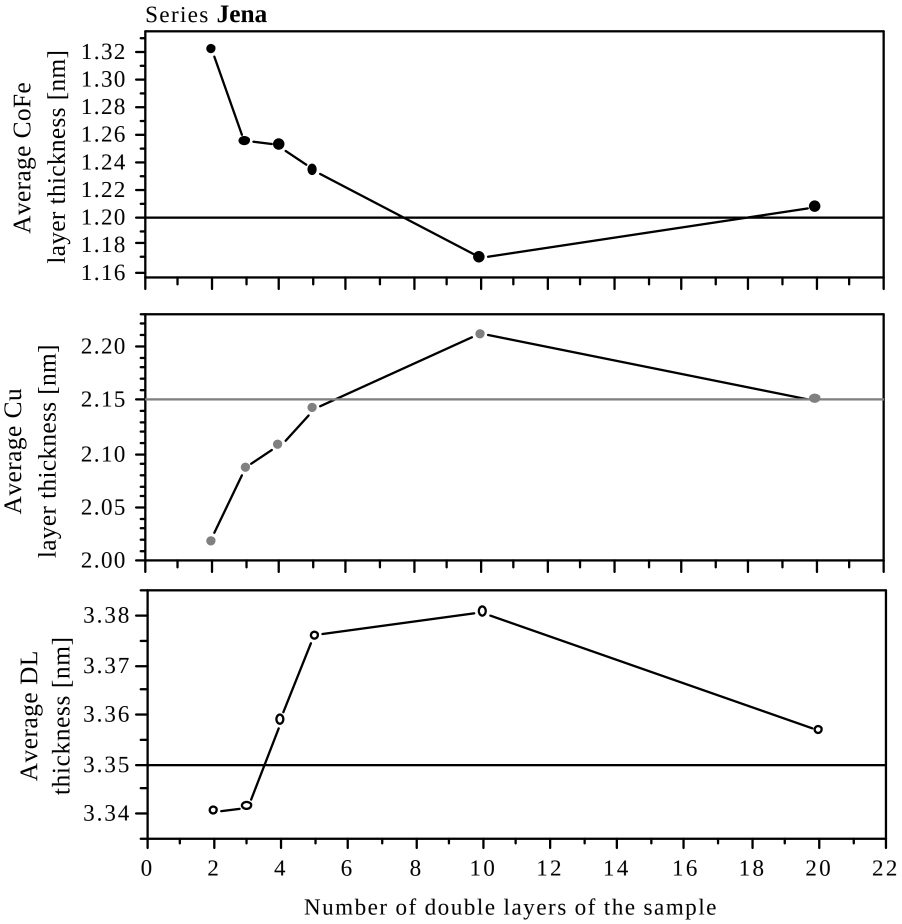

Figure 6.9: Average CoFe (upper row) and Cu (middle row) layer thickness as a function of the number of double layers of the samples of the series Jena. The values have been determined by a XRR fit of the whole stack. The black line at $d_{CoFe} = 1.2\,nm$ and the grey line at $d_{Cu} = 2.15\,nm$ mark the nominal thickness values. The double layer thickness is given in the lower row and the nominal double layer thickness is marked as a black line.

Bielefeld and Jena: the Cu layers up to the fifth double layer are characterized by an increasing thickness, maybe caused by a special growth behaviour. The CoFe layers on the other hand are decreasing in this range of initial growth, a fact which has not been seen for the Bielefeld samples.

Figure 6.10 compiles the XRR fit thickness results of series Bosch I. In contrast to the Bielefeld and Jena samples, the Bosch I series does not have a reduced Cu thickness for the first layers but an increased thickness instead. The maximum deviation from the nominal thickness of $d_{Cu} = 2.21\,nm$ is $\Delta t_{DL} = 0.09\,nm$.

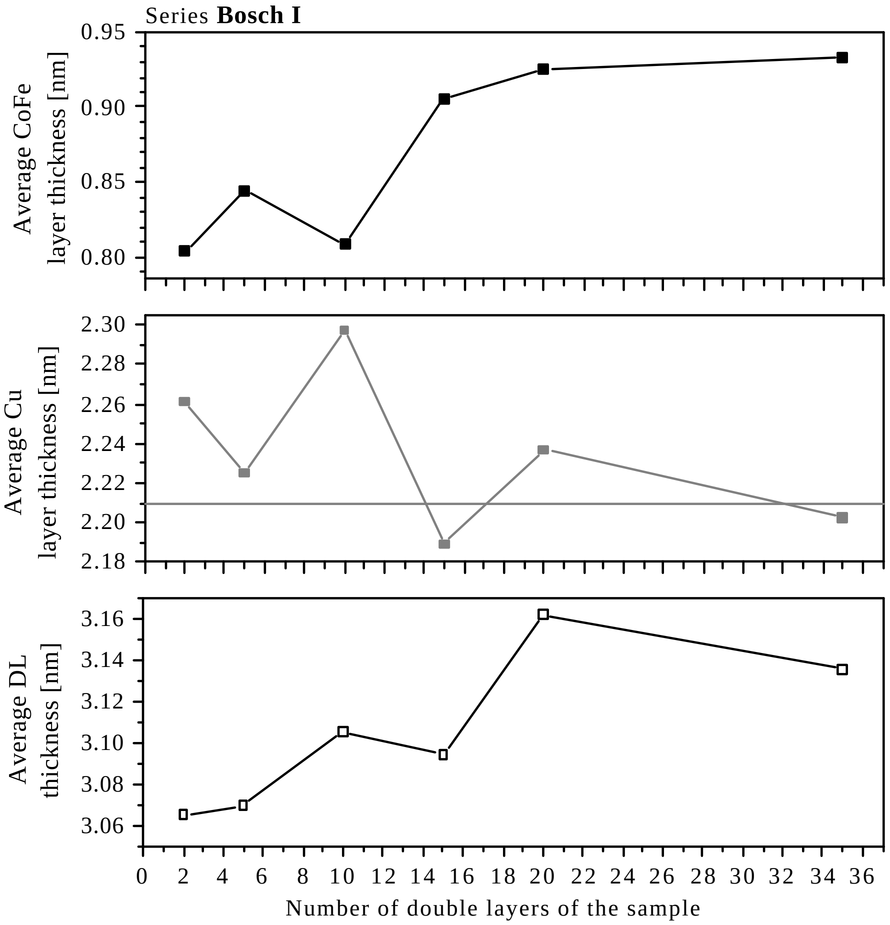

Figure 6.10: Average CoFe (upper row) and Cu (middle row) layer thickness as a function of the number of double layers of series Bosch I. The values have been determined by a XRR fit of the whole stack. The grey line at $d_{Cu} = 2.21\,nm$ marks the nominal Cu thickness and the double layer thickness is given in the lower row.

The CoFe thickness on the other hand does not come together at all with the nominal value of $d_{CoFe} = 1.2\,nm$. The samples with DL $= 2, 5, 10$ have a magnetic layer thickness of 0.80 to $0.85\,nm$ and the samples with DL $= 15, 20, 35$ reach a saturation CoFe thickness of about $0.92\,nm$ which is still about $3\,\text{Å}$ smaller than the nominal value. This striking difference is in agreement with the findings of D. Elefant: evaluating the AGM measurements of series Bosch I, he stated a missing magnetic material of 25 % for each CoFe layer which is exactly $3\,\text{Å}$ [ele01]. Therefore it has to be concluded that the thickness calibration of CoFe is not correct.

Besides the single layer thickness also the interface roughness has been determined via XRR and the results are drawn together for all the three series in

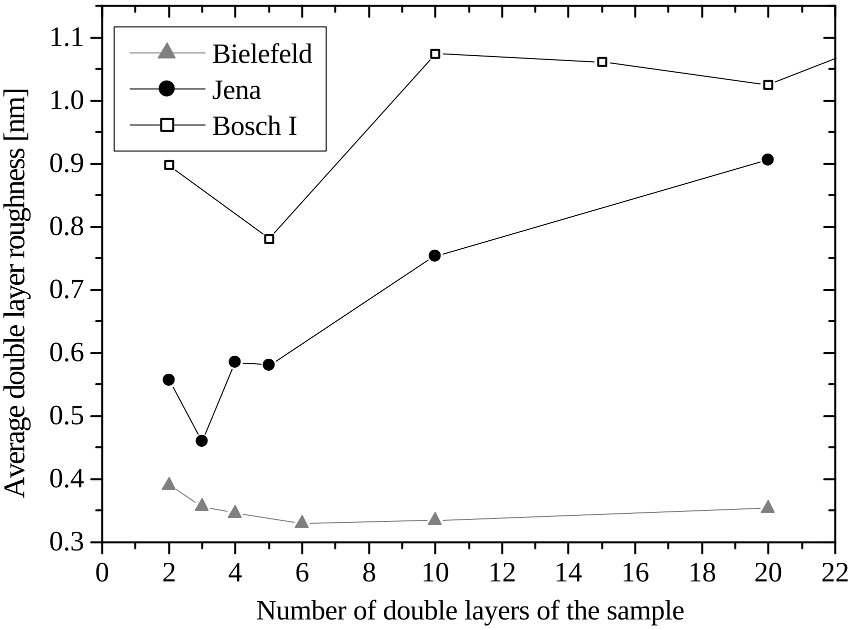

Figure 6.11: Average interface rms roughness as a function of the number of double layers of all series. The values have been determined by a XRR fit of the whole stack and the Co (CoFe) and Cu roughness have been averaged afterwards.

figure 6.11. Due to the delicate roughness determination when fitting a whole stack instead of every single layer, the roughness of the Co (CoFe) and Cu layers has been averaged.

The three series are characterized by very different roughness levels of the interfaces. The samples prepared in Bielefeld have very smooth interfaces with rms roughness $\sigma_{ave}$ in the range of 3.3 to 3.9 Å. In agreement to the different layer thickness of the first 5 double layers, this differing growth characterisitic is also reflected in an enhanced roughness. Samples of series Jena show a clearly larger interface roughness of 5 to 9 Å and an increasing behaviour with the number of double layers. The Bosch I samples are those with the highest interface roughness of 8 to 11 Å and a slight tendency to increase with DL.

Besides the interface roughness there is also the grain size of the samples which may have an influence on the transport characteristics and therefore on the GMR. The crystallite size in growth direction has been determined by analyzing the XRD Bragg peak width and using the Scherrer formula (see chapter 4.2.2). The XRD scans of all samples have a predominant Co/Cu and CoFe/Cu fcc [111] peak respectively, but only a small [200] peak. It is therefore only the [111] peak width which has been determined in order to calculate the crystallite size and the results for all series are drawn together in figure 6.12. In the upper graph of the figure the absolute values of crystallite size are given.

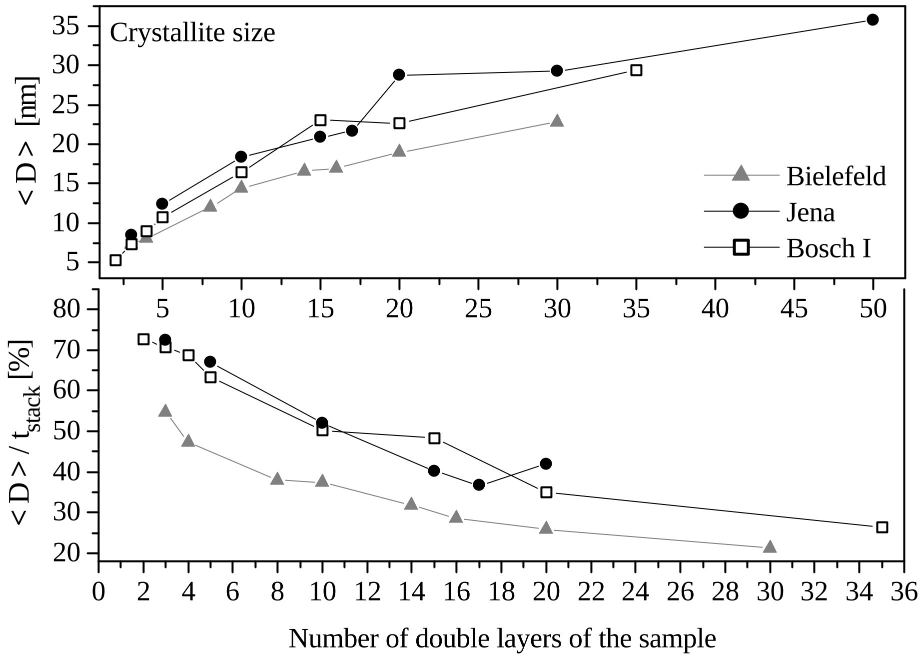

Figure 6.12: Crystallite size $\langle D \rangle$ in growth direction as a function of the number of double layers of all series. In the upper graph the absolute values as determined by the Scherrer formula of the [111] XRD peak are given. The fraction of the crystallite size compared to the thickness $t_{stack}$ of the whole layer stack is shown in the lower graph.

The total thickness of the layer stack is different for the three series and it is interesting to compare the proportion of grain size to the total stack thickness, which has already been precisely determined in the XRR fit. This percentage grain size is given in the lower graph of figure 6.12.

The comparison of the absolute grain size in growth direction of all series makes clear that Jena and Bosch I samples have larger grains than the series Bielefeld. This picture becomes even clearer when taking a look at the percentage grain sizes: having sputtered 3 double layers, the grains of the Jena and Bosch samples are as large as more than 70 % of the whole stack whereas the Bielefeld grains have only 55 % of the stack thickness. With increasing number of double layers the absolute crystallite size increases for all series but the percentage size values are decreasing. It is striking for the complete range of double layer variation that the absolute and percentage grain sizes of Jena and Bosch are approximately equal whereas these values are considerably smaller for the Bielefeld samples.

The microstructural characterization concerning interface roughness and crystallite size does a priori not give a clear correlation to the GMR effect ampli-

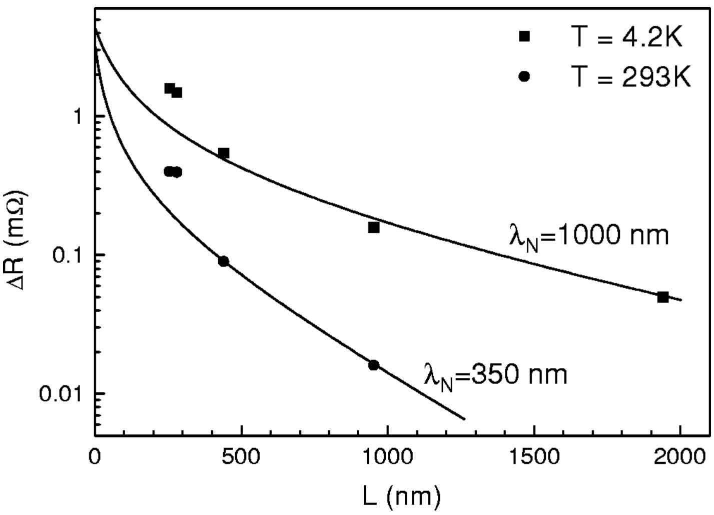

Figure 6.13: Spin signal $\Delta R$ as a function of the distance $L$ between two Py electrodes of a mesoscopic patterned $Py/Cu/Py$ spin valve. $\lambda_N$ is the spin-flip length in the Cu spacer at 4.2 and $293\,K$, respectively (from [jed01]).

tude and makes clear that it is not a single parameter which determines the GMR potential. It is whether the smallest roughness like that of the Bielefeld samples which yields the highest GMR nor the largest crystallite size as the contradictory GMR results of Jena and Bosch I prove. Therefore, the results have to be discussed on the basis of spin-dependent scattering inside the multilayer.

In chapter 3 the optimum conditions for large GMR values have been discussed. In general, the electrical resistivity in parallel magnetic configuration of a sample has to be small in order yielding a small denominator in the calculation of GMR. Therefore, all contributions to spin-independent scattering such as lattice dislocations and grain boundaries should be as few as possible. On the other hand, the spin-dependent scattering has to be as large as possible in order to have a large nominatior in the calculation of the GMR. It is therefore the relationship between spin-flip length and mean free path of the electrons in the nonmagnetic layer which plays the crucial role.

Jedema *et al.* have studied the spin valve signal $\Delta R$ of a mesoscopic patterned Py/Cu/Py spin valve [jed01]. They found the spin-flip length in Cu at room temperature to be as large as $\lambda_N = 350\,nm$ whereas it is $1\,\mu m$ at $4.2\,K$. The variation of the distance $L$ between the Py electrodes in the range of $250\,nm$ to $2\,\mu m$ revealed a $1/L$ dependence of the spin signal $\Delta R$, which is depicted in figure 6.13.

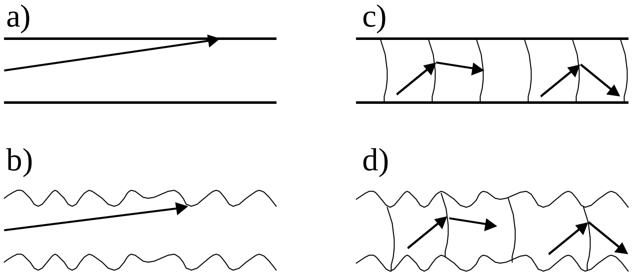

Figure 6.14: Comparison of scattering mechanisms in spacer layers of different microstructure. a) Without the presence of grain boundaries and roughness the distance $L$ the electron travels through the spacer is large. b) Rough interfaces will reduce $L$. c) In spacers with many grain boundaries $L$ depends on the scattering mechanism: diffuse scattering (left) can either enhance or reduce $L$, whereas specular scattering (right) effectively reduces $L$. d) In the presence of many grain boundaries (or other dislocations which trigger the scattering) rough interfaces have a marginal effect on $L$.

How do these results have to be transferred to the scattering mechanism in a multilayer? In Cu layers without dislocations and grain boundaries the spin-flip length $\lambda_N$ is supposed to be very large which is a favourable property due to the reduction of residual resistivity. The distance $L$ is equivalent to the distance an electron travels through the nonmagnetic layer from one magnetic layer to the next. This value will become large when the interfaces are perfectly smooth, which is depicted in figure (6.14 a). Unfortunately, a large value of $L$ will reduce the fraction of spin-dependent scattering. Therefore, the presence of roughness which reduces $L$ is more favourable than perfectly smooth interfaces (graph b in figure 6.14).

The spin-flip length $\lambda_N$ in the Cu layers depends on the number of scattering events inside the layer, because the spin will flip after a given number of non-spin-flip scattering events. The presence of dislocations and grain boundaries will reduce the spin-flip length drastically (graph 6.14 c). Figure 6.13 makes clear that the disadvantage of a small $\lambda_N$ can be overcome by a small value of $L$. But this demand is not so easy to be fulfilled for example by the presence of interface roughness because the scattering at dislocations and grain boundaries has to be also considered. The optimum property of these scattering events is specularity[4] in order to move the electrons inside the magnetic layers on the shortest way possible. Specular scattering has been discussed in the literature for many years and it is known to occur when the atomic ordering is disturbed only little. Because twins are those growth discontinuities which disturb the atomic ordering least, they should be the ideal trigger for specular scattering.

---

[4] A scattering event is called *specular* when the electron momentum in field direction is conserved.

Interface roughness on the other hand should play a minor role in the case of many discontinuities in the layers (graph d in figure 6.14). Put the other way round, in the presence of many dislocations and grain boundaries the interface roughness should be small in order to avoid its disadvantages such as loose spins and orange peel coupling.

Coming back to the present laboratory study, the microstructural results can be interpreted in the following way. In the presence of many double layers, the Bielefeld samples suffer from their fine grained microstructure resulting in a small value for $\lambda_N$. Nonetheless, the GMR effect values are quite good and it has to be concluded that the fraction of spin-dependent scattering is large. The very low interface roughness of these samples is a property which surely promotes this effect. In the case of only few double layers, the interface smoothness is supposed to be an advantage which cannot be seen here in comparison to the other series because of the wrong layer thickness of the first double layer. Series Jena is characterized by a very good combination of large crystallites and optimum roughness, i. e. large $\lambda_N$ and small $L$. This is in contrast to series Bosch I which also has large crystallites but interfaces that are far too rough.

It should be mentioned at last that besides the reduction of residual resistivity, large grains are supposed to mediate the antiferromagnetic exchange coupling more effectively than small grains because the electron standing waves spread out undisturbed.

### 6.6.3 Discussion of the Double Layer Variation Series

The microstructural features of the series have already been discussed and now the conclusions of all results concerning the double layer variation are drawn.

Samples of series Jena yield the highest GMR amplitudes for every number of double layers larger than 2. The microstructural characterization has revealed two decisive properties which can explain this finding. Firstly, the thickness of every layer of the stack does marginally fluctuate around the nominal value. Secondly, the advantage of large crystallite size is ideally combined with the presence of interface roughness. The only question left to answer is why the sample with only 2 double layers does not show antiferromagnetic exchange coupling. For the first 2 double layers a larger deviation concerning the Co and Cu thickness as well as a slightly enhanced roughness has been detected. These aspects characterize an initial growth process and seem to be the reason for the missing AF coupling. The special case of very few double layers is treated in the next chapter, but one may assume that in the case of only 2 double layers it is a good idea to choose a thicker buffer layer as well as slightly thicker magnetic layers to optimize the growth behaviour as well as the transport characteristics.

Series Bielefeld is handicapped by its first Cu layer which is far too thin for AF coupling. Furthermore, the GMR does not start with 3DL but with 4DL. Although the roughness of the first 3 double layers is enhanced, the values are small compared to Jena and cannot explain the missing AF coupling. Maybe it is a special feature of initial growth which hardens the establishment of the AF coupling, for example because of very small crystallites. Due to the non AF coupled first grown layers, the samples have an extended buffer which acts as a shunting and therefore reduces the GMR effect amplitude of all samples. Supposing the first double layer to have the correct Cu thickness and therefore the AF coupling to start one DL earlier, the Bielefeld data in figure 6.4 would be on the same level as Jena for the first 3 DL. Furthermore, taking into account the shunting in the present data, the Bielefeld GMR should be even higher than the Jena GMR, at least up to 3 or 4 DL. Despite of these considerations, the series Bielefeld does not reach the same level as series Jena in the presence of more than approximately 8 double layers. The explanation for this finding is the optimum microstructure of series Jena concerning residual resistivity and spin-dependent scattering.

The samples of series Bosch I have the lowest GMR effect amplitude for every number of double layers. This finding has to be explained with the very large interface roughness of the samples. One one hand, the AF coupling is clearly reduced which is reflected in the need for at least 4 DL to yield AF coupling. On the other hand, on this roughness level the presence of loose spins is most probable which reduce the spin-dependent scattering.

## 6.7 Conclusions

The scope of this laboratory all-embracing Co/Cu multilayer GMR study was to identify the ideal microstructure that yields large GMR effect amplitudes. The comparison of the different sample series has made clear that there are numerous contributions to the GMR effect and it was the variation of the number of double layers of each series that has given the deepest insight into the interplay between microstructure and GMR. The interdependence cannot be restricted to one single parameter of the microstructure. Whether the crystallite size nor the interface roughness alone determines the GMR potential of a multilayer but the right combination of both aspects.

The combination of large grains with moderate interface roughness as realized in the series Jena has been found to be an ideal candidate for good GMR. But the presence of smaller grains is not much worse if the interface roughness is also smaller. In case of the series Bielefeld, the fine grained polycrystalline structure shows a large fraction of spin-dependent scattering, a fact which surely cannot be transferred to any fine grained sample. The spin-dependent scattering depends sensitively on the kind of dislocation and specular scattering is supposed to be the ideal case.

The fact that large crystallites are no guarantee for large GMR is proven by series Bosch I. Although the grain size in growth direction is approximately identical to series Jena, samples of series Bosch I obtain much smaller GMR amplitudes. The very large interface roughness has been found to be the most probable explanation for this finding. Samples of series Bosch II are the ones with lowest GMR amplitude in this comparing study and this finding does not seem to be mainly the result of using the alloy CuAgAu instead of pure Cu but the result of nonideally chosen layer thickness. Firstly, figure 6.1 reveals that the choice of $t_{CuAgAu} = 2.21\,nm$ for the reference system would yield 21 % instead of 17 % for $t_{CuAgAu} = 2.27\,nm$, although the latter thickness should yield about 20 % when interpolating the neighbouring data points. Therefore, it is the wrong choice of the Fe buffer thickness, see figure 6.3, which has more severe consequences. Using a reference system with a buffer of $2.18\,nm$ Fe thickness instead of $t_{Fe} = 1.31\,nm$ would yield 21.5 % GMR effect amplitude instead of 17 %. Finally it has to be concluded that series Bosch I and Bosch II should give approximately the same GMR results if their reference layer stacks would be optimized equally well.

The considerations concerning the quality of series Bosch II reveal a further important finding of the laboratory comparison study: it is especially the layer thickness of the samples which has to be very well controlled in order to yield large effect amplitudes. It is a surprising result that despite accurately performed thickness calibration methods the series Bielefeld and Bosch I suffer from wrong thickness calibrations. This is why samples prepared in Bielefeld give away the first double layer and series Bosch I and II have a slightly too thin magnetic layer.

The interface roughness is one of the microstructural characteristics that determines the GMR potential of a multilayer and has become visible in the variation of each parameter.

Varying the spacer layer thickness in the range of the second AFCM revealed slightly differing peak positions for the four sample series. Figure 6.1 has to be corrected with regard to the spacer thickness of series Bielefeld. The microstructural analysis made clear that the Cu layers miss about $0.2\,nm$ and therefore the Bielefeld curve in figure 6.1 has to be shifted to the left by this amount. Doing this clearly distinguishes series Bielefeld from the other three. Speaking in terms of increasing spacer thickness, GMR is detected first for those samples which have the smallest interface roughness. This has to be explained with the sensitivity of antiferromagnetic exchange coupling. On one hand, interface roughness can disturb the standing electron waves which are responsible for the interlayer coupling and on the other hand, roughness can promote ferromagnetic exchange coupling by the mechanism of orange-peel.

The results of Parkin *et al.* agree the most with series Bielefeld [par91b]. Firstly, the spacer thickness of the second AFCM is about $1.9\,nm$ in both cases and secondly, the maximum GMR samples of both series yield the same effect amplitude of approximately $25\,\%$ in the presence of 16 double layers (see figure 6.4).

The interface roughness study of Paul *et al.* reveals a decrasing interface roughness the more bilayers are grown on the stack with $t_{Cu} = 2.20\,nm$. Up to $3\,DL$ the rms roughness of their layers is $0.9\,nm$ and yields about $5\,\%$ GMR amplitude. This value is quite large compared to the series Bosch I having about the same interface roughness. Increasing the bilayer number to 20 reduces the interface roughness to $0.54\,nm$ and enables the GMR to reach $20\,\%$ which is clearly smaller than series Bosch I. These findings emphasize to resume that it is not the crystallite size nor the interface roughness alone which determine the GMR of a multilayer but the right combination of both aspects. In the present case of Paul *et al.* the crystallite size has not been analyzed but the results might be interpretend in the way that large roughness values fit well to the grain structure of the first double layers because the transport properties are not enhanced with decreasing interface roughness, although the AF coupling has been proven to become much stronger [pau03].

Varying the magnetic layer thickness yielded best GMR amplitudes for the Bielefeld samples for very thin Co layers whereas the Jena samples were the best ones for $t_{CoFe} > 0.8\,nm$. This behaviour can also be explained with the smaller roughness of the Bielefeld samples which establish the magnetic layer scattering properties with thin Co already, whereas in this range the interface roughness of the Jena samples is larger than the layer thickness.

The buffer thickness variation has found to be hardest to explain but this is not too surprising because the buffer layer determines the growth conditions for the rest of the layer stack. Therefore the variation of buffer layer thickness will influence more than one microstructural characteristic. Whether the use of a buffer layer enhances the GMR and if so at which thickness this will happen depends on the preparation conditions, layer materials and thickness and does not follow a universal rule.

In the literature, the variation of buffer layer thickness has often shown to determine the interface roughness, for example by Lenczowski and coworkers [len94]. Using a Cu buffer of $20\,nm$ they obtained a GMR amplitude of $48\,\%$ at first AFCM. Enhancing the buffer thickness to $30\,nm$ led the GMR break down to $5\,\%$. They investigated the roughness of a 4 bilayer stack in both cases and found the surface roughness to be $0.5\,nm$ in the case of the $20\,nm$ buffer whereas it was $1.2\,nm$ when growing the $30\,nm$ Cu buffer. On the other hand, the buffer thickness had only marginal influence on the GMR at second AFCM. This example together with the investigations in this thesis make clear, that the interplay between microstructure and GMR is too complex to be reducable to only one parameter. Nonetheless, the interface roughness has been extensively studied because it has been supposed to be the crucial parameter.

Tsymbal and Pettifor give a review of the numerous interface studies performed on Fe/Cr and Co/Cu multilayers [tsy01]. Their survey of results makes clear that when speaking of interface roughness one has to carefully distinguish between atomic roughness and interdiffusion and furthermore, that atomic roughness has to be classified concerning amplitude and correlation length. But even the correct description of roughness does not enable a universal interdependence of roughness and GMR. Especially the comparison of Fe/Cr to Co/Cu multilayers gives opposing results: many researchers observed an enhancement of GMR in Fe/Cr systems with increasing roughness whereas this could not be confirmed for the Co/Cu samples. Tsymbal and Pettifor propose a significant change in the magnetic state of the Co atoms in the intermixed regions, the so called misaligned or “loose” spins. Nonetheless, the reduction of interface roughness does not guarantee the enhancement of GMR. This fact is proven not only in the present investigation but also e. g. by Christides *et al.*[5]

---

[5] Christides *et al.* performed a Co thickness variation from 0.8 to $3.1\,nm$ in the system $Si(100)/SiN_{100\,nm}/[Co_{t_{Co}}/Cu_{2.1\,nm}]_{30}/Co_{t_{Co}}$ and observed a decreasing GMR from 7 to 2 % with Co thickness although the roughness decreased from 0.9 to $0.3\,nm$ [chr98].

# Chapter 7

# From Multilayers to Trilayers

The double layer variation of the Co/Cu multilayer comparison study in chapter 6.6 revealed that the GMR amplitude of a multilayer decreases rapidly when the number of double layers is decreased below 10. The magnetic measurement of those samples made clear that the first layers grown on the substrate are not or only weakly antiferromagnetically coupled. On the other hand, in our laboratory we have sputtered trilayers of type $\{Py/Co/Cu/Co\}$ which show three distinct antiferromagnetic coupling maxima having GMR amplitudes of 15, 11 and 7 % for the first, second and third AFCM, respectively [hue02]. Those trilayers consist of only two magnetic layers and therefore should be equivalent to a multilayer stack with 2 double layers. But those multilayers in series Bielefeld, Jena and Bosch do not have a significant GMR effect at all as figure 6.4 has proven.

In the literature it is not clear up to now whether there is a principal difference between a trilayer and multilayer with only 2 double layers. In the previous chapter the question has been answered which microstructural feature are favourable for large GMR amplitudes. In this chapter the question shall be answered "what happens on the way from multilayer to trilayer?".

The experimental idea to find an answer to this question was to optimize the layer system for every given number of double layers, starting with a multilayer having 20 double layers, and to see whether there is a potential for GMR enhancement. If the answer is yes, then the crucial point is whether the thickness optimization is systematic and on which physical mechanism it is based.

## 7.1 Double Layer Optimization

In series Multi 1 the multilayer stack Py/[Co/Cu]$_\mathrm{n}$ has been optimized for five different double layer numbers $n = 20, 10, 6, 3, 2$. Starting with $n = 20$, the

Cu layer thickness was varied first, followed by the Co and the Py buffer layer thickness. Taking the system with largest GMR effect from this variation, the same procedure was performed for $n = 10$ and so on for $n = 6$ to $n = 2$. The sputtering conditions can be found in chapter 5.1, table *Multi 1*.

**Multi 1**

glass // $\mathrm{Py_z}$ / [ $\mathrm{Co_y}$ / $\mathrm{Cu_x}$ $]_\mathrm{n}$

Variation of $x, y, z$ for $n = 20, 10, 6, 4, 3, 2$.

The result of the variation i. e. the multilayer stack which yielded the highest GMR amplitude for the given number of double layers is given below:

$$\mathrm{Py}_{\,3.4\,\mathrm{nm}} \;/\; [\;\mathrm{Co}_{\,1.3\,\mathrm{nm}} \;/\; \mathrm{Cu}_{\,1.98\,\mathrm{nm}}\;]_{\,20}$$
$$\mathrm{Py}_{\,3.4\,\mathrm{nm}} \;/\; [\;\mathrm{Co}_{\,1.3\,\mathrm{nm}} \;/\; \mathrm{Cu}_{\,1.88\,\mathrm{nm}}\;]_{\,10}$$
$$\mathrm{Py}_{\,5.5\,\mathrm{nm}} \;/\; [\;\mathrm{Co}_{\,1.5\,\mathrm{nm}} \;/\; \mathrm{Cu}_{\,1.98\,\mathrm{nm}}\;]_{\,6}$$
$$\mathrm{Py}_{\,3.4\,\mathrm{nm}} \;/\; [\;\mathrm{Co}_{\,1.5\,\mathrm{nm}} \;/\; \mathrm{Cu}_{\,2.03\,\mathrm{nm}}\;]_{\,4}$$
$$\mathrm{Py}_{\,5.5\,\mathrm{nm}} \;/\; [\;\mathrm{Co}_{\,2.0\,\mathrm{nm}} \;/\; \mathrm{Cu}_{\,2.03\,\mathrm{nm}}\;]_{\,3}$$
$$\mathrm{Py}_{\,5.5\,\mathrm{nm}} \;/\; [\;\mathrm{Co}_{\,2.0\,\mathrm{nm}} \;/\; \mathrm{Cu}_{\,2.03\,\mathrm{nm}}\;]_{\,2}$$

In figure 7.1 the GMR amplitude of these optimized multilayers is compared with the double layer variation of the series Bielefeld and Jena, both series known from chapter 6.6. The results prove that the layer thickness of a multilayer system has to be adjusted when the number of double layers is changed in order to yield best GMR values. Doing this, the GMR amplitude is considerably enhanced and even the multilayer with only two double layers reaches 8.4 % GMR. Taking the value of 20 % GMR as a measure, the series Bielefeld needs 10 double layers to reach this level whereas the series Multi 1 manages this with only 6 double layers. Comparing series Multi 1 with series Jena which gave the best results in the laboratory comparison, makes clear that up to 6 double layers the optimization concept is superior.

Because the double layer optimization gave very good results especially for multilayers stacks of up to 10 double layers the question arose whether further GMR enhancement is possible. The variation of series Multi 1 was restricted to the parameters $x, y, z$ but alternatively, more layers in a multilayer can be separately varied. Unfortunately, the optimization of every layer is much too lavish, especially for a system with many double layers. Furthermore, when each magnetic layer in the system has a different thickness, the resulting multilayer has a very different character because of the different switching fields of the layers. Therefore, in a second optimization series called Multi 2 the number of parameters was increased by only 1: the first Co layer has been

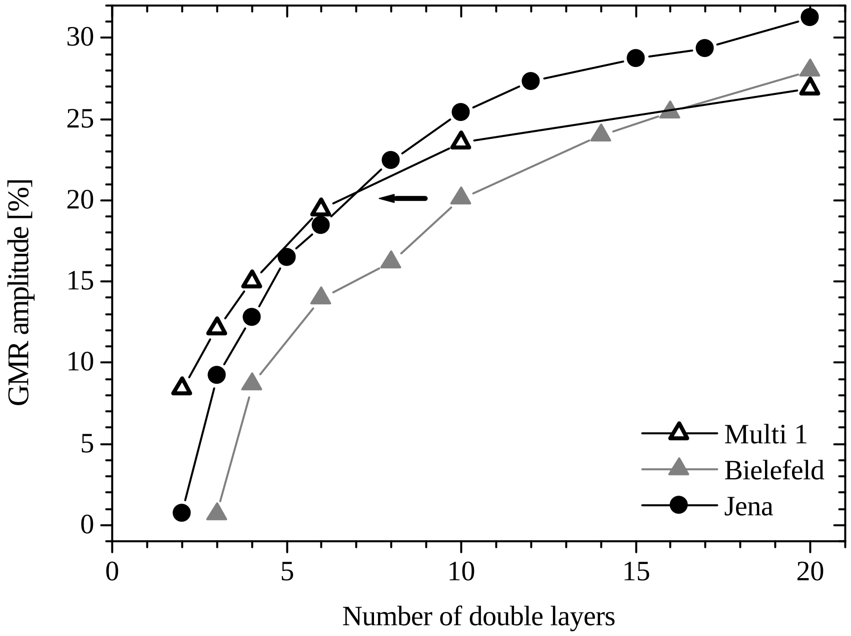

Figure 7.1: GMR amplitude as a function of the number of double layers. Series Multi 1 has been optimized for the given number of double layers. The graph compares the resulting GMR amplitude with those of series Bielefeld and Jena. In these series only the layer stack with 20 double layers had been optimized.

varied separately for three multilayer systems with 6, 4 and 2 double layers, respectively. Such a stacking sequence still has the character of a multilayer and the hypothesis of further potential of enhancement can also be proven. The sputtering parameters for these samples can be found in chapter 5.1, table *Multi 2*.

**Multi 2**

glass // $\mathrm{Py_z}$ / $\mathrm{Co_{y1}}$ / [ $\mathrm{Cu_x}$ / $\mathrm{Co_{y2}}$ $]_\mathrm{n}$

Variation of $x, y1, y2, z$ for $n = 5, 3, 1$

The multilayers with highest GMR amplitude of the variation series are given below and the corresponding GMR amplitude is depicted in figure 7.2.

$$\begin{array}{l}
\mathrm{Py}_{\,3.7\,\mathrm{nm}} \;/\; \mathrm{Co}_{\,2.0\,\mathrm{nm}} \;/\; [\;\mathrm{Cu}_{\,2.02\,\mathrm{nm}} \;/\; \mathrm{Co}_{\,1.6\,\mathrm{nm}}\;]_{\,5} \\
\mathrm{Py}_{\,3.7\,\mathrm{nm}} \;/\; \mathrm{Co}_{\,1.6\,\mathrm{nm}} \;/\; [\;\mathrm{Cu}_{\,2.02\,\mathrm{nm}} \;/\; \mathrm{Co}_{\,2.0\,\mathrm{nm}}\;]_{\,3} \\
\mathrm{Py}_{\,3.7\,\mathrm{nm}} \;/\; \mathrm{Co}_{\,2.9\,\mathrm{nm}} \;/\; [\;\mathrm{Cu}_{\,2.12\,\mathrm{nm}} \;/\; \mathrm{Co}_{\,2.9\,\mathrm{nm}}\;]_{\,1}
\end{array}$$

The sample with 2 double layers denoted by $n = 1$ is the “original” trilayer. The samples with 4 and 6 double layers reveal higher GMR amplitudes than

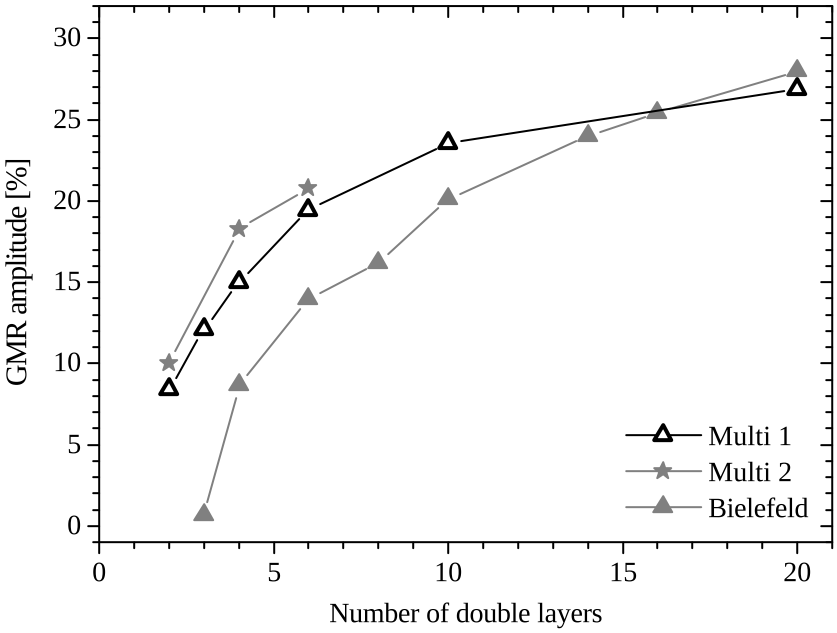

Figure 7.2: GMR amplitude as a function of the number of double layers. Series Multi 1 and Multi 2 have been optimized for the given number of double layers. Furthermore, in series Multi 2 one additional layer thickness parameter has been varied.

the corresponding samples of series Multi 1 and thus prove the thesis of further enhancement potential.

The increase in GMR effect obtained in both variation series Multi 1 and Multi 2 is based on the same mechanism: the more layers build up the multilayer stack the more their thickness has to be reduced. Put the other way round, the less double layers a multilayer contains, the more the layer thickness has to be increased. The reason for the first formulation is the shunting effect. When the antiferromagnetic coupling is established and the whole layer stack is thick enough to enable sufficient spin-dependent scattering, then the shunting plays a crucial role. On the other hand, when the number of layers of the stack is drastically reduced, shunting plays a minor role. In this case it is most important to yield antiferromagnetic coupling as well as optimum conditions for spin dependent scattering. As a consequence, the thickness of all layers has to be chosen very carefully. Firstly, the spacer thickness has to guarantee the AF coupling. Secondly, the magnetic layers have to be thick enough to reduce the outer boundary influence and to yield enough spin-dependent scattering.

Furthermore, the laboratory comparison study in the previous chapter revealed an initial growth mechanism which has not been cleared up in detail. But the proper choice of the buffer layer is an additional parameter to yield optimum scattering conditions. The interface roughness is a sensitive parameter in the case of only few layers and it can be stated, that the layers have to be very smooth in order not to disturb the AF coupling.

## 7.2 Buffer Layer Optimized Multilayers

The results of the series Multi 1 and Multi 2 give the general recipe how to obtain high GMR amplitudes in case of a multilayer stack with a few or with many double layers. The magnetic characterization of the multilayers in chapter 6 made clear that in a multilayer stack of 20 double layers with large GMR amplitude a number of layers directly grown on the buffer are weakly coupled. The question is, whether the GMR amplitude of such a multilayer could be enhanced when building the stack up of optimally coupled double layers. In order to test this proposal sophisticated layer stacks have been sputtered of type $\mathrm{Py_z/[Co_{y1}/Cu_x]/[Co_{y2}/Cu_x]/[Co_{y3}/Cu_x]/}$... with $y1 > y2 > y3$.... No further increase of the GMR effect amplitude has been achieved with these stacking sequences. On the contrary, due to the differing magnetic layer thickness in the stack the samples have lost their multilayer switching characteristic and showed different switching fields.

Despite of the fact of non-multilayer type GMR characteristic it is not clear to see a priori why no GMR enhancement could be achieved. In order to make a further test concerning this finding a comparison study of two double layer variation series has been performed. The first series starts with an AF-coupled trilayer having 5 % GMR amplitude. The second series differs from the first one only by a thinner buffer layer of $3.4\,nm$ instead of $8.1\,nm$, but the sample that corresponds to the AF-coupled trilayer does not show GMR. The GMR characteristic of both samples is shown in the inset of figure 7.3. The stacking sequence of both series is given beow and the sputter parameters are identical to those of series *Multi 1*.

| |
|---|
| glass/ $\mathrm{Py_{8.1\,nm}/[Co_{1.1\,nm}/Cu_{2.0\,nm}]_n}$<br>$n = 1, 2, 3, 4, 5, 6, 8, 10, 14, 16, 20.$ |
| glass // $\mathrm{Py_{3.4\,nm}/[Co_{1.1\,nm}/Cu_{2.0\,nm}]_n}$<br>$n = 1, 2, 3, 4, 5, 6, 8, 10, 14, 16, 20.$ |

It is most probable to assume that the magnetic layers of the non-GMR trilayer are not antiferromagnetically coupled, a statement which is based on the results of the laboratory comparison study of the previous chapter. Concerning the amount of AF-coupling the sample series which is based on the AF-coupled trilayer has a clear advantage. Figure 7.3 compares the GMR amplitude of the

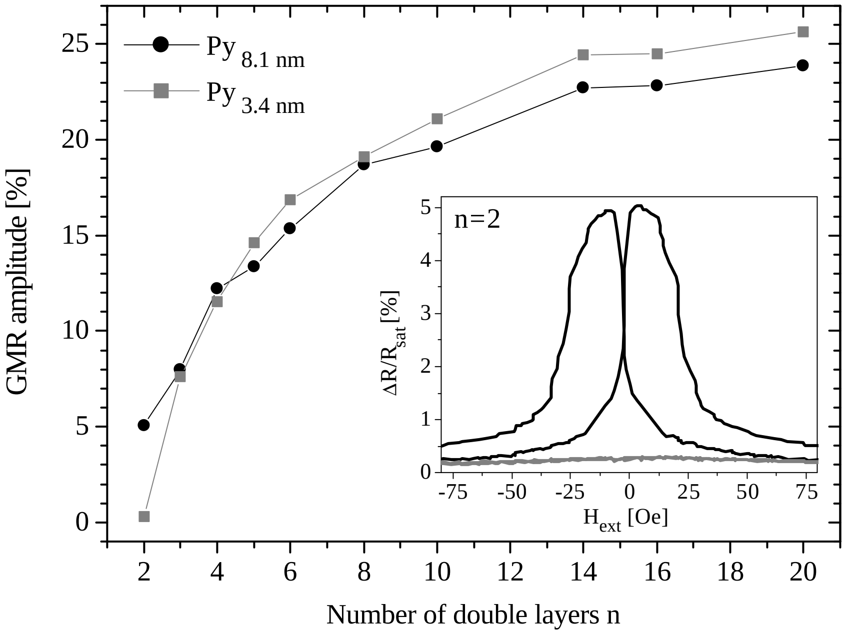

Figure 7.3: GMR amplitude as a function of the number of double layers of the series $Py_z/[Co_{1.1\,nm}/Cu_{2.0\,nm}]_n$ with $z$ being 3.4 and 8.1 $nm$, respectively. The 3.4 $nm$ buffer has been optimized for 20 double layers whereas the 8.1 $nm$ buffer is suited for the trilayer system $Py/Co/Cu/Co$.

series as a function of the number of double layers. It is astounding to see that with only one bilayer additionally grown on the trilayer stack the difference in GMR of both series becomes marginal. In the range of 4 to 5 double layers the slope of the series cross each other and the samples that started with the uncoupled trilayer yield larger effect amplitudes. Having sputtered 20 bilayers for both stacks the difference in amplitude is 26 to 24 %.

The conclusions of the sophisticated multilayer stacking and of the buffer layer optimized comparison study are the following. The enhancement of AF coupling in the undermost bilayers by increasing the buffer layer thickness and / or the thickness of the bilayer is a successful concept to obtain larger GMR amplitudes as long as the number of double layers remains small. This concept fails when sputtering a large number of bilayers because the shunting of the thicker buffer or bilayer compensates or even destroys the effect of a larger AF-coupled layer fraction.

# Chapter 8

# Temperature Stability and Recrystallization

The evolution of GMR with increasing temperature is one of the main points of interest for technical application. Equivalently to the results concerning the GMR itself, even the temperature stability of the multilayers depends to some extent on the manufacturing process.

Zhang *et al.* [zha94] found that multilayers at the second AFCM with a Cu thickness of $2.17\,nm$ but thin Co layers of $1.15\,nm$ start to decrease in GMR when annealed at $250°C$ for four hours. In the course of annealing the GMR amplitude passes a maximum before the deterioration starts. Samples of the same series with thinner Cu show a loss of GMR amplitude at lower temperatures.

Multilayers with thicker Co have been found to be more temperature stable, as the results of Ebert *et al.* [ebe03a], Małkiński *et al.* [mal00] and Rätzke *et al.* [rae99] show: these groups tested multilayers with Co thickness of $1.5\,nm$ and did not find a significant decrease of the initial GMR amplitude after annealing up to $320°C$ [ebe03a], $350°C$ [rae99] and $380°C$ [mal00] respectively. All groups documented a considerable increase in GMR which they draw back to a reduction of defect density and improvement of homogeneity of magnetic structure.

The temperature stability of Co/Cu multilayers sputtered in our laboratory fit quite well to these results: Samples of the type $Py_{2.1\,nm}/[Cu_{2.0\,nm}/Co_{1.3\,nm}]_{60}$ have been annealed in successive steps of increasing temperature up to $450°C$. In each step the annealing temperature has been increased by $25°C$. The annealing time of one step was 20 minutes and after each step the sample was cooled down to room temperature in order to measure its magnetoresistance. The evolution of the GMR amplitude during this annealing procedure is shown

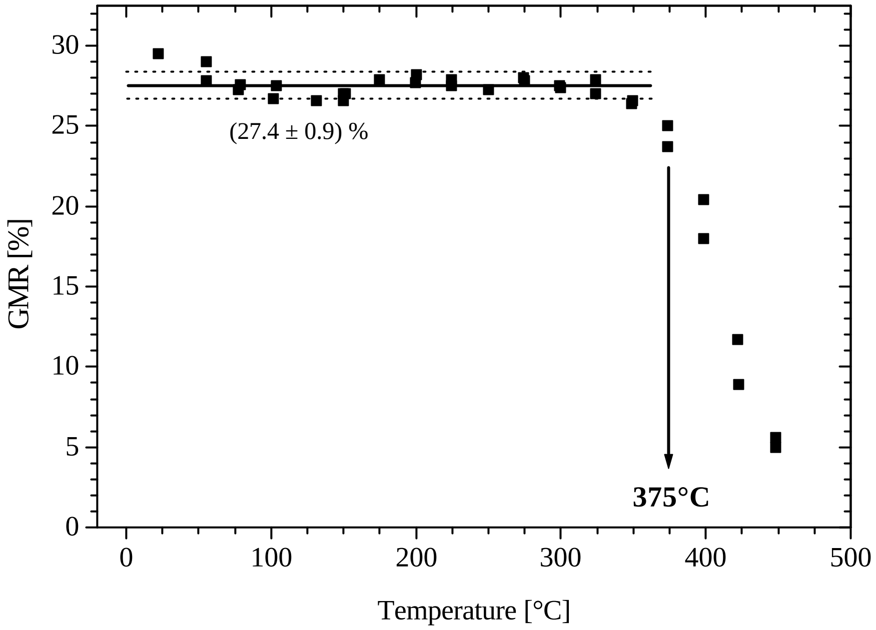

Figure 8.1: GMR amplitude of the sample $Py_{2.1\,nm}/[Cu_{2.0\,nm}/Co_{1.3\,nm}]_{60}$ at room temperature after successive annealing in steps of $25°C$ for 20 minutes each.

in figure 8.1. In contrast to the groups mentioned above, we did not find a significant increase of the GMR at moderate temperatures but a relatively stable value of $(27.4 \pm 0.9)\,\%$ GMR up to $350°C$. At $375°C$ the GMR starts to decrease significantly.

All results concerning the temperature stability presented so far are confirming a short time stability. For sensor applications in hot environments on the other hand e. g. in automotive industry, the multilayers must resist temperatures $200°C \leq T \leq 360°C$ in the course of manufacturing as well as temperatures in the range $150°C \leq T \leq 200°C$ during 40000 hours of operation. The multilayers mentioned above do not fulfill this need: Ebert *et al.* [ebe03b] performed lifetime tests of Co/Cu multilayers and they predict a lifetime of only 9300 hours at constant temperature of $150°C$. An alternative choice of the working point increases the lifetime to 45000 hours, but still the multilayers cannot withstand higher temperatures than $150°C$. The replacement of the interlayer material Copper by the alloy $Cu_{85}Ag_{10}Au_5$ was predicted to enhance the temperature stability [dau97]. But Ebert and coworkers could not confirm this prediction [ebe03c]. Furthermore, any change of material or stacking sequence of the system requires separate time consuming lifetime tests. Therefore the search for alternative ways to enhance the long-term temperature stability of Co/Cu multilayers is still not finished.

## 8.1 Intention of the Study

The common procedure to determine the temperature stability of multilayer systems is either to anneal the sample in increasing temperature steps in the way shown in figure 8.1 or to continuously heat the samples to temperatures sensitive to GMR changes. Microstructural changes taking place during the stepwise heat treatment can considerably differ from those occuring when heating up the sample directly to much higher temperatures than studied so far. The different microstructural changes depending on the temperature profile can be understood in terms of recovery and recrystallization. Both processes remove defects within the material in order to reduce the total energy of the system. When the annealing of the sample at moderate temperatures has led to a considerable reduction of dislocations in the course of recovery, while the temperature was not high enough to activate recrystallization processes, then a further temperature increase need not initiate recrystallization any more because of a decreased driving force [hum91]. Therefore, recrystallization can only occur after heating up the sample directly to sufficient high temperatures. This phenomenon we discovered in the course of a temperature study of $Py/Cu/Co$-systems:

The annealing at $450°C$ for 24 hours of the multilayer system $Si/SiO_2//[Py_{3\,nm}/Cu_{6\,nm}/Co_{3\,nm}/Cu_{6\,nm}]_{20}$ triggered a complete crystalline reorientation of the sample from a polycrystalline [111] texture in the as prepared state to a [100] quasi single crystalline state after annealing. The most striking aspect of the microstructural evolution is the preservation of the layered structure of the sample. The TEM micrographs of the as prepared sample and after the annealing given in figure 8.2 prove these results.

The investigation of a $Co_{10\,nm}/Cu_{20\,nm}/(Ni_{79}Fe_{21})_{25\,nm}$ layer stack with tomographic atom probe shows the segregation of Fe atoms at the Co/Cu interface and the diffusion of Ni atoms into the grain boundary in Cu after annealing at $350°C$ for $30\,min$ as demonstrated in figure 8.3 ([schlei01], [schlei01b]). The Co/Cu layers on the other hand retain their layered structure as a consequence of their immiscibility. Auger measurements of a $[Co/Cu/Py/Cu]$ multilayer confirmed these results.

Encouraged by this finding of recrystallized $[Co/Cu/Py/Cu]$ multilayers the search for a way to increase the temperature stability of Co/Cu multilayers beyond $350°C$ started. The vital question was if it is possible to gain a quasi single crystalline Co/Cu multilayer after immediate heating to very high temperatures of minimum $400°C$ which also would show GMR. This sample should retain or increase its GMR effect amplitude under further annealing. Furthermore, this way to ultimate temperature stability could be integrated ideally into the industrial production of multilayer structures as a back end process.

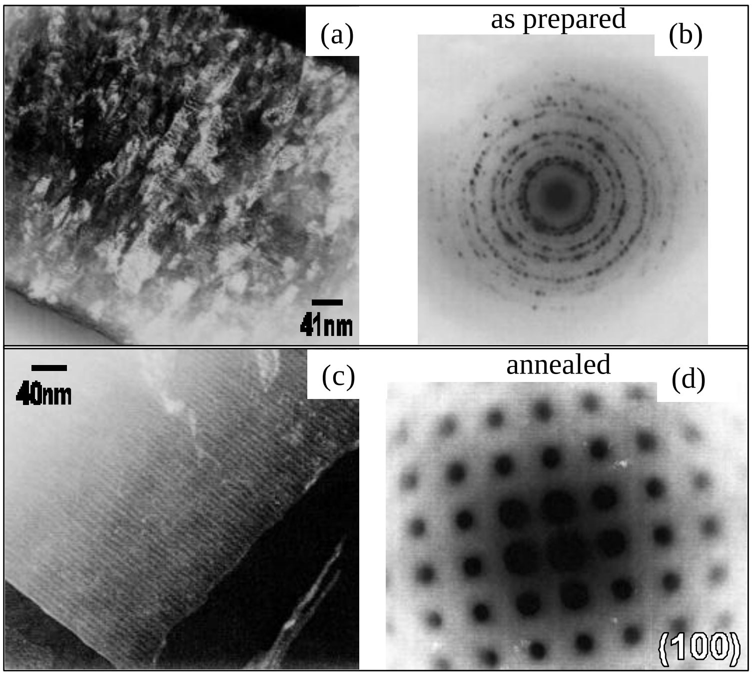

Figure 8.2: Transmission electron micrographs of the multilayer $Si/SiO_2//[Py_{3\,nm}/Cu_{6\,nm}/Co_{3\,nm}/Cu_{6\,nm}]_{20}$ as prepared (a) and (b) and after annealing at $450°C$ for 24 hours (c) and (d). (a) and (c) are cross sectional bright-field micrographs. (b) and (d) show the corresponding selected-area electron diffraction patterns. The micrographs prove that the layered structure of the sample is preserved during annealing while changing from polycrystalline to quasi single crystalline, oriented in fcc [100] direction.

The results of the tomographic atom probe also revealed that the use of a Py buffer is not the material of desire to improve the microstructure of the as prepared sample because Fe atoms and Ni as well tend to segregate to the Co/Cu interface. As a consequence no significant GMR effect amplitude was measured.

## 8.2 Investigation Overview

Multilayers of type $Si/SiO_2//Co_{3.8\,nm}/Cu_{t_{Cu}}/[Co_{2.0\,nm}/Cu_{t_{Cu}}]_{40}$ have been prepared[1] and annealed for 1 hour at $500°C$. Besides this series, samples with varying Co thickness at selected Cu thickness have been investigated as well. Due to the diffusion of Ni and Fe as mentioned above, these multilayer structures do not contain a Permalloy buffer layer.

---

[1] See chapter 5 for sputter conditions, series **Thermo 1**.

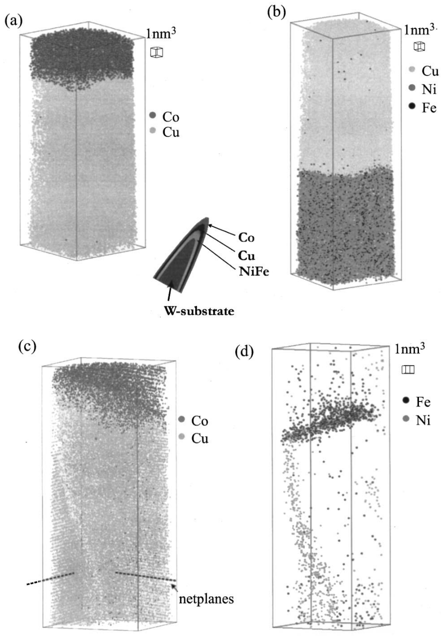

Figure 8.3: Three-dimensional reconstructions of atom probe measurement of the trilayer $Co_{10\,nm}/Cu_{20\,nm}/Py_{25\,nm}$ (a) as prepared Co-Cu interface, (b) as prepared Cu-Py interface. After 30 min annealing at $350^{\circ}C$ Ni and Fe atoms have interdiffused into the Cu and the Co-Cu interface: in (c) only Co and Cu atoms and in (d) only Fe and Ni atoms are shown, both images taken at the Co-Cu interface [schlei01].

The GMR effect of all the samples has been measured in the as prepared state and after the annealing procedure. Due to the very high annealing temperature it was not possible to measure the resistance of the samples *in situ.* MOKE measurements were performed before and after annealing and selected samples have been measured in the AGM.

To characterize the microstructure of the multilayer systems XRR and XRD measurements were performed before and after annealing. The XRD data were analyzed in two ways: Firstly, the position, integrated intensity and FWHM of the diffraction peaks in the angle range of $25^{\circ} \leq 2\Theta \leq 60^{\circ}$ were identified by profile fitting with the *ProFit* program. Secondly, the multilayer satellites occuring in annealed samples have been analysed with the *SlerfWin* program to determine the interatomic distances of the individual Cu and Co layers as well as roughness, interdiffusion and the distribution of grain sizes. The x-ray reflectometry measurements were fitted using the *WinGixa* program.

Due to the wealth of experimental results and their association with each other the results are given without any interpretation in sections 8.3 to 8.5 followed by a discussion involving all results in section 8.6.

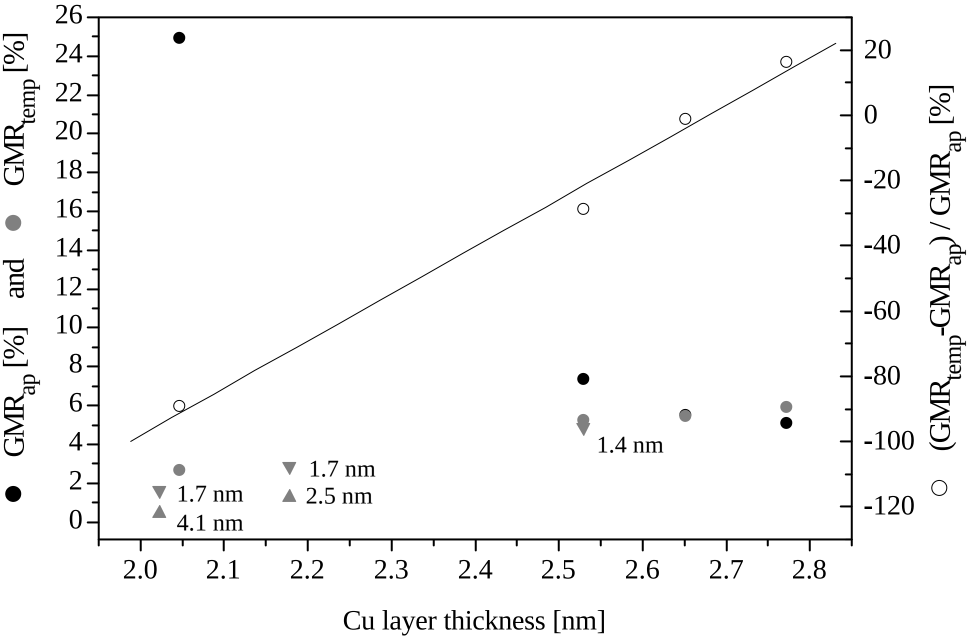

Figure 8.4: GMR effect amplitude as a function of Cu thickness: full dots represent the system $Co_{3.8\,nm}/Cu_{t_{Cu}}/[Co_{2.0\,nm}/Cu_{t_{Cu}}]_{40}$ in as prepared (black) and annealed state (grey). The open circles show the relative difference of both values. The triangles correspond to GMR amplitudes of samples with different Co thickness which are indicated beside each symbol. All samples have been annealed at $500°C$ for 1 hour.

## 8.3 GMR Characteristics

Searching for a Co/Cu multilayer with considerable GMR effect after the annealing process, the layer thickness of Cobalt and Copper have been varied. The GMR effect amplitudes of multilayers $Co_{3.8\,nm}/Cu_{t_{Cu}}/[Co_{2.0\,nm}/Cu_{t_{Cu}}]_{40}$ before and after annealing at $500°C$ as a function of the Cu spacer layer thickness are given in figure 8.4 and in figure 8.5 the corresponding GMR characteristics are summarized.

In the as prepared state the effect amplitude (black dots) decreases with increasing Cu thickness above $t_{Cu} = 2.05\,nm$ which is in agreement with the oscillating antiferromagnetic coupling behaviour of Co/Cu multilayers having their second antiferromagnetic coupling maximum at around $2.1\,nm$. The GMR effect amplitude after annealing (grey dots) decreased for Cu thickness below $2.65\,nm$. The GMR effect amplitude of the sample with $t_{Cu} = 2.65\,nm$ remains unchanged, whereas the sample with $t_{Cu} = 2.77\,nm$ shows an increase in the effect amplitude. The relative change of the effect amplitude (open circles) shows a linear increase with a correlation coefficient of $R = -0.996$ (solid line).

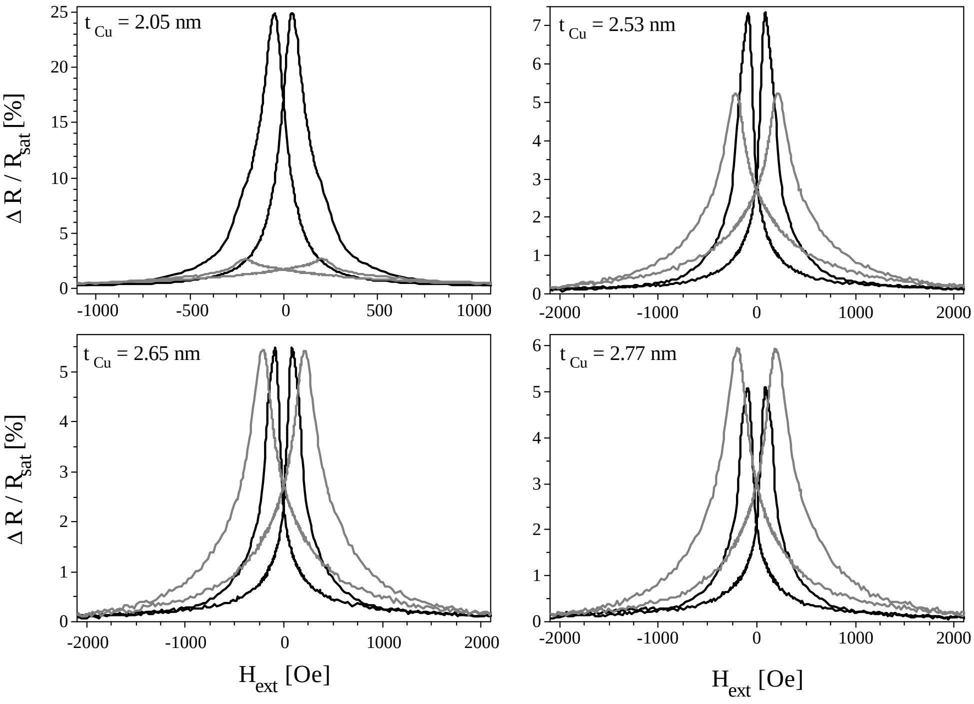

Figure 8.5: Magnetoresistance loops as prepared (black) and after annealing (grey) of the multilayers type $Co_{3.8\,nm}/Cu_{t_{Cu}}/[Co_{2.0\,nm}/Cu_{t_{Cu}}]_{40}$ given in the overview figure 8.4.

Within the variation of the Cu thickness the highest GMR effect after annealing is 5.9 % for the sample with $t_{Cu} = 2.77\,nm$ and a Cobalt thickness of $2.0\,nm$. Because the initial GMR value is much higher for a Copper thickness around $2.1\,nm$ one idea to get higher GMR values after annealing was to increase the Co thickness in order to prevent the layers from being destructed. But this variation did not lead to any enhancement as the upwards pointing triangles in figure 8.4 show (for clarity only the GMR amplitude after annealing is given.). Also a decreased Co thickness, indicated in figure 8.4 by downwards pointing triangles, does not yield a higher effect amplitude. On the other hand, sample series annealed in testing experiments clearly indicated a minimum Co thickness of about $1.4\,nm$ in order to retain the GMR effect amplitude.

The results of the annealing experiments do not completely agree with the GMR amplitudes found by Hecker *et al.* [hec03]: annealing of the multilayer $[Co_{2.2\,nm}/Cu_{2.1\,nm}]_{30}/Co_{2.2\,nm}$ at $400°C$ for 1 hour increased the initial GMR value of 24 % to a maximum at 30 %. The annealing at $500°C$ for 1 hour of an equivalent sample on the other hand reduced the initial amplitude to about 12 %. This loss in amplitude is rather small compared to multilayers with similar thicknesses of $t_{Co} = 2.0\,nm$, $t_{Cu} = 2.05\,nm$ and $t_{Co} = 2.5\,nm$, $t_{Cu} = 2.18\,nm$ given in figure 8.4. Their GMR amplitudes decrease to less

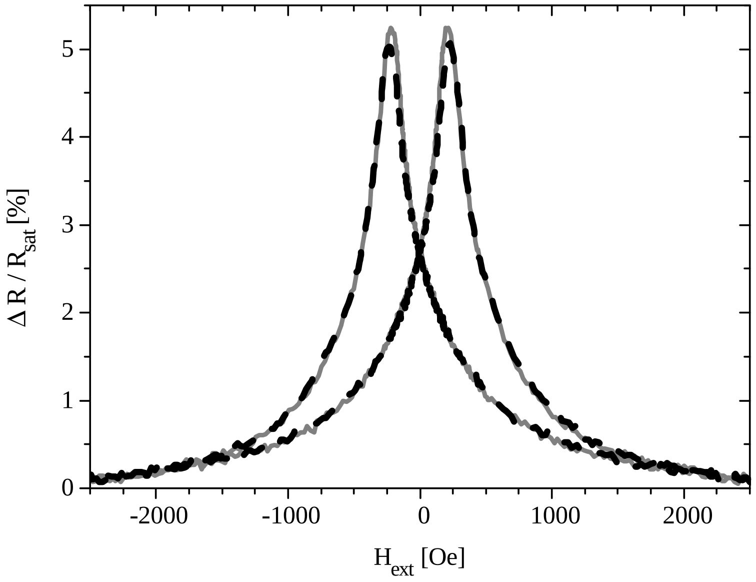

Figure 8.6: Magnetoresistance loops of the multilayer $Co_{3.8\,nm}/Cu_{2.53\,nm}/[Co_{2.0\,nm}/Cu_{2.53\,nm}]_{40}$ after inital annealing at $500°C$ for 1 hour (grey line) and after long time heating at $400°C$ for 64 hours (broken black line). The GMR characteristic before any annealing process is given in figure8.5.

than 3 %. The reason for the differing temperature stability of the multilayers can only be answered with the knowledge of the differences in microstructure of the sample series and of the break down mechanism of the GMR.

Now that Co/Cu multilayers have been found having GMR effect amplitudes of around 5 % after annealing the next question is whether these systems are temperature stable under further annealing at temperatures below that of primary annealing. This has been tested for the sample with $t_{Cu} = 2.53\,nm$ which has been further annealed at 400° C for 64 hours. Figure 8.5 compares the GMR characteristic of the as prepared sample and after initial annealing at $500°C$. The GMR characteristic after the long time annealing at $400°C$ is given in figure 8.6 together with the initially annealed one. The differences in GMR characteristics are marginal and therefore the absolute temperature stability of recrystallized Co/Cu multilayers has been successfully proven.

In the upper graph of figure 8.7 a compilation of maximum and saturation resistance of the series $Co_{3.8\,nm}/Cu_{t_{Cu}}/[Co_{2.0\,nm}/Cu_{t_{Cu}}]_{40}$ before and after annealing is given. The as prepared saturation resistance decreases with increasing Cu thickness due to shunting in the larger layer thickness. The maximum resistance is characterized by a steeper decrease than the saturation resistance. This fact is revealed best by the difference between these two values which is given as $\Delta R_{ap}$ in the lower graph. $\Delta R_{ap}$ reveals the magnetic properties of

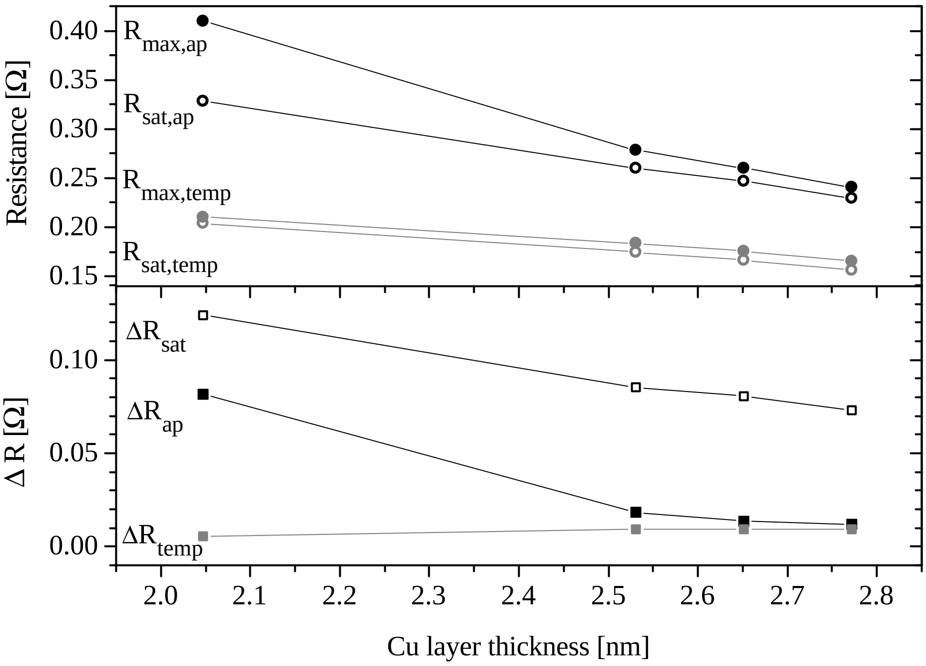

Figure 8.7: The upper graph shows maximum (full dots) and saturation (open dots) resistance of the samples $Co_{3.8\,nm}/Cu_{t_{Cu}}/[Co_{2.0\,nm}/Cu_{t_{Cu}}]_{40}$ in as prepared (black) and annealed state (grey) ($500°C$ for 1 hour). In the lower graph the absolute difference of maximum to saturation resistance for as prepared (black full squares) and annealed (grey squares) samples are given as well as the difference of the saturation resistance in both states (open squares).

the sample and therefore the reduced antiferromagnetic coupling at high Cu thickness. After the annealing process the saturation resistance of the samples is decreased by a factor 1.5 to 1.6 and the absolute difference in saturation resistance is shown in the lower graph as $\Delta R_{sat}$. The difference in saturation resistance decreases almost linearly with increasing Cu thickness. The difference between maximum and saturation resistance of the annealed samples, $\Delta R_{temp}$, is also given in the lower graph. The comparison between $\Delta R_{ap}$ and $\Delta R_{temp}$, which reveals the evolution of GMR amplitude, shows that the annealed value for the sample with $t_{Cu} = 2.05\,nm$ has decreased enormously whereas the other values have decreased much less, approaching the as prepared value for the sample with $t_{Cu} = 2.77\,nm$

In figure (8.8) the saturation field $H_{Sat}$ and the coercivity $H_C$ of the samples $Co_{3.8\,nm}/Cu_{t_{Cu}}/[Co_{2.0\,nm}/Cu_{t_{Cu}}]_{40}$ before and after annealing are shown. The coercivity has been determined as the magnetic field value where the peak of the GMR loop reaches is maximum. The saturation field of all samples has increased considerably after annealing by at least a factor of two but the amount of increase is the smaller the thicker the Cu layers are. The coercive

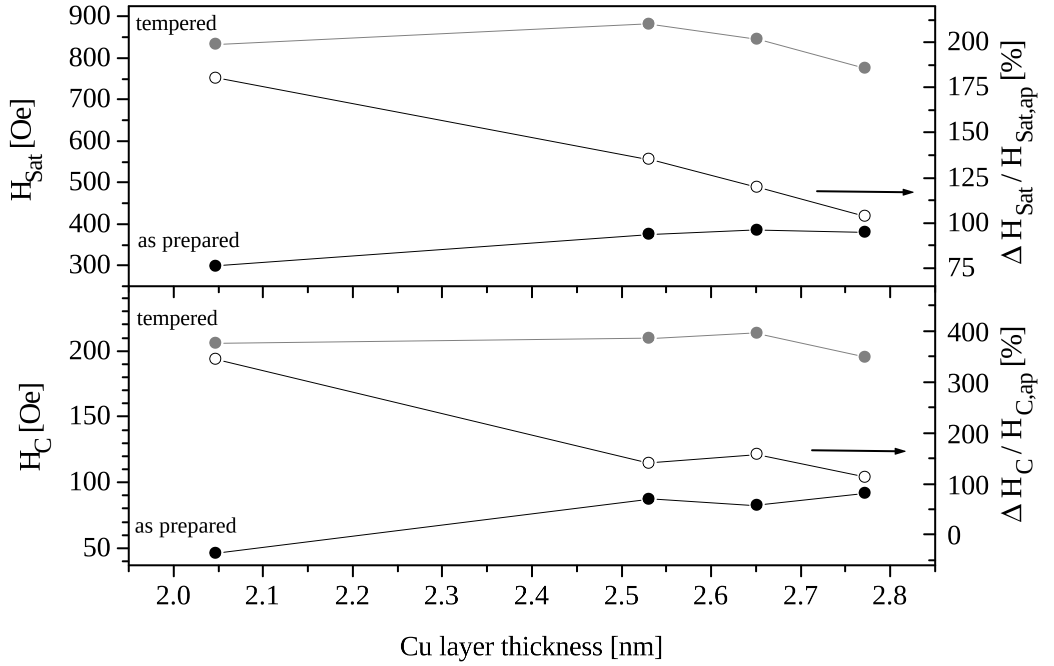

Figure 8.8: The upper graph shows the GMR saturation field and the lower graph shows the GMR coercivity (peak maximum field) of system $Co_{3.8\,nm}/Cu_{t_{Cu}}/[Co_{2.0\,nm}/Cu_{t_{Cu}}]_{40}$ as prepared (black) and annealed at $500°C$ for 1 hour (grey). The open circles show the relative difference of tempered to as prepared values and the lines are guides to the eyes.

field increased during annealing to values around 210 Oe for all samples. As the as prepared value of $H_C$ increases with $t_{Cu}$ the relative change is decreasing. Furthermore, the crossover of the magnetoresistance loops remained constant as can be seen in the graphs of figure 8.5.

In section 8.6 the GMR characteristics of the sample with $t_{Cu} = 2.77\,nm$ will be calculated based on the results of microstructural investigation. The calculation of GMR with the program *GMRSim* enables to determine the coupling strength as well as the anisotropy constant of the sample as prepared and after annealing.

## 8.4 Magnetic Characteristics

In order to measure the magnetic properties of the samples MOKE measurements have been performed so as to determine their coercivity and saturation field as well as the slope of the hysteresis loops, also called squareness, defined as the ratio of remanent to saturation magnetization $M_R/M_S$. Furthermore,

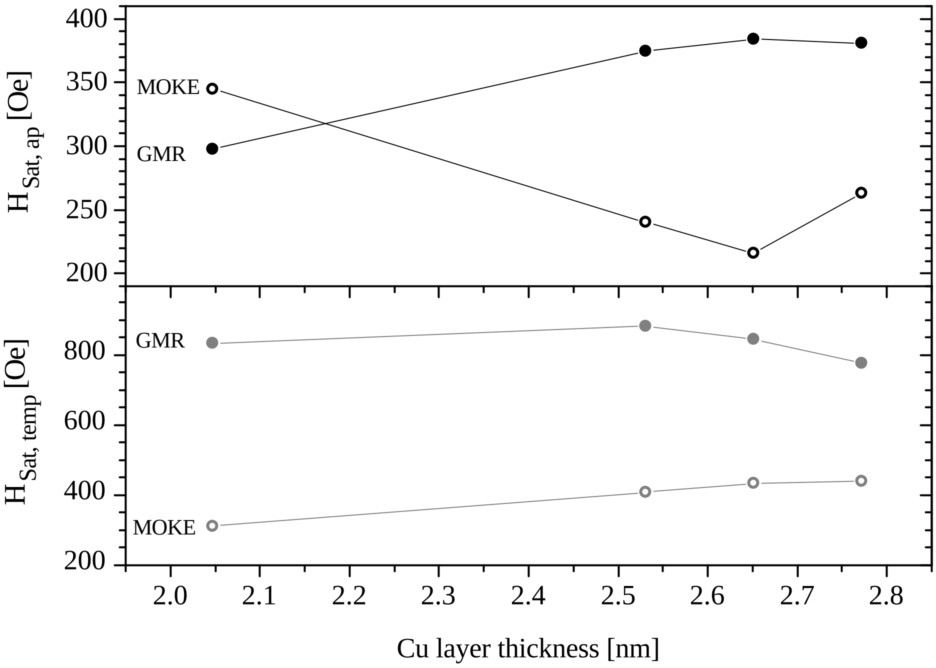

Figure 8.9: Comparison of saturation field of the series $Co_{3.8\,nm}/Cu_{t_{Cu}}/[Co_{2.0\,nm}/Cu_{t_{Cu}}]_{40}$ of GMR loop (full dots) with MOKE loops (open dots) as prepared (black) and annealed at 500°$C$ for 1 hour (grey).

angle resolved AGM measurements of the sample with $t_{Cu} = 2.77\,nm$ as prepared and after annealing have been made in order to determine the magnetic anisotropy.

The saturation field of the MOKE loops is considerably smaller than that of the GMR loops and shows different dependencies on the Cu thickness as is shown in figure 8.9. For as prepared samples the MOKE saturation field decreases with increasing Cu thickness which reveals the weakening antiferromagnetic coupling. The relatively high value for the sample with $t_{Cu} = 2.77\,nm$ does not fit in this explanation. The GMR saturation values on the other hand show a controversal behaviour on increasing field with increasing Cu thickness. For the annealed samples the MOKE saturation field increases approximately linearly for thicker Cu layers. In comparison to the as prepared samples all values have increased except for the one with thinnest Cu. The large differences to the GMR saturation values will have to be discussed in section 8.6.

The slope of the MOKE loops is very interesting because it reveals the antiferromagnetic coupling. In figure 8.10 the $M_R/M_S$ values for as prepared and annealed samples are given together with the complete MOKE loops of two samples in the insets. The smallest squareness can be found for the sample with $t_{Cu} = 2.05\,nm$ in as prepared state which is the sample at the second

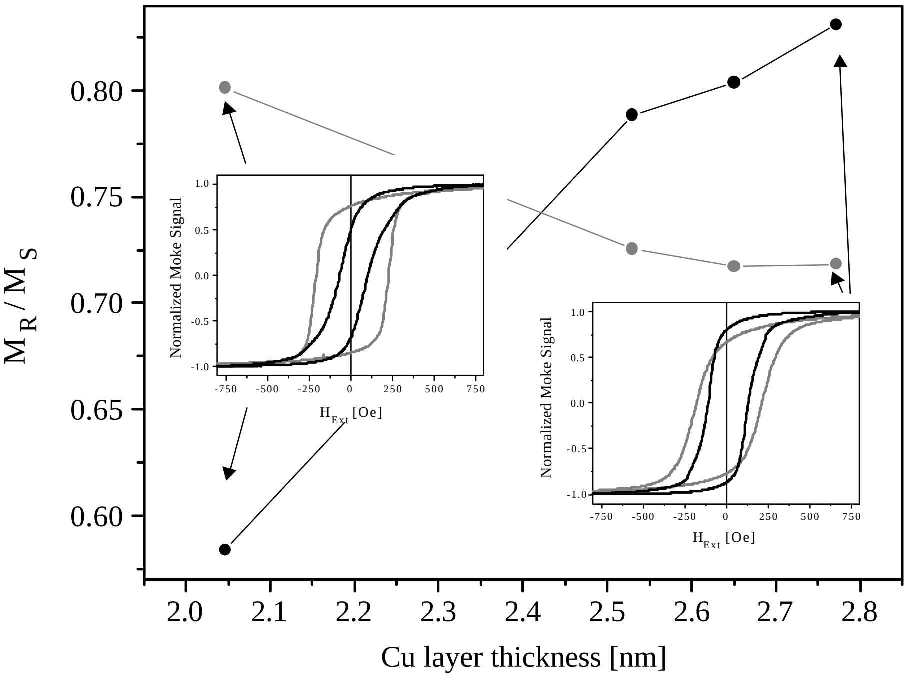

Figure 8.10: Squareness of MOKE hysteresis loops as a function of Cu thickness of the series $Co_{3.8\,nm}/Cu_{t_{Cu}}/[Co_{2.0\,nm}/Cu_{t_{Cu}}]_{40}$ as prepared (black) and annealed at $500°C$ for 1 hour (grey). The inset on the left shows the MOKE loops as prepared (black) and annealed (grey) for the sample with $t_{Cu} = 2.05\,nm$ and the one on the right for $t_{Cu} = 2.77\,nm$.

antiferromagnetic coupling maximum. Accordingly, the squareness increases with increasing Cu thickness due to the decreasing coupling strength. The squareness of the annealed samples on the other hand shows the controversal behaviour: it decreases with increasing Cu thickness and for all samples with $t_{Cu} \geq 2.5\,nm$ the squareness is smaller than in the as prepared state. Therefore it can be concluded that the coupling strength has increased during annealing.

The comparison of coercivity of MOKE and GMR loops reveals an interesting discrepancy for the as prepared samples: $H_C$ determined by MOKE is about $30\,Oe$ higher than the peak field value of the magnetoresistance loops. One possible explanation for the difference might be the limited depth detectable by MOKE, the skin depth of 10 to $20\,nm$. Therefore in case of the sample with thickest Cu only 4 double layers determine the MOKE signal. One possibility to clear up this discrepancy is to measure the samples with AGM, the method that detects the magnetic signal of the whole sample. On the left side of figure 8.11 a compilation of MOKE, AGM and GMR loop of the sample with $t_{Cu} = 2.77\,nm$ in as prepared state is made. It has to be stated that neither MOKE nor AGM loop gives consistent results to the GMR characteristics: $H_C$

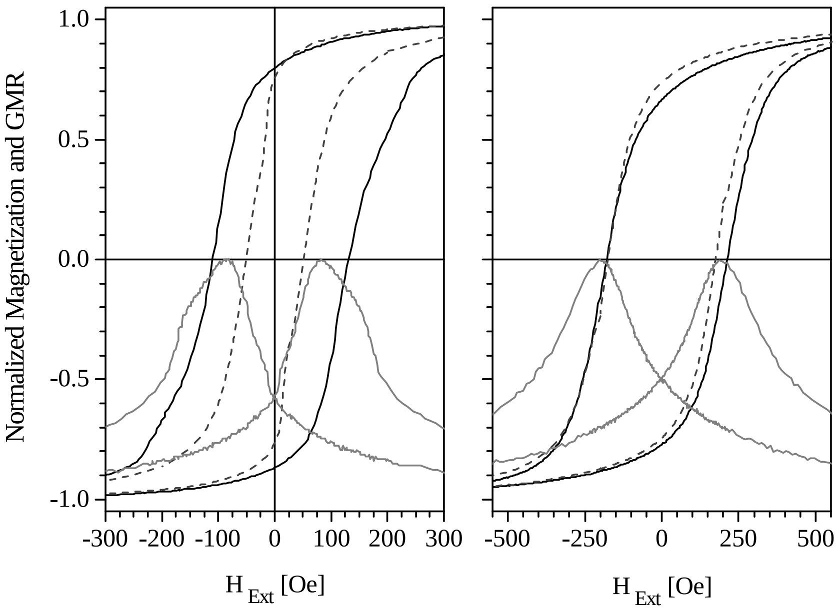

Figure 8.11: Determination of coercivity by MOKE (black line), AGM (dotted line) and GMR (grey line) of the sample $Co_{3.8\,nm}/Cu_{2.77\,nm}/[Co_{2.0\,nm}/Cu_{2.77\,nm}]_{40}$. Left graph: As prepared, right graph: after annealing.

of MOKE is about $30\,Oe$ higher and $H_C$ of AGM is $40\,Oe$ smaller than the peak field of GMR.

The only possible explanation for this discrepancy is a microstructural evolution of magnetic characteristics and coupling strength during the growth of the layer stack. The large difference of coercive field of MOKE and AGM measurement is an indication for this fact. The topmost four Co layers are magnetically harder compared with the whole stack but the antiferromagnetic coupling of these layers is weaker (this fact is drawn from the comparison of $M_R/M_S$ value). Due to these inhomogeneous magnetic characteristics the transport measurement can reveal an averaged behaviour and the antiferromagnetic arrangement which shows the highest resistance does not necessarily have to be the same that gives a zero magnetization.

For the tempered sample on the other hand all three methods yield the same value for $H_C$ and the MOKE loop fits the AGM loop very well (figure 8.11, right graph). It can be concluded that in the course of annealing a homogenization process has taken place, yielding the same magnetic and coupling behaviour for all layers inside the stack.

For the determination of anisotropy of the samples the relative change of coercivity has been measured with AGM for the sample with $t_{Cu} = 2.77\,nm$ and the results are shown in figure 8.12. The sample has been rotated by the

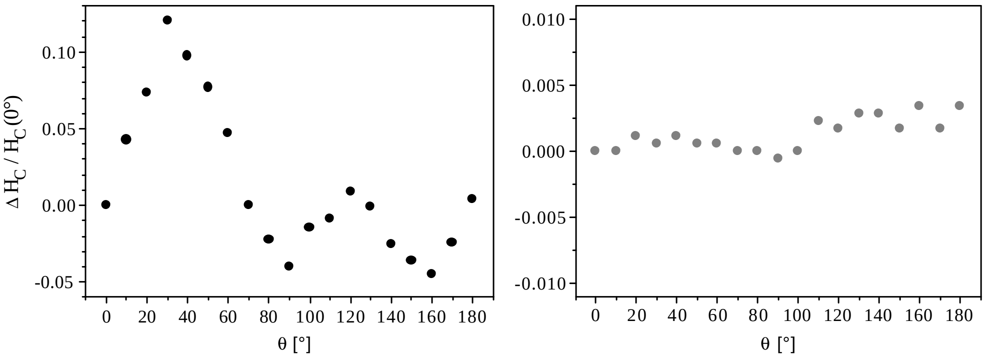

Figure 8.12: Change of coercivity relative to the 0° orientation of AGM hysteresis loops of the sample $Co_{3.8\,nm}/Cu_{2.77\,nm}/[Co_{2.0\,nm}/Cu_{2.77\,nm}]_{40}$ as prepared (left) and annealed (right). All measurements have been performed with the magnetic field parallel to the layer plane and the sample was rotated by the angle $\Theta$.

angle $\Theta$ for each measurement and the external magnetic field is parallel to the layers in every case. For the as prepared sample given in the left graph a biaxial magnetic anisotropy is detected. After the annealing the anisotropy has almost vanished completely as the graph on the right reveals. The biaxial anisotropy of the as prepared sample originated in the course of layer growth. This is a known fact, caused by the external magnetic field in the surrounding area of the sputter sources. During the thermal recrystallization process the sample has lost its magnetic “sputter source memory”. This effect has been confirmed by Hecker *et al.* [hec03].

## 8.5 Microstructure Characteristics

In the previous section the GMR and magnetic characteristics have been investigated and many of these characteristics can only be explained with the knowledge of the microstructure of the multilayers.

### 8.5.1 Peak Profile Fitting of XRD Scans

Large angle x-ray diffraction measurements of the samples have been performed before and after annealing. For the exact determination of peak position, peak area and width the angle range from 35 to 60° 2$\Theta$ has been analysed with peak profiling (*ProFit* ) because of overlapping peaks. In figure 8.13 the XRD scans of the samples $Co_{3.8\,nm}/Cu_{2.05\,nm}/[Co_{2.0\,nm}/Cu_{2.05\,nm}]_{40}$ and $Co_{3.8\,nm}/Cu_{2.77\,nm}/[Co_{2.0\,nm}/Cu_{2.77\,nm}]_{40}$ are shown as prepared and after annealing together with the resolved peak profiles as determined by *ProFit.*

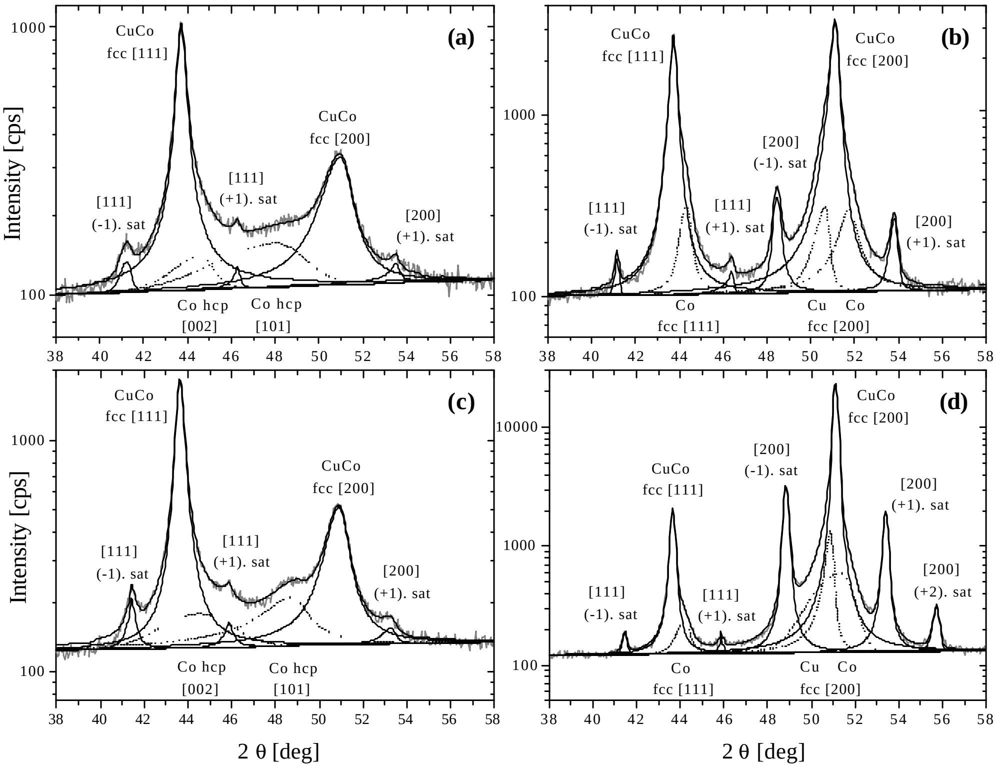

Figure 8.13: XRD scans of the samples $Co_{3.8\,nm}/Cu_{2.05\,nm}/[Co_{2.0\,nm}/Cu_{2.05\,nm}]_{40}$ (a)+(b) and $Co_{3.8\,nm}/Cu_{2.77\,nm}/[Co_{2.0\,nm}/Cu_{2.77\,nm}]_{40}$ (c)+(d) together with the resolved peak profiles as determined by *ProFit*. (a)+(c): as prepared; (b)+(d): annealed at $500°C$ for 1 hour. The grey line is the measured profile and the black line directly upon is the resulting fit profile, added up of the single peak profiles indicated in the graphs (note the logarithmic intensity scale.)

## As Prepared Samples

In the as prepared state the samples are polycrystalline and show peaks of [111] and [200] fcc orientation as well as small satellites around both orientations. The fcc [111] peak at about 43.6° 2Θ corresponds to the averaged peak position of Cu [111] and Co [111] and the resulting position depends on the single layer thickness.[2] The same considerations are valid for the fcc [200] peak around 50.9° 2Θ. Very small satellites of first order can be seen around the fcc [111] position and at least one first order satellite of [200] orientation. Furthermore, the angle range below the [200] peak is of enhanced intensity which may be related to the Co hcp [101] orientation (PDF bulk value: 47.46° 2Θ) produced by very small crystallites. Peak profiling gives a very broad peak

---

[2] PDF bulk values (see also appendix C): $2\Theta_{Cu[111]} = 43.36°, 2\Theta_{Co[111]} = 44.26°$. Cobalt and Copper do not show separate peaks due to their small layer thickness as has been explained in section 4.2.4.

placed at about 48.5° $2\Theta$. The peak position deviates up to 1.3° $2\Theta$ from the powder diffraction file value which may be associated to lattice distortions. Furtermore, this peak is hard to localize due to its broadness and so the value determined by ProFit may be associated with a considerable error. Peak profiling is complicated further: the fcc [200] peak shows a satellite of (+1). order, but maybe the (−1). order satellite is also present and adds up with the hcp [101] peak. Attempts to fit both peaks failed and this stresses the fact that the exact peak values of the hcp [101] peak fitted to the measurement has to be taken with care. This has to be kept in mind especially when discussing the size of the hcp [101] crystallites. The average value for the hcp crystallite size for the three samples of the series determined with *ProFit* is $(2.8 \pm 0.9)\,nm$. This value is too high to correspond to the Co layers inside the stack having a thickness of $2\,nm$ only, but the crystallites can be located inside the Co buffer layer of $3.8\,nm$. This is reasonable because this Co buffer layer is growing directly on the silicon oxide of the substrate and is not influenced by coherency strains from adjacent Cu layers.

In fitting the three peaks of fcc and hcp crystallite orientation mentioned so far together with three satellites the measured profile is approximated quite well. There is a small chance that not only the Co hcp [101] but also the hcp [002] orientation may be present and therefore a second fitting procedure containing this peak has been performed. The result is a profile which approximates the measurement equally well but the shape of the (−1). order [111] satellite as well as that of the hcp [101] peak is more harmonic and therefore the presence of hcp [002] grains seems to be reasonable. The average size in growth direction of the hcp [002] grains is $(3.0 \pm 1.1)\,nm$ which is also higher than the Co layer thickness inside the stack and therefore has to be attributed to the Co buffer layer. The presence of the hcp [002] peak influences the shape of the fcc [111] peak: the FWHM is decreased as well as the integrated intensity. These values represent the crystallite size and the volume fraction of the crystallites and so the question arises how much of the hcp contribution should be taken into account. Whether a hcp [002] peak is added to the pattern or not, the profile can be approximated well in both cases and therefore the truth may be in between both possibilites. So, finally, the average values of FWHM and integrated intensity of both fitting procedures have been taken.

### Annealed Samples

After the annealing process the microstructure of the samples has significantly changed. The most striking difference is the enormous increase of intensity of the fcc [200] main peak and its corresponding satellites. Furthermore, the intensity of the [200] peak and its satellites is increasing the thicker the Cu layers. For Cu thickness of $2.77\,nm$ the satellite of (+2). order appears. The hcp orientations on the other hand have disappeared which can be explained with the transformation of hcp Co to fcc Co at $422°C$ [mas90]. Peak profiling of the fcc [111] and [200] peaks together with their satellites gives good results but still contains differences compared to the measurement: firstly, the measured [111] main peak shows an enhanced slope on the right and secondly, the [200] main peak is enhanced on both sides in such a way that the profiling program cannot adjust the slope. During the annealing process with temperatures above 400°C there is the possibility of layer breakup and grain agglomeration. Therefore single Cu and Co contributions may have to be taken into account and in a second fitting procedure the peaks have been added to the profile. The fitting result shows three additional fcc peaks: Co [111], Co [200] and Cu [200]. Together with these three orientations the measured profiles are approximated very well and especially the Co [111] peak reproduction seems to be reliable. The mean crystallite size averaged over the three samples is $(17 \pm 2)\,nm$ and shows a slight tendency to decrease with increasing Cu thickness. But care has to be taken concerning the results of the [200] peaks of the pure materials Co and Cu. Their peaks are placed on either side of the [200] main peak and there is a large variety of peak shape combinations of the three peaks which all give the correct resulting profile. This can be seen in the large fluctuations of the FWHM of the peaks which give the crystallite sizes and which do not show an interdependence with the Cu thickness. Again averaged over all samples, the mean sizes are $(20 \pm 14)\,nm$ for Cu [200] and $(12 \pm 9)\,nm$ for Co [200]. It is therefore hard to say which profile combination is the right one and FWHM values as well as integrated intensities cannot be determined reliably for each peak. But it does make sense to take the sum of integrated intensities of all three peaks to yield the total volume fraction of [200]. For the determination of crystallite size of [200] coherent grains the average of both profile fitting possibilities is taken (with and without single Cu and Co contributions). In the same way the FWHM and integrated intensity of the [111] main peak were taken and again the sum of both peaks give the [111] volume fraction.

The average size of crystallites in fcc [111] and [200] orientation as prepared and after annealing have been calculated with the help of the Scherrer equation (4.17) and are given in figure 8.14. For as prepared specimens the crystallites in [111] orientation are larger than the [200] grains and their size increases linearly with increasing Cu thickness up to $25\,nm$ for $t_{Cu} = 2.77\,nm$. The [200] grains have 6.5 to $8.2\,nm$, also increasing with Cu thickness, and so their size is about one third of the [111] size in all cases. During the annealing process an enormous grain growth took place and the thicker the Cu layers the more the grains have grown. Crystallites oriented in [111] direction grew by a factor 2.3 to 3.3 and [200] grains are even 5.4 to 9.3 times larger after the annealing. The final average sizes of both orientations are similar and reach up to $80\,nm$ for the sample with thickest Cu layers.

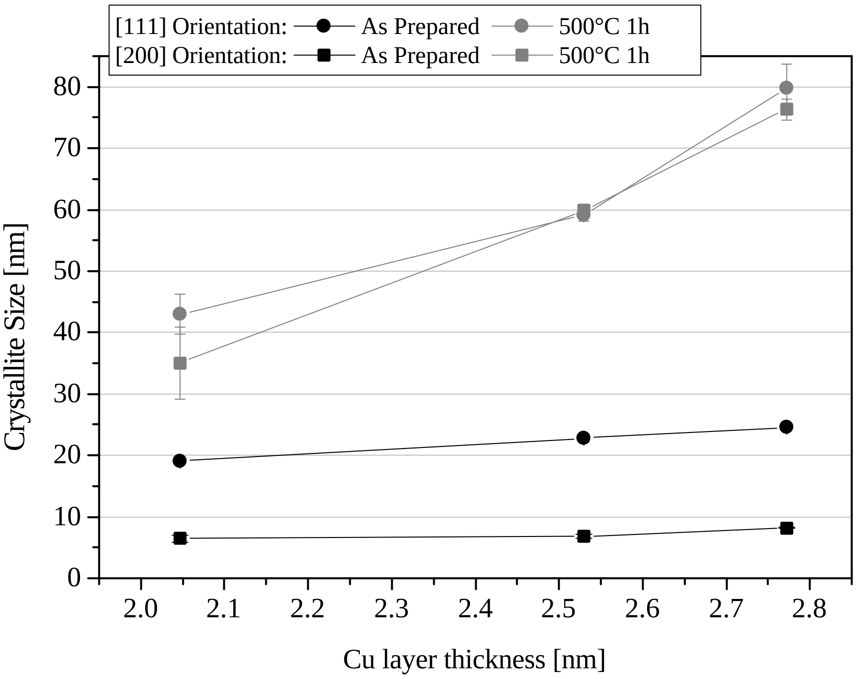

Figure 8.14: Crystallite size of [111] (dots) and [200] (squares) orientation of the series $Co_{3.8\,nm}/Cu_{t_{Cu}}/[Co_{2.0\,nm}/Cu_{t_{Cu}}]_{40}$ as prepared (black) and annealed (grey). The error range of each data point is marked by bars.

The most interesting aspect of the texture is the dominating fcc [200] behaviour of the samples after the annealing process and the question is how the volume fraction on fcc [111] and [200] grains has changed. An estimation of these values has been made in the following way for the as prepared samples:

$$\mathrm{Vol}_{[111]} = \frac{I_{[111]}}{I_{[111]} + 2 \cdot I_{[200]}} \quad \text{and} \quad \mathrm{Vol}_{[200]} = \frac{2 \cdot I_{[200]}}{I_{[111]} + 2 \cdot I_{[200]}} \tag{8.1}$$

The integrated intensity of the [200] peak is multiplied by the factor 2 because of its weaker scattering behaviour (see appendix C). The Co hcp contributions have not been considered here, but the calculation has been performed twice: firstly, the integral intensities for the profiles without Co hcp [002] peak and secondly, the intensities of the profile with [002] peak have been taken. The Co hcp [101] has been considered in both profiles. The average of both volume fractions and its standard deviation is shown in figure 8.15.

After the annealing the first calculation was made according to equation (8.1) for the profile without consideration of single Co and Cu peaks. The second calculation is based upon the profile that contains pure Co and Cu contribu-

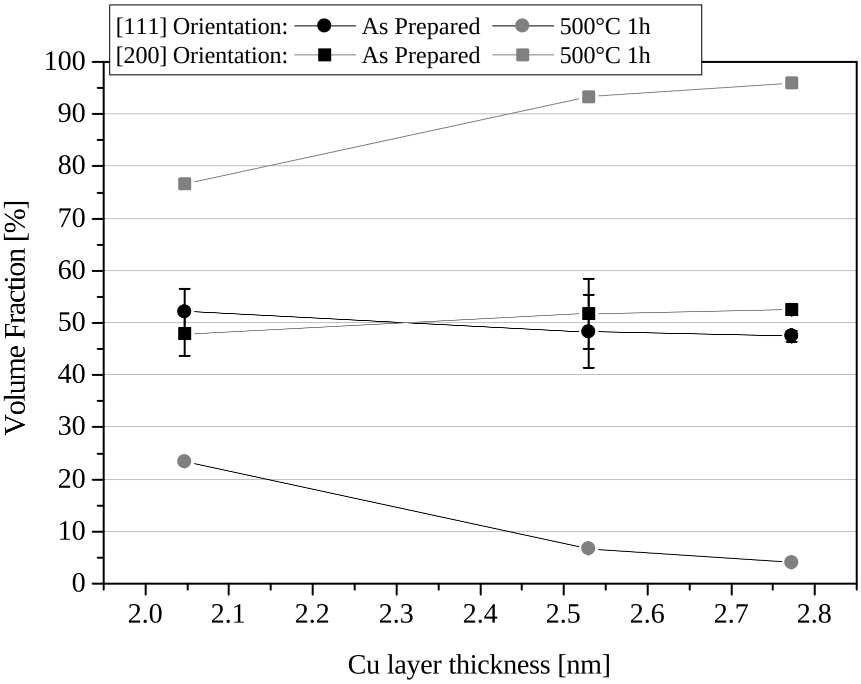

Figure 8.15: Volume fraction of crystallites of [111] (dots) and [200] (squares) orientation of the series $Co_{3.8\,nm}/Cu_{t_{Cu}}/[Co_{2.0\,nm}/Cu_{t_{Cu}}]_{40}$ as prepared (black) and annealed (grey). The error range of each data point is marked by bars.

tions where the total fcc volume is given by

$$\mathrm{Vol}_{\text{fcc total}} = I_{CuCo[111]} + I_{Co[111]} + 2 \cdot I_{CuCo[200]} + 1.9 \cdot I_{Cu[200]} + 2.2 \cdot I_{Co[200]} \quad (8.2)$$

and then the [111] and [200] fractions are calculated as

$$\mathrm{Vol}_{[111]} = \frac{I_{CuCo[111]} + I_{Co[111]}}{\mathrm{Vol}_{\text{fcc total}}} \quad (8.3)$$

$$\mathrm{Vol}_{[200]} = \frac{2 \cdot I_{CuCo[200]} + 1.9 \cdot I_{Cu[200]} + 2.2 \cdot I_{Co[200]}}{\mathrm{Vol}_{\text{fcc total}}} \quad (8.4)$$

The average of both volume fractions each and their standard deviations are also shown in figure 8.15. The as prepared samples show equal fractions of around 50% for [111] and [200] crystallites. The error bars show that it is not possible to decide whether there is a slight texture for the two samples with $t_{Cu} \leq 2.6\,nm$ and only the sample with $t_{Cu} = 2.77\,nm$ shows a little more [200] fraction. The situation changes drastically for the annealed samples. Now clearly crystallites having [200] orientation take at least 75% of the sample volume and this amount increases with thicker Cu layers to even 96%.

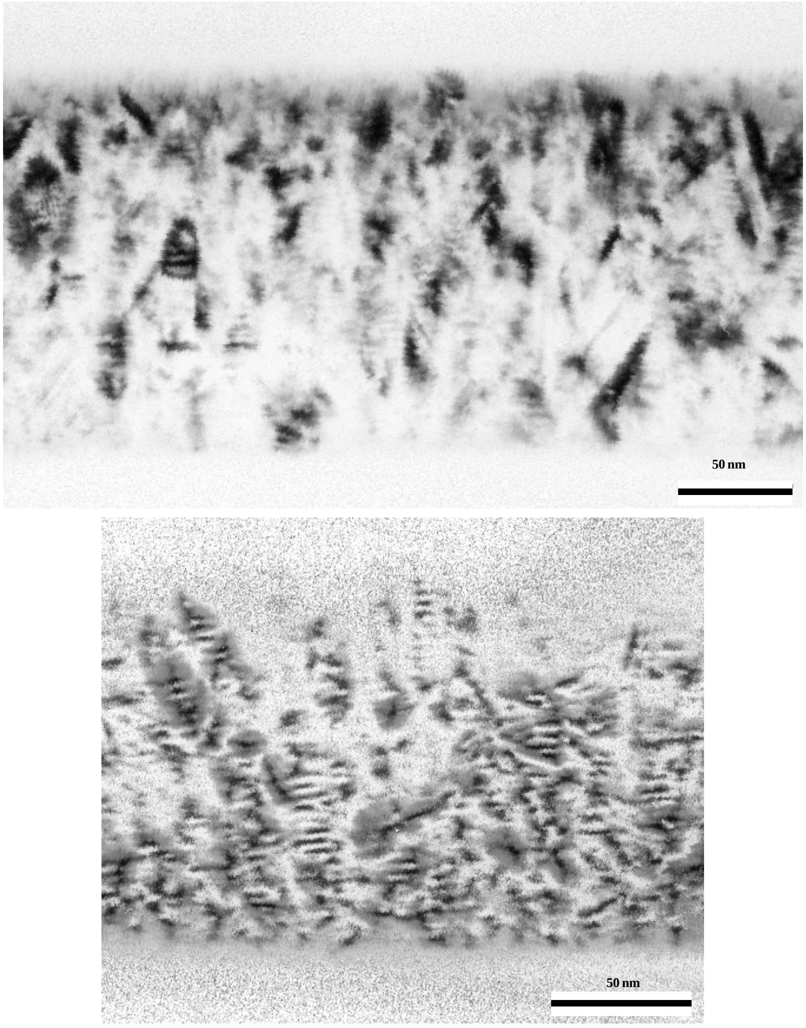

Figure 8.16: TEM cross-section micrographs of the as prepared sample $Co_{3.8\,nm}/Cu_{2.65\,nm}/[Co_{2.0\,nm}/Cu_{2.65\,nm}]_{40}$. Grains having vertical size of 5 to $50\,nm$ and an average lateral size of approximately $20\,nm$ can be identified. The lower micrograph is contrast enhanced in order to identify the layered structure of the grains.

### 8.5.2 TEM Analysis on Selected Samples

Transmission Electron Microscope measurements of the sample $Co_{3.8\,nm}/Cu_{2.65\,nm}/[Co_{2.0\,nm}/Cu_{2.65\,nm}]_{40}$ as prepared and after annealing were performed by G. Schmitz at the University of Münster.

A cross-section micrograph of the as prepared sample is given in figure 8.16. It reveals a polycrystalline microstructure with grains of average lateral size of approximately $20\,nm$. The distribution of grain size in vertical direction is larger and varies mainly between 5 and $50\,nm$. The distribution of vertical

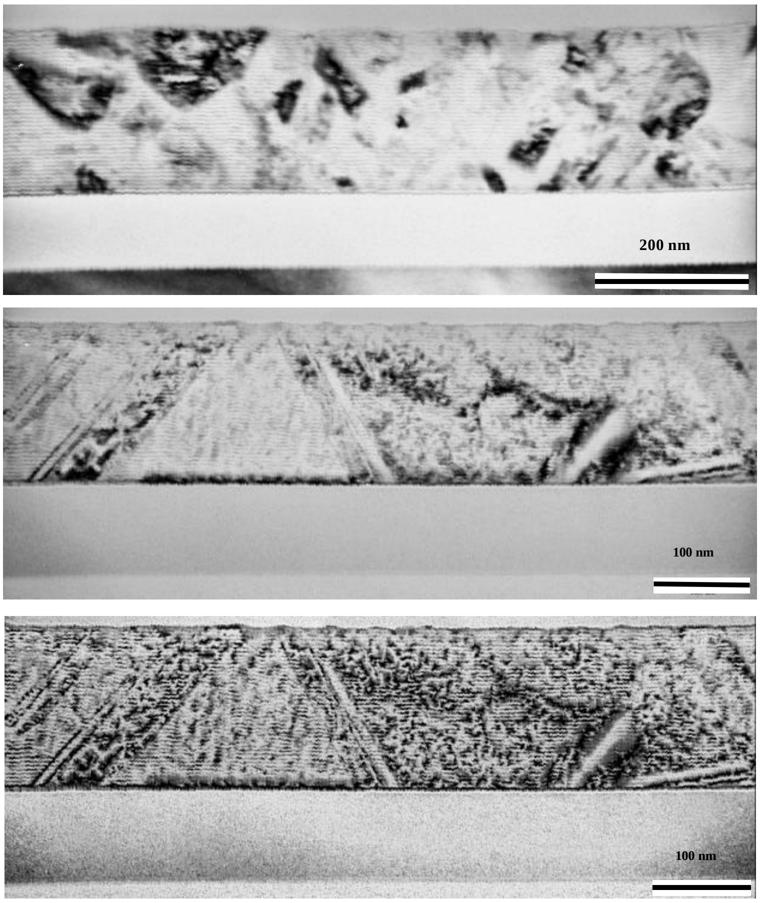

Figure 8.17: The graphs on on top and in the middle are TEM cross-section micrographs of different parts of the sample $Co_{3.8\,nm}/Cu_{2.65\,nm}/[Co_{2.0\,nm}/Cu_{2.65\,nm}]_{40}$ after annealing. Grains have grown to a vertical size of 15 to 200 $nm$ and a lateral size of 15 $nm$ to 140 $nm$. The contrast enhanced image of the micrograph in the middle is given below.

grain size is in good agreement to the crystallite size determined by XRD with mean crystallite size of 25 $nm$ in [111] direction and 8.2 $nm$ in [100] direction. For a better identification of single layers the contrast of the micrograph was enhanced (bottom graph of figure 8.16). The question is whether the layer normal of adjacent grains differs considerably. Although in the filtered image no layers in directly neighboured grains can be identified it can be seen that whenever the layer structure is visible the layer normal is parallel to the normal of the whole stack.

The diffraction pattern of the as prepared sample is given in the left graph of figure 8.18. It depicts the polycrystalline structure of the sample with the presence of some grains in every orientation of larger size yielding distinctive spots on the diffraction radius. The assignment of diffraction circle radius $r$

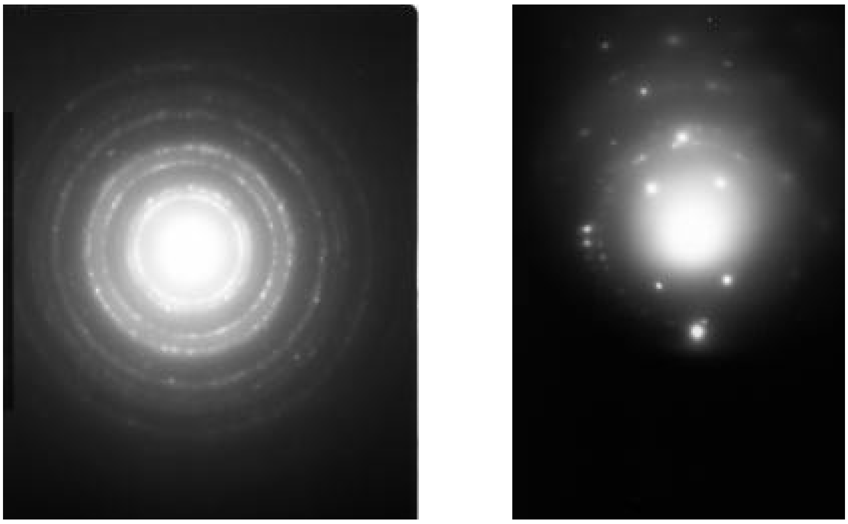

Figure 8.18: Selected-area electron diffraction patterns of the micrographs in figure 8.16 and 8.17. The pattern on the left proves the polycrystalline fcc structure of the as prepared sample and the right pattern reveals the transformation to a quasi single crystalline [100] structure with only a small fraction of polycrystalline material left.

to interplanar lattice spacing $d$ was performed according to the relation

$$d = \frac{\lambda \cdot L}{r} \tag{8.5}$$

with $\lambda$ and $L$ being the electron wavelength and the camera length, respectively [rei97]. The data reveals a very good agreement to the averaged fcc spacings of Co and Cu, the innermost circle being of [111] and the neighboured one of [200] orientation. The comparison of crystallite size of [111] and [100] grains gained from XRD analysis in figure 8.14 with the electron diffraction pattern yields a good agreement: the larger average size of [111] oriented grains results in a nearly closed diffraction circle of very high intensity whereas the [200] diffraction circle shows distinctive spots of enhanced intensity caused by single grains being larger than the mean size. Furthermore, no evidence for the diffraction of Co hcp has been found in the pattern which confirms the hypothesis that hcp crystallites are only present in the buffer layer.

After the annealing process the grain size has considerably increased both in lateral and in vertical direction. Cross-section micrographs of two different parts of the annealed sample are drawn together in figure 8.17. The lateral distribution of grain size is in the range of 15 to 140 $nm$ whereas in growth direction the grains reach from 15 to 200 $nm$ which is the whole stack. This again is in very good agreement to the average XRD crystallite size of 80 $nm$ for grains of [111] as well as [100] orientation. Besides the large grain growth another most strinking fact is the very good layer replication which can be identified in the contrast enhanced micrograph given in the lower graph of figure 8.17.

The right graph in figure 8.18 is the diffraction pattern of the annealed sample. The distorted pattern consists of very intense diffraction spots which can be attributed to fcc [100] oriented single crystallites and this pattern is superimposed on parts of polycrystalline diffraction circles caused by small crystallites. These facts concerning the electron transmission measurements are in agreement to the x-ray diffraction pattern. Due to the distortion of the pattern and the missing orientation along a zone axis a quantitative assignment of diffracted spots is not possible.

During preparation of the samples for TEM investigation another interesting fact has shown up: The layer stack of the as prepared sample removed itself from the substrate which has to be explained with the presence of large stresses of the layer stack. The annealed sample on the other hand was not stressed as much and thus it was lying plain on the substrate even after sample thinning. The occurence of stress in the samples and its importance for recrystallization will be discussed in detail in section 8.7.

The microstructural characterization mostly agrees with the findings of Hecker *et al.* [hec03]: their as prepared multilayer $[Co_{2.2\,nm}/Cu_{2.1\,nm}]_{30}/Co_{2.2\,nm}$ is also polycrystalline with a mean crystallite size of $20\,nm$ for [111] oriented grains. The ratio of hardly detectable [100] to [111] oriented grains has been quantified to 0.1. TEM analysis of their samples revealed a columnar structure with lateral grain size between 6 and $40\,nm$. The annealing at $400°C$ for 1 hour also initiated a recrystallization to a [100] coherent multilayer structure without a considerable reduction of grains in [111] direction. The [100] to[111] orientation ratio increased to 100 while the grains extended vertically through the whole stack and laterally up to $5\,\mu m$. When the annealing was performed at $500°C$ for 1 hour then the [111] crystallite fraction of their sample vanished and furthermore a starting transformation to a granular-like structure has been detected.

### 8.5.3 Multilayer Satellite Analysis

The pronounced satellites of the fcc [200] peak of the annealed samples enable the analysis of the diffraction scan with *SlerfWin* to determine the interplanar distances of the single layers, $d_{Cu}$ and $d_{Co}$ and also to yield microstructural parameters like roughness, interdiffusion and the distribution of grain sizes (see Chapter 4.2.4 for the physical principles and Chapter 4 for the description of the program.) In figure 8.19 the measurement and its calculation are shown for the samples with $t_{Cu} = 2.05\,nm$ and $t_{Cu} = 2.77\,nm$.

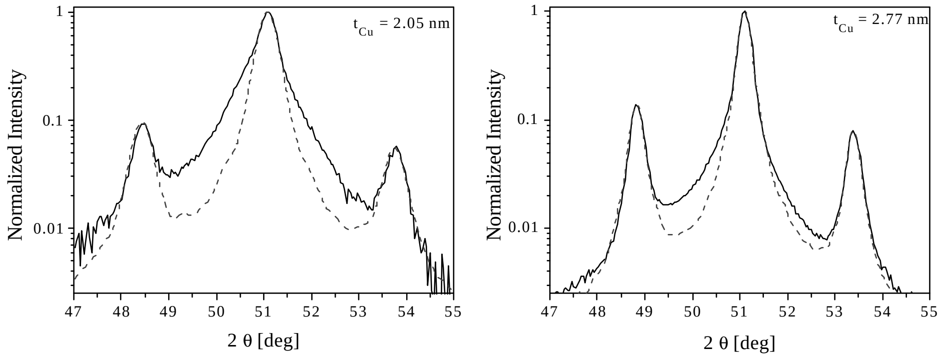

Figure 8.19: XRD measurements (full lines) in the range of multilayer satellites of the annealed samples with $t_{Cu} = 2.05\,nm$ (left) and $t_{Cu} = 2.77\,nm$ (right) and the calculation according to *SlerfWin* (dotted line). The intensity of the scans was normalized to one and the logarithmic scale enables a better view of the satellites.

Unfortunately, the analysis is complicated because of the pure Cu and Co fcc [200] peaks underneath the coherent peak, which lead to a broad and asymmetric peak shape. Altough this extraordinary profile cannot be fitted by the program care has to be taken in order not to misrepresent the results and it has to be discussed which parameters can reliably be determined by the program. The most important fact is, that the position and shape of the satellites is influenced only marginally by the additional peaks and so the interplanar distances can be safely determined. For the same reason the deviation of monolayers and the interface thickness should not be influenced to a high degree by the additional peaks. But care has to be taken with the average grain thickness and its deviation because these parameters determine the shape of the main peak.[3]

The results for the interplanar spacings $d_{Cu}$ and $d_{Co}$ in growth direction of the Cu and Co layers are shown in figure 8.20 as a function of the nominal Cu thickness. For all samples the Cu interplanar spacing is larger than the bulk value whereas the Co interplanar spacing is smaller as it would be in the bulk. This can be easily understood in terms of the coherency strains of the layers: A Co film growing on a Cu substrate, both in fcc [200] orientation, has an in plane distance smaller than the Cu substrate and this misfit is 1.97%. When growing coherently, the atoms at the interface try to adjust their in-plane distances and so the Co lattice at the interface is stretched whereas the

---

[3] The results of the peak profiling enable to eliminate the additional pure Cu and Co peaks and therefore it is possible to take the profiles determined there for the analysis with *SlerfWin* . This strategy has not been followed because the peak determination was too ambiguous. The exemplary comparison of both strategies gave exactly the same results even for the doubtful parameters. The corrected main peak profile could be fitted better than the uncorrected one but deviations in the peak base were still there.

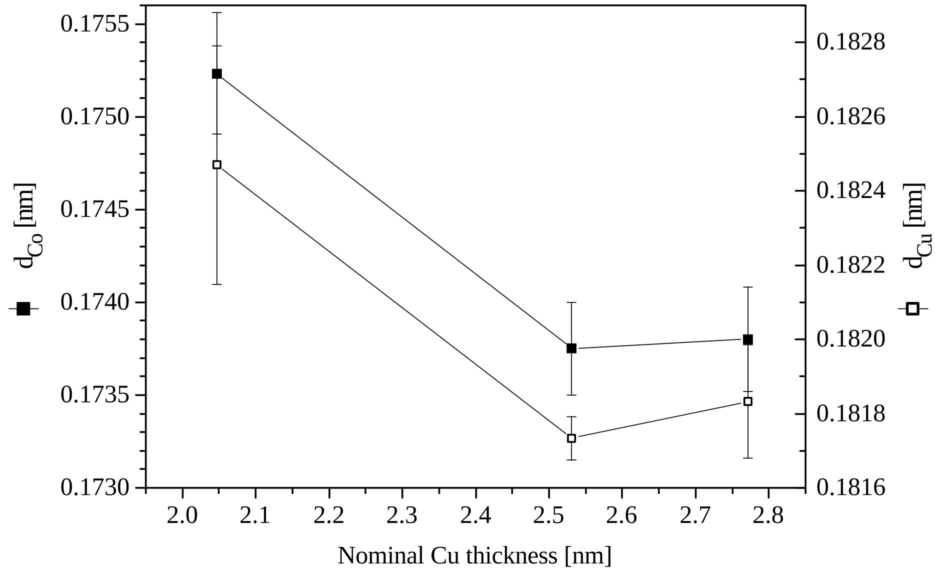

Figure 8.20: Interplanar spacing of [200] Cu (open squares) and Co (full squares) of the series $[Co_{3.8\,nm}/Cu_{t_{Cu}}/[Co_{2.0\,nm}/Cu_{t_{Cu}}]_{40}$ after annealing at $500°C$ for 1 hour, determined via fit to the XRD multilayer satellites. The bulk values are $d_{Co} = 0.17723\,nm$ and $d_{Cu} = 0.18073\,nm$ [PDF].

Cu lattice is compressed. The in-plane strain on the other hand leads to a strain in the out-of-plane direction in order to keep a constant volume of the unit cell. Therefore the interplanar distance in growth direction of the Co atoms decreases whereas the distance of the Cu atoms increases and the cubic bulk state has converted to a tetragonal cell.

How much the interplanar spacings are strained depends on the thickness of the Co layers as well as of the Cu layers. If the thickness of the layers of one material is kept constant then the strain of this layer is still dependent on the layer thickness of the neighbouring material. The thicker the neighbouring layers become the less they will adjust their interplanar spacing so as to match the other material and thus this other layer has to adjust itself more to the neighbouring interplanar distance (see figure 8.27 on page 150) [alp94]. Exactly this behaviour is revealed in the experiment when taking a look at figure 8.20 again. Although the thickness of the Co layers is kept constant, their lattice strain increases with increasing Cu thickness. For $t_{Cu} = 2.05\,nm$ and $t_{Co} = 2.0\,nm$ Co is compressed by 1.13% of its bulk value and Cu is stretched by 0.96%. When the Cu thickness is increased to $t_{Cu} = 2.53\,nm$ and $t_{Cu} = 2.77\,nm$, the strain on the Co atoms is increased to 1.96% and 1.94%, respectively, whereas the Cu strain is released to 0.55% and 0.61%, respectively. Strain in multilayers and the energy associated with it is further discussed in section 8.7.

| Fit values | | | | | Nominal values | | | | |
|---|---|---|---|---|---|---|---|---|---|
| $t_{Cu}^{fit}$ [nm] | $n_{Cu}^{fit}$ [ML] | $t_{Co}^{fit}$ [nm] | $n_{Co}^{fit}$ [ML] | $t_{DL}^{fit}$ [nm] | $t_{Cu}$ [nm] | $n_{Cu}$ [ML] | $t_{Co}$ [nm] | $n_{Co}$ [ML] | $t_{DL}$ [nm] |
| 1.80 | 9.89 | 1.88 | 10.72 | 3.68 | 2.05 | 11.33 | 1.97 | 11.14 | 4.02 |
| 2.56 | 14.10 | 1.50 | 8.62 | 4.06 | 2.53 | 14.00 | 1.97 | 11.14 | 4.50 |
| 2.67 | 14.71 | 1.62 | 9.03 | 4.29 | 2.77 | 15.34 | 1.97 | 11.14 | 4.74 |

Table 8.1: The number of monolayers $n_{Co}^{fit}$, $n_{Cu}^{fit}$ and the layer thickness $t_{Co}^{fit}$, $t_{Cu}^{fit}$ as determined by *SlerfWin*. The nominal layer thickness $t_{Co}$, $t_{Cu}$ have been determined via the sputtering rates and the nominal number of monolayers $n_{Co}$, $n_{Cu}$ have been calculated under assumption of bulk interplanar distances.

With the determination of the interplanar distances also the number of monolayers $n_{Co}$ and $n_{Cu}$ which build up one layer is given and therefore the layer thickness can be calculated. The calculated layer thickness $t_{Co}^{fit}$ and $t_{Cu}^{fit}$ is given in table 8.1 together with the nominal layer thickness which has been determined by calibration of the sputtering rates. With the assumption of bulk interplanar distances the number of monolayers for the nominal layer thickness has been calculated and is also given in the table.

The thickness values determined by the satellite fit for the Cu layers are close to the nominal ones, except for the thinnest Cu which has $0.2\,nm$ less according to the fit than it should have nominally. The fitted Co thickness on the other hand deviates considerably except for the case of thinnest Cu. The other two samples seem to “miss” about two monolayers of Cobalt each. The explanation for these results is hard to find and cannot be answered with microstructural differences between the calibration single layers and the multilayers like in chapter 6.6.2. The samples investigated here do not have a [111] texture which could explain a smaller thickness. Another possibility is a systematic error concerning the Co sputtering rate calibration due to special effects of the sputter machine such as power supply offsets: under the assumption that all Co layers have about two monolayers less than determined by calibration, the result for the sample with thinnest Cu can be interpreted as an artefact of the fit. This hypothesis is quite reasonable because this sample is the one having the smallest satellites, which can lead to ambiguous fitting results. Unfortunately, this hypothesis is hard to prove especially because the XRD scans of the as grown samples cannot be analysed with *SlerfWin* and so the initial interplanar distances and number of monolayers are not known.

Further microstructural parameters determined by the satellite fit are given in table 8.2. The satellite peak slopes are adjusted best by assuming layer

| $t_{Cu}$ [nm] | $\sigma_{Cu}$ [ML] | $\sigma_{Co}$ [ML] | $\sigma_{int}$ [ML] | $\langle D_g \rangle$ [nm] | $\sigma_{Dg}$ [nm] | $\overline{D_g}$ [nm] |
|---|---|---|---|---|---|---|
| 2.05 | 0.5 | 0.5 | 0.5 | 7.15 | 8.94 | 10.66 |
| 2.53 | 0.5 | 0.5 | 0.5 | 5.33 | 16.00 | 15.19 |
| 2.77 | 0.5 | 0.5 | 0.5 | 7.11 | 17.78 | 17.38 |

Table 8.2: Microstructural parameters determined by *SlerfWin* as a function of the nominal Cu thickness $t_{Cu}$: the monolayer deviations of Cu and Co, $\sigma_{Cu}$, $\sigma_{Co}$ according to the roughness of the interfaces; the half interface thickness $\sigma_{int}$ as a measure for interdiffusion; the average grain size $\langle D_g \rangle$ and its deviation $\sigma_{Dg}$ give the characteristics of a Gaussian distribution. The calculated mean of this distribution is given in the last column as $\overline{D_g}$.

deviations $\sigma_{Cu} = \sigma_{Co}$ of 0.5 monolayers for all three samples which means that the roughness of the layers is about $0.9\,nm$. The half interface thickness $\sigma_{int}$ is also 0.5 monolayers for all samples and so interdiffusion at the interfaces is of no great relevance. Both informations seem to be reliable: the roughness of the layers should not be too high because during the annealing process a smoothening of the interfaces might be expected in order to minimize the interfacial energy. Interdiffusion should not take place because of the miscibility gap of Co and Cu (see appendix D). The parameters determining the main peak shape are the average grain size $\langle D_g \rangle$ and its standard deviation $\sigma_{Dg}$ according to a Gaussian distribution. The results given in table 8.2 show that the average grain size is quite small. As the distribution is cut at zero grain size the true mean grain size has to be recalculated and is given as $\overline{D_g}$. This value should be comparable to the value calculated via the Scherrer equation, shown in figure 8.14.

It is obvious that the mean grain size does not correspond to the one determined via the Scherrer equation. In fact, the values determined here are a factor of 3 to 4.5 smaller. Although the determination of the crystallite sizes is hardened due to overlapping peak this clear discrepancy may be an indication for a grain distribution which does not correspond to a Gaussian one at all.

A complete analysis of the annealed samples with *SlerfWin* is not possible, because the satellites of the [111] coherent grains are too small for a reliable analysis. Furthermore, the as prepared samples do not have satellites of sufficient intensity in [111] as well as in [100] orientation.

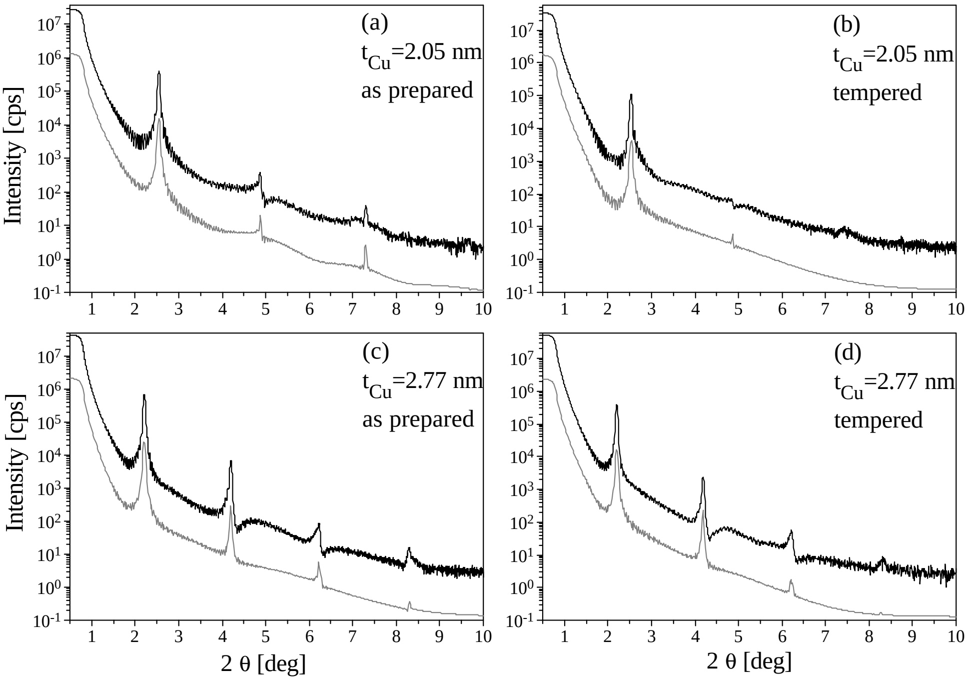

Figure 8.21: XRR measurements (black lines) and their fit (grey lines) for the samples with $t_{Cu} = 2.05\,nm$ (upper row) and $t_{Cu} = 2.77\,nm$ (lower row). The fit curve is set off for clarity.

### 8.5.4 X-Ray Reflectometry

X-ray reflectometry measurements have been performed before and after annealing of the samples and were analysed with the fitting program *WinGixa* (see Chapter 4.3.2). Due to the large number of 82 sputtered single layers the fitting procedure is based on the multilayer model stack $SiO_2//Co/[Cu/Co]_{40}/Cu/CuO$ and the thickness and roughness of the layers has been varied (11 parameters). In figure 8.21 the measurements and their fit is shown for the two samples with $t_{Cu} = 2.05\,nm$ and $t_{Cu} = 2.77\,nm$. The fitting procedure with this model allows to approximate the measured data quite well which indicates a good replication of the layers. Constraints have to be made concerning the roughness values $\sigma_{Cu}$ and $\sigma_{Co}$: they could not be attributed unambiguously to their layer but showed an exchangeable behaviour. The mean value $(\sigma_{Cu} + \sigma_{Co})/2$ on the other hand is a reliable parameter and is discussed in the following. The results are given in table 8.3.

When studying the parameters of the as prepared samples it is striking that for all three samples the Cu layer thickness is smaller than expected from sputtering calibration. The difference is about the same for all samples and its average is 0.33 nm. The Co layer thickness on the other hand is closer to the

| As prepared | | | | Tempered | | | | Difference | |
|---|---|---|---|---|---|---|---|---|---|
| $t_{Cu}$ [nm] | $t_{Co}$ [nm] | $t_{DL}$ [nm] | $\sigma^{ave}_{CuCo}$ [nm] | $t_{Cu}$ [nm] | $t_{Co}$ [nm] | $t_{DL}$ [nm] | $\sigma^{ave}_{CuCo}$ [nm] | $\Delta t_{DL}$ [nm] | $\Delta\sigma^{ave}_{CuCo}$ [nm] |
| 1.71 | 1.95 | 3.66 | 0.50 | 1.44 | 2.23 | 3.67 | 0.81 | 0.018 | 0.32 |
| 2.24 | 1.82 | 4.06 | 0.53 | 2.08 | 1.98 | 4.06 | 0.97 | 0.001 | 0.44 |
| 2.42 | 1.87 | 4.29 | 0.65 | 2.35 | 1.95 | 4.30 | 0.88 | 0.012 | 0.22 |

Table 8.3: The single layer thickness $t_{Cu}$, $t_{Co}$ and their sum, the double layer thickness $t_{DL}$ as well as the average roughness of both $\sigma^{ave}_{CuCo}$ as determined by *WinGixa*. The last two columns give the differences of double layer thickness and average roughness between the as prepared and tempered samples.

nominal value but differs a little for every sample. The mean value is $1.88 \pm 0.06$ nm and therefore it is 0.09 nm smaller than the sputter calibration value. The average roughness of the layers increases with increasing Cu thickness from 0.5 to 0.65 nm.

The parameters of the tempered samples show greatly varying layer thickness: the thinner the Cu layers of the as prepared sample, the more their thickness has changed after the annealing process. For the sample with thinnest Cu the fit value $t_{Cu}$ is decreased by $0.26\,nm$, the following sample by $0.16\,nm$ and the last sample by $0.07\,nm$ only. The double layer thickness $\Delta t_{DL}$ on the other hand has remained constant. Consequently, the Co thickness is increased after the annealing. The roughness has increased considerably to $0.89\,nm$, averaged for all annealed samples.

How do these parameters have to be interpreted? The best way to draw consequences is to compare these results with those gained by satellite analysis and also with the GMR characteristics.

The GMR measurements reveal that the layer replication of the as prepared samples must be quite good and the average roughness of $0.56\,nm$ according to the XRR fits confirms this observation. Similar values for the interface roughness have also been found by [hec01a] and [lan98] for Cu/Co multilayers with comparable GMR effect amplitude. The layer thickness determined by XRR fit on the other hand has to be taken with care: the second antiferromagnetic coupling maximum of Co/Cu multilayers is usually found in the Cu thickness range of 1.9 to $2.4\,nm$. The sample with thinnest Cu investigated here approximately shows the maximum effect amplitude of 27 % yielded by series **Bielefeld** for a Cu thickness of $1.9\,nm$. A Cu thickness below $1.8\,nm$ will give a clearly smaller GMR amplitude and a multilayer having only $t_{Cu} = 1.7\,nm$ is unlikely to yield 25 % GMR. Furthermore, the GMR amplitudes of the other samples match best with series **Bielefeld** with the nominal Cu thickness.

On the other hand, the double layer thickness determined via XRR fit is most reliable due to the double layer Bragg peak position. Additionally, there is almost perfect agreement between $t_{DL}$ determined by XRR and by multilayer satellite fit. In summary, the most probable explanation is the hypothesis stated in the previous section: the nominal Co thickness is too large due to an error of the Co sputter rate calibration.

So far, the XRR fit results of the as prepared samples have been discussed. But the layer thickness deviations are even more extraordinary when adjusting the reflectometry measurements of the samples after annealing: the Cu thickness is considerably decreased for the samples with nominal Cu thickness of 2.05 and $2.53\,nm$, for the sample with $t_{Cu} = 2.77\,nm$ this effect is not so strong. When comparing these results with those determined by satellite analysis there is no agreement and the two samples with thicker Cu have thickness values very close to the nominal ones. On the other hand, there is very good agreement between the double layer thickness and the interface roughness. In *SlerfWin* the layer deviations are 0.5 monolayers which is $0.89\,nm$ averaged for Co and Cu layers. This is in perfect agreement to the XRR fit result.

Taking into account the GMR measurements of the annealed samples, it can be seen that the extraordinary decrease of Cu thickness is related to the loss of GMR effect amplitude: the thinner the Cu the more GMR effect is lost. Therefore, the reason for the XRR fitting results may be found in the way the layer structure is changed during the annealing process and this aspect will be further discussed in the following section.

## 8.6 Discussion of Magnetoresistive, Magnetic and Microstructural Changes during Annealing

The breakdown of the GMR amplitude of the sample with thinnest Cu of nominally $2.05\,nm$ has to be explained with the destruction of the layer structure which leads to a breakdown of the antiferromagnetic coupling of the magnetic layers. Before discussing the observed changes of magnetic and transport properties of the samples during annealing, the way how such a destruction could take place is discussed.

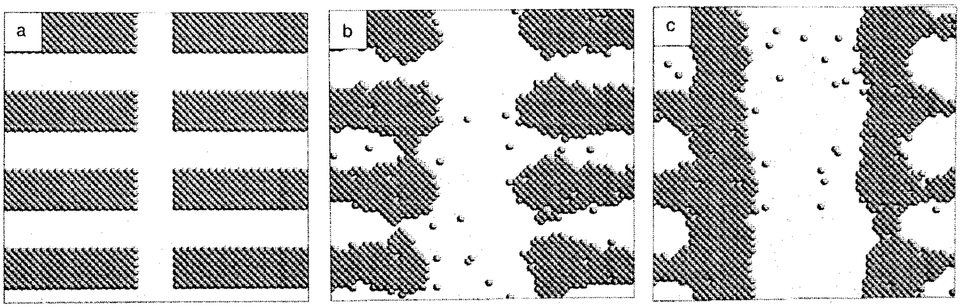

Figure 8.22: Simulated cross section view of thin slices of a Co/Cu multilayer with 11 ML thick Co and Cu layers, Co atoms are shown only. The phase morphology near a grain boundary after simultaneous break-up of all Co layers evolves from (a) initial condition, (b) formation of first magnetic short circuits, to (c) complete fusion of Co layers (from [bob01a]).

### 8.6.1 Hypothesis of Layer Destruction Mechanism

One mechanism leading to a destruction of the layered structure may be the local break-up of Co layers due to grain boundary diffusion of Cu into Co layers, which has been found experimentally by Rätzke *et al.* [rae99]. As a reason for the breaks in Co but not in Cu they suggested the higher grain boundary energy in Co and therefore the favoured diffusion of Cu atoms at Co grain boundaries occurs.

A second mechanism resulting in destructed layers without the presence of grain boundaries was found by Bobeth, Ullrich, Pompe *et al.* [pom99], [bob99], [ull00], [bob01b] who performed Monte-Carlo simulations on the thermally activated rearrangement of atoms in multilayer stacks of ideally planar initial layer structure. They found a hole formation in the material with the smaller layer thickness and proposed thermally induced roughening of the interfaces as initial mechanism, leading to lateral thickness variations as the first step. The second step is the thinning of those layer parts whith thickness smaller than a critical value due to the predominance of interface energy. The third step is the dissolution of this layer part resulting in a hole [bob99]. In the picture of our Co/Cu multilayers holes in the Co layers would not explain the decrease in antiferromagnetic coupling so far. But the Monte-Carlo simulations show furthermore, that in the later course of annealing thicker layers will thicken and that especially the parts of the broken layer directly neighboured to the hole may become bulges which grow and lead to a fusion of adjacent layers of the same material [bob01b].

Figure 8.22 shows how this process leads to shortcuts of the Co layers and explains the loss of antiferromagnetic coupling. But the simulations also reveal that the hole formation takes a longer time of annealing the thicker the layers are and that the dependence of the time during which no hole occurs exponentially depends on the thickness [ull00]. If this mechanism of hole formation would be the only reason for the breakdown of GMR observed in our multilayers, then the idea of sputtering multilayers with thicker Co should have given better results concerning the GMR after annealing. But this was not the case. Therefore it must be concluded, that there are more aspects leading to the loss of GMR.

The simulations mentioned above have been made for ideally planar interfaces as the starting point. But the experiments reveal that Co/Cu multilayers exhibit interface roughness as well as high-angle grain boundaries which extend perpendicular through many layers, leading to a distortion of the interface planarity as has been identified in the TEM micrograph in figure 8.16.

Different grain boundary energies within the two materials can cause a shrinkage of the grain boundary segments with higher energy. When taking into account the results of the Monte-Carlo simulations concerning the thermal decomposition of the layers, then it is obvious that the thinned layer parts along grain boundaries are preferred candidates for hole formation during annealing, especially as the distance between different grain boundaries is usually large compared to the thickness of the individual layers. Furthermore, Bobeth *et al.* have shown, that along such a grain boundary the formation of shortcuts is much more likely than in the course of a single layer breakthrough because bulges of many subsequent layers grow at the same lateral position [bob99]. This picture of layer deterioration is consistent with the experimental results found for samples with thicker or thinner Co at Cu thickness of $2.55\,nm$. When the Co layers form bulges around the holes which have occured along a grain boundary then the distance for the bulges to connect through the Cu layers remains the same and only the choice of thicker layers for both materials, Co and Cu may impede the process. The only objection to this model is that the hole formation itself should take a longer time in samples with thicker Co.

A further hint in answering the question of layer destruction comes from Langer *et al.* [lan99] and Larson *et al.* [lar99] who found even in Co/Cu multilayers in their as prepared state magnetic shortcuts again due to high-angle grain boundaries showing distortions in the form of vertical shifts of the layers. Figure 8.23 shows the schematics of vertical layer shift at high-angle grain boundaries in a moderate case without magnetic shortcuts.

In summary, the formation of holes and layer break up especially at grain boundaries seems to be reasonable because of the presence of grain boundaries and interface roughness. Nonetheless, no direct proof of theses hypotheses has been found within the scope of this work.

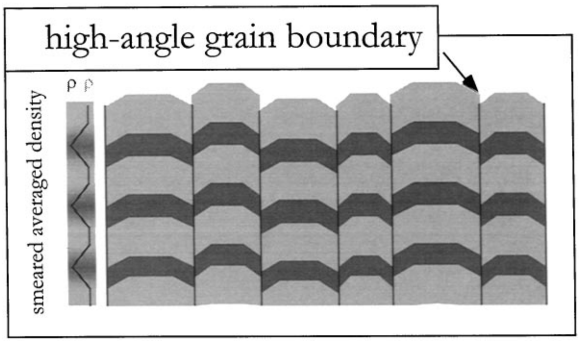

Figure 8.23: Schematic representation of columnar grains and the vertical shift of layers at high-angle grain boundaries. On the left the averaged vertical density (greyscale) and the resulting refractive index (black line) is depicted in order to explain the effect of layer shift on the rms-roughness determined via XRR (from [lan99]).

### 8.6.2 Calculation of GMR Characteristics

The program *GMRSim* calculates GMR characteristics of a model layer stack with given anisotropy constants and coupling strength. On the other hand, the adjustment of calculated to measured GMR characteristics enables to determine the anisotropy and coupling constants of the sample. With the microstructural knowledge of the Co/Cu multilayers gained in section 8.5 a model layer stack for the calculation can be drawn. The considerations are focused on the sample with thickest Cu layers of $t_{Cu} = 2.77\,nm$ because this sample is characterized by the best layer structure after annealing. No attempt was made to adjust those samples which have strongly lost GMR effect amplitude after annealing because their layer structure is not preserved and thus a calculation of GMR with *GMRSim* is not the method of choice.

The sample $Co_{3.8\,nm}/Cu_{2.77\,nm}/[Co_{2.0\,nm}/Cu_{2.77\,nm}]_{40}$ can be modeled in the following way:

As prepared: Except for the buffer layer all Co layers are grown fcc with half of the grains oriented in [111] and the other half in [100] direction (in terms of volume fraction). Therefore the crystalline anisotropy is biaxial and its value $K_{bi}$ can be assumed as half the one of purely [100] oriented grains as this direction is the hard one in fcc crystals. Because there is a magnetic field present during sputtering the grains are magnetically aligned, resulting in the biaxial anisotropy measured with AGM. This alignment is equivalent to an induced uniaxial anisotropy $K_{ind}$ with an angle $\phi_{ind}$. The bilinear antiferromagnetic coupling constant $J_L$ has to be adjusted in the range typical for Co/Cu multilayers in second AFCM and also a small biquadratic coupling constant $J_Q$ has to be taken into account due to interface roughness and / or loose spins.

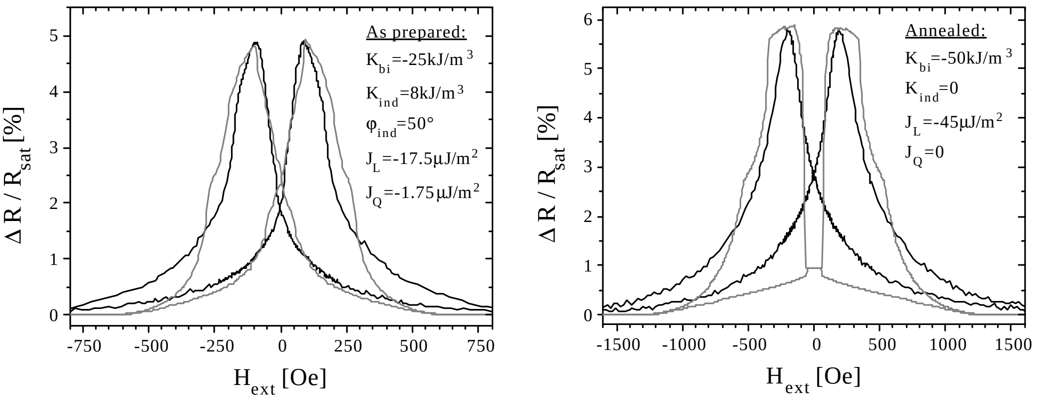

Figure 8.24: Comparison of measured GMR characteristics (black) and those calculated with *GMRSim* (grey) of the sample $Co_{3.8\,nm}/Cu_{2.77\,nm}/[Co_{2.0\,nm}/Cu_{2.77\,nm}]_{40}$ as prepared (left graph) and after annealing (right graph). The anisotropy and coupling parameters for the calculation are given in each graph.

Annealed: After the recrystallization process nearly all of the crystallites are oriented in [100] direction. Therefore, one crystalline magnetic hard direction is in the layer plane and the crystalline anisotropy constant $K_{bi}$ can be well approximated by the value for thin [100] oriented fcc Co films determined by [liu96], which is $K_{bi} = -50\,kJ/m^3$. The induced anisotropy on the other hand has vanished as the AGM measurement shows. The TEM measurements reveal a perfect layer structure and also because of the recrystallization of grains it might be concluded that no more loose spins are present and therefore $J_Q$ is zero. The only parameter to be adjusted is the bilinear coupling constant $J_L$ and this parameter should show a clear increase.

Figure 8.24 compares the measured GMR loops with the calculated ones that approximate the measurement best. The fact that such a good approximation is achieved confirms that both models assumed are close to reality.

The result for the as prepared sample clearly reveals an induced uniaxial anisotropy of $K_{ind} = -8\,kJ/m^3$ with the angle $\phi_{ind} = 50°$. The bilinear coupling constant was determined to be $J_L = -0.0175\,mJ/m^2$ and the biquadratic constant to be $J_Q = 0.1 \cdot J_L$. The bilinear coupling constant of the annealed sample has increased by a factor 2.6 to $J_L = -0.045\,mJ/m^2$.

The comparison of the values with results of other groups (see also table 2.2 on page 10) widely confirms their reasonability: Hecker *et al.* [hec03] determined the initial antiferromagnetic coupling to be $-0.015\,mJ/m^2$ for the multilayer $[Co_{2.2\,nm}/Cu_{2.1\,nm}]_{30}/Co_{2.2\,nm}$ having 24 % GMR effect amplitude.

Lenczowski *et al.* [len94] on the other hand have found the antiferromagnetic coupling constant to be $-0.068\,mJ/m^2$ for a [100] oriented sample

$[Co_{1.6\,nm}/Cu_{2.0\,nm}]_{100}$ having 40 % GMR effect amplitude at room temperature. Furthermore, they yielded an anisotropy constant of $K_1 = -80\,kJ/m^3$.

Finally, Giron *et al.* [gir92] deduced an upper limit of $-0.01\,mJ/m^2$ for the antiferromagnetic coupling strength and an anisotropy constant $K_1 = -20\,kJ/m^3$ in the [100] oriented system $[Co_{1.5\,nm}/Cu_{1.84\,nm}]_{30}$ with about 6 % GMR effect amplitude.

Therefore, the anisotropy constants determined with *GMRSim* agree well with the results of other groups and so does the antiferromagnetic coupling constant of the as prepared sample. The increase of the AF coupling during annealing has been expected because of the stronger coupling in [100] orientation and also because of the obvious improvement of the layer structure proven by TEM. But on the other hand, this increase raises further questions: if the layers are coupled that strongly and additionally their layer structure is of high quality, then why does the GMR effect amplitude not also distinctively increase? This point will be discussed in detail at the end of this section (page 143).

The microstructural findings and the GMR calculation results concerning anisotropy and coupling constants now enable to interprete the magnetic and magnetoresistance properties of the sample series:

**Magnetic Characteristics**

The saturation field $H_{Sat}$ of the samples measured with MOKE (see figure 8.9) does not only reveal the changes in antiferromagnetic coupling but also the enhancement of crystalline anisotropy with texture change to [100].

The decreasing saturation field of as prepared samples with increasing Cu thickness is a consequence of a weaker AF coupling which is proven by the evolution of the hysteresis loop slope in figure 8.10. The fact that the higher value of $H_{Sat}$ for the sample with thickest Cu does not fit into this series may be explained with the higher volume fraction of [100] oriented crystallites in this sample, accompanied by a stronger anisotropy.

The distinct increase of crystalline anisotropy during the recrystallization to [100] direction is the reason for the increase of the saturation field after annealing. Additionally, the values for $H_{Sat}$ which are increasing with $t_{Cu}$ in contrast to the as prepared samples reflect the change in AF coupling: a comparison with the squareness of the MOKE loops in figure 8.10 confirms the increasing coupling strength with Cu thickness.

The interplay of anisotropy and AF coupling sensitively affects the coercivity of the samples. The as prepared samples have a smaller coupling strength with increasing Cu thickness whereas the anisotropy of the samples is approximately constant. Therefore the coercivity is increasing with $t_{Cu}$ due to the weakening potential of the coupling force to align the magnetic layers antiparallel around zero field.

After the annealing process the clear increase of crystalline anisotropy leads to the increase of $H_C$ with almost constant values up to $t_{Cu} = 2.65\,nm$. The increased AF coupling of the sample with $t_{Cu} = 2.77\,nm$ results in a smaller value for $H_C$.

Another magnetic characteristic of the multilayers has been found while comparing different measurement techniques, and this is the inhomogenity of the as prepared samples. Due to the microstructural evolution during growth of the stack the magnetic properties of a layer depends on its position inside the stack. Additionally to their inhomogeneous layer properties the samples reveal an induced uniaxial anisotropy caused by the magnetron sputter sources. The annealing process on the other hand transformes the structure to be homogenious throughout the stack and also to loose its induced anisotropy.

### Transport Measurements

The resistance of the as prepared samples ($R_{sat,ap}$ in figure 8.7) decreases with $t_{Cu}$ which is primarily caused by shunting in the Cu layers. Also the larger grain size (and possibly a smaller defect density) of the samples is a contribution to this finding. The difference of saturation to maximum resistance $\Delta R_{ap}$ distinctively decreases with Cu thickness clearly because of the weakening antiferromagntic coupling, resulting in a decreasing GMR effect amplitude (figures 8.4 and 8.5).

After annealing the saturation resistance $R_{sat,temp}$ of all samples compared to its initial value is decreased significantly which can be attributed to the grain growth and also to healing out of defects. Furthermore it proves that no considerable interdiffusion of Co and Cu takes place, because this would enhance the resistance. The fact that the difference $\Delta R_{sat}$ becomes smaller with thicker Cu layers is a hint on the differences in microstructural modification during annealing: concerning the larger grain sizes after annealing $\Delta R_{sat}$ would have been expected to increase with $t_{Cu}$. Therefore it must be the change in layered structure that causes this finding. The TEM results indicate a good layer quality after annealing of the sample with $t_{Cu} = 2.77\,nm$. The other important fact confirmed by MOKE is that the AF coupling after annealing is decreased most for thinnest Cu, resulting in the loss of GMR effect amplitude. Finally, for samples having thin Cu layers the destruction of the layer structure accompanied by grain agglomeration of pure Co and Cu has to be attributed to the enhanced loss of saturation resistance.

### Resume

Taking all the results together it is most probable that the layer structure of the sample with thinnest Cu of $2.05\,nm$ is destroyed at least by ferromagnetic bridges between the Co layers weakening the antiferromagnetic coupling. This interpretation becomes even more evident when taking a closer look at the microstructural results: Firstly, this sample shows the smallest grain growth of all samples. Secondly, this sample has transformed the smallest volume fraction of [111] to [100].

This is a hint that much of the strain energy which increases during grain growth has initiated the formation of defects in these samples instead of turning to a crystalline transition.

Thirdly, the reflectometry data shows a strong reduction of Cu thickness after the annealing process and an according increase of the Co thickness, whereas the interface roughness has increased only as much as within the other samples. This may also be explained with the special way of layer destruction in this sample: Within the columnar grains the layer structure is of rather good quality, but during growth the grains are vertically shiftet, resulting in magnetic shortcuts. This shift may also be an explanation for the extraordinary layer thickness determined by XRR fitting: The reflectometry method averages over many grains. When the grains are shifted along each other then the XRR method detects an average density, even if each of the grains has a good interface quality. This effect is schematically depicted in figure 8.23 on page 139.

The amount of layer destruction is smaller for samples with $t_{Cu} \geq 2.5\,nm$: On one hand, these samples have formed larger grains with maintained layer structure. On the other hand, the number of defects, especially in form of magnetic bridges, is supposed to be considerably smaller due to the larger layer thickness.

The transformation to a dominating [100] orientation after annealing results in a higher crystalline anisotropy and also in an increased antiferromagnetic coupling in case of intact layer structure. Despite of the perfect layer structure and more than doubling of the AF coupling of the sample with $t_{Cu} = 2.77\,nm$ the GMR effect increased only marginally. The only explanation for this is the missing scattering potential of the sample with large grains, good layer quality and only few defects.

### Low Temperature Measurements

In order to clear up the finding of small GMR increase in spite of structural improvement of the annealed sample with $t_{Cu} = 2.77\,nm$, transport measurements down to $10\,K$ have been performed. The as prepared as well as the annealed sample have been patterned to a line of width $20\,\mu m$ and length $1.74\,mm$. The results of the experiment are given in figure 8.25.

The top graph in figure 8.25 compares the resistivity of the as prepared with that of the annealed sample for maximum magnetic field, i. e. in the configuration of parallel alignment of the magnetic layers. In this configuration the

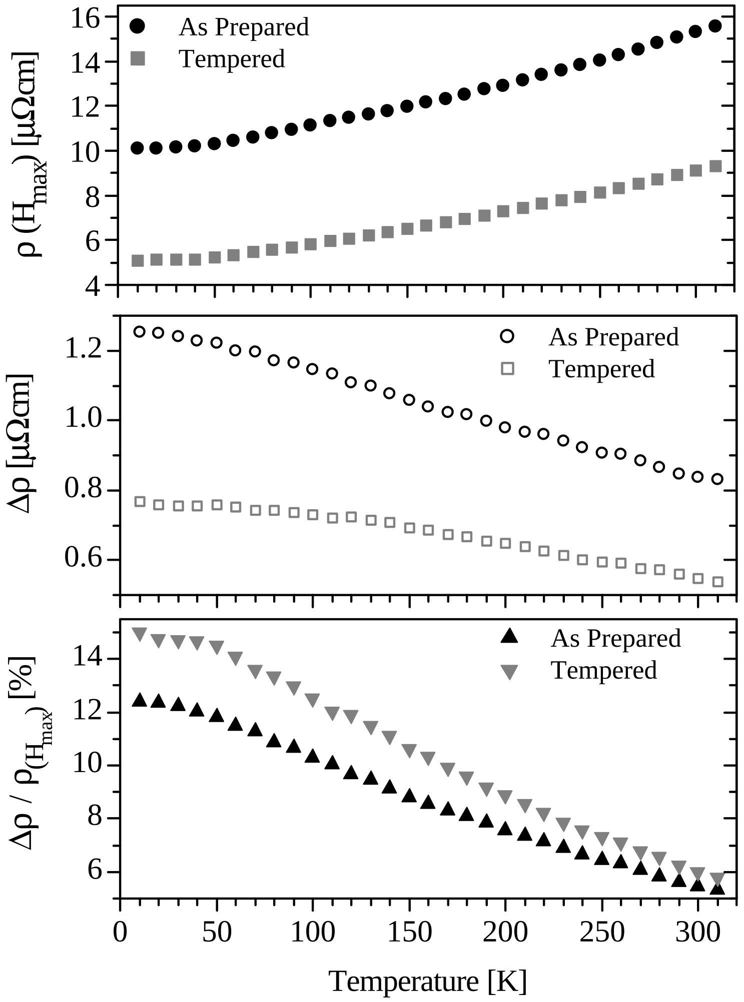

Figure 8.25: Temperature dependence of the resistivity in parallel alignment of the magnetic layers $\rho(H_{max})$, the difference between the resistivity in antiparallel and parallel configuration $\Delta\rho$, and the GMR of the sample $[Co_{3.8\,nm}/Cu_{2.77\,nm}/[Co_{2.0\,nm}/Cu_{2.77\,nm}]_{40}$ as prepared and after annealing at $500°C$ for 1 hour.

structural differences of the sample become obvious: in the course of annealing, the resistivity at $310\,K$ has decreased from $15.6\,\mu\Omega cm$ to $9.3\,\mu\Omega cm$. This resistivity drop by a factor 1.7 has already been stated in section 8.3, figure 8.7. Cooling both samples down to $10\,K$ gives a resistivity of $10.0\,\mu\Omega cm$ and $5.1\,\mu\Omega cm$ in the as prepared and annealed case, respectively. As the temperature dependent contributions of the resistivity, i. e. the phonon and spin-disorder scattering, are frozen out to a great extent at $10\,K$, the resistivity can be regarded as the residual resistivity which is a measure for the structural disorder (see chapter 3). The residual resistivity of the annealed sample is almost a factor of 2 smaller than that of the as prepared sample which indicates that in fact much of the structural disorder has vanished in the course of annealing. In detail this is the reduced number of grain boundaries which has been unambiguously proven by the TEM micrographs. Furthermore, it is reasonable that the number of dislocations is reduced and because the melting point is considerably smaller for Copper ($1083°C$) than for Cobalt ($1495°C$), it can be concluded that the annihilation of defects has been more efficiently performed in Cu than in Co. Another important scattering contribution to the residual resistivity is the roughness and intermixing of the interfaces. The experiments explained in detail in the sections above could not draw a clear picture of these properties before and after annealing, although the findings of a well defined layered structure in the TEM micrographs and of multilayer satellites in the XRD measurement of the sample with thickest Cu make clear that the structural improvement of the interfaces concerning disorder and coherency is very likely.

The difference between the resistivity in parallel $\rho(H_{max})$ and antiparallel $\rho(H_C)$ configuration of the magnetic layers, shortly denoted as $\Delta\rho$, reflects the magnetic characteristic of the multilayer correlated with the spin-dependent scattering. The quantity $\Delta\rho$, given in the middle graph of figure 8.25, is clearly larger for the as prepared sample than for the annealed sample. This finding is in perfect agreement to the discovery of chapter 6 where it has been stated that in large grains the long mean-free path prevents the electrons from being scattered in the magnetic layers unless the interfaces are rough. The annealed sample on the other hand is characterized by very large grains and smooth interfaces and is therefore not the ideal candidate for GMR. The fact that it shows a considerable GMR amplitude has to be attributed to its small residual resistance.

Another characteristic of the as prepared sample is the increasing $\Delta\rho$ with decreasing temperature whereas there is a smaller increase of this quantity for the annealed sample. The fact that the spin-dependent scattering is temperature dependent can be explained with the existence of loose spins at the interfaces: these weakly coupled spins are not aligned with the magnetization of the magnetic layer but are characterized by a fluctuating orientation at high temperatures. With decreasing temperature, these loose spins can more easily aligned with the magnetic layer and therefore do less disturb the spin-dependent scattering. The fact that $\Delta\rho$ of the as prepared sample increases more than $\Delta\rho$ of the annealed sample indicates the presence of loose spins which are reduced during annealing.

The relation of $\Delta\rho$ to $\rho(H_{max})$ gives the GMR effect amplitude, given in the lower graph of figure 8.25. At $310\,K$ the annealed sample has only a slightly larger GMR amplitude of 5.8 % compared to the as prepared sample with 5.3 %. With decreasing temperature this quantity increases up to 15.0 % for the annealed sample which is clearly higher than the amplitude of the as prepared sample with $12.4\,\%$ at $10\,K$.

In conclusion, the as prepared sample is characterized by a distinctively higher spin-dependent scattering compared to the annealed sample. In the as prepared state the microstructure with small grains and many dislocation gives rise to a high residual resistance. Although this is a priori not favourable to yield a high GMR amplitude, this kind of microstructure enables a high fraction of spin-dependent scattering. The annealed sample on the other hand profits from its reduced residual resistance. The microstructure characterized by large grains, few dislocations and coherent interfaces which enables a better antiferromagnetic coupling of the magnetic layers is not the ideal candidate to yield a large amount of spin-dependent scattering. This finding is in perfect agreement to the results of chapter 6 which stated that a very long mean free path largely prevents the electrons from being scattered inside the magnetic layers and at the interfaces. The fact that the GMR amplitude is slightly larger than that of the as prepared sample is only caused by the reduced residual resistance!

## 8.7 Elasticity Strain as the Driving Force of Recrystallization

In this final section the question shall be answered why the Co/Cu multilayers recrystallize into a [100] oriented coherent texture during the annealing at high temperatures. A possible explanation for the initiation of recrystallization is the reduction of elastic energy caused by strain and this thesis will be proven. Before the corresponding energies are calculated a short introduction into the relationship of stress and strain is given.

The way how a thin solid film of length $l$, width $w$ and thickness $t$ is stretched by the amount $\Delta l$ when an external force $F_\perp$ is applied perpendicular to the area $A = wt$ is described by *Hooke's law*

$$\sigma = Y\epsilon \tag{8.6}$$

where the tensile stress $F_\perp/A$ is usually denoted as $\sigma$ and the strain $\Delta l/l$ as $\epsilon$. $Y$ is the elasticity modulus, also called Young's modulus. Equivalently, the relationship between shear stress $F_\parallel/A = \tau$ of a force applied parallel to the area $A$ and shear strain $\delta/l = \gamma$ is given by

$$\tau = G\gamma \tag{8.7}$$

where $G$ is the shear modulus and $\delta$ is the shear displacement of the film of length $l$.

Hook's law (8.6) and (8.7) is equivalent to the spring law in mechanics. When considering a thin solid film, stress and strain are tensors since one vector of force acts on each of the three planes of the film:

$$\vec{\sigma} = \begin{pmatrix} \sigma_{xx} & \sigma_{xy} & \sigma_{xz} \\ \sigma_{yx} & \sigma_{yy} & \sigma_{yz} \\ \sigma_{zx} & \sigma_{zy} & \sigma_{zz} \end{pmatrix} \quad \text{and} \quad \vec{\epsilon} = \begin{pmatrix} \epsilon_{xx} & \epsilon_{xy} & \epsilon_{xz} \\ \epsilon_{yx} & \epsilon_{yy} & \epsilon_{yz} \\ \epsilon_{zx} & \epsilon_{zy} & \epsilon_{zz} \end{pmatrix} \tag{8.8}$$

Accordingly, the elasticity stiffness tensor $c_{ijkl}$ has $3^4 = 81$ elements:

$$\sigma_{ij} = \sum_{k,l=1}^{3} c_{ijkl}\epsilon_{kl} \tag{8.9}$$

Due to the symmetry of the tensors of elasticity strain, considerable simplifications are possible leading to the *Voigt* notation with the elastic stiffness matrix $c_{ij}$ having elements from $c_{11}$ to $c_{66}$ [san99]. Besides the elastic stiffness constant $c_{ij}$ the elastic compliance constant $s_{ij}$ is commonly used. Both are a 6 x 6 matrix that relates the stress and strain tensors:

$$\sigma = \parallel c \parallel \epsilon \quad \text{and} \quad \epsilon = \parallel s \parallel \sigma \tag{8.10}$$

The total energy involved in a strained thin film is calculated as

$$E_{elastic} = \int \sigma d\epsilon = \frac{1}{2} Y \epsilon^2 \tag{8.11}$$

which again is in analogue to the potential energy of a spring in classical mechanics.

When a film of a material with the bulk lattice constant $d_{hkl}^{film}$ is grown on a substrate with bulk lattice constant $d_{hkl}^{substrate}$, then the misfit $\eta$ between film and substrate is defined as

$$\eta = \frac{\mid d_{hkl}^{substrate} - d_{hkl}^{film} \mid}{d_{hkl}^{film}} \tag{8.12}$$

During the growth of the film on the substrate this mismatch can be relaxed by the introduction of interfacial dislocations and the film will become incoherent, i. e. the in-plane lattice constants of both materials will not approximate each other but instead the dislocations at the interface enable the film to grow with its bulk lattice constant (see upper right graph in figure 8.26). As a consequence, those films are not strained.

Incoherent growth is usually the case for material combinations having a misfit of more than 2%. If on the other hand the misfit of the two materials is less than 2% the film has a good chance to grow coherently on the substrate, i. e. the in-plane lattice constant is the same in substrate and film at the interface (see graph on lower right side in figure 8.26). But even if the mismatch of the materials is small enough to enable coherent growth also the thickness of the film determines the growth mode. Because of the strain energy being proportional to the volume of the strained material but the energy associated with dislocations being proportional to the area, there exists a critical thickness $t_c$ below which coherent growth is energetically favourable but above which the production of dislocations is favoured. This critical thickness is determined via minimization of the total energy, being the sum of elastic and edge dislocation energy and is determined as [tu92]

$$\frac{t_c}{b} = \frac{G_{hkl} x}{4\pi\eta Y_{hkl}} \left[ \ln\left(\frac{t_c}{b}\right) + 1 \right] \qquad x = 1, 2 \tag{8.13}$$

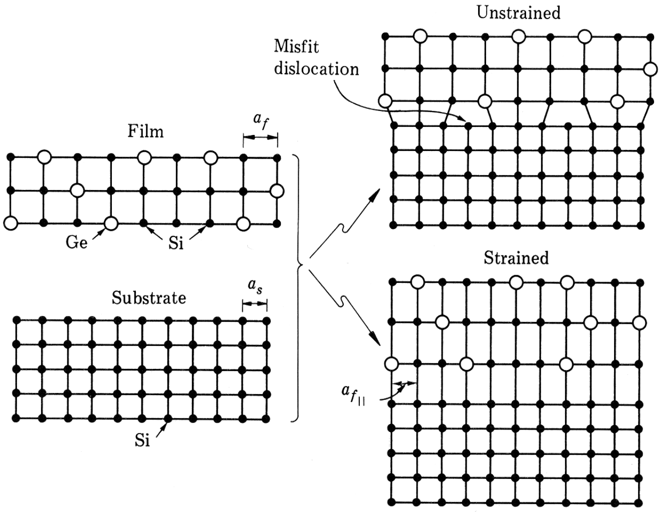

Figure 8.26: Growth characteristics of a $Ge_xSi_{1-x}$ film (upper left side) on a Si single-crystal substrate (lower left graph). The graph on the upper right depicts the case of incoherent growth with formation of misfit dislocations. The lower right graph is a diagram of coherent film growth (from [tu92]).

The factor $x$ is equal to 1 for a single thin film grown on a substrate but it is equal to 2 in case of a film sandwiches between two considerably thicker layers of the other material which both support coherent growth [joh96].

The parameter $b$ is the Burgers vector of the dislocation, $G_{hkl}$ is the shear modulus and $Y_{hkl}$ is Young's modulus:

$$\frac{1}{G_{hkl}} = s_{44} - 2\left[(s_{11} - s_{12}) - \frac{s_{44}}{2}\right]\Gamma_{hkl} \tag{8.14}$$

$$\frac{1}{Y_{hkl}} = s_{11} - 2\left[(s_{11} - s_{12}) - \frac{s_{44}}{2}\right]\Gamma_{hkl} \tag{8.15}$$

with

$$\Gamma_{hkl} = (h^2k^2 + k^2l^2 + l^2h^2) \tag{8.16}$$

where $h, k, l$ are the direction cosines that relate the direction normal to the interface. $\Gamma_{hkl}$ is 0 for the [100] orientation whereas it is 1/3 for the case of [111] direction. The elastic constants for Co [hea84] and Cu [hea79], all values given in $(TPa)^{-1}$, are

$$\begin{array}{lll} s_{11}^{Co} = 8.81 & s_{12}^{Co} = -3.51 & s_{44}^{Co} = 7.83 \\ s_{11}^{Cu} = 15.0 & s_{12}^{Cu} = -6.3 & s_{44}^{Cu} = 13.3 \end{array} \tag{8.17}$$

The critical thickness for Co and Cu is given in table 8.4. For the calculations the Burgers vector was approximated by $b_{111} = \frac{a_{film}}{\sqrt{2}}$. The values for a

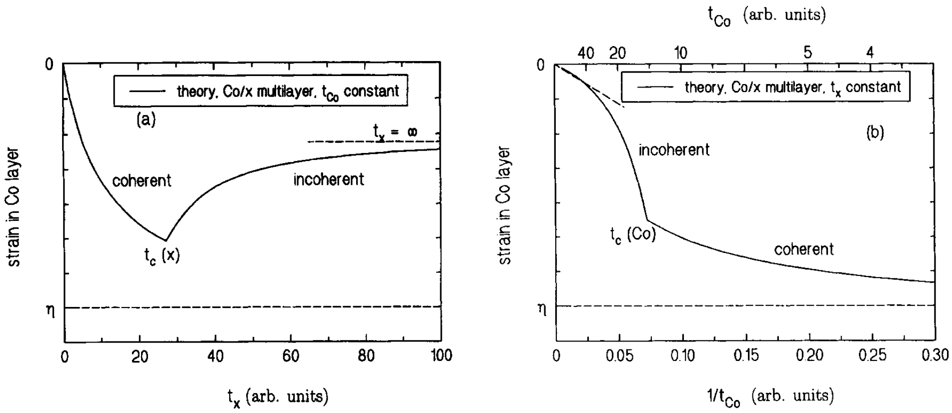

Figure 8.27: Behaviour of strain in Co layers within a multilayer made up of Co and another material x having a lattice constant $a_{Co} < a_x$. The graph on the left shows the variation of the layer thickness $t_x$ of the material x in case of a fixed Co layer thickness $t_{Co}$ and on the right the Co layer thickness at fixed $t_x$ is varied (from [alp94]).

film sandwiched between the other material are clearly larger than the single layer thickness of the multilayers investigated in the previous sections and thus coherent growth is most probable.

| | single film<br>[111] | sandwich<br>[111] | single film<br>[100] | sandwich<br>[100] |
|---|---|---|---|---|
| Co on Cu | 6.06 | 14.69 | 4.36 | 10.77 |
| Cu on Co | 6.58 | 15.90 | 4.59 | 11.30 |

Table 8.4: Critical layer thickness of Co and Cu. All values are given in *nm*.

In a multilayer of two elastic materials the strain of the layers and their critical thickness depend on the relative magnitude of the elastic constants, the thickness of the layers and the mismatch. The interplay of strain and layer thickness in a multilayer consisting of Co and another material has been investigated by van Alphen *et al.* and is shown in figure 8.27.

Now that the relationship of stress and strain in thin films and multilayers are clear, the strain energy is calculated. Coherent growth is accompanied by lattice strain: the constraint on the in-plane lattice constant leads to a distortion of the unit cell which in case of a cubic unit cell will be a tetragonal distortion. In case the film has a smaller lattice constant than the substrate the in-plane lattice constant is stretched, resulting in a reduced height of the unit cell.

The in-plane strain $\epsilon_{\|}$ is defined as

$$\epsilon_{\|} = \frac{(d_{hkl}^{film})_{\|} - d_{hkl}^{bulk}}{d_{hkl}^{bulk}} \tag{8.18}$$

where $(d_{hkl}^{film})_{\|}$ is the in-plane lattice constant of the deposited film material, $d_{hkl}^{bulk}$ on the other hand is the lattice constant in the bulk or unstrained state. In a XRD measurement only the out-of-plane lattice constant $(d_{hkl}^{film})_{\perp}$ can be determined but not the in-plane lattice constant $(d_{hkl}^{film})_{\|}$. Therefore, the relationship between out-of-plane and in-plane strain is useful [san99]:

$$\epsilon_{\|} = -\frac{1}{2}\frac{c_{11}^{film}}{c_{12}^{film}}\epsilon_{\perp} \tag{8.19}$$

with

$$\epsilon_{\perp} = \frac{(d_{hkl}^{film})_{\perp} - d_{hkl}^{bulk}}{d_{hkl}^{bulk}} \tag{8.20}$$

The elastic energy per area of the film, given in equation 8.11, can be shown to be

$$E_{elastic} = (\epsilon_{\|})^2 B_{hkl} t \tag{8.21}$$

for a cubic crystal [tu92], where t is the film thickness and $B_{hkl}$ is a function of the elastic constants, depending on the growth direction:

$$B_{hkl} = \left(\frac{c_{11} + 2c_{12}}{2}\right)\left[3 - \frac{(c_{11} + 2c_{12})}{c_{11} + 2(2c_{44} - c_{11} + c_{12})\Gamma_{lmn}}\right] \tag{8.22}$$

with

$$\Gamma_{lmn} = (l^2m^2 + m^2n^2 + n^2l^2) \tag{8.23}$$

where $l, m, n$ are the direction cosines that relate the direction normal to the interface. $\Gamma_{lmn}$ is 0 for the [100] direction whereas it is 1/3 for the case of [111] orientation. In this case equation 8.22 is simplified to

$$B_{100} = \frac{(c_{11} + 2c_{12})(c_{11} - c_{12})}{c_{11}} \tag{8.24}$$

$$B_{111} = \frac{6(c_{11} + 2c_{12})c_{44}}{c_{11} + 2c_{12} + 4c_{44}} \tag{8.25}$$

For the calculation of the total strain energy of a Co/Cu multilayer with $N$ double layers the strain energies of every layer have to be added up:

$$
\begin{aligned}
E^{total}_{elastic} &= N[B^{Cu}_{hkl} \cdot t_{Cu} \cdot (\epsilon^2_{Cu})_{\|} + B^{Co}_{hkl} \cdot t_{Co} \cdot (\epsilon^2_{Co})_{\|}] \\
&= \frac{N}{2} \cdot B^{Cu}_{hkl} \cdot t_{Cu} \cdot \frac{C^{Cu}_{11}}{C^{Cu}_{12}} \cdot \left( \frac{(d^{Cu\text{-}film}_{hkl})_{\perp} - d^{Cu-bulk}_{hkl}}{d^{Cu-bulk}_{hkl}} \right)^2 \\
&+ \frac{N}{2} \cdot B^{Co}_{hkl} \cdot t_{Co} \cdot \frac{C^{Co}_{11}}{C^{Co}_{12}} \cdot \left( \frac{(d^{Co\text{-}film}_{hkl})_{\perp} - d^{Co-bulk}_{hkl}}{d^{Co-bulk}_{hkl}} \right)^2
\end{aligned} \tag{8.26}
$$

Now the calculations for Co/Cu multilayers are made:

The bulk lattice constants for fcc Cobalt and Copper are $a^{Co} = 0.35447\,nm$ and $a^{Cu} = 0.36146\,nm$. The misfit can be calculated to be

$$
\eta^{\text{Cu on Co}} = 1.94\% \qquad \text{and} \qquad \eta^{\text{Co on Cu}} = 1.97\% \tag{8.27}
$$

The elastic constants for Co [hea84] and Cu [hea79] and the corresponding values for the constant $B$, all values given in $GPa$, are

$$
\begin{array}{lll}
c^{Co}_{11} = 242 & c^{Co}_{12} = 160 & c^{Co}_{44} = 128 \\
c^{Cu}_{11} = 169 & c^{Cu}_{12} = 122 & c^{Cu}_{44} = 75.3
\end{array} \tag{8.28}
$$

$$
\begin{array}{ll}
B^{Co}_{100} = 288.025 & B^{Co}_{111} = 401.877 \\
B^{Cu}_{100} = 114.858 & B^{Cu}_{111} = 261.262
\end{array} \tag{8.29}
$$

The experiments treated in the previous sections revealed, that Co/Cu multilayers consist of grains in [111] as well as in [100] orientation with corresponding volume fractions $Vol_{[111]}$ and $Vol_{[100]}$ which have been determined via profile fitting of the XRD scans. Therefore, the total elastic energy (8.26) of the sample is given by

$$
\begin{aligned}
E^{total}_{elastic} &= Vol_{[111]} \cdot E^{111}_{elastic} + Vol_{[100]} \cdot E^{100}_{elastic} \\
&= Vol_{[111]} \cdot \frac{N}{2} \cdot B^{Cu}_{111} \cdot t_{Cu} \cdot \frac{C^{Cu}_{11}}{C^{Cu}_{12}} \cdot \left( \frac{(d^{Cu-film}_{111})_{\perp} - d^{Cu-bulk}_{111}}{d^{Cu-bulk}_{111}} \right)^2 \\
&+ Vol_{[111]} \cdot \frac{N}{2} \cdot B^{Co}_{111} \cdot t_{Co} \cdot \frac{C^{Co}_{11}}{C^{Co}_{12}} \cdot \left( \frac{(d^{Co-film}_{111})_{\perp} - d^{Co-bulk}_{111}}{d^{Co-bulk}_{111}} \right)^2 \\
&+ Vol_{[100]} \cdot \frac{N}{2} \cdot B^{Cu}_{100} \cdot t_{Cu} \cdot \frac{C^{Cu}_{11}}{C^{Cu}_{12}} \cdot \left( \frac{(d^{Cu-film}_{100})_{\perp} - d^{Cu-bulk}_{100}}{d^{Cu-bulk}_{100}} \right)^2 \\
&+ Vol_{[100]} \cdot \frac{N}{2} \cdot B^{Co}_{100} \cdot t_{Co} \cdot \frac{C^{Co}_{11}}{C^{Co}_{12}} \cdot \left( \frac{(d^{Co-film}_{100})_{\perp} - d^{Co-bulk}_{100}}{d^{Co-bulk}_{100}} \right)^2
\end{aligned} \tag{8.30}
$$

If the out-of plane lattice constants $(d_{hkl}^{film})_\perp$ for Co and Cu in [100] as well as in [111] orientation are known for the as prepared and the annealed state, then the difference in elastic energy of both states can be calculated. Based on XRD scans, these lattice constants can only be determined via a fit to the superlattice satellites and furthermore, for a reliable fit the intensity of the satellites must not be too small. Unfortunately, this criterion is fulfilled only for the superlattice satellites of [100] orientation after the annealing process and thus solely the parameters $(d_{100}^{Co-film})_\perp$ and $(d_{100}^{Cu-film})_\perp$ can be determined, as was done in the previous section (figure 8.20). For the annealed samples this is not too bad because the [100] orientation is the one having the main volume fraction in the samples. But the as prepared samples consist of [111] and [100] orientation to about equal fractions and therefore the calculation of the elastic energy based on experimental lattice constants is not possible. In spite of these difficulties an estimation of energy gain during recrystallization can be made on the basis of the volume fraction of the different orientations in the samples:

Under equal strain, the elastic energy in a [111] oriented Co/Cu material is higher than the energy in a [100] structure due to the elastic properties of the materials which is revealed in the values for the constant $B$, see equation 8.29. The interplanar distances $(d_{100}^{Co-film})_\perp$ and $(d_{100}^{Cu-film})_\perp$ have been determined experimentally and as the same unit cell is concerned in [111] oriented grains, the approximation of equal relative strain in both orientations is made:

$$(\epsilon_{100}^{Co})_\perp = (\epsilon_{111}^{Co})_\perp \quad \text{and} \quad (\epsilon_{100}^{Cu})_\perp = (\epsilon_{111}^{Cu})_\perp \tag{8.31}$$

Then equation 8.30 simplifies to

$$\begin{aligned} E_{elastic}^{total} &= \\ & \frac{N}{2} \cdot \frac{C_{11}^{Co}}{C_{12}^{Co}} \cdot t_{Co} \cdot \left(\epsilon_\perp^{Co}\right)^2 \left(Vol_{[100]} \cdot B_{100}^{Co} + Vol_{[111]} \cdot B_{111}^{Co}\right) \\ + & \frac{N}{2} \cdot \frac{C_{11}^{Cu}}{C_{12}^{Cu}} \cdot t_{Cu} \cdot \left(\epsilon_\perp^{Cu}\right)^2 \left(Vol_{[100]} \cdot B_{100}^{Cu} + Vol_{[111]} \cdot B_{111}^{Cu}\right) \end{aligned} \tag{8.32}$$

where the volume fractions of as prepared and annealed samples have been determined in the previous section, see figure 8.15. Furthermore, for the calculation the film thickness as determined by XRR on the as prepared samples (table 8.3) has been taken and the difference in energy was calculated per interface atom. The results are given in figure 8.28.

The calculations show that in fact a considerable reduction of elastic energy in the order of $0.8\,eV$ per interface atom is achieved by recrystallization into a [100] texture. On the other hand, the dislocation energy in a film averaged

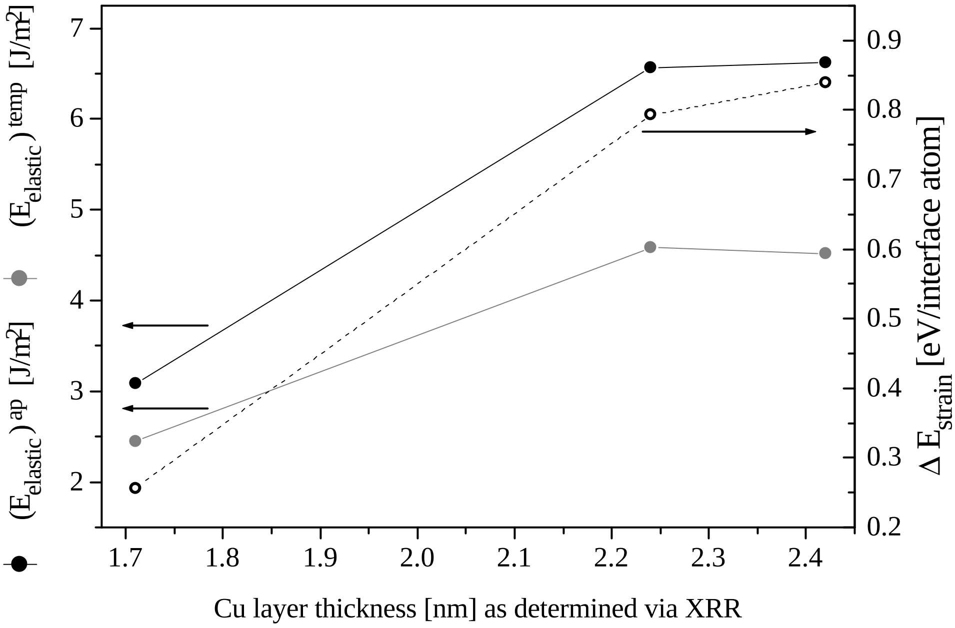

Figure 8.28: Elastic energy of as prepared and annealed samples (left scale) and the difference of energy per interface atom (right scale).

over all atoms is in the order of $10^{-6}\,eV$ per atom [tu92]. Compared to the energy that the annihilation of dislocations would yield, the gain of elastic strain energy due to recrystallization is incredibly larger and can therefore be regarded as the driving force for recrystallization.

For the reason of completeness it shall be mentioned, that additionally to the loss of elastic energy the samples will lose dislocation energy due to the annihilation of defects as well as grain boundary energy due to grain growth.

## 8.8 Conclusion

In this chapter the phenomenon of recrystallization of Co/Cu multilayers during annealing at sufficient high temperatures around $500°C$ has been investigated. The adequate choice of Co and Cu layer thickness enables to produce a multilayer stack which preserves or even enhances its GMR effect amplitude after the initial annealing process. Furthermore, it has been proven that after the recrystallization these multilayers are long term stable up to temperatures below the inital annealing temperature. From the point of view of technical application these multilayer systems are the ideal candidates for the integration in back-end process where the short-term annealing is performed and afterwards they are suited as GMR sensors in hot environments.

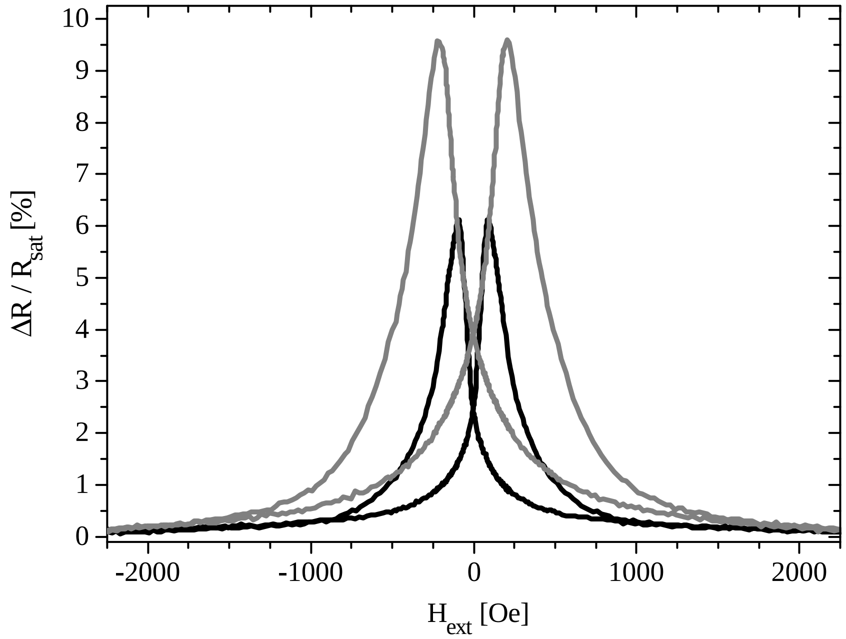

Figure 8.29: Sample $Co_{3.8\,nm}/Cu_{2.65\,nm}/[Co_{2.0\,nm}/Cu_{2.65\,nm}]_{40}$ as prepared (black) and after annealing at 400°$C$ for 1hour (grey). In contrast to the samples investigated in the sections above this one was positioned differently above the sputter source.

Additionally to the finding of "ultimate temperature stability" for the first time a closed interpretation model of layer degradation and recrystallization has been given that links the results of transport, magnetic and microstructure measurements and reveals the interplay of layer quality, grain size and orientation with crystalline anisotropy, antiferromagnetic coupling and GMR.

Finally, it is important to note that the increase in GMR effect amplitude discussed in the sections above is not the end of the line. Figure 8.29 presents the highest increase in GMR effect amplitude from 6 % as prepared up to 9.5 % after annealing that has been found in the experiments. This sample has the same stacking sequence and layer thickness of $t_{Co} = 2.0\,nm$ and $t_{Cu} = 2.65\,nm$ like the one investigated in the previous sections, but its position relative to the sputtering source was slightly different. Although the annealing temperature was only 400°$C$ this is not the reason for the higher increase which has been proven by tests concerning the annealing temperatures. Besides the long-term temperature stability and the possibility of back-end processing the GMR amplitude of 9.5 % is a further well-suited characteristic for the application.

# Chapter 9

# Summary

For the first time in Co/Cu multilayer research a study has been performed which compares sample series that have been prepared in three different laboratories and which comprises a very large number of samples of each series that have been varied in spacer thickness, magnetic layer thickness, buffer thickness and number of double layers. The aim of the first experimental part of the thesis was to overcome the laboratory-limited point of view in concern of the interdepence of microstructure and GMR and to identify the ideal type of microstructure that has the potential to yield large GMR effect amplitudes.

The investigation of the sample series revealed that the nature of the ideal microstructure cannot be reduced to one parameter but that it is the interplay of grain size, defect density and type of defects with the interface roughness which determines the proportion of spin-dependent transport. The explanation for this finding has been given in terms of the optimum combination of mean-free path and spin-diffusion length.

It has been found that moderately large grains together with a moderate interface roughness obtain the largest GMR amplitudes and that smaller grains combined with smooth interfaces also yield good GMR effect.

Based on these insights into the transport properties it can be concluded that the ideal GMR multilayer microstructure is characterized by smooth interfaces together with a lattice defect structure that scatters specularly to its greatest part. Smooth interfaces enable highest antiferromagnetic exchange coupling and do not have loose spins which disturb the spin-dependent scattering. Specular scattering guarantees that the electrons in the spacer will effectively reach the next magnetic layer on the shortest way.

The variation of the number of double layers that make up the multilayer stack revealed non-antiferromagnetically coupled undermost bilayers of different number depending on the preparation laboratory. This is in contrast to antiferromagnetically coupled trilayers having a GMR effect amplitude of 11 %. The investigation of multilayers with reduced number of double layers in the second experimental part of this thesis has proven the need for the adjustment of the buffer as well as the Co and Cu thickness in order to gain antiferromagnetic coupling in the presence of only few bilayers. The control of the grain growth of the first layers has been identified as one cruicial point of this finding together with the increased role of outer boundary scattering and with the reduced influence of shunting.

For layer stacks with only a few double layers, thicknesses different from those for multilayers are needed. Thus, multilayers have been prepared in which the optimized bilayers are added up. Although the antiferromagnetic coupling of the undermost layers has been achieved this did not enhance the GMR of the corresponding multilayer with many bilayers because of the increased shunting of the undermost layers. To the best of my knowledge, there has not been performed a comparable study in the literature before.

The third experimental part of this thesis was dedicated to the discovery of a peculiar recrystallization of Co/Cu multilayers in the course of a short-time high-temperature annealing. It has been proven that the adequate choice of Co and Cu thickness in the multilayer stack enables to preserve and even enhance the GMR effect amplitude during the process of recrystallization. The long-term temperature stability of the recrystallized samples has been proven and with it a Co/Cu multilayer system has been presented wich is ideally suited for the application in hot environments.

A closed model has been given for the mechanism of layer degradation in those multilayers having unsuited layer thickness as well as for the recrystallization in appropriate systems. It links the results of transport, magnetic and microstructure measurements with the interplay of layer quality, grain size and texture with crystalline anisotropy, antiferromagnetic exchange coupling and GMR. The results of the first experimental part of this thesis concerning the interplay of microstructure and GMR have been completely confirmed for the recrystallized multilayers having an extraordinary large grain size. The investigation of the recrystallization process has been completed by the determination of lattice strain at the Co/Cu interfaces as being its driving force.

# Appendix A

# Useful Relations for X-Rays

Wavelength and photon energy relationship:

$$E = h\nu = h\frac{c}{\lambda} = \frac{1.239434 \cdot 10^{-4} eV}{\lambda[cm]} \tag{A.1}$$

For $CuK_{\alpha_1}$ radiation the wavelength and energy are:

$\lambda_{CuK_{\alpha_1}} = 1.5406 \cdot 10^{-8} cm$

$E_{CuK_{\alpha_1}} = 8.045 keV$

The absorption of x-rays in a material with thickness $t$ is described via the equation

$$I_t = I_0 \exp(-\mu t) \tag{A.2}$$

where $I_0$ is the incoming intensity of the x-ray beam, $I_t$ is the intensity transmitted and $\mu[\frac{1}{cm}]$ is the linear absorption coefficient.

When dividing $\mu$ by the density $\rho$ of the given material the mass absorption coefficient $\frac{\mu}{\rho}[\frac{cm^2}{g}]$ is yielded, which is a quantity independent of the physical and chemical state of the material [klu74].

# Appendix B

# Optical Constants

The optical constants of the elements and compounds used in the multilayer stacks investigated are given in table B.1 for the $CuK_{\alpha_1}$ wavelength $\lambda = 0.15406nm$. For the calculation of $\delta$ and $\beta$ (see equations (4.38) and (4.39)) of the compounds the weighted average of $f_1$, $f_2$ and the atomic weight of the constituting elements are taken and the density has to be known.

| Element<br>Compound | $f_1$ | $f_2$ | $\delta$<br>$[10^{-5}]$ | $\beta$<br>$[10^{-6}]$ | $\rho$<br>$[g/cm^3]$ | $\Theta_c$<br>[deg] |
|---|---|---|---|---|---|---|
| Si | 14.3 | 0.325 | 0.7606 | 0.1729 | 2.33 | 0.223 |
| Fe | 24.85 | 3.21 | 2.2472 | 2.9022 | 7.87 | 0.384 |
| Co | 24.61 | 3.564 | 2.3834 | 3.4510 | 8.90 | 0.396 |
| Ni | 25.01 | 0.5243 | 2.4324 | 0.5099 | 8.90 | 0.400 |
| Cu | 27.03 | 0.6079 | 2.4437 | 0.5496 | 8.96 | 0.401 |
| Ag | 47.18 | 4.266 | 2.9447 | 2.6631 | 10.50 | 0.440 |
| Au | 74.99 | 7.721 | 4.7166 | 4.8562 | 19.30 | 0.556 |
| $SiO_2$ | 10.12 | 0.131 | 0.7136 | 0.0921 | 2.20 | 0.216 |
| $Ni_{81}Fe_{19}$ | 24.98 | 1.035 | 2.3968 | 0.9927 | 8.70 | 0.397 |
| $Co_{90}Fe_{10}$ | 24.63 | 3.529 | 2.3696 | 3.3942 | 8.80 | 0.394 |
| $Cu_{85}Ag_{10}Au_5$ | 31.44 | 1.329 | 2.6005 | 1.0994 | 9.63 | 0.413 |

Table B.1: $f_1 = f_0 + \Delta f'$ and $f_2 = \Delta f''$, the real and imaginary part of the atomic scattering factor, respectively, the optical constants $\delta$, $\beta$ and the density $\rho$ of the elements and compounds are taken from [cxro]. These values were used as starting values for the fitting of the reflectivity scans with WinGixa. Additionally the critical angle $\Theta_c$ is given, which has been calculated according to $\Theta_c = \sqrt{2\delta}$.

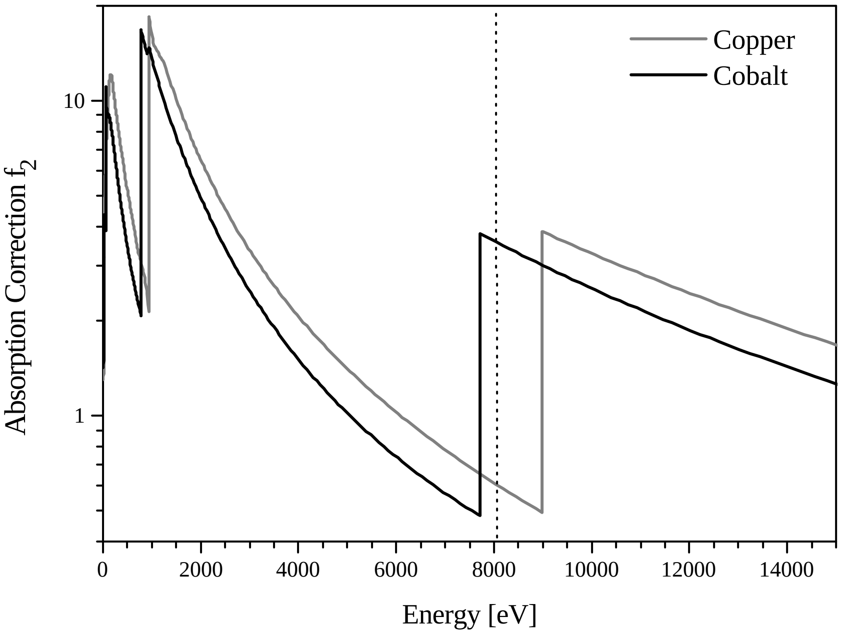

Figure B.1: Absorption edges of Cobalt (black) and Copper (grey). The dotted grey line marks the energy of 8046 eV corresponding to $CuK_\alpha$ radiation. From [cxro].

Figure (B.1) shows the absorption correction $f_2$ of Copper and Cobalt. The corresponding energy of $CuK_\alpha$ radiation is in the middle between two absorption edges.

# Appendix C

# Crystal Structures and Powder Diffraction Files

The following tables give crystallographic information on the materials of which the investigated multilayers have been built up. The angle of diffraction $2\,\Theta$ has been calculated for $\lambda = 1.54184\,\text{Å}$ (Cu $K_{average}$), according to Bragg's law. In case the lattice constant $a$ was not taken from the Powder Diffraction File but from [mas90] this is indicated in the table. The intensity of diffraction signal was taken from [PDF] and is given for a fixed divergence slit as well as for the variable one.

| **Crystal Structures and Lattice Parameters** | | | | | | |
|---|---|---|---|---|---|---|
| Element | T [$^\circ C$] | P [$GPa$] | Pearson | Space Group | $a[nm]$ | $c[nm]$ |
| $\epsilon$Co | 25 | atm | $hP2$ | $P6_3/mmc$ | 0.25071 | 0.40686 |
| $\alpha$Co | $> 422$ | atm | $cF4$ | $Fm\overline{3}m$ | 0.35447 | |
| Cu | 25 | atm | $cF4$ | $Fm\overline{3}m$ | 0.36146 | |
| $\alpha$Fe | 25 | atm | $cI2$ | $Im\overline{3}m$ | 0.28665 | |
| $\gamma$Fe | $> 912$ | atm | $cF4$ | $Fm\overline{3}m$ | 0.36467 | |
| $\delta$Fe | $> 1394$ | atm | $cI2$ | $Im\overline{3}m$ | 0.29315 | |
| $\epsilon$Fe | 25 | $> 13$ | $hP2$ | $P6_3/mmc$ | 0.2468 | 0.396 |
| Ni | 25 | atm | $cF4$ | $Fm\overline{3}m$ | 0.35240 | |

Table C.1: Crystal Structures and Lattice Parameters $a$, $c$ of Allotropes of the Metallic Elements at temperature T and Pressure P [mas90].

<table>
<tr><th colspan="5"><b>Copper</b><br>fcc, $a = 3.6146$ Å [mas90]</th></tr>
<tr><th>$hkl$</th><th>$d_{hkl}$ [Å]</th><th>$2\,\Theta$ [deg]</th><th>$I_{fixed}$ [%]</th><th>$I_{variable}$ [%]</th></tr>
<tr><td>1 1 1</td><td>2.0869</td><td>43.359</td><td>100</td><td>100</td></tr>
<tr><td>2 0 0</td><td>1.8073</td><td>50.499</td><td>46</td><td>53</td></tr>
<tr><td>2 2 0</td><td>1.2780</td><td>74.205</td><td>20</td><td>33</td></tr>
<tr><td>3 1 1</td><td>1.0898</td><td>90.042</td><td>17</td><td>33</td></tr>
<tr><td>2 2 2</td><td>1.0434</td><td>95.262</td><td>5</td><td>10</td></tr>
<tr><td>4 0 0</td><td>0.9037</td><td>117.105</td><td>3</td><td>7</td></tr>
<tr><td>3 3 1</td><td>0.8292</td><td>136.765</td><td>9</td><td>23</td></tr>
</table>

Table C.2: Copper [PDF, # 04-0836].

<table>
<tr><th colspan="5"><b>$\alpha$-Cobalt</b><br>fcc, $a = 3.5447$ Å</th></tr>
<tr><th>$hkl$</th><th>$d_{hkl}$ [Å]</th><th>$2\,\Theta$ [deg]</th><th>$I_{fixed}$ [%]</th><th>$I_{variable}$ [%]</th></tr>
<tr><td>1 1 1</td><td>2.0465</td><td>44.258</td><td>100</td><td>100</td></tr>
<tr><td>2 0 0</td><td>1.7723</td><td>51.567</td><td>40</td><td>46</td></tr>
<tr><td>2 2 0</td><td>1.2532</td><td>75.924</td><td>25</td><td>41</td></tr>
<tr><td>3 1 1</td><td>1.0688</td><td>92.327</td><td>30</td><td>57</td></tr>
<tr><td>2 2 2</td><td>1.0233</td><td>97.770</td><td>12</td><td>24</td></tr>
</table>

Table C.3: $\alpha$-Cobalt [PDF, # 15-0806].

| **$\epsilon$-Cobalt**<br>hcp, $a = 2.5071\,\text{Å}$, $c = 4.0686\,\text{Å}$ [mas90] | | | | |
|---|---|---|---|---|
| $hkl$ | $d_{hkl}$ [Å] | $2\,\Theta$ [deg] | $I_{fixed}$ [%] | $I_{variable}$ [%] |
| 1 0 0 | 2.1712 | 41.595 | 20 | 12 |
| 0 0 2 | 2.0343 | 44.539 | 60 | 40 |
| 1 0 1 | 1.9155 | 47.464 | 100 | 70 |
| 1 0 2 | 1.4845 | 62.572 | 1 | 1 |
| 1 1 0 | 1.2535 | 75.902 | 80 | 85 |
| 1 0 3 | 1.1502 | 84.168 | 80 | 93 |
| 2 0 0 | 1.0856 | 90.491 | 20 | 25 |
| 1 1 2 | 1.0672 | 92.502 | 80 | 100 |
| 2 0 1 | 1.0489 | 94.610 | 60 | 76 |
| 0 0 4 | 1.0172 | 98.563 | 20 | 26 |

Table C.4: $\epsilon$-Cobalt [PDF, # 05-0727].

| **$\alpha$-Iron**<br>bcc, $a = 2.8665\,\text{Å}$ | | | | |
|---|---|---|---|---|
| $hkl$ | $d_{hkl}$ [Å] | $2\,\Theta$ [deg] | $I_{fixed}$ [%] | $I_{variable}$ [%] |
| 1 1 0 | 2.0269 | 44.710 | 100 | 100 |
| 2 0 0 | 1.4333 | 65.079 | 20 | 28 |
| 2 1 1 | 1.1702 | 82.412 | 30 | 52 |
| 2 2 0 | 1.0135 | 99.048 | 10 | 20 |
| 3 1 0 | 0.9065 | 116.525 | 12 | 27 |
| 2 2 2 | 0.8275 | 137.384 | 6 | 15 |

Table C.5: $\alpha$-Iron [PDF, # 06-0696].

**Cobalt-Iron** $Co_{90}Fe_{10}$

fcc, $a = 3.5549\,\text{Å}$ [mas90]

| $hkl$ | $d_{hkl}$ [Å] | $2\,\Theta$ [deg] | $I^*_{fixed}$ [%] | $I^*_{variable}$ [%] |
|---|---:|---:|---:|---:|
| 1 1 1 | 2.0524 | 44.125 | 100 | 100 |
| 2 0 0 | 1.7775 | 51.408 | 40 | 46 |
| 2 2 0 | 1.2568 | 75.668 | 25 | 41 |
| 3 1 1 | 1.0718 | 91.985 | 30 | 57 |
| 2 2 2 | 1.0262 | 97.394 | 12 | 24 |

Table C.6: $Co_{90}Fe_{10}$. Lattice constant calculated from pure Materials Co and Fe according to Vegard's law with Fe fcc $a = 3.6467\,\text{Å}$ and Co fcc $a = 3.5447\,\text{Å}$ [mas90]. $^*$ intensities refer to pure $\alpha$-Cobalt [PDF, # 15-0806].

**Permalloy** $(Ni_{81}Fe_{19})$

fcc, $a = 3.54854\,\text{Å}$ [mas90]

| $hkl$ | $d_{hkl}$ [Å] | $2\,\Theta$ [deg] | $I^*_{fixed}$ [%] | $I^*_{variable}$ [%] |
|---|---:|---:|---:|---:|
| 1 1 1 | 2.0488 | 44.208 | 100 | 100 |
| 2 0 0 | 1.7743 | 51.507 | 60 | 69 |
| 2 2 0 | 1.2546 | 75.828 | 30 | 49 |
| 3 1 1 | 1.0699 | 92.198 | 40 | 76 |
| 2 2 2 | 1.0244 | 97.628 | 10 | 20 |
| 4 0 0 | 0.8871 | 120.685 | - | - |
| 3 3 1 | 0.8141 | 142.514 | 10 | 25 |

Table C.7: Permalloy. Lattice constant calculated from pure Materials Ni and Fe according to Vegard's law with Fe fcc $a = 3.6467\,\text{Å}$ and Ni fcc $a = 3.5240\,\text{Å}$ [mas90]. $^*$ intensities refer to the alloy $FeNi_3$ ([PDF, #38-0419]).

| **Silicon**<br>fcc, $a = 5.43088\,\text{Å}$ | | | | |
|---|---|---|---|---|
| $hkl$ | $d_{hkl}$ [Å] | $2\,\Theta$ [deg] | $I_{fixed}$ [%] | $I_{variable}$ [%] |
| 1 1 1 | 3.1355 | 28.466 | 100 | 100 |
| 2 0 0 | 2.7154 | 32.987 | - | - |
| 2 2 0 | 1.9201 | 47.344 | 55 | 90 |
| 3 1 1 | 1.6375 | 56.172 | 30 | 57 |
| 2 2 2 | 1.5678 | 58.909 | - | - |
| 4 0 0 | 1.3577 | 69.195 | 6 | 14 |
| 3 3 1 | 1.2459 | 76.450 | 11 | 28 |
| 4 2 2 | 1.1086 | 88.121 | 12 | 34 |
| 5 1 1 | 1.0452 | 95.055 | 6 | 18 |
| 3 3 3 | 1.0452 | 95.055 | - | - |
| 4 4 0 | 0.9601 | 106.835 | 3 | 10 |
| 5 3 1 | 0.9180 | 114.237 | 7 | 24 |
| 6 0 0 | 0.9051 | 116.796 | - | - |
| 6 2 0 | 0.8587 | 127.735 | 8 | 29 |
| 5 3 3 | 0.8282 | 137.131 | 3 | 11 |

Table C.8: Silicon [PDF, # 27-1402].

# Appendix D

# Co-Cu Binary Phase Diagram

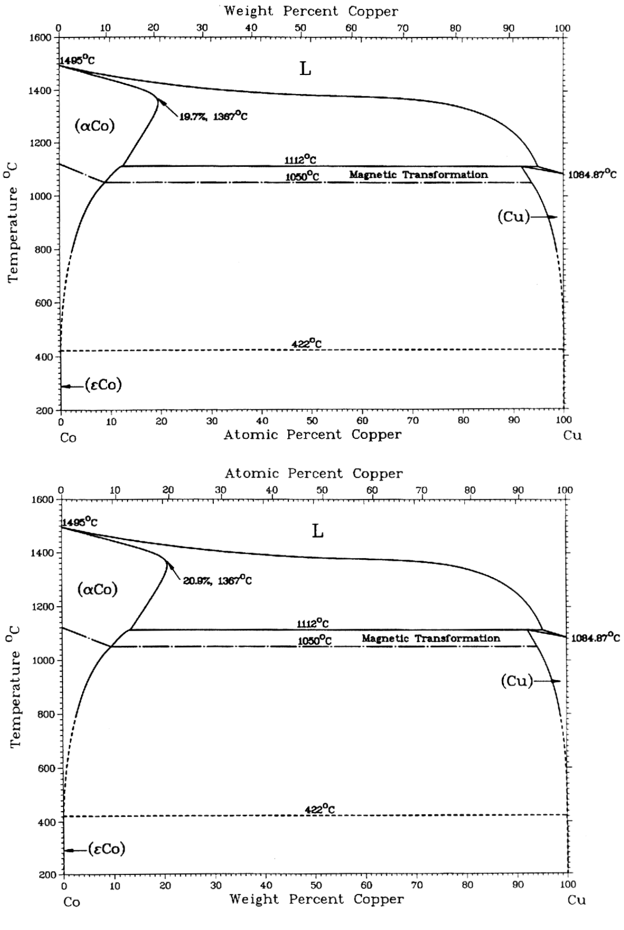

Figure D.1: Binary phase diagram of Co-Cu (from [mas90]).

.

# Bibliography

[alp94] E. A. M. van Alphen, S. G. E. te Velthuis, H. A. M. de Gronckel *et al.* : NMR study of the strain in Co-based multilayers. Phys. Rev. B 49 (1994) 17336 - 17341.

[bai88] M. N. Baibich, J. M. Broto, A. Fert, *et al.* : Giant magnetoresistance of (001)Fe/(001)Cr magnetic superlattices. Phys. Rev. Lett. 61 (1988) 21, 2472 - 2475.

[bin89] G. Binasch, P. Grünberg, F. Saurenbach, W. Zinn: Enhanced magnetoresistance in layered magnetic structures with antiferromagnetic interlayer exchange. Phys. Rev. B 39 (1989) 4828 - 4830.

[bis89] D. L. Bish, J. E. Post (Eds.): Modern Powder Diffraction. Reviews in mineralogy, Volume 20. Washington: Mineralogical Society of America 1989.

[blo94] P. J. H. Bloemen, M. T. Johnson, M. T. H. van de Vorst *et al.* : Magnetic layer thickness dependence of the interlayer exchange coupling in (001) Co/Cu/Co. Phys. Rev. Lett. 72 (1994) 764 - 767.

[bob99] M. Bobeth, M. Hentschel, G. Diener *et al.* : Theoretical investigation of the thermal stability of nanoscale layered systems. Mat. Sci. Forum Vols. 294 - 296 (1999) 613 - 616.

[bob01a] M. Bobeth, M. Hecker, W. Pompe *et al.* : Thermal stability of nanoscale Co/Cu multilayers. Z. Metallkd. 92 (2001) 810 - 819.

[bob01b] M. Bobeth, A. Ullrich, W. Pompe: Monte Carlo investigation of thermal stability and morphology development of coherent multilayers at elevated temperatures. Defect Diff. Forum 194 - 199 (2001) 1787 - 1792.

[boed93] P. Bödeker, A. Abromeit, K. Bröhl *et al.* : Growth and x-ray characterization of Co/Cu (111) superlattices. Phys. Rev. B 47 (1993) 2353 - 2361.

[boe94] D. K. G. de Boer: Influence of the roughness profile on the specular reflectivity of x-rays and neutrons. Phys. Rev. B 49 (1994) 5817 - 5820.

[boe95a] D. K. G. de Boer: X-ray reflection and transmission by rough surfaces. Phys. Rev. B 51 (1995) 5297 - 5305.

[boe95b] D. K. G. de Boer, A. J. G. Leenaers, W. W. van den Hoogenhof: Glancing-incidence x-ray analysis of thin-layered materials: a review. X-Ray Spectrometry 24 (1995) 91 - 102.

[boe96] D. K. G. de Boer: X-ray scattering and x-ray flourescence from materials with rough interfaces. Phys. Rev. B 53 (1996) 6048 - 6064.

[bru91] P. Bruno, C. Chappert: Oscillatory coupling between ferromagnetic layers separated by a nonmagnetic metal spacer. Phys. Rev. Lett. 67 (1991) 1602 - 1605.

[bru95] P. Bruno: Theory of interlayer magnetic coupling. Phys. Rev. B 52 (1995) 411 - 439.

[bru99] P. Bruno: Theory of Interlayer Exchange Coupling. In: Magnetische Schichtsysteme, 30. IFF-Ferienkurs. Forschungszentrum Jülich GmbH, Institut für Festkörperforschung. Jülich 1999. P. B8.1 - B8.39.

[brue92] H. Brückl: In-situ Rastertunnelmikroskopie zum Wachstum und Transportverhalten dünner Cr/Au-Mehrlagenschichten. Dissertation, University of Regensburg (1992).

[BS93] Heinz Niedrig (Ed.): Optik. Bergmann Schaefer Lehrbuch der Experimentalphysik, Band 3. Berlin, New York: Walter de Gruyter 1993.

[bue99] D. E. Bürgler: Zwischenschichtaustauschkopplung: Abhängigkeit vom Schichtaufbau und der Qualität der Grenzflächen. In: Magnetische Schichtsysteme, 30. IFF-Ferienkurs. Forschungszentrum Jülich GmbH, Institut für Festkörperforschung. Jülich 1999. P. B10.1 - B10.24.

[bun00] H. J. Bunge: Grain Orientation and Texture. In: Industrial Applications of X-Ray Diffraction. Eds.: F. H. Chung, D. K. Smith. New York, Basel: Marcel Dekker 2000. P. 919 - 974.

[chr98] C. Christides, S. Logothetidis, M. Gioti *et al.* : Structural, magnetotransport, and optical properties of sputtered Co/Cu multilayers examined as a funtion of Co layer thickness at the second antiferromagnetic maximum. J. Appl. Phys. 83 (1998) 7757 - 7768.

[chu00] F. H. Chung, D. K. Smith: The Principles of Diffraction Analysis. In: Industrial Applications of X-Ray Diffraction. Eds.: F. H. Chung, D. K. Smith. New York, Basel: Marcel Dekker 2000. P. 3 - 35.

[cle87] B. M. Clemens, J. G. Gay: Effect of layer-thickness fluctuations on superlattice diffraction. Phys. Rev. B 35 (1987) 9337 - 9340.

[cle92] B. M. Clemens, J. A. Bain: Stress determination in textured thin films using x-ray diffraction. Mat. Res. Soc. Bulletin 17 (1992) 46 - 51.

[coe91] R. Coehoorn: Period of oscillatory exchange interactions in Co/Cu and Fe/Cu multilayer systems. Phys. Rev. B 44 (1991) 9331 - 9337.

[cul78] B. D. Cullity: Elements of X-Ray Diffraction. Reading (Massachusetts), Menlo Park (California); London; Amsterdam; Don Mills (Ontario); Sydney: Addison Wesley Publishing Company 1978; Second Edition.

[cxro] Website of the Center for X-Ray Optics, Berkeley: http://www-cxro.lbl.gov (December 20th, 2002).

[dau97] J. M. Daughton, US Patent No. 5,617,071, April 1st, 1997.

[dem94] S. O. Demokritov, E. Tsymbal, P. Grünberg *et al.* : Magnetic-dipole mechanism for biquadratic interlayer coupling. Phys. Rev. B 49 (1994) 720 - 723.

[dem98] S. O. Demokritov: Biquadratic interlayer coupling in layered magnetic systems. J. Phys. D: Appl. Phys. 31 (1998) 925 - 941.

[die94] B. Dieny: Giant magnetoresistance in spin-valve multilayers. J. Magn. Magn. Mater. 136 (1994) 335 - 359.

[dosch96] H. Dosch: Röntgen- und Neutronenstreuung an Oberflächen und Grenzflächen. In: Streumethoden zur Untersuchung kondensierter Materie. Vorlesungsskripte des 27. IFF-Ferienkurses. Eds.: Forschungszentrum Jülich GmbH, Institut für Festkörperforschung. Jülich 1996. C12.1 - 44.

[dum35] J. W. H. DuMont and J. P. Youtz. Phys. Rev. B 48 (1935) 703.

[duv94] J. L. Duvail, A. Fert, L. G. Pereira, D. K. Lottis: Calculation of the temperature dependence of the giant MR and application to Co/Cu multilayers. J. Appl. Phys. 75 (1994) 7070 - 7072.

[ebe03a] J. Ebert, B. Stahl, M. Ghafari and H. Hahn: Thermische Stabilität von GMR-Multilagen. Talk at the final meeting of BMBF Leitprojekt “Magnetoelektronik”, Gerlingen Schillerhöhe, April 25th 2003.

[ebe03b] J. Ebert: Langzeitstabilität von GMR-Multilagen im System CoFe/Cu und CoFe/CuAgAu. Final report of BMBF main project “Magnetoelektronik”, 2003.

[ebe03c] J. Ebert, M. Ghafari, B. Stahl and H. Hahn: Annealing of $Co_xCu_{1-x}/Cu$ multilayers. Submitted to J. Phys. D.

[edw91b] D. M. Edwards, J. Mathon, R. B. Muniz: A resistor network theory of the giant magnetoresistance in magnetic superlattices. IEEE Trans. Magn. 27 (1991) 3548 - 3552.

[edw91c] D. M. Edwards, J. Mathon, R. B. Muniz, M. S. Phan: Oszillations of the exchange in magnetic multilayers as an analog of de Haas-van Alphen effect. Phys. Rev. Lett. 67 (1991) 493 - 496.

[ege92] W. F. Egelhoff Jr. and M. T. Kief: Antiferromagnetic coupling in Fe/Cu/Fe and Co/Cu/Co multilayers on Cu(111). Phys. Rev. B 45 (1992) 7795 - 7804.

[ele01] D. Elefant: Short report for the “Leitprojekt Magnetoelektronik” on the problem of magnetically dead layers. October 15th, 2001.

[ele02] D. Elefant, D. Tietjen, R. Schäfer *et al.* : High-field magnetoresistance, giant magnetoresistance, and superparamagnetism in Co/Cu multilayers. J. Appl. Phys. 91 (2002) 8590 - 8592.

[few00] P. F. Fewster: Thin Films and Multilayers. In: Industrial Applications of X-Ray Diffraction. Eds.: F. H. Chung, D. K. Smith. New York, Basel: Marcel Dekker 2000. P. 777 - 791.

[fow92] D. E. Fowler: MOKE. In: Encyclopedia of Materials Characterization. Eds.: C. R. Brundle, C. A. Evans, Jr., S. Wilson. Boston: Butterworth-Heinemann 1992. P. 723 - 735.

[GI99] Philips Analytical: X'Pert Graphics & Identify. Software for X-Ray Diffraction. Philips Electronics N. V. 1996 - 1999, Version 1.2b, 22-Nov-1999.

[gij97] M. A. M. Gijs, G. E. W. Bauer: Perpendicular giant magnetoresistance of magnetic multilayers. Adv. Phys. 46 (1997) 285 - 445.

[gir92] F. Giron, P. Boher, Ph. Houdy *et al.* : Anisotropic differential magnetoresistance of Cu/Co(100) multilayers. J. Appl. Phys. 72 (1992) 4710 - 4713.

[gir93] F. Giron, P. Boher, Ph. Houdy *et al.* : Magnetoresistance in fcc (100) Co/Cu multilayers: modeling with Cu spatial thickness fluctuations. J. Magn. Magn. Mater. 121 (1993) 318 - 321.

[gla91] G. Gladyszewski: High resolution studies of interfacial effects by small and large angle x-ray diffraction. Thin Solid Films 204 (1991) 473 - 484.

[gla98] G. Gladyszewski, S. Labat, P. Gergaud, O. Thomas: Structure characterization of metallic multilayers by symmetric and asymmetric x-ray diffraction. Thin Solid Films 319 (1998) 78 - 80.

[gla00] G. Gladyszewski *et al*: Structure of Ag/Fe superlattices probed at different length scales. Thin Solid Films 366 (2000) 51 - 62.

[got98] G. Gottstein: Physikalische Grundlagen der Materialkunde. Berlin, Heidelberg: Springer Verlag 1998.

[gro00] R. Gross, A. Marx: Grundlagen der Magnetoelektronik. Vorlesungsskript zur Vorlesung im WS 2000/2001. Walther-Meissner-Institut, Lehrstuhl für Technische Physik, Walter-Meissner-Straße 8, D-85748 Garching.

[gru86] P. Grünberg, R. Schreiber, Y. Pang *et al.* : Layered magnetic structures: evidence for antiferromagnetic coupling of Fe layers across Cr interlayers. Phys. Rev. Lett. 57 (1986) 2442 - 2445.

[gru99] P. Grünberg: Zwischenschichtaustauschkopplung: Phänomenologische Beschreibung, Materialabhängigkeit. In: Magnetische Schichtsysteme, 30. IFF-Ferienkurs. Forschungszentrum Jülich GmbH, Institut für Festkörperforschung. Jülich 1999. P. B9.1 - B9.21.

[gur93] B. A. Gurney, V. S. Speriosu, J.-P. Nozieres *et al.* : Direct measurement of spin-dependent conduction-electron mean free paths in ferromagnetic metals. Phys. Rev. Lett. 71 (1993) 4023 - 4026.

[hal93] M. J. Hall, B. J. Hickey, M. A. Howson *et al.* : Magnetoresistance of Co/Cu superlattices grown by molecular beam epitaxy. Phys. Rev. Lett. 47 (1993) 12785 - 12793.

[hea79] R. F. S. Hearmon: The Elastic Constants of Non-Piezoelectric Crystals. In: Landolt-Börnstein Numerical Data and Functional Relationships in Science and Technology Group III Vol. 11. Berlin: Springer 1979.

[hea84] R. F. S. Hearmon: The Elastic Constants of Crystals and other Anisotropic Materials. In: Landolt-Börnstein Numerical Data and Functional Relationships in Science and Technology Group III Vol. 18. Berlin: Springer 1984.

[hec01a] M. Hecker, L. van Loyen, D. Tietjen *et al.* : Influence of annealing on structural properties of metallic multilayers. Mat. Sci. Forum Vols. 378 - 381 (2001) pp. 370 - 375.

[hec01b] M. Hecker, D. Tietjen, D. Elefant *et al.* : Thermally activated deterioration processes in Co/Cu GMR multilayers. J. Appl. Phys. 89 (2001) 7113 - 7115.

[hec03] M. Hecker, J. Thomas, D. Tietjen *et al.* : Thermally induced modification of GMR in Co/Cu multilayers: correlation among structural, transport, and magnetic properties. J. Phys. D 36 (2003) 564 - 572.

[hei00] S. Heitmann: Charakterisierung und Analyse von Cu/Py-Mehrlagensystemen mit variierenden Kupferschichtdicken. Diploma Thesis, University of Bielefeld, 2000.

[holl98] H. Holloway, D. J. Kubinski: Magnetoresistive Co/Cu multilayers: Hysteresis, polycrystallinity, and irreversible changes on magnetization. J. Appl. Phys. 83 (1998) 2705 - 2714.

[hol93] V. Holý, J. Kuběna I. Ohlídal *et al.* : X-ray reflection from rough layered systems. Phys. Rev. B 47 (1993) 15896 - 15903.

[hol94] V. Holý, T. Baumbach: Nonspecular x-ray reflection from rough multilayers. Phys. Rev. B 49 (1994) 10668 - 10676.

[hol99] V. Holý: Diffuse x-ray reflection from multilayers with rough surfaces. J. Mat. Science: Mat. El. 10 (1999) 223 - 226.

[Holy99] V. Holý, U. Pietsch, T. Baumbach: High-resolution x-ray scattering from thin films and multilayers. Springer Tracts in Modern Physics Vol. 149. Berlin, Heidelberg, New York: Springer Verlag 1999.

[hue02] A. Hütten, T. Hempel, S. Heitmann, and G. Reiss: The limit of the giant magnetoresistance effect in only three layers. Phys. Stat. Sol. (a) 189 (2002) 327 - 338.

[hum91] J. F. Humphreys: Recrystallization and Recovery. In: Materials Science and Technology Vol. 15: Processing of Metals and Alloys. Vol. Ed.: R. W. Cahn. Weinheim, VCH Verlagsgesellschaft 1991.

[jed01] F. J. Jedema, A. T. Filip and B. J. van Wees: Electrical spin injection and accumulation at room temperature in an all-metal mesoscopic spin valve. Nature 410 (2001) 345 - 348.

[jen96] R. Jenkins, R. L. Snyder: Introduction to X-Ray Powder Diffractometry. New York, Chichester, Brisbane, Toronto, Singapore: John Wiley & Sons, Inc. 1996.

[joh92a] M. T. Johnson, S. T. Purcell, N. W. E. McGee *et al.* : Structural dependence of the oscillatory exchange interaction across Cu layers. Phys. Rev. Lett. 68 (1992) 2688 - 2691.

[joh92b] M. T. Johnson, R. Coehoorn, J. J. de Vries *et al.* : Orientational dependence of the oscillatory exchange interaction in Co/Cu/Co. Phys. Rev. Lett. 69 (1992) 969 - 972.

[joh96] M. T. Johnson, P. J. H. Bloemen, F. J. A. den Broeder, J. J. de Vries: Magnetic anisotropy in metallic multilayers. Rep. Prog. Phys. 59 (1996) 1409 - 1458.

[kie31] H. Kiessig: Interferenz von Röntgenstrahlen an dünnen Schichten. Annalen der Physik 5. Folge, Bd. 10 (1931) 769 - 788.

[klu74] H. P. Klug, L. E. Alexander: X-Ray Diffraction Procedures. New York, London, Sydney, Toronto: John Wiley & Sons, Inc. 1974; Second edition.

[kop93] K. Kopitzki: Einführung in die Festkörperphysik. 3rd rev. Ed. Stuttgart: Teubner 1993.

[kra00] I. Kraus, N. Ganev: Residual Stress and Stress Gradients. In: Industrial Applications of X-Ray Diffraction. Eds.: F. H. Chung, D. K. Smith. New York, Basel: Marcel Dekker 2000. P. 793 - 811.

[kri94] H. Krischner, B. Koppelhuber-Bitschnau: Röntgenstrukturanalyse und Rietveldmethode. Braunschweig: Friedr. Vieweg & Sohn Verlagsgesellschaft mbH 1994, 5th editon.

[kub97a] D. J. Kubinski, H. Holloway: Giant magnetoresistance in $\mathrm{Co_{1-x}Cu_x}$/Cu multilayers: A new approach to reduced magnetoresistive hysteresis. J. Appl. Phys. 82 (1997) 322 - 325.

[kub97b] D. J. Kubinski, H. Holloway: Co/Cu multilayers with reduced magnetoresistive hysteresis. J. Magn. Magn. Mater. 165 (1997) 104 - 107.

[lan98] J. Langer: Zur Morphologie gesputterter Co/Cu- und CoZr/Cu-Viellagenschichten unter besonderer Berücksichtigung der strukturellen Grenzflächeneigenschaften. Dissertation, Friedrich-Schiller-Universität Jena (1998).

[lan99] J. Langer, J. Kräußlich, R. Mattheis, *et al.* : Characterisation of interfacial properties in sputtered Co/Cu multilayers: X-ray reflectometry compared with TEM and AFM. J. Magn. Magn. Mater. Vols. 198 - 199 (1999) 644 - 646.

[lan00] J. I. Langford: Line Profiles and Sample Microstructure. In: Industrial Applications of X-Ray Diffraction. Eds.: F. H. Chung, D. K. Smith. New York, Basel: Marcel Dekker 2000. P. 751 - 775.

[lan00b] J. I. Langford, D. Louër, P. Scardi: Effect of a crystallite size distribution on X-ray diffraction line profiles and whole-powder pattern fitting. J. Appl. Cryst. 33 (2000) 964 - 974.

[lar99] D. J. Larson, A. K. Petford-Long, A. Cerezo, G. D. W. Smith: Three-dimensional atom probe studies of metallic multilayers. Acta Mater. 47 (1999) 4019 - 4024.

[len94] S. K. J. Lenczowski *et al.* : Interpretation of the giant magnetoresistance effect in Co/Cu(100) multilayers with the quantum model of giant magnetoresistance. Phys. Rev. B 50 (1994) 9982 - 9988.

[liu96] X. Liu, M. M. Steiner, R. Sooryakumar *et al.* : Exchange stiffness, magnetization, and spin waves in cubic and hexagonal phases of cobalt. Phys. Rev. B 53 (1996) 12166 - 12172.

[mal00] L. Małkiński, J.-Q. Wang, W. Zhou, T. Kondenkandath: Influence of annealing on magnetoresistance of Co/Cu multilayers. Thin Solid Films 375 (2000) 59 - 63.

[mas90] T. Massalski (Ed.): Binary Alloy Phase Diagrams, second edition. ASM International 1990.

[mat91] J. Mathon: Exchange interactions and giant magnetoresistance in magnetic multilayers. Contemporary Physics 32 (1991) 143-156.

[mat97] J. Mathon, M. Villeret, A. Umerski *et al.* : Quantum-well theory of the exchange coupling in magnetic multilayers with application to Co/Cu/Co(001). Phys. Rev. B 56 (1997) 11797 - 11809.

[MC92] Encyclopedia of Materials Characterization. Eds. C. R. Brundle, C. A. Evans, Jr., S. Wilson. Boston, London, Oxford: Butterworth-Heinemann 1992.

[mos91] D. H. Mosca, F. Petroff, A. Fert *et al.* : Oscillatory interlayer coupling and giant magnetoresistance in Co/Cu multilayers. J. Magn. Magn. Mater. 94 (1991) L1 - L5.

[mot64] N. F. Mott: Electrons in Transition Metals. Advances in Physics 13 (1964) 325 - 420.

[gui94] T. R. McGuire, J. M. Harper, C. Cabral, Jr., T. S. Plaskett: Giant magnetoresistance in Co/Cu multilayers after annealing J. Appl. Phys. 76 (1994) 6601 - 6603.

[mic95] C. Michaelsen: On the structure and homogeneity of solid solutions: the limits of conventional X-ray diffraction. Phil. Mag. A 72 (1995) 813 - 828.

[mro98] S. Mrozek: Vergleich des Riesenmagnetowiderstandes und Magnetismus von granularen, kontinuierlichen und diskontinuierlichen Viellagensystemen. Diploma Thesis, University of Bielefeld (1998).

[nev80] L. Névot, P. Croce: Charactérisation des surfaces par réflexion rasante de rayons X. Application à l'étude du polissage de quelques verres silicates. Revue Phys. Appl. 15 (1980) 761.

[noy87] I. C. Noyan, J. B. Cohen: Residual Stress. Measurement by Diffraction and Interpretation. New York, Berlin, Heidelberg, London, Paris, Tokyo: Springer 1987.

[par54] L. G. Parratt: Surface studies of solids by total reflection of x-rays. Phys. Rev. 95 (1954) 359 - 369.

[par90] S. S. P. Parkin, N. More, K. P. Roche: Oscillations in exchange coupling and magnetoresistance in metallic superlattice structures: Co/Ru, Co/Cr, and Fe/Cr. Phys. Rev. Lett. 64 (1990) 2304 - 2307.

[par91b] S. S. P. Parkin, R. Bhadra, K. P. Roche: Oscillatory magnetic exchange coupling through thin copper layers. Phys. Rev. Lett. 66 (1991) 2152 - 2155.

[pau03] A. Paul, T. Damm, D. E. Bürgler *et al.* : Correlation of magnetotransport and structure in sputtered Co/Cu multilayers. J. Phys.: Cond. Mat. 15 (2003) 2471 - 2491.

[pay93] A. P. Payne, B. M. Clemens: Influence of roughness distributions and correlations on x-ray diffraction from superlattices. Phys. Rev. B 47 (1993) 2289 - 2300.

[PDF] The Powder Diffraction File. International Centre for Diffraction Data. Release 1999.

[pen95] A. S. Penfold: Magnetron Sputtering. In: Handbook of Thin Film Process Technology. Eds.: D. A. Glocker, S. I. Shah. Bristol, Philadelphia: Institute of Physics Publishing 1995. Pages A.3.2:1 - A.3.2:27.

[pom99] W. Pompe, A. Ullrich, M. Bobeth: Modelling of microstructure development in nanoscale layered systems. Mat. Res. Soc. Symp. Proc. 562 (1999) 153 - 158.

[pre96] W. Press, M. Tolan: Spekuläre und nicht-spekuläre Reflexion von Röntgen- und Neutronenstrahlen. In: Streumethoden zur Untersuchung kondensierter Materie. Vorlesungsskripte des 27. IFF-Ferienkurses. Eds.: Forschungszentrum Jülich GmbH, Institut für Festkörperforschung. Jülich 1996. C11.1 - 36.

[ps] P. Schmollngruber, Robert Bosch GmbH, private communication.

[qiu92] Z. Q. Qiu, J. Pearson, and S. D. Bader: Oscillatory interlayer magnetic coupling of wedged Co/Cu/Co sandwiches grown on Cu(100) by molecular beam epitaxy. Phys. Rev. B 46 (1992) 8659 - 8662.

[rae99] K. Rätzke, M. J. Hall, D. B. Jardine *at al* : Evolution of microstructure and magnetoresistance in Co/Cu multilayers during annealing. J. Magn. Magn. Mater. 204 (1999) 61 - 67.

[rei97] L. Reimer: Transmission Electron Microscopy. Springer Series in Optical Sciences Volume 36, 4th edition. Berlin, Heidelberg, New York: Springer 1997.

[rm] R. Mattheis, Institute for Physical High Technology, Jena, private communication.

[ros87] P. L. Rossiter: The electrical resistivity of metals and alloys. Cambridge, London, New York: Cambridge University Press 1987.

[sac02] M. D. Sacher: Präparation und Charakterisierung von Mehrfachbarrieren für magnetische Tunnelelemente. Diploma Thesis, University of Bielefeld, 2002.

[san99] D. Sander: The correlation between mechanical stress and magnetic anisotropy in ultrathin films. Rep. Prog. Phys. 62 (1999) 809 - 858.

[sav91] D. E. Savage, J. Kleiner, N. Schimke *et al.* : Determination of roughness correlations in multilayer films for x-ray mirrors. J. Appl. Phys. 69 (1991) 1411 - 1424.

[scher18] P. Scherrer: Estimation of the size and internal structure of colloidal particles by means of Röntgen. Nachr. Ges. Wiss. Göttingen, Math.-Phys. Kl.2 (1918) 96 - 100.

[schlei01] J. Schleiwies: Nanoanalyse höchster Auflösung von metallischen Schichtsystemen. Dissertation, University of Göttingen, 2001.

[schlei01b] J. Schleiwies, G. Schmitz, S. Heitmann, A. Hütten: Nanoanalysis of Co/Cu/NiFe thin films by tomographic atom probe. Appl. Phys. Lett. 78 (2001) 3439 - 3441.

[schlom95] J.-P. Schlomka, M. Tolan, L. Schwalowsky *et al.* : X-ray diffraction from Si/Ge layers: Diffuse scattering in the region of total external reflection. Phys. Rev. B 51 (1995) 2311 - 2321.

[schrey93] A. Schreyer, K. Bröhl, J. F. Ankner *et al.* : Oscillatory exchange coupling in Co/Cu(111) superlattices. Phys. Rev. B 47 (1993) 15334 - 15337.

[schrey94] A. Schreyer: Spin Polarized Neutron Reflectometry and X-Ray Scattering on Exchange Coupled Superlattices. Dissertation, Ruhr-Universität Bochum (1994).

[schul99] I. K. Schuller, S. Kim, and C. Leighton: Magnetic superlattices and multilayers. J. Magn. Magn. Mater. 200 (1999) 571 - 582.

[seg73] A. Segmüller, A. E. Blakeslee: X-ray diffraction from one-dimensional superlattices in GaAs$_{1-x}$P$_x$ Crystals. J. Appl. Cryst. 6 (1973) 19 - 25.

[sin88] S. K. Sinha, E. B. Sirota, S. Garoff, H. B. Stanley: X-ray and neutron scattering from rough surfaces. Phys. Rev. B 38 (1988) 2297 - 2311.

[sin91] S. K. Sinha: Reflectivity using neutrons or X-rays? A critical comparison. Physica B 173 (1991) 25 - 34.

[sin94] S. K. Sinha: X-ray diffuse scattering as a probe for thin film and interface structure. J. Phys. (France) III 4 (1994) 1543 - 1557.

[slo91] J. C. Slonczewski: Fluctuation mechanism for biquadratic exchange coupling in magnetic multilayers. Phys. Rev. Lett. 67 (1991) 3172 - 3175.

[slo93] J. C. Slonczewski: Origin of biquadratic exchange in magnetic multilayers. J. Appl. Phys. 73 (1993) 5957 - 5962.

[sny99] R. L. Snyder: X-Ray Diffraction. In: X-Ray Characterization of Materials. Eds.: E. Lifshin. Weinheim, New York, Chichester u.a.: Wiley-VCH 1999. P. 1 - 103.

[sta98] C. Stamm, Ch. Würsch, S. Egger, D. Pescia: Amplification of the short-wavelength oscillations in exchange coupled Co-films by low-temperature deposition. J. Magn. Magn. Mater. 177 - 181 (1998) 1279 - 1280.

[ste88] M. B. Stearns: Microcrystalline and interface structure of metallic multilayers from x-ray spectra. Phys. Rev. B 38 (1988) 8109 - 8113.

[sti93] M. D. Stiles: Exchange coupling in magnetic heterostructures. Phys. Rev. B 48 (1993) 7238 - 7258.

[sti99] M. D. Stiles: Interlayer exchange coupling. J. Magn. Magn. Mater. 200 (1999) 322 - 337.

[sturm96] K. Sturm: Wechselwirkung von thermischen Neutronen und Röntgenstrahlen mit Atomkernen und Elektronen. In: Streumethoden zur Untersuchung kondensierter Materie. Vorlesungsskripte des 27. IFF-Ferienkurses. Eds.: Forschungszentrum Jülich GmbH, Institut für Festkörperforschung. Jülich 1996. A2.1 - 30.

[sud00] D. Sudfeld: Aufbau eines Meßplatzes für magnetfeldabhängige Messungen der Magnetisierung und des Magnetowiderstands dünner Schichten. Written work presented for an examination, University of Bielefeld (2000).

[tho99] J. Thomas, K. Brand, A. A. Gorbunov, K. Wetzig: Morphology and structure of nanoscale Co-Cu multilayers. Fresenius J. Anal. Chem. 365 (1999) 263 - 268.

[tsy01] E. Y. Tsymbal, D. G. Pettifor: Perspectives of giant magnetoresistance. Sol. Stat. Phys. 56 (2001) 113 - 237.

[tu92] K.-N. Tu, J. W. Mayer, L. C. Feldman: Electronic Thin Film Science (For Electrical Engineers and Materials Scientists). New York: Macmillan Publishing Company 1992.

[ull00] A. Ullrich, M. Bobeth, W. Pompe: Monte Carlo investigation of the thermal stability of coherent multilayers. Scripta mater. 43 (2000) 887 - 892.

[van89] J. Vancea: Unconventional features of free electrons in polycrystalline metal films. International Journal of Modern Physics B 3 (1989) 1455 - 1501.

[vin82] G. H. Vineyard: Grazing-incidence diffraction and the distorted-wave approximation for the study of surfaces. Phys. Rev. B 26 (1982) 4146 - 4159.

[war69] B. E. Warren: X-Ray Diffraction. Reading (Massachusetts), Menlo Park (California); London; Don Mills (Ontario): Addison Wesley Publishing Company 1969.

[web95] W. Weber, R. Allenspach, and A. Bischof: Exchange coupling across Cu(100): A High-Precision Study. Europhys. Lett. 31 (1995) 491 - 496.

[WinGixa] Philips Analytical: WinGixa. Software for the Simulation and Fit of X-Ray Reflectometry Scans. Philips Analytical X-Ray B.V. - Almelo, The Netherlands. Philips Electronics N. V. 1998, Version 1.102b, 03-Nov-1998.

[XP00] X'Pert PRO User's Guide. Philips Analytical B.V. - Almelo, The Netherlands. Koninklijke Philips Electronics N. V. 2000.

[yaf87a] Y. Yafet: RKKY interactions across yttrium layers in Gd-Y superlattices. J. Appl. Phys. 61 (1987) 4058 - 4060.

[yaf87b] Y. Yafet: Ruderman-Kittel-Kasuya-Yosida range function of a one-dimensional free-electron gas. Phys. Rev. B 36 (1987) 3948 - 3949.

[yon63] Y. Yoneda: Anomalous surface reflection of x-rays. Phys. Rev. 131 (1963) 2101 - 2013.

[zab94] H. Zabel: X-ray and neutron reflectivity analysis of thin films and superlattices. Appl. Phys. A 58 (1994) 159 - 168.

[zha94] H. Zhang, R. W. Cochrane, Y. Huai *et al.* : Effect of annealing on the giant magnetoresistance of sputtered Co/Cu multilayers. J. Appl. Phys. 75 (1994) 6534 - 6536.

# Publications and Conferences

## Publications

A. Hütten, S. Mrozek, S. Heitmann, T. Hempel, H. Brückl, and G. Reiss: *Evolution of the GMR-effect amplitude in copper/permalloy-multilayered thin films.* Acta Mat. 47 (1999) 4245 - 4252.

S. Heitmann, A. Hütten, T. Hempel, W. Schepper,G. Reiss, and C. Alof: *Interplay of antiferromagnetic coupling in copper/permalloy combination multilayers.* J. Appl. Phys. 87 (2000) 4849 - 4851.

J. Schleiwies, G. Schmitz, S. Heitmann, and A. Hütten: *Nanoanalysis of Co/Cu/NiFe thin films by tomographic atom probe.* Appl. Phys. Lett. 78 (2001) 3439 - 3441.

S. Heitmann, A. Hütten, T. Hempel, W. Schepper and G. Reiss: *Enhanced GMR amplitude and temperature stability of copper/permalloy combination multilayers.* J. Magn. Magn. Mater. 226 (2001) 1752 - 1754.

A. Hütten, T. Hempel, S. Heitmann, and G. Reiss: *The limit of the giant magnetoresistance effect in only three layers.* Phys. Stat. Sol. A 189 (2002) 327 - 338.

M. Y. Zhuravlev, W. Schepper, S. Heitmann, H. Vinzelberg, P. Zahn, I. Mertig, H. O. Lutz, A. V. Vedyayev, G. Reiss, and A. Huetten: *Reliable prediction of giant magnetoresistance characteristics.* Phys. Rev. B 65 (2002) No. 144428.

D. Sudfeld, K. Wojczykowski, W. Hachmann, S. Heitmann, K. Rott, T. Hempel, S. Kämmerer, R. Jutzi, A. Huetten, and G. Reiss: *Magnetic cobalt nanocrystals organized in patches and chains.* IEEE Trans. Mag. 38 (2002) 2601 - 2603.

G. Reiss, H. Brückl, A. Hütten, J. Schmalhorst, M. Justus, A. Thomas, and S. Heitmann: *Spinelectronics and its application.* Phys. Stat. Sol. B 236 (2003) 289 - 302.

T. Luciński, A. Hütten, H. Brückl, T. Hempel, S. Heitmann, and G. Reiss: *Magnetoresistive properties of* $Ni_{80}Fe_{20}/Co1/CuAgAu/Co2$ *pseudo-spin-valves.* Phys. Stat. Sol. A 196 (2003) 97 -100.

S. Kämmerer, S. Heitmann, D. Meyners, D. Sudfeld, A. Thomas, A. Huetten, and G. Reiss: *Room-temperature preparation and magnetic behaviour of* $Co_2MnSi$ *thin films.* J. Appl. Phys. 93 (2003) 7945 - 7947.

T. Luciński, M. Kopcewicz, A. Hütten, H. Brückl, S. Heitmann, T. Hempel, and G. Reiss: *Magnetic and mössbauer study of Fe/Si multilayers.* J. Appl. Phys. 93 (2003) 6501 - 6503.

T. Luciński, M. Kopcewicz, A. Hütten, H. Brückl, S. Heitmann, T. Hempel, and G. Reiss: *Magnetic properties of Fe/Si and Co/Si multilayers.* Materials Science-Poland 21 (2003) 25 - 27.

T. Luciński, A. Hütten, H. Brückl, S. Heitmann, T. Hempel, and G. Reiss: *Magnetoresistance study of* $Ni_{80}Fe_{20}/Co1/CuAgAu/Co2$ *asymmetric sandwiches.* J. Magn. Magn. Mater. 269 (2004) 78 - 88.

## Patent

Co-author: *Magnetoresistives Element.* Filed for patenting in cooperation with Robert Bosch GmbH 1999.

## Conferences

1999 Frühjahrstagung der Deutschen Physikalischen Gesellschaft (Münster): *Kennlinien und Temperaturstabilität von kombinierten Cu/Py Vielfachschichtsystemen.* (Vortrag)

1999 Annual Conference on Magnetism and Magnetic Materials (San Jose, CA, USA): *Interplay of Antiferromagnetic Coupling in Cu/Py Combination Multilayers.* (Poster)

2000 Frühjahrstagung der Deutschen Physikalischen Gesellschaft (Regensburg): *Wechselwirkung unterschiedlicher antiferromagnetischer Kopplungen in Cu/Py Kombinationsschichten.* (Talk)

2000 International Conference on Magnetism and Magnetic Materials (Recife, Brazil): *Enhanced GMR Amplitude and Temperature Stability of Copper/Permalloy Combination Multilayers.* (Poster)

2001 Frühjahrstagung der Deutschen Physikalischen Gesellschaft (Hamburg): *Temperaturstabilität von Sandwiches und Multilagen.* (Vortrag)

2001 International Symposium on Metallic Multilayers (Aachen): *Enhancing spin dependent scattering in simple sandwich structures .* (Poster)

# Danksagung

An dieser Stelle möchte ich all denen ganz herzlich danken, die mit ihrer Unterstützung sowie Rat und Tat zu dieser Arbeit beigetragen haben.

An erster Stelle gilt dies für meine Betreuer Prof. Günter Reiss und PD Dr. Andreas Hütten. Sie haben diese Arbeit nicht nur durch die Aufgabenstellung und materielle Unterstützung ermöglicht, sondern waren stets in fachlichen und menschlichen Fragen erreichbar. Darüberhinaus war diese Zeit geprägt durch Andreas' unerschütterlichen Optimismus, von dem ich hoffe ein Stückchen mitzunehmen!

Den Assistenten PD Dr. Hubert Brückl und Dr. Jan Schmalhorst sowie Dr. Willi Schepper möchte ich für Diskussionen und Ratschläge danken als auch für ein Arbeitsklima, dass sich durch Interesse und Offenheit für die Arbeit aller ausgezeichnet hat.

Herrn Prof. Guido Schmitz und Herrn Dr. Jörg Schleiwies danke ich für die sehr gute Zusammenarbeit im Rahmen des DFG-Projekts "Mikroanalyse höchster Auflösung von magnetischen Funktionsschichten der Sensortechnik" sowie für TEM-Aufnahmen.

Der Robert Bosch GmbH und dem IPHT Jena danke ich für die Bereitstellung der Co/Cu-Multilagen Probenserien sowie für die erfolgreiche Zusammenarbeit im Rahmen des Leitprojekts "Magnetoelektronik" des Bundesministeriums für Bildung und Forschung.

Bei Herrn Dr. O. Anderson, Schott Glaswerke Mainz, möchte ich mich ganz herzlich für die unbürokratische Einführung in die Röntgenreflektometrie bedanken.

Tobias Hempel danke ich für die langjährige und diskussionsreiche Zusammenarbeit. Ein herzliches Dankeschön geht an Sven Kämmerer für die prompte und zuverlässige Hilfe gerade in der Zeit des Zusammenschreibens sowie für die ergänzenden Röntgenscans und die Tieftemperaturmessungen.

Besonderer Dank gilt auch all denen, die Messungen für mich durchgeführt haben sowie denen, die die benötigen Apparaturen aufgebaut und gewartet haben:

Inga Ennen (MOKE, AGM), Dr. Jan Schmalhorst (Ofen, Moke), Daniel Starke (Auswerteprogramm für GMR und Moke), Ingo Rohde (Ofen, GMR), Dr. Andy Thomas (Sputteranlage), Dr. Karsten Rott (Strukturierung), Jan Bornemeier (Bonden), Dirk Meyners (AFM), Daniela (Auswertung TEM) sowie den zahlreichen studentischen Hilfskräften.

Herzlich bedanken möchte ich mich auch bei Dr. Maik Justus, Dr. Olaf Höbel sowie Volker Güth für die kompetente und schnelle Hilfe bei allen Fragen zu Software und PC. Marlene Hahn und Annette Panhorst danke ich für die gute Zusammenarbeit. Auch bei der Elektronik- und der Mechanikwerkstatt bedanke ich mich für schnelle, zuverlässige und sehr freundliche Hilfe.

Dem gesamten D2-Team spreche ich ein besonders herzliches Dankeschön aus für die hervorragende Arbeitsatmosphäre und die schöne Zeit.

Der Deutschen Forschungsgemeinschaft danke ich für die Unterstützung meiner Arbeit durch das Projekt “Mikroanalyse höchster Auflösung von magnetischen Funktionsschichten der Sensortechnik” sowie dem Folgeprojekt.

Der Miele & Cie. KG danke ich für die flexible Gleitzeitregelung sowie für das Verständnis und die Unterstützung in der Zeit des Fertigstellens der Arbeit.

Für die unermüdliche Unterstützung danke ich meinen Eltern, allen Freunden und ganz besonders meinem Verlobten Rolf. Er hat einen Orden verdient!